Relationship between Asphalt Binder Fatigue Properties and Mixture Fatigue Performance

by

Zhaoxing Xie

A dissertation submitted to the Graduate Faculty of
Auburn University
in partial fulfillment of the
requirements for the Degree of
Doctor of Philosophy of Science

Auburn, Alabama
August 4, 2018

Keywords: Asphalt Binder Fatigue Properties, Mixture Fatigue Performance, Relationship

Approved by

Nam Tran, Chair, Assistant Director, National Center for Asphalt Technology
Randy West, Director, National Center for Asphalt Technology
Michael Heitzman, Assistant Director, National Center for Asphalt Technology
David Timm, Brasfield & Gorrie Professor, Civil Engineering
Maria Auad, Director and Professor, Chemical Engineering

ABSTRACT

Fatigue cracking caused by repeated traffic loading is one of the major distresses in asphalt pavement. To control fatigue cracking, the current Superpave binder specification requires a maximum value of 5,000 kPa for the binder loss modulus ($G^* \times \sin(\delta)$) at the intermediate temperature. However, recent research has shown that this criterion may not be a good indicator of the laboratory and field fatigue cracking performance of asphalt mixtures. Therefore, it is desirable to identify another binder property and/or test method that can better predict the fatigue cracking performance of asphalt mixtures. The objective of this study was to investigate the relationship between asphalt binder properties and mix fatigue performance, and to find another binder property and/or test method for evaluating asphalt binder fatigue property.

A laboratory experiment including sixteen asphalt binders representing a wide range of performance grades used in the United States was first conducted. Several binder tests were conducted on each binder. In addition, these binders were used in a 9.5-mm nominal maximum aggregate size mix design for uniaxial and flexural fatigue tests. The binder fatigue/fracture properties were evaluated through the following index parameters: modified linear amplitude sweep fatigue life, loss modulus, delta Tc, loss tangent, crossover frequency, rheological index, and Glover-Rowe value. The mix fatigue properties were investigated through the traditional phenomenological approach, the dissipated energy approach, and the simplified viscoelastic

continuum damage approach. The relationship between binder properties and mix fatigue performance was then evaluated.

Results of this study indicated that the modified linear amplitude sweep test could be a promising test to evaluate the binder fatigue property as the results from this test exhibited better correlations with mix fatigue performance, compared to the other binder properties.

ACKNOWLEDGEMENTS

I would first like to acknowledge my advisor and committee chair, Dr. Nam Tran, for his guidance and support during these years. Dr. Tran has been an excellent guide, and he not only taught me knowledge but also the philosophy of work and life. His invaluable guidance has benefited my study, work style and life. His well-organized and effective style of work has had deep impact on me. I am so grateful and honored to have been his student.

Secondly, I would like to thank Dr. Randy West, Dr. Michael Heitzman, and Dr. David Timm for serving as my committee members. Their valuable and constructive suggestions and comments have benefited this dissertation and are helpful for my future work.

Thirdly, I would like to thank Pamela Turner and Adam Taylor for their assistance and work during this research. Ms. Pamela and Mr. Taylor always answered my questions with patience. I would also like to thank Tina Ferguson for her hard work for this study. Additionally, I would like to thank other members of NCAT family for their help. It was a wonderful experience for me to study and live in Auburn as a member of NCAT family and Tiger Family.

Next, I would like to thank Dr. Donald Christensen from Advanced Asphalt Technologies for sharing their research data. Dr. Christensen is the principal investigator of the NCHRP 9-50 project, and I have learned a lot from his new approach towards asphalt binder fatigue.

Finally, I would like to thank my wife, Peifen Wu, for her love and support. I cannot imagine completing this dissertation and my study in Auburn without her companionship. I wish to thank my parents, parents-in-law, and brother for their support and encouragement throughout my study.

TABLE OF CONTENTS

LIST OF TABLES

LIST OF FIGURES

CHAPTER 1 – INTRODUCTION

1.1 Problem Statement

Fatigue cracking is one of the major distresses in an asphalt pavement, which is caused by repeated traffic loading. There are two types of fatigue cracking: bottom-up cracking and top-down cracking. Bottom-up cracking (**Figure 1**) develops from the bottom of the asphalt layer towards the surface, and it results from the tensile strain at the bottom of the asphalt layer due to traffic loading. Top-down cracking (**Figure 2**) originates at the surface and develops down, which is caused by shear and tensile stresses on the pavement surface under heavily loaded tires.

Figure 1. Bottom-up Cracking (Gibson et al., 2012)

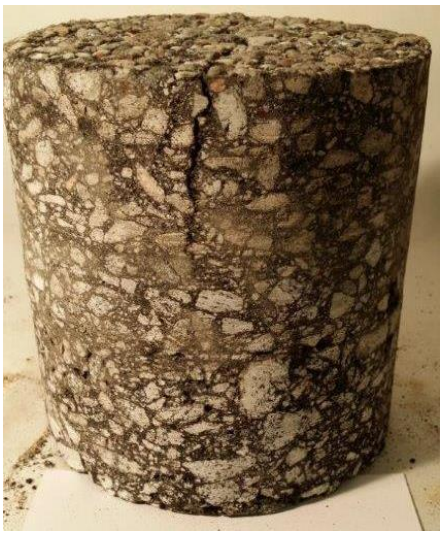

Figure 2. Top-down Cracking (Moore, 2016)

Fatigue cracking is affected by the several factors: 1) traffic load and volume, 2) pavement structure, 3) subgrade modulus, 4) pavement drainage capacity, and 5) asphalt mixture fatigue property. For a specific asphalt mixture, the asphalt binder fatigue property is one of the most important factors affecting mixture fatigue performance. It is important to have a measure of the fatigue characteristics of binders to avoid the premature fatigue distresses in the asphalt pavement. In the current Superpave binder specification, a maximum value of 5,000 kPa for the binder loss modulus ($G^*\sin(\delta)$) at selected intermediate temperatures is required for all binders after 20-hour pressure aging vessel (PAV) aging, ensuring their satisfactory fatigue performance. The criterion of 5,000 kPa for $G^*\sin(\delta)$ was developed based on the data from the Zaca-Wigmore road test sections built in the mid to late 1950s (**Figure 3**). As shown in **Figure 3**, a dramatic increase in field fatigue cracking was observed when the estimated loss modulus of the binder exceeded a value of about 3 MPa. Based on this observation, the Strategic Highway Research Program (SHRP) researchers recommended a limit of 3 MPa for $G^*\sin(\delta)$. However, the Federal Highway Administration (FHWA) Asphalt Expert Task Group (ETG) adjusted this limit to 5 MPa, which is

used in the current specification of American Association of State Highway and Transportation Officials (AASHTO) M 320 (Gibson et al., 2012).

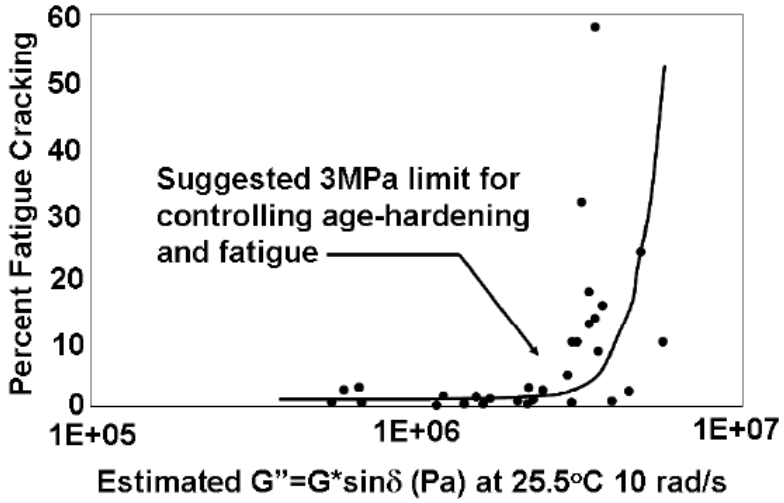

Figure 3. Estimated Loss Modulus (G") vs. Field Cracking in Zaca-Wigmore Test Road (Anderson and Kennedy, 1993)

However, G*sin(δ) has not shown a strong correlation with laboratory fatigue results of mixtures and field fatigue performance in the recent studies (Deacon et al., 1997; Bahia et al., 2001; Stuart et al., 2001; Tsai and Monismith, 2005; Gibson et al., 2012). For example, Bahia et al. (2001) explored the correlations between asphalt binder G*sin(δ) and mixture fatigue life through laboratory tests on four aggregate gradations and nine asphalt binders. In this study, the dynamic shear rheometer (DSR) tests were performed on the rolling thin film oven (RTFO)-aged binders at the temperatures where G*sin(δ) is equal to 5,000 kPa for the PAV-aged binders, and bending beam fatigue (BBF) tests were conducted on the short-term oven aged mixtures. A loading frequency of 10 Hz was used for the test and controlled strains ranging from 250 to 750

microstrains. **Figure 4** shows the correlations between G*sin(δ) and mixture fatigue life, indicating the correlations between the binder G*sin(δ) and the mixture fatigue life and were weak.

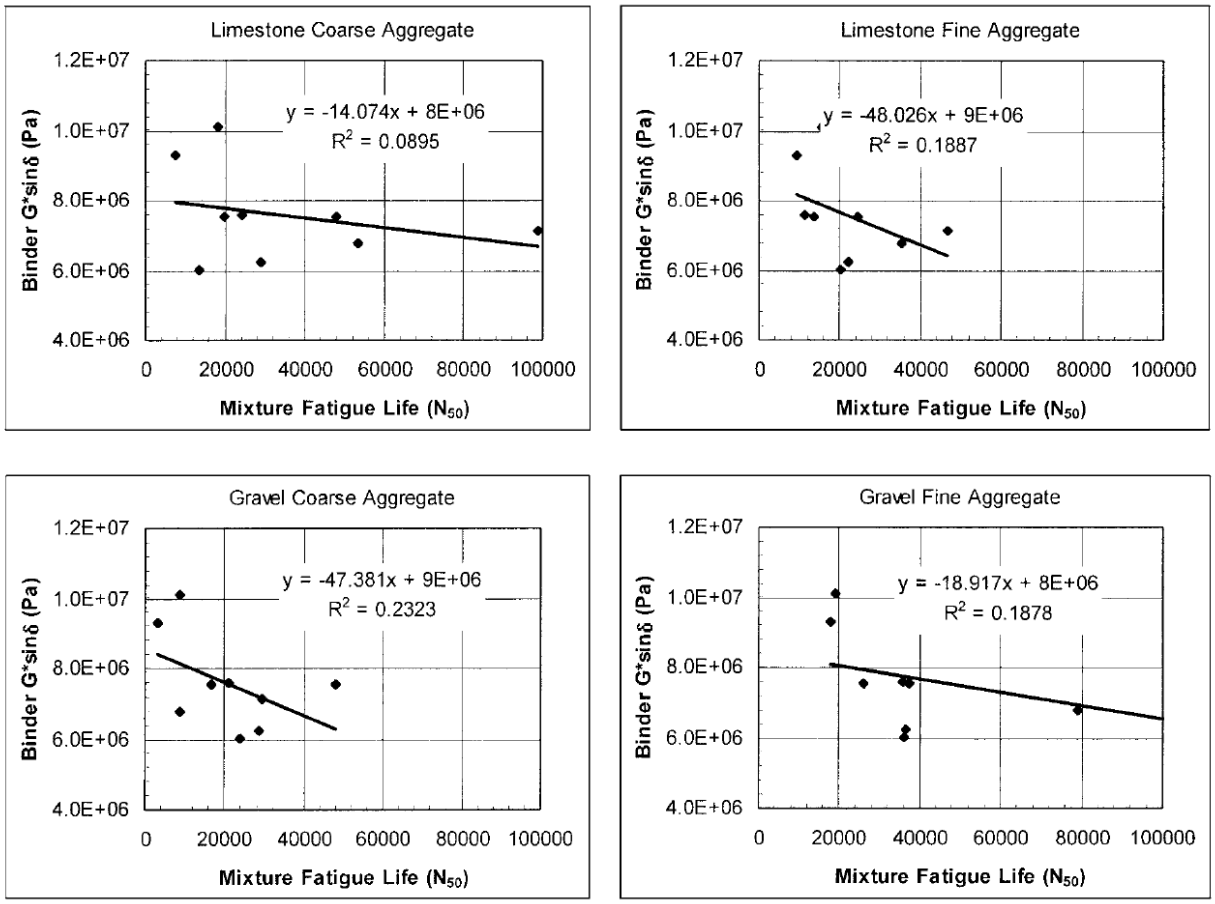

Figure 4. Correlation between G*sin(δ) and Mixture Fatigue Life (Bahia et al., 2001)

In addition to the laboratory property comparison, Stuart et al. (2001) compared binder G*sin(δ) values to the field performance in the FHWA accelerated loading facility (ALF) experiment (**Figure 5**). They found that the G*sin(δ) had a good and expected relationship with ALF fatigue life in the thinner pavements (100-mm asphalt layer), while the opposite trend was observed in the thicker pavements (200-mm asphalt layer).

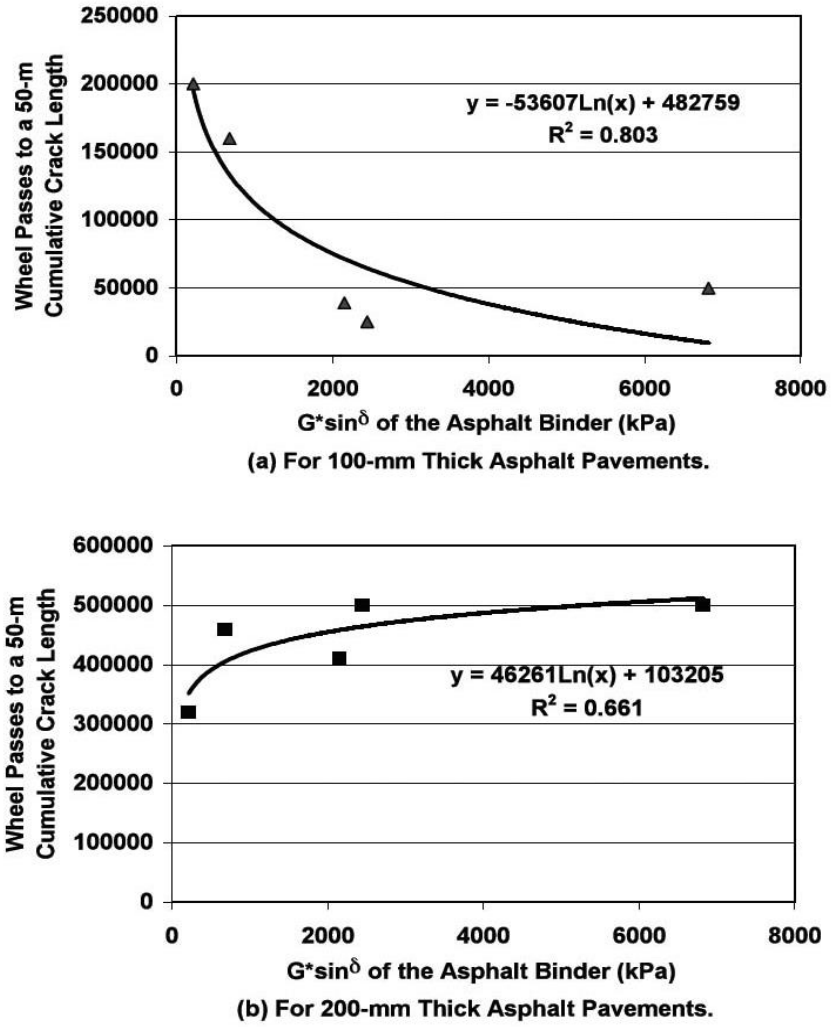

Figure 5. Binder G*sin(δ) vs. FHWA-ALF Fatigue Life (Stuart et al., 2001)

1.2 Objectives and Scope of Work

Since the current criterion for binder fatigue may not be a good indicator of the laboratory and field fatigue performance of asphalt mixtures, it is desirable to identify another binder property and/or test method that can have better correlations with mixture fatigue performance. The objectives of this study were to 1) determine relationships between asphalt binder properties and mix fatigue, and 2) recommend another binder property and/or test method for evaluating asphalt binder fatigue. To achieve these objectives, sixteen asphalt binders representing a wide range of

performance grades used in the United States were selected. A dense-grade mix design was used for evaluating all the binders. Binder properties were evaluated using performance grading (PG), frequency sweep, and modified linear amplitude sweep (LAS). Mixture fatigue properties were determined using the flexural fatigue, dynamic modulus, and uniaxial fatigue tests.

1.3 Organization of Dissertation

This dissertation consists of nine chapters. This chapter (Chapter 1) includes the problem statement, the objectives and scope of this research. Chapter 2 presents a literature review on the mechanism of fatigue cracking, factors affecting fatigue cracking, laboratory fatigue cracking tests, and the previous research findings on the correlations between binder properties and mix fatigue. Chapter 3 describes the experimental plans. Chapters 4 and 5 discuss the test results of the binders and mixes, respectively. Chapter 6 presents the effect of pavement structure on the fatigue performance. Chapter 7 presents the correlations between asphalt binder properties and mixture fatigue performance. Chapter 8 discusses the field validation using the results from the 2009 Group Experiment sections on the National Center for Asphalt Technology (NCAT) Pavement Test Track. Chapter 9 presents the conclusions and recommendations.

CHAPTER 2 – LITERATURE REVIEW

2.1 Mechanism of Fatigue Cracking

At the microscopic level, fatigue is a process of a crack initiation and propagation. During crack initiation, microcracks grow until a critical size of about 7.5 mm is reached. In crack propagation, macrocracks grow until the pavement layer fails (Little et al., 2001). During crack initiation and propagation, the material modulus reduces with increasing loading cycles.

There are two kinds of fatigue cracking: bottom-up cracking and top-down cracking. Bottom-up cracking generally occurs in a thinner asphalt pavement. **Figure 6** shows the bottom-up cracking mechanism: for a thinner asphalt pavement under the traffic loading, the greatest tensile strain generally occurs at the bottom of the asphalt layer; when this strain is greater than the endurance limit of the asphalt mix, fatigue damage starts at the bottom of the asphalt layer and gradually propagates to the surface. During the cracking propagation phase, the shear stress at the crack tip contributes to the growth of cracking. Bottom-up fatigue cracking typically shows up as alligator cracks in the wheel paths (**Figure 7**).

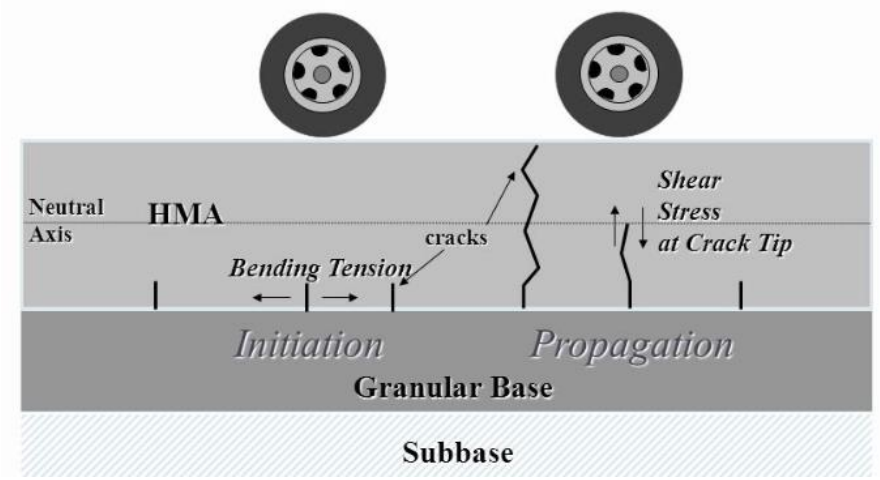

Figure 6. Bottom-Up Fatigue Cracking Mechanisms (NCAT Course Presentation, 2011)

Figure 7. Bottom-Up Fatigue Cracking Example (Vrtis, 2017)

Top-down cracking generally occurs in a thicker asphalt pavement. The failure mechanism of top-down cracking is more complex than the classical bottom-up fatigue cracking. Heavy traffic loading is considered the major cause of top-down cracking. Top-down cracking may be caused by high shear stresses in the asphalt surface near the tire, and the tensile stresses in the asphalt surface some distance from the tire (**Figure 8**). Top-down fatigue cracking typically shows up as longitudinal cracks near or in between the wheel paths.

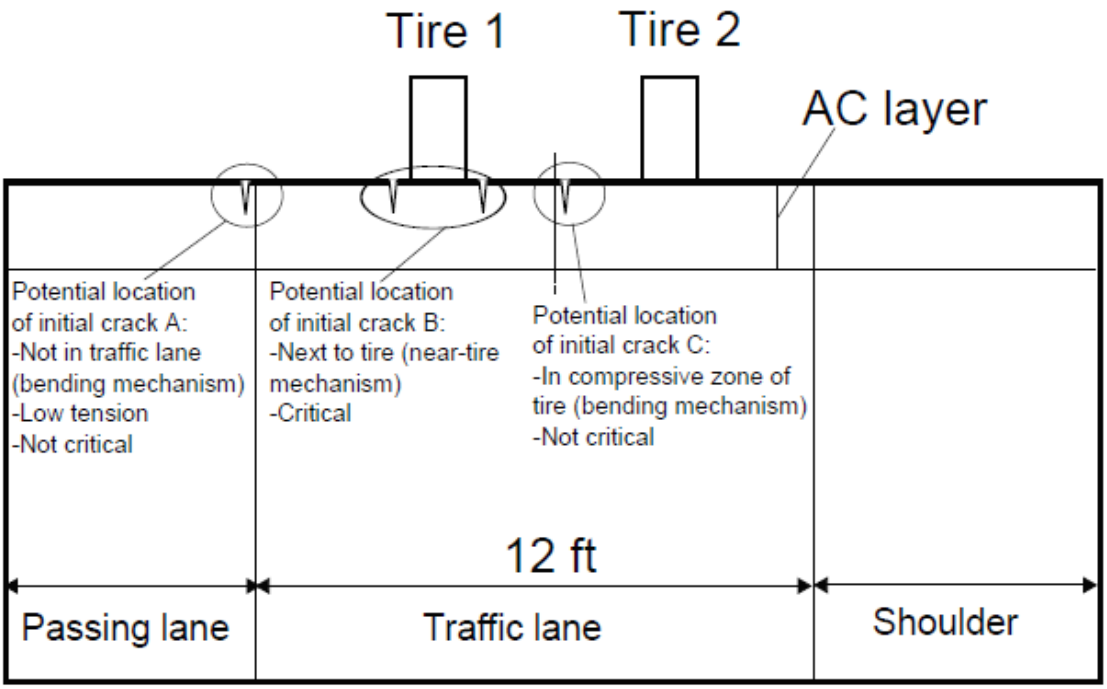

Figure 8. Proposed Top-Down Cracking Mechanisms (Zou and Roque, 2011)

2.2 Material Factors Affecting Fatigue Cracking

Mixture Properties

Mixture properties affecting mixture fatigue behavior include mixture stiffness and volumetric properties. SHRP-A-404 report (1994) documented that, for a given asphalt binder, reducing the stiffness (increasing the air void content) decreased the fatigue life; whereas, for a given air void content, decreasing the stiffness (changing the asphalt type) increased the fatigue life.

Volumetric factors affecting pavement fatigue performance are air void content, the volume of effective binder (VBE) and the voids in the mineral aggregate (VMA) of the mixture. Generally, the fatigue life of asphalt pavements increases with decreasing in-place air void content (increasing in-place density or increasing binder content). **Table 1** summarizes the effect of air voids on the

fatigue performance. It is seen from **Table 1** that a 1% decrease in air voids improves fatigue life by 8.2% – 43.8%, depending on the mixture types and experiments. For a specific pavement, fatigue life increases with increasing VBE and VMA (increasing the binder content). Insufficient VBE and VMA could lead to earlier fatigue cracking and durability problems. Thus, minimum VBE and VMA values are required in Superpave mixture design to ensure a satisfactory fatigue performance.

Table 1. Effect of Air Voids on Fatigue Performance (Tran et al., 2016)

Study	Lab/Field Experiment	Mix Type	Air Voids Evaluated	Increase in Fatigue Life for 1% Decrease in Air Voids
UCB (Epps and Monismish 1969)	Lab	British Standard	4 - 14%	20.6%[1]
		California Fine	5 - 8%	43.8%[1]
		California Coarse	2.5 – 7%	33.8%[1]
UCB (Harvey and Tsai 1996)	Lab	California Dense-Graded	1 - 3% 4 - 6% 7 - 9%	15.1%[1]
WesTrack (Epps et al. 2002)	Lab	Fine	4, 8, 12%	13.5%[1]
		Fine-Plus	4, 8, 12%	13.3%[1]
		Coarse	4, 8, 12%	9.0%[1]
	Field	Fine/Fine-Plus	4, 8, 12%	21.3%[1]
		Coarse	4, 8, 12%	8.2%[1]
AI (Fisher et al. 2010)	Lab	9.5 mm Dense-Graded	4 – 11.5%	9.2%

[1] (Seeds et al. 2002)

Asphalt Binder Properties

Binder fatigue and fracture properties have been related to mixture fatigue performance. For example, Hintz et al. (2011) reported that the accelerated binder fatigue life from LAS testing exhibited a promising correlation with measured cracking in actual pavements from the Long-Term Pavement Performance (LTPP) program. Gibson et al. (2012) documented that the direct tension strain at failure exhibited a reasonably good correlation to laboratory mixture fatigue tests and to fatigue performance in the ALF lanes.

Aging of asphalt binders in the surface layer will accelerate top-down fatigue cracking. Generally, the aging level of binder is the highest at the surface and gradually decreases with the pavement depth as the binder in the surface is exposed to ultraviolet (UV) radiation and oxygen. The primary factors affecting binder aging are the environmental temperature and the in-place air voids of the asphalt pavement. Binder aging is more severe in high-temperature weather than in low-temperature. Binder aging increases with increasing in-place air voids. Age-hardening ratios increase 5% to 14% for each 1% increase in field air voids at a mean average ambient temperature of 15.6°C (Anderson, 2014).

Healing

Healing in asphalt pavements is generally considered the capability of the asphalt mixture to self-recover its mechanical properties (e.g., modulus and fatigue life) to some degree after a rest time due to the viscoelastic nature of binders and the closure of cracks (Little et al., 2001). Two main types of healing in asphalt mixtures exist: adhesive healing at the asphalt-aggregate interface and cohesive healing within the asphalt binder. The main factors affecting healing in asphalt pavements are the rest periods, environmental temperature, and binder properties. The amount of recovery of mixture mechanical properties increases with increasing rest time and healing temperature (Balbissi 1983; Kim 1988; Daniel and Kim 2001). Kim et al. (1990) reported that healing potential is related to the flow property of the asphalt and its composition (e.g., the amounts of longer-chained aliphatic molecules in the saturates). Additionally, healing is also affected by the crack width prior to the rest period (Si et al., 2002; Shen et al., 2016): a narrower crack takes shorter time to heal, but a wider crack takes longer time to heal.

2.3 Fatigue/Fracture Tests and Property Parameters for Binder

The ***LAS*** (AASHTO TP 101) is conducted using the DSR to evaluate the fatigue performance of asphalt binders. The specimens are aged using RTFO or PAV, and prepared consistently with AASHTO T 315 using the 8-mm parallel plate geometry with a 2-mm gap setting. The testing temperature is the intermediate pavement temperature determined from the performance grade of the asphalt binder according to AASHTO M 320. During fatigue testing, the specimens are tested under shear loads using a frequency sweep to determine the rheological properties and then tested using a series of oscillatory load cycles at linearly increasing amplitudes at a constant frequency to induce accelerated fatigue damage. After testing, the test data is analyzed using the viscoelastic continuum damage (VECD) mechanics approach.

The ***double edge-notched tension (DENT)*** test has recently been used to characterize the ductile and brittle properties of asphalt binders. In this testing, a rectangular test coupon of asphalt binder is prepared with 45 notches on both sides at the center of the specimen. The specimen is pulled at a constant deflection rate of 50 mm/min in a water bath of 15°C until failure. Typically, three sets of specimens are prepared with three ligament lengths of 5 mm, 10 mm and 15 mm (the ligament length is the distance between the notches at the midpoint of the specimen). After the testing, the work to failure and the critical crack tip opening displacement (CTOD) are calculated to explore the fatigue cracking resistance of asphalt binders.

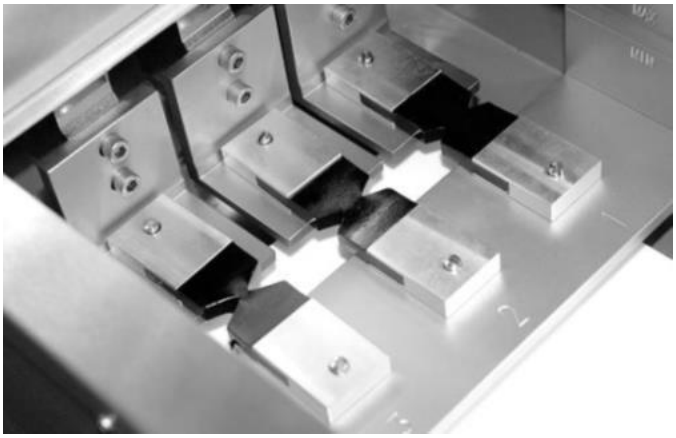

Figure 9. DENT Test Setup for Asphalt Binder (Gibson et al., 2012)

The ***single edge- notched beam (SENB)*** test is a fracture test that can be conducted on a modification of the BBR device (Velasquez et al., 2011). In this test, a standard-sized BBR specimen is notched and then tested at a constant displacement rate of 0.01 mm/sec until failure. Various fracture parameters including notched strength, strain at failure, and fracture toughness can be determined from this test. Notched specimens ensure failure occurs at a constant location, making the calculation of stresses and strains accurate. The notched test also provides an indication of fracture properties in the presence of flaws, which could be a better indicator of asphalt binder performance in asphalt mixtures.

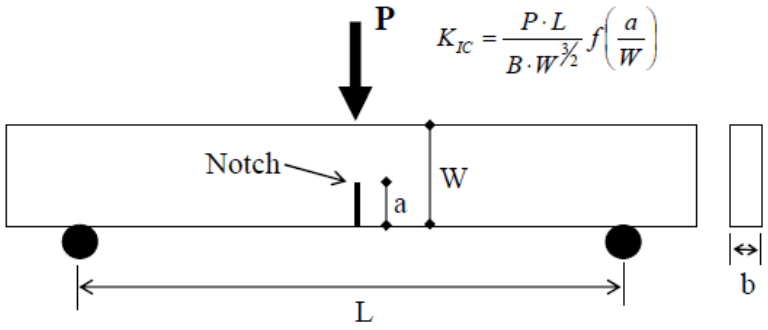

Figure 10. SENB Test Schematic (Velasquez et al., 2011)

In addition to the above binder tests and G*sin(δ) criteria mentioned in Chapter 1, the following parameters have been used to evaluate the cracking resistance of binders:

1) ***Crossover Frequency (ω_c) and Rheological Index*** (R)

ωc is defined as the frequency at which the phase angle is equal to 45 degrees at the reference temperature. R is the difference between the glassy modulus and the complex modulus (G*) at the crossover frequency, which is generally computed using **Equation 1**. **Figure 11** shows ω_c and R in the G* master curve. As the asphalt binders age, ω_c decreases and R increases, resulting in a flattening of the master curve.

$$R = \frac{(\log 2) * \log(\frac{G^*(\omega)}{Gg})}{\log(1 - \frac{\delta(\omega)}{90})} \qquad (1)$$

Where,

R = rheological index,

G*(ω) = complex shear modulus at frequency ω, in Pa,

Gg = glassy modulus, in Pa, and

δ(ω) = phase angle at frequency ω, degree.

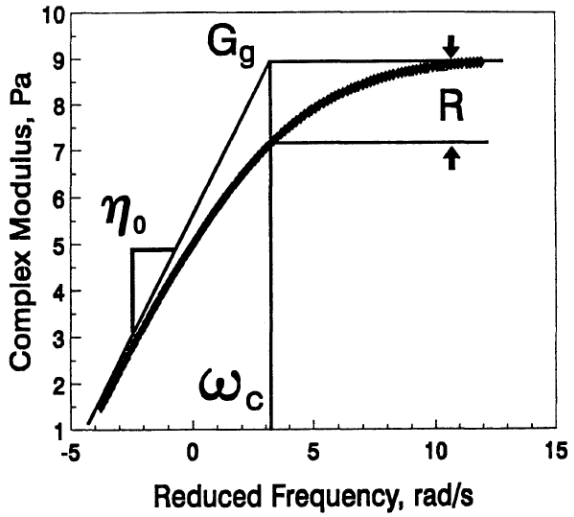

Figure 11. Schematic of Definition of Rheological Index (Petersen et al. 1994)

Some research documented that the combination of ω_c and R could catch the relative aging level of binders (Mogawer et al., 2015, Rahbar et al., 2017). For example, Mogawer et al. (2015) evaluated the effect of aging on two binders (PG 64-22 and PG 76-22) using the ω_c – R value space, as shown in **Figure 12**. Two binders in **Figure 12** were observed to migrate from the upper left to the lower right as the aging level increases. That means that the binder at the lower right could be susceptible to cracking than that at the upper left in the ω_c–R value space.

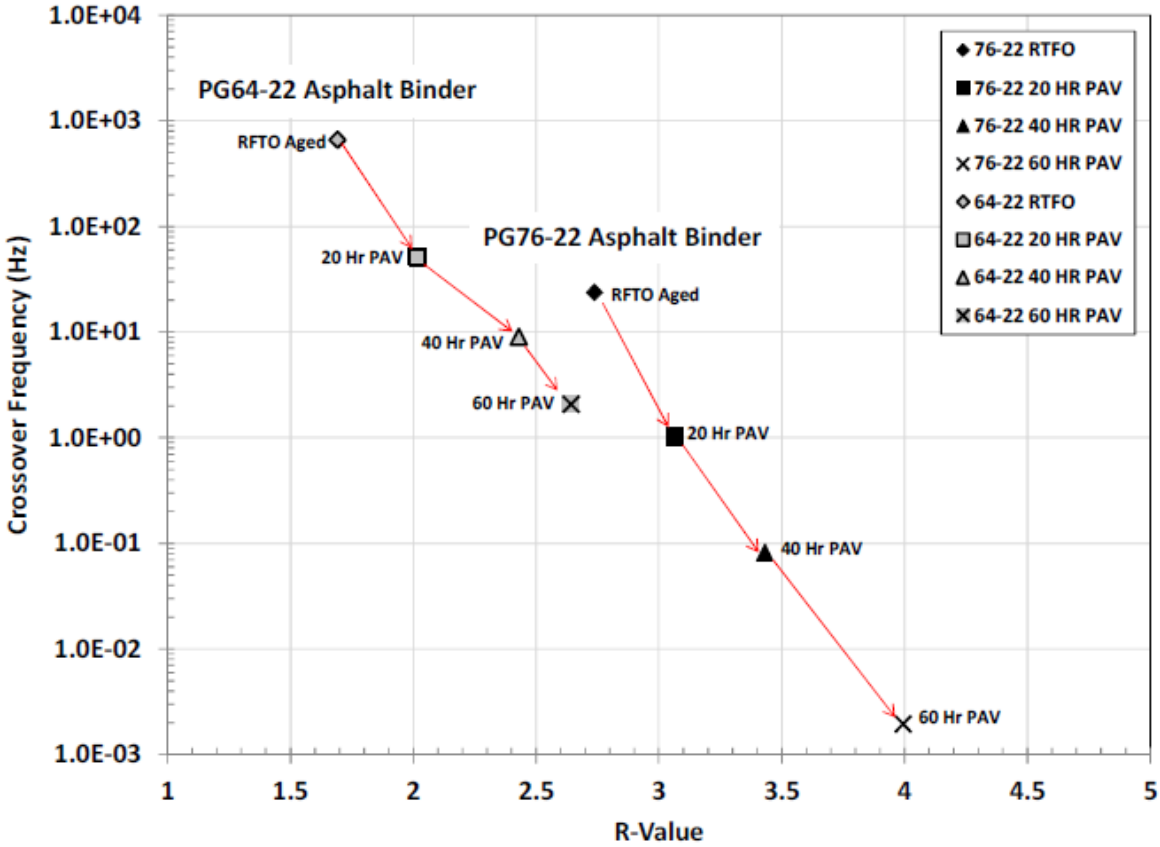

Figure 12. ω_c vs. R Value (Mogawer et al., 2015)

2) ***Glover-Rowe (G-R) Parameter***

The G-R parameter is a surrogate ductility parameter that relates the storage modulus, G'= G*cos(δ), and the dynamic viscosity, η'. A simplified form of the G-R parameter that uses values easily obtained from the DSR frequency sweeps was suggested by Rowe (2011) and is shown in **Equation 2**. Glover et al. (2005) documented that G-R parameter had a good correlation with the ductility of binders, as shown in **Figure 13**. Based on field non-load associated cracking levels, G-R thresholds were set: a G-R value of 180 kPa corresponds to the onset of cracking, while a value of 450 kPa or greater represents significant cracking issues (Anderson et al., 2011; Rowe 2014). Generally, G-R values are plotted in a Black Space plot to investigate the effect of aging on binder properties, as shown in **Figure 14**.

As the asphalt binders age, the binder stiffness increases and the phase angle decreases, resulting in their position shifting from the lower right to the upper left in the Black Space plot.

$$G - R = \frac{G'}{\frac{\eta'}{G'}} = \frac{G^*(cos\delta)^2}{sin\delta} \qquad (2)$$

Where,

G* = complex shear modulus of binder at 15°C and 0.005 rad/sec., and

δ = phase angle of binder at 15°C and 0.005 rad/sec.

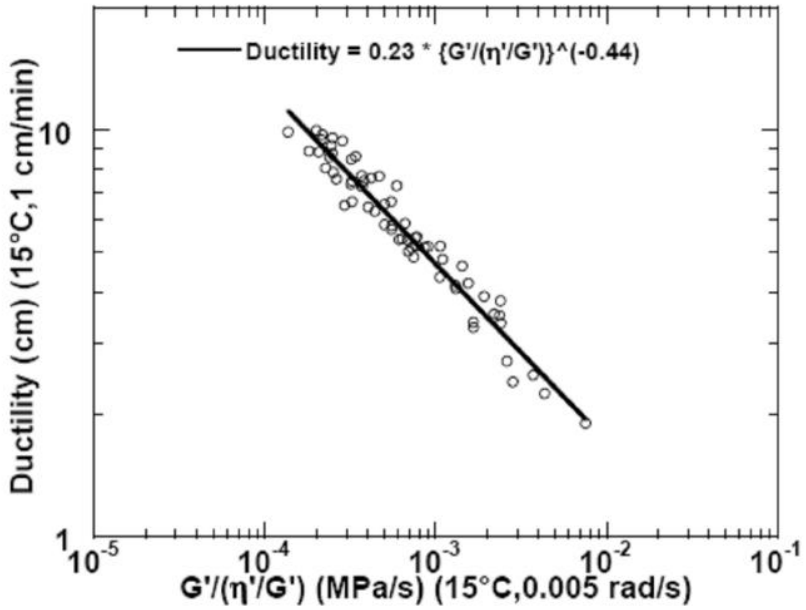

Figure 13. Correlation between Ductility and Glover-Rowe Value (Glover et al., 2005)

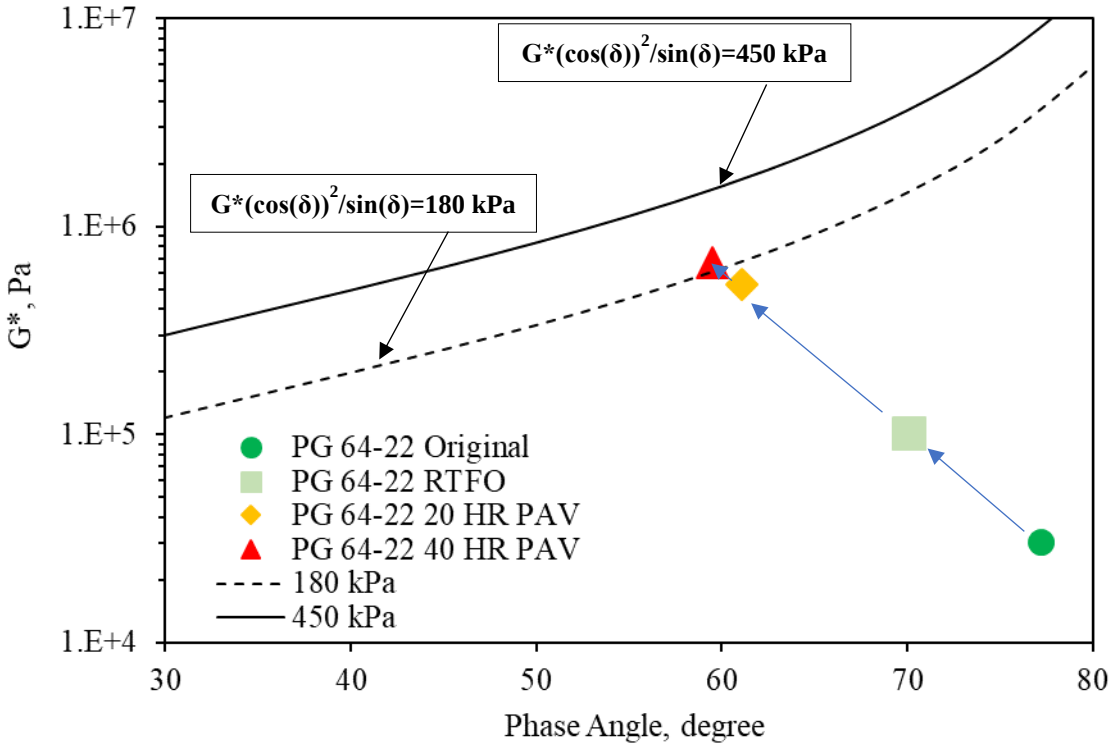

Figure 14. Typical Glover-Rowe Diagram (15°C/0.005 rad/sec.) (Xie et al., 2018)

3) *Delta Tc* (ΔTc)

ΔTc is the numerical difference between the two low-temperature continuous grades based on the BBR results (see **Equation 3**). As an asphalt binder ages, it loses ductility and its ΔTc becomes more negative (**Figure 15**), making asphalt binders more likely to crack. As an asphalt binder ages, the binder loses ductility and its ΔTc becomes more negative (Figure 35), making asphalt binders more likely to crack. Anderson et al. (2011) set a limit of ΔTc $\leqslant -2.5$°C for when there is an identifiable risk of cracking and a preventive action should be considered. Rowe (2011) recommended that at ΔTc $\leqslant -5$°C, immediate remediation should be considered.

$$\text{Delta Tc} = \text{T}_{cont,S} - \text{T}_{cont,m} \qquad (3)$$

Where,

$T_{cont,S}$ = temperature at which the stiffness criteria of 300 MPa is met, °C and

$T_{cont,m}$ = temperature at which the m-value criteria of 0.300 is met, °C

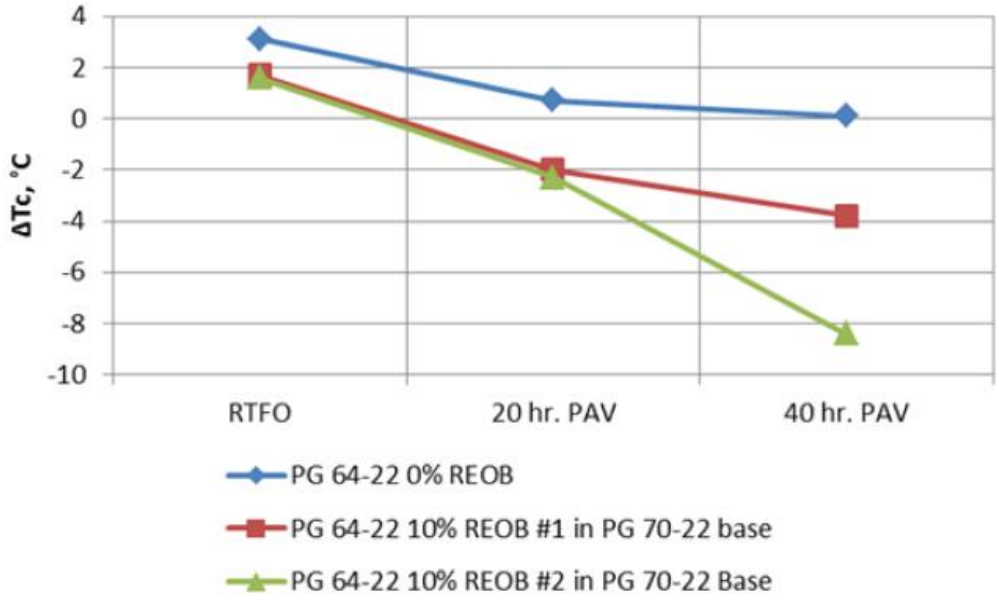

Figure 15. Relationship between Delta Tc and Aging Time (Corrigan, 2016)

4) Loss tangent (G"/G')

Loss tangent (**Equation 4**) is the ratio of the shear loss modulus G" (viscous part) to the shear storage modulus G' (elastic part), representing the ratio of energy lost to the energy stored in a cyclic deformation (Goodrich 1988). Goodrich (1988) reported that loss tangent values of binders had a good correlation with flexural fatigue lives of corresponding asphalt concrete. Button et al. (1996) documented that there was a strong correlation between the loss tangent at 10 rad/sec. and 10°C of the aged binders and fatigue cracking in Texarkana test pavements after 7-year traffic, as shown in **Error! Reference source not found.**.

$$\text{Loss Tangent} = \tan(\delta) = G''/G' \qquad (4)$$

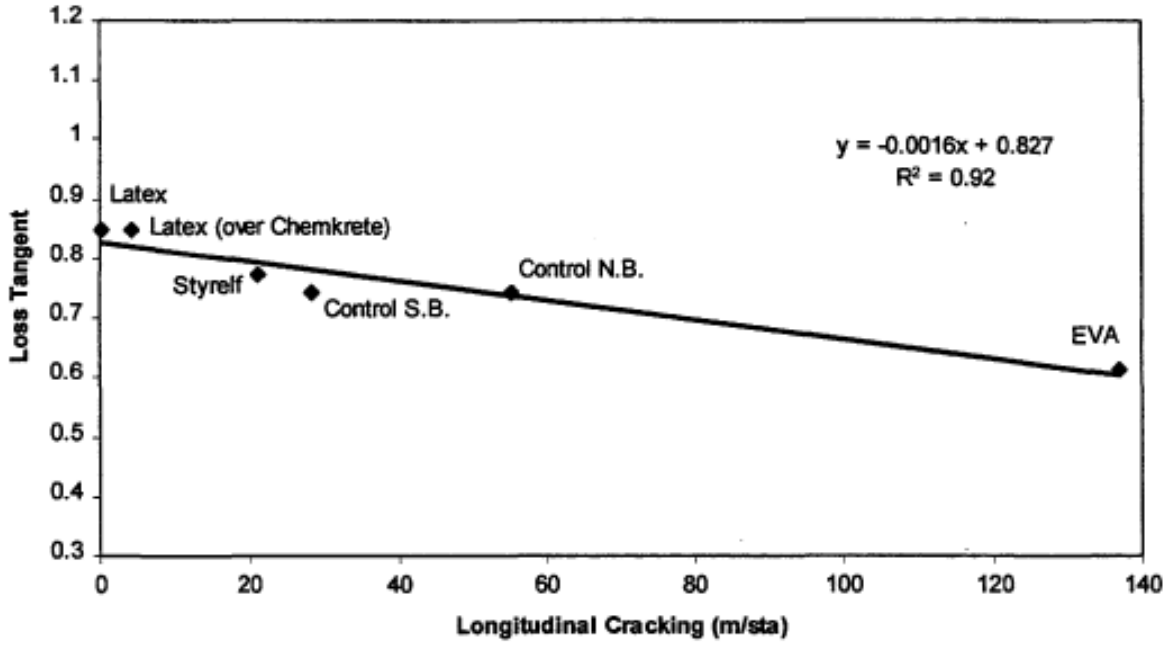

Figure 16. Loss Tangent vs. Field Longitudinal Cracking (Button et al. 1996)

2.4 Laboratory Fatigue Tests for Mixture

B***ending beam fatigue (BBF)*** testing ***(***AASHTO T321) has been widely used to characterize the resistance to bottom-up cracking of asphalt concrete. In this test procedure, a 380-mm by 50-mm by 63-mm beam is held by four equally-spaced clamps and a sinusoidal loading at a typical frequency of 10 Hz is applied at the two inner clamps (**Figure 17**). The magnitude of the load applied by the actuator and the deflection measured at center of beam is recorded and used to calculate the flexural stiffness. The stiffness at the 50th loading cycle is typically defined as the initial stiffness of the beam. AASHTO T321-14 defines the failure point as the number of cycles where the peak of the product of the flexural stiffness times the number of cycles occurs. This concept is illustrated graphically in **Figure 18**.

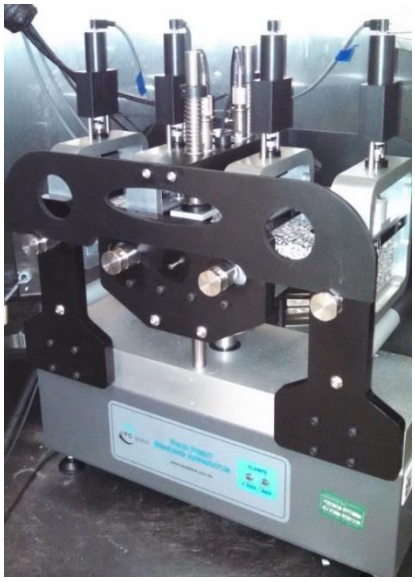

Figure 17. IPC Global BBF Testing Apparatus with Fixed Reference Retrofit

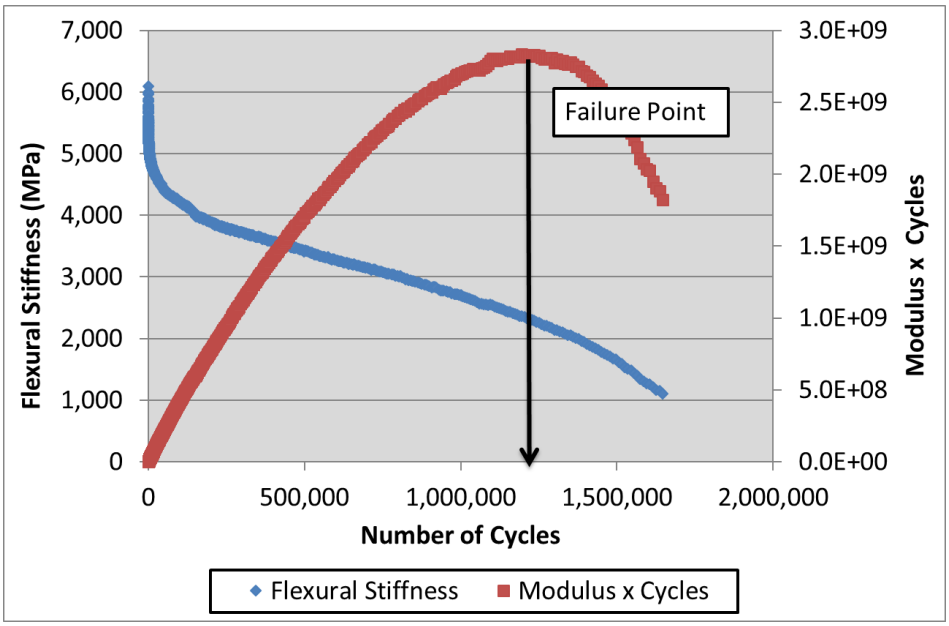

Figure 18. Example of Bending Beam Fatigue Failure Point

Direct tension cyclic fatigue test (AASHTO TP 107) is used to characterize fatigue performance of asphalt mixtures. In this test procedure, a repeated pull-pull loading at a frequency of 10 Hz is

applied on a specimen with 100-mm diameter and 130-mm thickness which is glued to the top and bottom platens (**Figure 19**). At least three replicate specimens are tested at three different strain levels to produce a wide range of fatigue life (from 1,000 to 100,000). The testing temperature is determined based on the PG of the binder used: (high PG + low PG)/2 -3. After testing, the characteristic relationship between the rate of released pseudo strain energy (G^R) and fatigue life (N_f), and endurance limit are predicted to evaluate fatigue behavior of asphalt mixtures with the simplified viscoelastic continuum damage (S-VECD) model. The observed failure point is defined as the number of cycles where a sharp sudden decrease in the phase angle occurred (**Figure 20**). Additionally, dynamic modulus testing (AASHTO TP 79) must also be performed as part of the fatigue performance analysis.

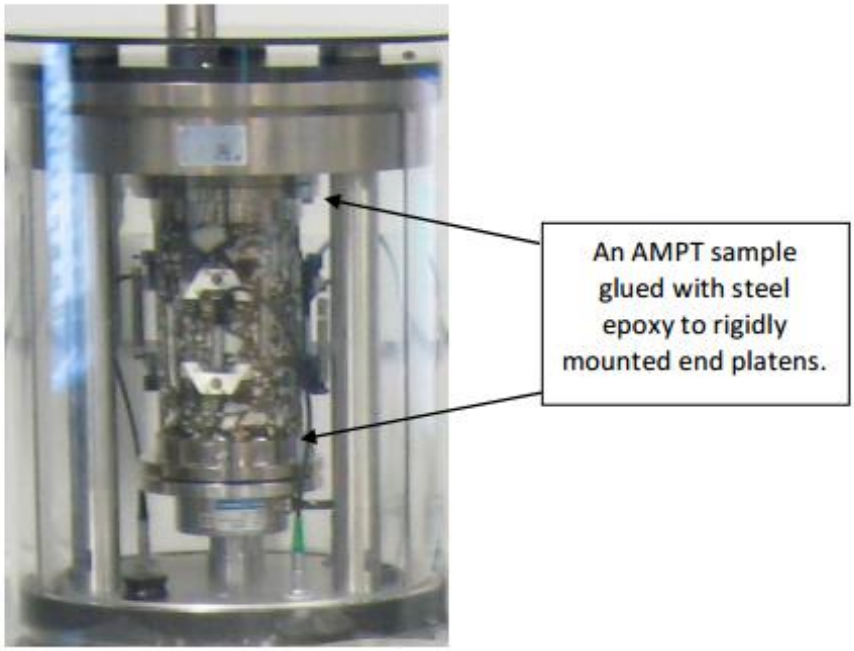

Figure 19. Direct Tension Cyclic Fatigue Test Setup

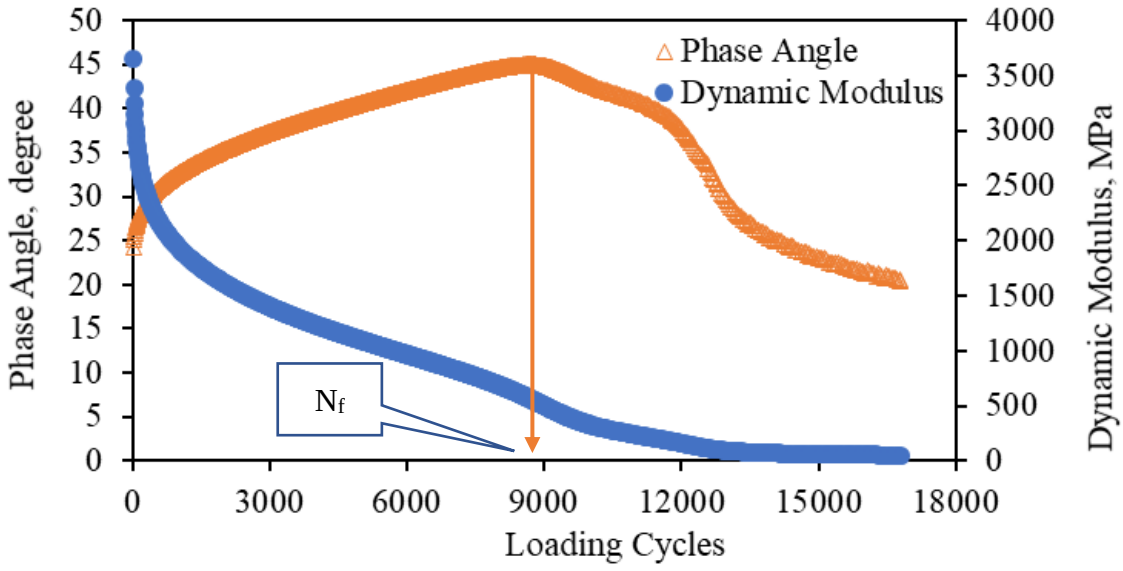

Figure 20. Example of Direct Tension Cyclic Fatigue Test Failure Point

2.5 Approaches to Analyzing Laboratory Fatigue Test Data

2.5.1 Traditional Phenomenological Approach

The traditional phenomenological approach is widely used to evaluate mix fatigue property due to its simplicity. In the approach, cycles to failure (N_f) is a function of the tensile strain/stress (**Equations 5 and 6**). To account for the impact of loading frequency and temperature, Monismith et al. (1985) developed a modified fatigue model by introducing the stiffness (**Equation 7**). In this study, **Equations 5 and 7** were used to analyze the data from flexural fatigue and uniaxial fatigue tests.

$$N_f = k_1(\frac{1}{\varepsilon_0})^{k_2} \qquad (5)$$

$$N_f = k_1(\frac{1}{\sigma_0})^{k_2} \qquad (6)$$

$$N_f = k_1 \left(\frac{1}{\varepsilon_0}\right)^{k_2} (\frac{1}{S_0})^{k_3} \qquad (7)$$

Where,

N_f = number of cycles to failure,

ε_0 and σ_0 = initially applied stain and stress amplitudes, respectively,

S_0 = initial stiffness of asphalt material, and

k_1, k_2 and k_3= material constants.

2.5.2 Dissipated Energy Approach

Dissipated Energy (DE) Concept

Figure 21 compares the deflection behavior during loading and unloading between ideal elastic and viscoelastic materials. For an ideal elastic material, the load-deflection curve during loading overlaps that during unloading, indicating that all the energy stored in the material during loading is recovered after unloading and that no energy is dissipated. For a viscoelastic material, the load-deflection curves during loading and unloading are different, producing a hysteresis loop. **Figure 21** shows typical stress-strain hysteresis loops at various cycles in a strain-controlled flexural fatigue test. The area within the stress-strain hysteresis loop is defined as dissipated energy per cycle. For a sinusoidal loading condition, the dissipated energy per cycle can be calculated through **Equation 8**. Dissipated energy is responsible for two parts: 1) the heat energy due to the flow of viscous part of binder, and 2) the released energy for cracking damage (Little, 1995). For each loading cycle, the loss of energy due to material mechanical work and other environmental influence remains almost unchanged. Therefore, if the dissipated energy starts to change dramatically, it could be explained as the development of damage (Zhou 2007).

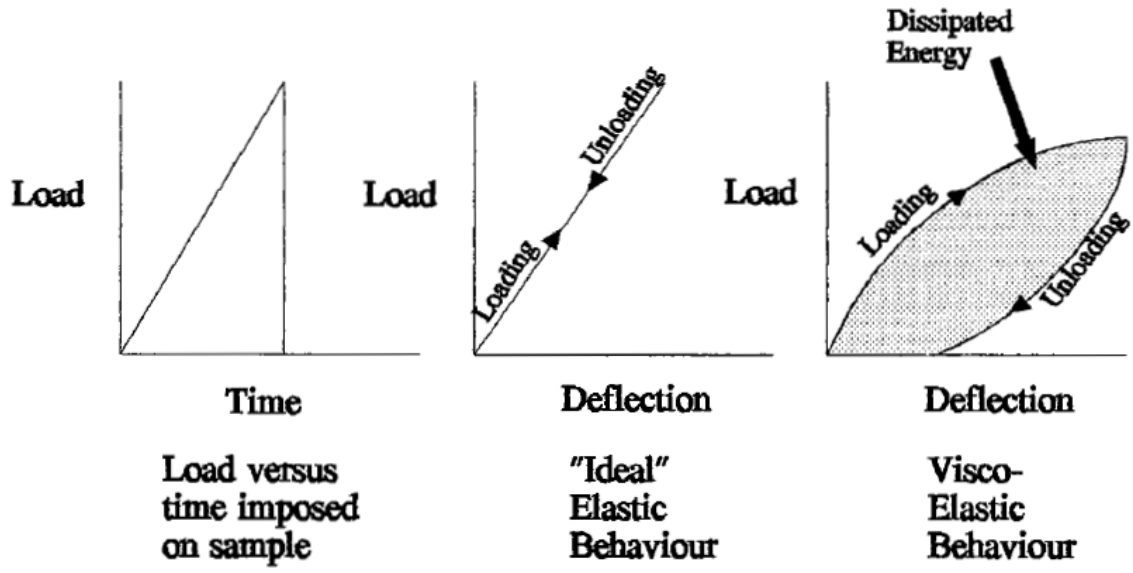

Figure 21. Ideal Elastic and Viscoelastic Deflection Behavior (Rowe, 1996)

$$W_i = \pi \cdot \sigma_i \cdot \varepsilon_i \cdot \sin \varphi_i \qquad (8)$$

Where,

W_i is the dissipated energy at cycle i, in J/m^3,

$\sigma_i and\ \varepsilon_i$ are the stress (in Pa) and strain amplitude (in mm/mm) at cycle i, respectively, and

φ_i is the phase angle at cycle i, degree.

Cumulative Dissipated Energy (CDE)

The dissipated energy approach has been used to explore the fatigue property of asphalt materials by researchers (Van Dijk, 1975; Van Dijk and Vesser, 1977; Rowe, 1996; Carpenter et al., 1997 and 2003; Shen, 2006). Van Dijk (1975) found a strong relationship between the cumulative dissipated energy to failure and loading cycles to failure. This relationship can be characterized by **Equations 9**. The cumulative dissipated energy to failure is the area under the curve between dissipated energy and number of loading cycles. Rowe (1996) reported that the relationship

between the cumulative dissipated energy to failure and cycles to failure was affected by temperatures and loading modes.

$$W_N = A(N_f)^Z \qquad (9)$$

Where,

W_N is the cumulative dissipated energy to failure, J/m^3

$$W_N = \int_0^{Nf} W_i \qquad (10)$$

N_f is the number of cycles to failure, and A and Z are material constants.

Ratio of Dissipated Energy Change

Carpenter and Jansen (1997) suggested using the change in dissipated energy to relate damage accumulation and fatigue life. Carpenter et al. (2003, 2005) used the ratio of dissipated energy change (RDEC, see **Equation 11** and **Figure 22**) as an energy parameter to evaluate the fatigue damage in asphalt mixes. Shen (2006) reported that the RDEC eliminates the dissipated energy that does not produce crack extension damage and the RDEC at plateau stage (plateau value, see **Figure 22**) had a unique correlation with fatigue life (**Figure 23**), which is independent of temperatures, loading modes, and mix types.

$$RDEC = \frac{DE_{n+1} - DE_n}{DE_N} \qquad (11)$$

Where,

RDEC = ratio of dissipated energy change,

DE_n = dissipated energy produced in load cycle n, in J/m^3, and

DE_{n+1} = dissipated energy produced in load cycle n+1, in J/m^3.

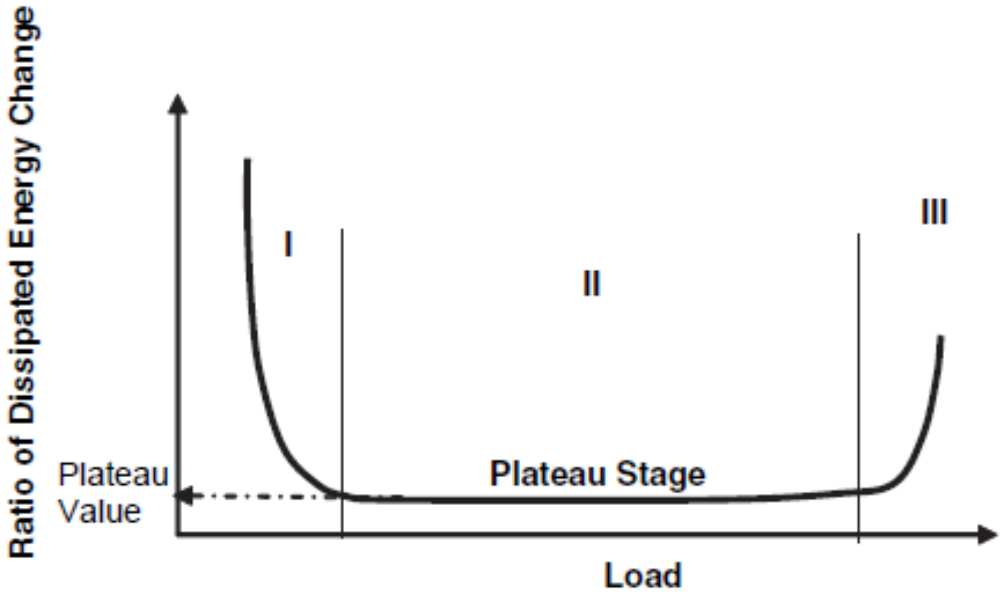

Figure 22. Typical RDEC Plot (Carpenter et al. 2003)

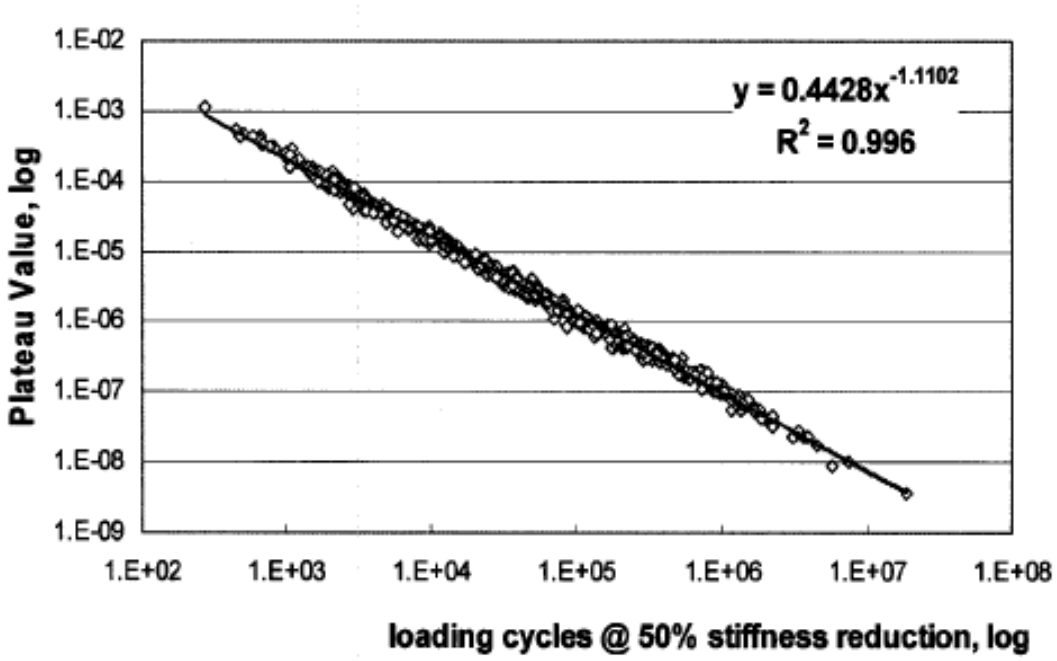

Figure 23. Plateau Value vs. Cycles to Failure (Shen, 2006)

2.5.3 Viscoelastic Continuum Damage Mechanics Approach

The viscoelastic continuum damage (VECD) mechanics approach is based on the elastic-viscoelastic correspondence principle, the work potential theory, and the temperature-time superposition principle (Kim and Little, 1990; Daniel and Kim, 2002; Underwood et al., 2010). The elastic-viscoelastic correspondence principle is used to model the viscoelastic behavior of a material by replacing physical strain with pseudo strain (**Equation 12**). The time-temperature superposition principle combines their effects on asphalt mixture response by shifting modulus values at different temperatures to a certain reference temperature. The work potential theory (Schapery, 1990) is then applied to model damage growth (Underwood et al., 2010).

$$\varepsilon^R = \frac{1}{E_R}\int_0^t E(t-\tau)\frac{d\varepsilon}{d\tau}d\tau \qquad (12)$$

Where,

ε^R = pseudo strain,

ε = actual strain,

E_R = reference modulus, which is an arbitrary constant, and

E (t) = relaxation modulus.

In this model, a damage parameter, S, is defined as all the structural changes that result in reduced stiffness as asphalt mixture undergoes loading. Stiffness reduction is defined by the pseudo stiffness, which is typically normalized for specimen-to-specimen variability by the initial pseudo stiffness, I, and denoted as C (**Equation 13**) (Underwood et al., 2010).

$$C = \frac{\sigma}{\varepsilon^{R}{}_{*I}} \qquad (13)$$

The three fundamental functions for the continuum damage theory based on Schapery's work potential theory are:

1) the pseudo strain energy density function,

$$W^R = f(\varepsilon^R, S) = \frac{1}{2}\sigma\varepsilon^R = \frac{1}{2}(\varepsilon^R)^2 C \quad (14)$$

2) the stress-pseudo strain relationship,

$$\sigma = \frac{\partial W^R}{\partial \varepsilon^R} = C(S)\varepsilon^R \quad (15)$$

3) the damage evolution law,

$$\frac{dS}{dt} = \left(-\frac{\partial W^R}{\partial S}\right)^{\alpha} \quad (16)$$

Where,

W^R = pseudo strain energy density,

ε^R = pseudo strain,

S = damage parameter (internal state variable), and

α = damage evolution rate.

In the VECD analysis, the pseudo stiffness (C) and the damage parameter (S) are calculated to produce a damage characteristic curve, which is only related to material property and is independent of loading and temperature (Sabouri and Kim 2014). After that, the fatigue life of mixes is predicted according to the failure criteria developed based on the dissipated pseudo strain energy (DPSE). Sabouri and Kim (2014) developed the G^R failure criterion. G^R is defined as the rate of change of the averaged released pseudo strain energy (per cycle) throughout the entire history of the test, which is related to the fatigue life **(Equation 17).** Once a characteristic relationship (G^R-N_f) has been obtained, it can be applied to predict the fatigue life of asphalt mixture for any loading levels and test temperatures.

$$G^R = \frac{\int_0^{Nf} W_C^R}{N_f^2} \qquad (17)$$

Where,

W_C^R is the released pseudo strain energy (see **Figure 24**), and

N_f is the number of cycles to failure.

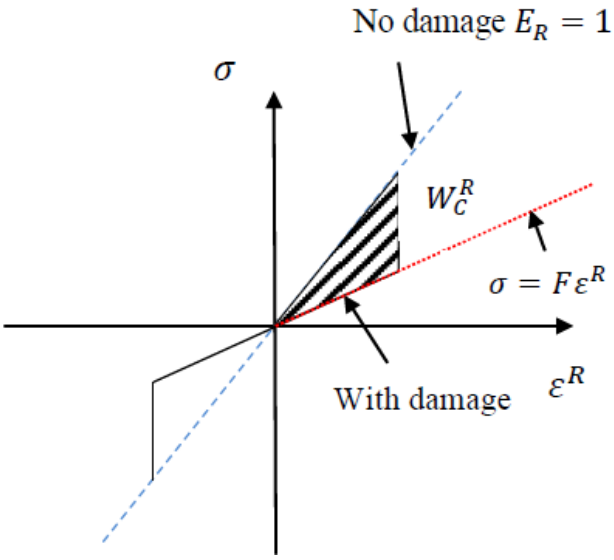

Figure 24. Released Pseudo Strain Energy in Stress-Pseudo Strain Space (Zhang 2012)

2.6 Correlation between Asphalt Binder Properties and Mixture Fatigue Performance

SHRP-A-404 report (Tayebali et al., 1994) documented the G*sin(δ) had no robust relationship with the simulated fatigue performance of asphalt pavement (**Table 2**). In the study, eight binders without modifiers and two aggregate sources - 100% crushed limestone (RH) and partially crushed gravel (RD) - were used. Binder DSR and mix fatigue tests were conducted at the same temperature and frequency: 20°C and 10Hz. DSR tests were conducted on thin film oven test (TFOT)-aged binders. Flexural beam controlled-strain tests were performed on the short-term aged mixes (135°C for four hours) at two air void contents (4% and 7%) and two strain levels (400 and 700 micro-

strain). An in-situ mix performance was simulated by linear elastic layer analysis of the response of three typical pavement structures to a 44.4 kN wheel load and dual tires with 690 kPa contact pressure.

Table 2. Binder Properties vs. Simulated Pavement Fatigue Life (Tayebali et al., 1994)

Aggregates	Voids	Coefficient of Determination Fatigue Life Versus	
		Binder Loss Stiffness ($G^* \sin\delta$)	Binder Complex Stiffness (G^*)
Three-Layer Structure (10.2 cm [4 in.] Asphalt-Aggregate Layer)			
RD	Low	0.02	0.01
RD	High	0.04	0.02
RH	Low	0.03	0.06
RH	High	0.21	0.32
All Aggregates and Air-Void Contents		0.00	0.00
Three-Layer Structure (15.2 cm [6 in.] Asphalt-Aggregate Layer)			
RD	Low	0.02	0.06
RD	High	0.07	0.10
RH	Low	0.09	0.14
RH	High	0.12	0.12
All Aggregates and Air-Void Contents		0.01	0.02
Two-Layer Structure (25.4 cm [10 in.] Asphalt-Aggregate Layer)			
RD	Low	0.07	0.12
RD	High	0.17	0.22
RH	Low	0.24	0.30
RH	High	0.00	0.00
All Aggregates and Air-Void Contents		0.06	0.08

Bahia et al. (2001) documented that G*sin(δ) has not shown strong correlations with mixture fatigue life, and these results were already shown in Chapter 1. Additionally, a poor correlation between the binder G*sin(δ) and the mixture fatigue life was also found by Tsai and Monismith (2005) (**Figure 25**).

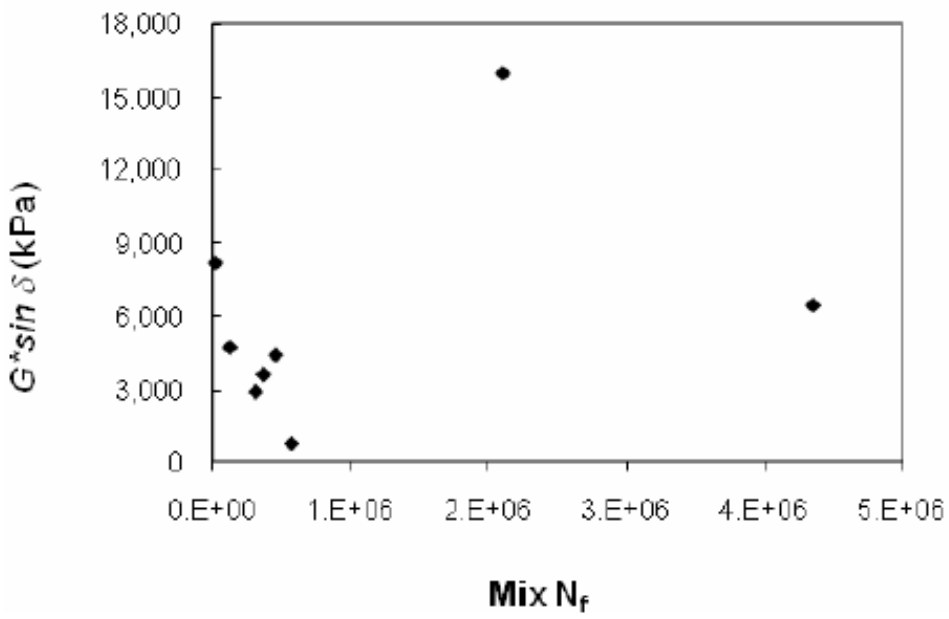

Figure 25. Comparison of G*sin(δ) and Mix Fatigue Life (Tsai and Monismith, 2005)

Johnson et al. (2007) investigated the correlation between the DSR cyclical fatigue life of binders and mixture fatigue life. DSR cyclical fatigue life tests of binders were performed under a constant strain level (1% and 2%) and a cyclical shear loading using the DSR, and the testing temperatures were 10°, 20°, and 30°C to match the mixture BBF tests from the earlier study. In this project, the effect of healing on binder fatigue life was also investigated: one set paused the test between cycles, known as "precision-sampling" method, and another set used continuous loading without a rest between cycles. **Figure 26** and **Figure 27** show the correlations between DSR cyclical fatigue life of binders and mixture BBF fatigue life. It was observed that DSR cyclical fatigue life

with healing exhibited a good correlation with mixture fatigue life (**Figure 26**), while DSR fatigue life without healing had a poor correlation with BBF results (**Figure 27**).

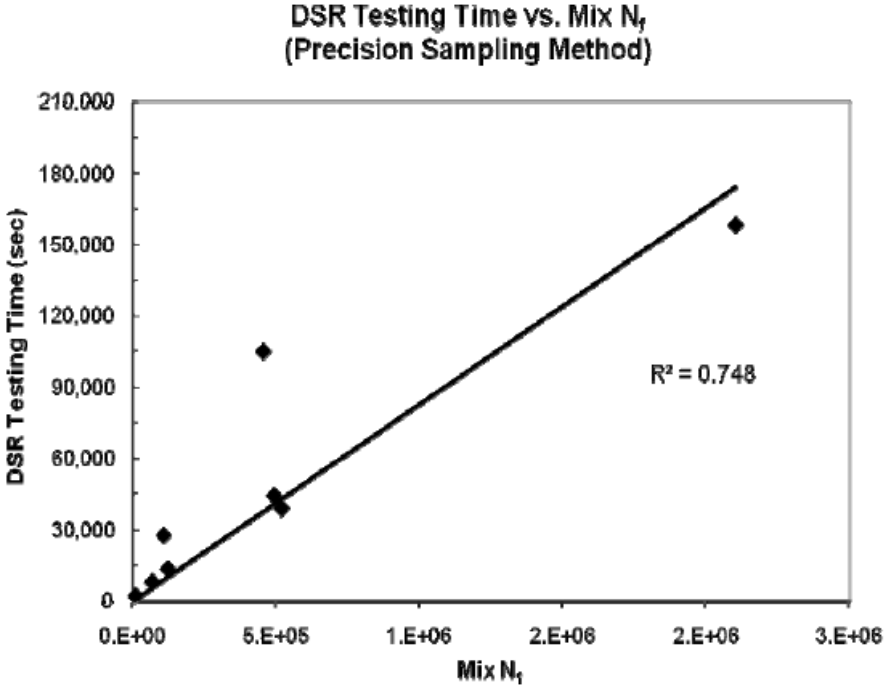

Figure 26. DSR Testing Time vs. Mixture Fatigue Life (Johnson et al., 2007)

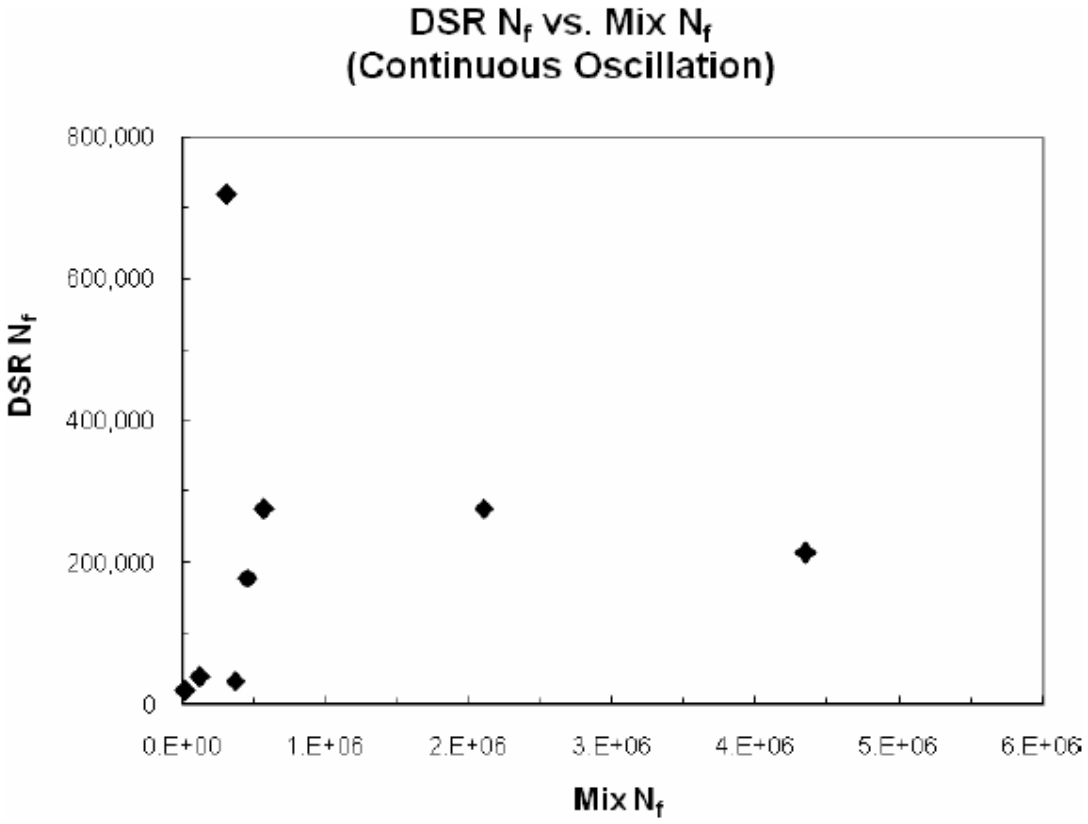

Figure 27. DSR Fatigue Life vs. Mix Fatigue Life (Johnson et al., 2007)

Mannan et al. (2015) compared mixture BBF fatigue life to asphalt binder fatigue life using two provisional test procedures: LAS and time sweep. BBF was performed on the mixes at 20°C using four strain levels (400, 600, 800, and 1000 micro-strains) and three loading frequencies (1, 5, and 10HZ). LAS tests were performed at 20°C and used strains ranging from 1 to 30% in accordance with AASHTO TP 101. The time sweep was performed at 20°C, three frequencies (1, 5, and 10 HZ) and four strain levels (4, 6, 8, and 10%). In this study, two asphalt mixtures, one with 35% recycled asphalt pavement (RAP) and one with no RAP, were evaluated. The testing results indicated that there were strong correlations between mixture fatigue life and both binder tests evaluated (**Figure 28** and **Figure 29**).

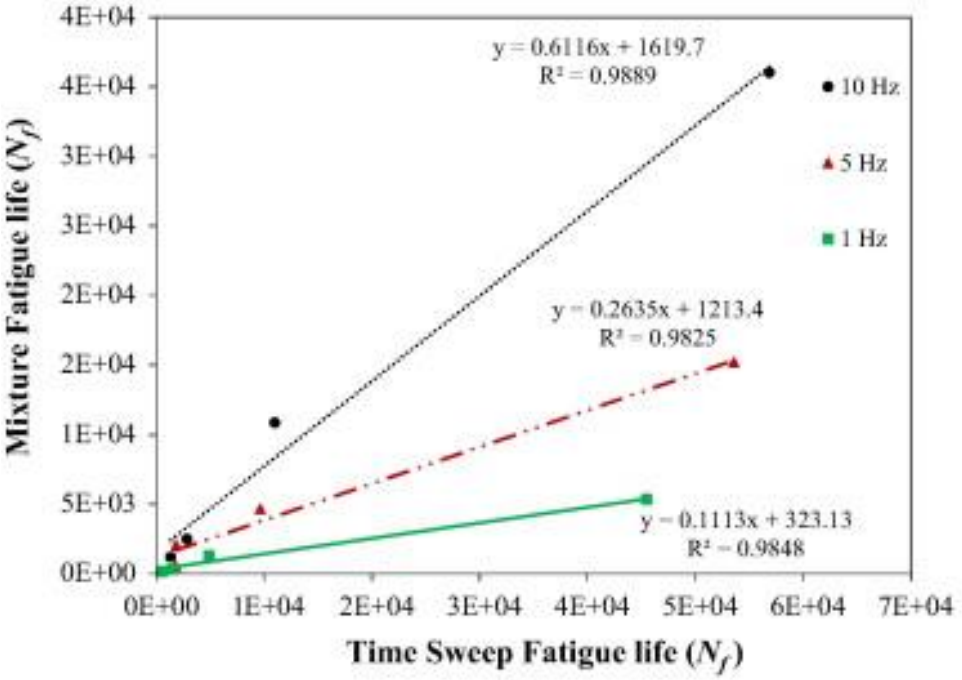

(a)

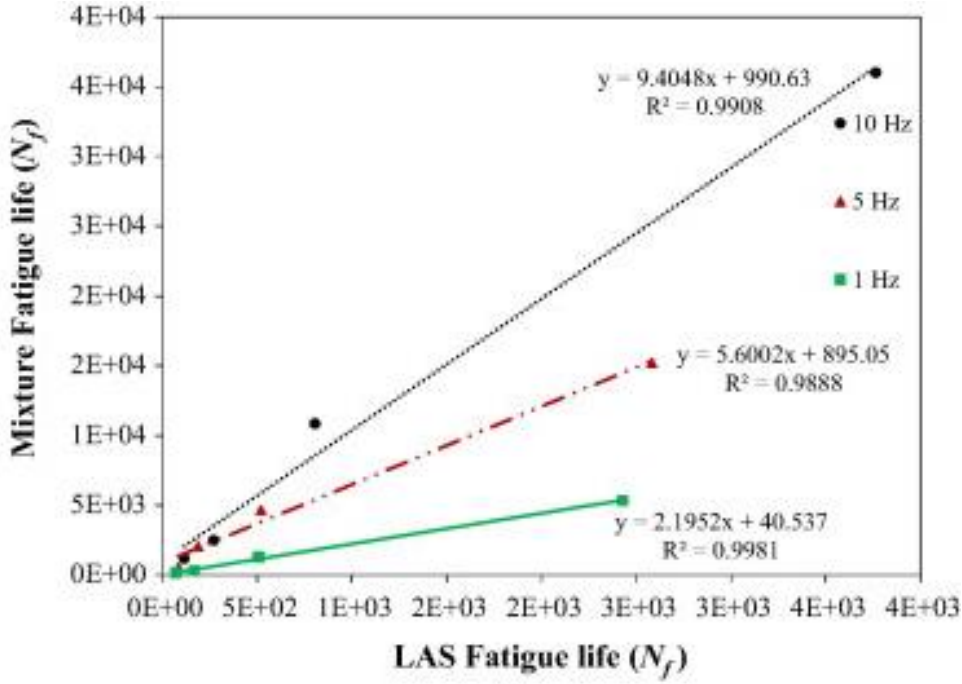

(b)

Figure 28. Comparison of Mixture and Asphalt Binder Fatigue for 35% RAP Mixture (Mannan et al., 2015)

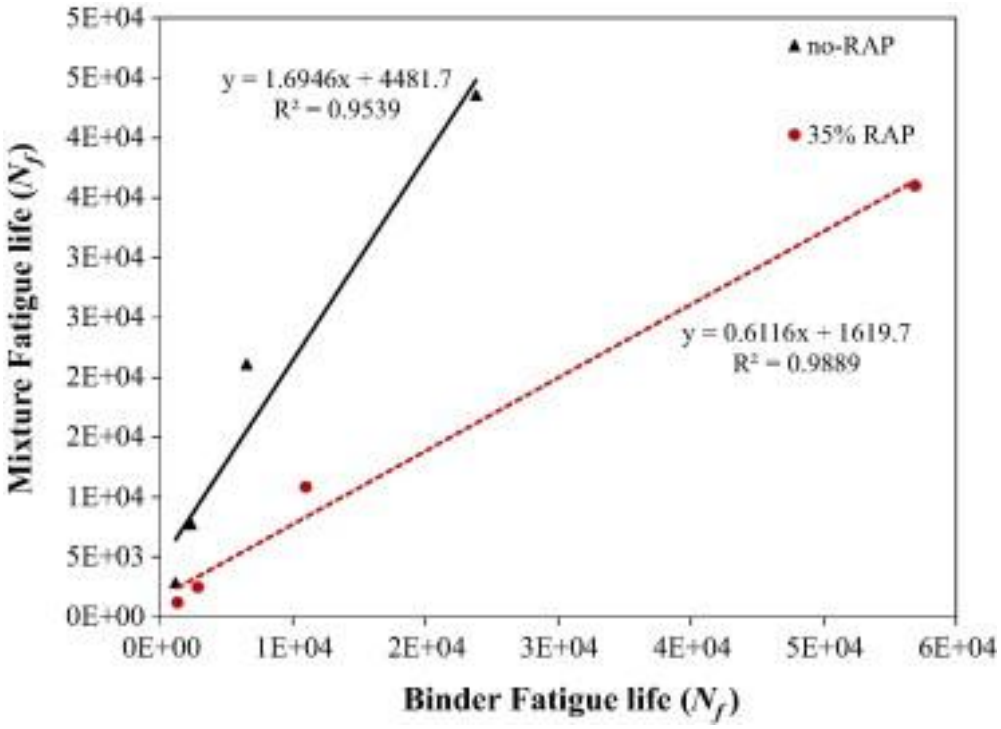

Figure 29. Binder Fatigue Life vs. Mixture Fatigue Life (Mannan et al. 2015)

Stuart et al. (2001) compared BBF fatigue life to the field performance of four lanes in the FHWA-ALF experiment: lanes 1 and 2 consisted of a 100-mm layer of asphalt mix over a 560-mm unbound crushed aggregate base and a prepared subgrade, and lanes 3 and 4 were a 200-mm layer of asphalt mix over a 460-mm unbound crushed aggregate base and a prepared subgrade. ALF and BBF tests were performed at three temperatures: 10°, 19°, and 28°C. **Figure 30** shows the correlations between the number of ALF passes to a crack length of 50-mm and the BBF fatigue life. It was observed that there were good correlations between FHWA-ALF fatigue life and BBF fatigue life, especially at the testing temperature of 28°C. In this project, asphalt binder G*sin(δ) was also compared to ALF fatigue life, and it was observed that the correlation between asphalt binder G*sin(δ) and ALF fatigue life in the thinner pavements (100-mm asphalt layer) was

opposite to one for the thicker pavements (200-mm asphalt layer). The testing results were shown in Chapter 1.

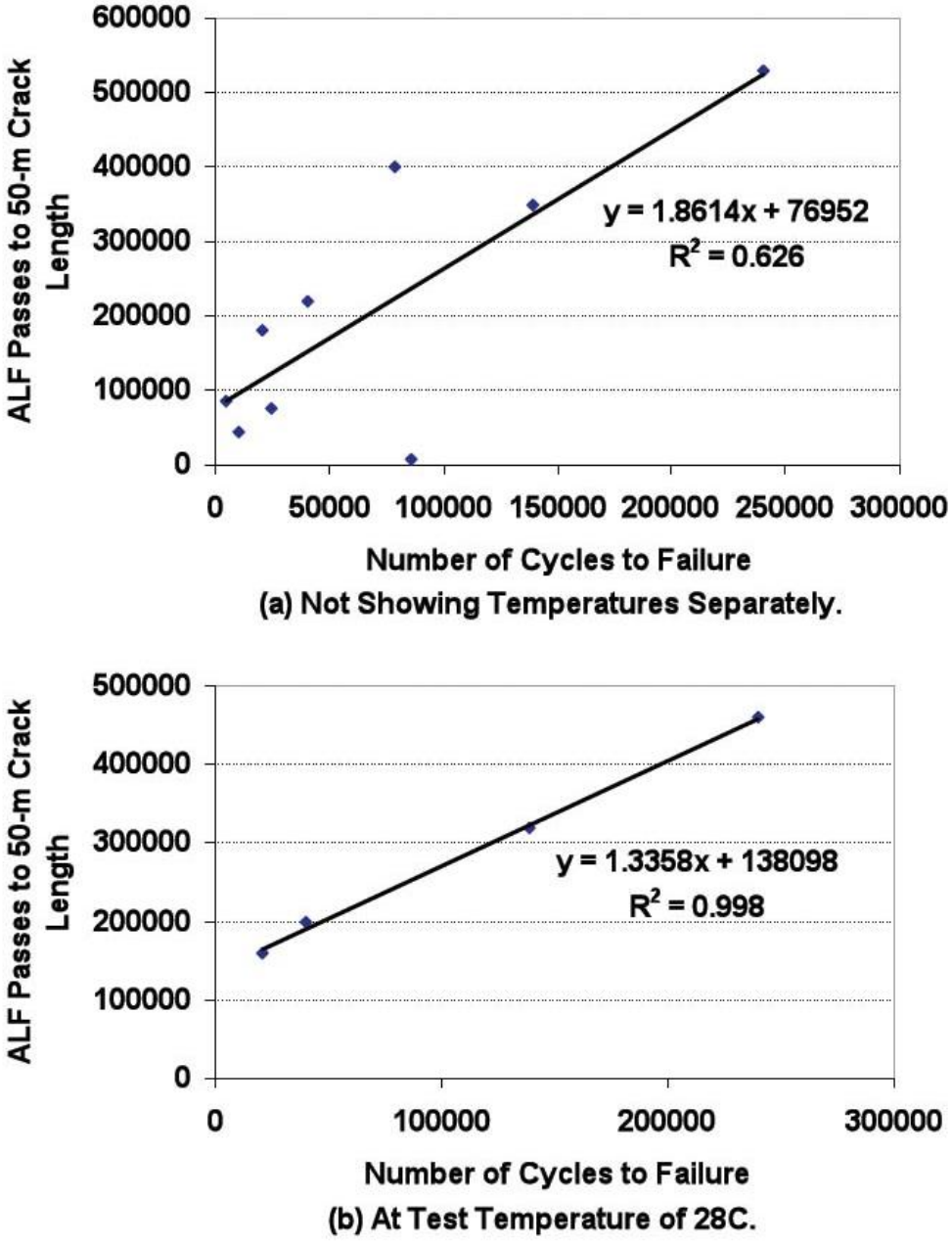

Figure 30. BBF Fatigue Life vs. FHWA-ALF Cracking (Stuart et al., 2001)

2.7 Summary

Based on the literature review above, the following findings can be offered: 1) asphalt binder properties is one of the important factors affecting mix fatigue performance; 2) some researchers reported that G*sin(δ) showed the poor relationship with mix fatigue performance; 3) the results of the binder fatigue tests under a repeated loading showed high correlations with mix fatigue performance; 4) the mix fatigue life of BBF test exhibited a high correlation with field pavement fatigue performance; and 5) energy-based analysis approaches for fatigue analysis exhibited some advantages to evaluate binder and mixture fatigue performance, compared to the traditional analysis approach.

CHAPTER 3 – EXPERIMENTAL PLAN

This study was a part of the National Cooperative Highway Research Program (NCHRP) 9-59 project, and the experimental plan was consulted with and approved by the NCHRP 9-59 panel. Sixteen asphalt binders with a wide range of performance properties were selected for this study so that correlations between asphalt binder properties and asphalt mixture fatigue performance would be applicable to many binders commercially available. The research team was attempted but not able to sample all of the binders from production facilities; thus, some of the binders were blended in laboratories to meet specific performance grades. Also, since this project was not intended to evaluate performance characteristics of specific asphalt binders but to evaluate the correlations between the binder and mixture performance characteristics, the research team agreed with the technical panel and the suppliers that information about suppliers and modifiers/additives used in the binders would not be included in any publications related to NCHRP 9-59 Project; and thus, it is not be included in this dissertation.

3.1 Materials

The binders used in this study include eight polymer modified binders, three binders with different additives, and five straight binders, as shown in **Table 3**. Since fatigue cracking in the field pavement generally occurs after the asphalt binder experiences long-term aging, an extreme aging test was used on all the binders to simulate the long-term aging in the field pavement according to

AASHTO PP 78-17: 85 minutes RTFO at 163°C + 40 HR PAV at 100°C. After the 40-hour PAV aging, binder property tests were conducted.

Table 3. Binders for Laboratory Experiment

Binder ID No.	Polymer/Additive
B1	Polymer
B2	Polymer
B3	Polymer/Additive
B4	Polymer
B5	Polymer
B6	Polymer
B7	No
B8	No
B9	No
B10	Polymer
B11	No
B12	No
B13	Additive
B14	Additive
B15	Polymer
B16	Additive

A 9.5-mm nominal maximum aggregate size (NMAS) mix design with all virgin materials was used for mixture testing in this study. The mix was designed at a design compaction effort (N_{design}) of 80 gyrations. The aggregate blend in the mix consisted of granite 89, natural sand, limestone 8910 and granite M10. The asphalt binder content in the mix design using Binder 8 was 6.0%. This binder content was used to evaluate all the binders (except for B10) to avoid the impact of the binder content on the fatigue performance although the optimum asphalt content could be slightly different for various binders. The optimum asphalt content for the mix with B10 was 6.42% as B10 included crumb rubber, which was not considered as an asphalt binder in this study.

The design gradation is shown in **Figure 31**, and the asphalt content and volumetric properties are summarized in **Table 4**.

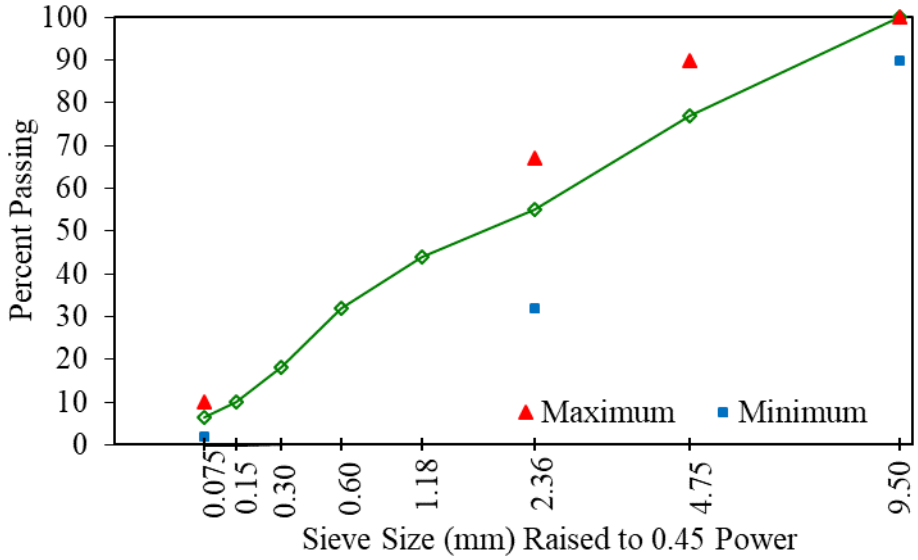

Figure 31. Aggregate Gradation for Asphalt Mix

Table 4. Volumetric Properties in Mix Design

Volumetric Properties	Results	Control Points
AC, %	6.0	--
Air Voids, %	4.0	4.0
VMA, %	16.8	> 15.0
VFA, %	76.0	--
P_{be}, %	5.56	--
D/A Ratio	1.1	0.6 – 1.2

The heated aggregate blend and asphalt binder were mixed at the temperatures shown in Table 5, and the mixing temperatures were determined based on the previous experiences and the

recommendations of binder suppliers. After mixing, the loose mixes were short-term conditioned in an oven at 135°C for four hours in accordance with AASHTO R30. After the short-term aging, the loose mix samples were spread out in large pans and long-term conditioned in another oven at 95°C for five days prior to compaction for preparing test specimens. The long-term aging processes were conducted based on the previous study conducted by Elwardany et al. (2017). More information about this loose mix aging procedure follows.

1. Short-term oven aged (STOA) each loose mix sample following AASHTO R30 at 135°C for four hours.
2. Separated each short-term aged loose-mix sample into several pans, and ensured each pan had a relatively thin layer of loose mix (approximately equal to the NMAS of the mix).
3. Placed the pans with loose mix in an oven and long-term aged the loose mix samples at 95°C for five days (**Figure 32**). The loose mix was agitated once per day during this process, and the pans in the oven were rotated once per day to minimize any effects of potential oven temperature gradient and/or draft on the degree of loose mix aging.
4. After long-term aging, the samples were taken out of the oven and mixed together to obtain a uniform sample.
5. The loose mix was reheated at the compaction temperatures for approximately three hours, and the compaction was performed when the compaction temperature was reached. Compaction temperatures for 16 mixes are summarized in **Table 5**. Compaction temperatures for long-term aged mixes were determined based on the recommendation in the previous study conducted by Elwardany et al. (2017).

Figure 32. Loose Mix Long-term Aging in Oven

Table 5. Mixing and Compaction Temperatures for Mixtures

Binder ID No.	Mixing Temperature, °F	Compaction Temperature, °F
B1	335	325
B2	315	305
B3	315	305
B4	295	285
B5	305	295
B6	315	305
B7	285	275
B8	295	285
B9	295	285
B10	315	305
B11	305	295
B12	315	305
B13	295	285
B14	295	285
B15	295	285
B16	305	295

3.2 Testing Plan

3.2.1 Binder Testing Plan

To characterize the binder fatigue properties, frequency sweep and modified LAS tests were performed by Advanced Asphalt Technologies, LLC (AAT) on the 40 hr PAV-aged binders. In addition, the binder performance grading (DSR and BBR tests) and frequency sweep tests were conducted at NCAT on the binders recovered from nine long-term aged mixes. After the above testing, the following parameters were computed to evaluate binder properties: complex modulus and phase angle master curve, fatigue life, $G^* \times \sin(\delta)$, Delta Tc, loss tangent, crossover frequency, rheological index, and Glover-Rowe value. **Table 6** shows the binder testing matrix used in this study. Due to budget limitations, only nine recovered binders were evaluated using PG and frequency sweep tests

3.2.2 Mixture Testing Plan

Uniaxial and flexural fatigue tests were conducted on long-term aged (LTA) mixtures at NCAT. Uniaxial fatigue testing was performed on mixtures made with all 16 binders in accordance with AASHTO TP 107-14. Two testing temperatures were used for each binder based on the purchase grade in this study: (high PG + low PG)/2 -3 and (high PG + low PG)/2 +3. For example, the testing temperatures for PG64-22 binder are (64-22)/2 - 3 = 18°C and (64-22)/2 + 3 = 24°C.

As requested by the panel for NCHRP 9-59, flexural fatigue testing was performed only on nine long-term aged mixes in accordance with AASHTO T321-14. These nine mixes included the binders with a wide range of performance properties: polymer modified binders with different polymer contents, binders with different additives, and straight binders with various sources and

PG grades. Flexural fatigue tests were performed at 10° and 20°C. **Table 6** presents the mixture testing matrix used in this study.

Table 6. Binder and Mix Testing Plan

Binder ID No.	Binder Testing				Mixture Testing		
	PG	Frequency Sweep		LAS	Dynamic Modulus	Uniaxial Fatigue	Flexural Fatigue
	Binder Extracted from LTA Mixes at NCAT		40-hr PAV-Aged Binder at AAT		Mix aging 4 hrs @135°C and 5 days @ 95°C at NCAT		
B1			√	√	√	√	
B2			√	√	√	√	
B3	√	√	√	√	√	√	√
B4	√	√	√	√	√	√	√
B5			√	√	√	√	
B6	√	√	√	√	√	√	√
B7	√	√	√	√	√	√	√
B8	√	√	√	√	√	√	√
B9			√	√	√	√	
B10			√	√	√	√	
B11	√	√	√	√	√	√	√
B12			√	√	√	√	
B13	√	√	√	√	√	√	√
B14			√	√	√	√	
B15	√	√	√	√	√	√	√
B16	√	√	√	√	√	√	√

Flexural Fatigue Test

The flexural fatigue (or BBF) was conducted in accordance with AASHTO T321-14. Six to eight beam specimens were tested for each mix as additional specimens were tested when results were variable. Within each set of six beam specimens, different strain levels were used to produce a range of fatigue life (from 10,000 to 1,000,000 cycles). The specimens were compacted in a kneading beam compactor (**Figure 33**), and then trimmed to the testing dimensions of 380 ± 6 mm long, 63 ± 2 mm wide, and 50 ± 2 mm high. Furthermore, the orientation in which the beams were compacted (top and bottom) was marked and maintained for the fatigue testing. An air void content of 7 ± 1% was targeted for test specimens after trimming.

Figure 33. Kneading Beam Compactor.

During each test, a beam was held by four equally-spaced clamps, and a sinusoidal load was applied at a frequency of 10 Hz at the two inner clamps to yield a pre-determined target strain level at the center of the specimen. Testing was performed at 10°C and 20°C. **Table 7** summarizes the testing conditions and specimen requirements. Data acquisition software was used to record load

cycles, applied loads, and beam deflections. The software also computed and recorded the maximum tensile stress, maximum tensile strain, phase angle, beam stiffness, dissipated energy, and cumulative dissipated energy at user-specified cycle intervals. The stiffness at the 50th loading cycle is defined as the initial stiffness of the beam. The failure point is the number of cycles where the peak of the product of the flexural stiffness times the number of cycles occurs. The test data were screened for data quality based on the recommendation in the previous study: the acceptable difference between two results is 0.69 (on a log basis) (Prowell et al., 2010).

Table 7. Testing Conditions and Specimen Requirements for BBF Test

Parameter	Value/Type
Target Test Temperature (°C)	10 and 20
Loading Frequency (Hz)	10
Loading Waveform	Sinusoidal
Specimen Size	380 ± 6 mm in Length 63 ± 2 mm in Width 50 ± 2 mm in Height
Target Specimen Air Voids	7 ± 1%

Dynamic Modulus

To characterize the fatigue characteristics of each mixture using the S-VECD model, the dynamic modulus of the mixture was determined to quantify the linear viscoelastic (LVE) characteristics of the mix. The dynamic modulus test was performed in accordance with AASHTO T378-17 in an IPC Global Asphalt Mixture Performance Tester (AMPT), as shown in **Figure 34**. The specimens were prepared in accordance with AASHTO R83-17. The specimens were compacted to a height of 180 mm and a diameter of 150 mm, then cut and cored to meet the specifications. Three

replicate specimens were prepared for each mix. The temperatures and frequencies used for testing were in accordance with AASHTO R84-17. The highest temperature was selected based on the high-performance grade of the base binder being tested. Dynamic modulus testing was performed unconfined and test data were screened for data quality in accordance with the limits set in AASHTO T378-17.

Figure 34. IPC Global Asphalt Mixture Performance Tester

Table 8. Testing Conditions and Specimen Requirements for Dynamic Modulus Test

Parameter	Value
Temperature (°C)	4, 20, and 40/45
Loading Frequency (Hz)	10, 1, 0.1, and 0.01
Specimen Size	100-mm in Diameter 150-mm in Thickness
Specimen Air Voids	7 ± 0.5%

Uniaxial Fatigue Test

The uniaxial fatigue test was performed in accordance with AASHTO TP 107-14. Three to four specimens were tested for each mix as more specimens were tested when test results were variable. The specimens with dimensions of 150 mm in diameter and 180 mm in height were compacted in a Superpave gyratory compactor, and then trimmed to the dimensions of 100-mm in diameter and 130-mm in height. An air void content of 7 ± 0.5 % was targeted for test specimens after trimming. Two test temperatures were used based on the performance grade of the binder used: (high PG + low PG)/2 -3 and (high PG + low PG)/2 +3. **Table 9** summarizes the testing conditions and specimen requirements. To conduct this test, a uniaxial fatigue sample was glued with steel epoxy to two end platens using a gluing jig. The test specimen and end platens were then attached with screws to the actuator and reaction frame of the AMPT, prior to installing linear variable displacement transformers (LVDTs) on the specimen.

Table 9. Testing Conditions and Specimen Requirements for Uniaxial Fatigue Test

Parameter	Value
Temperature (°C)	(high PG + low PG)/2 -3 and (high PG + low PG)/2 +3
Loading Frequency (Hz)	10
Specimen Size	100-mm in diameter 130-mm in thickness
Specimen Air Voids	7 ± 0.5%

Each test consisted of two steps: fingerprint dynamic modulus test and cyclic fatigue test. The fingerprint test was performed in the tension-compression mode of loading. During the test, the load level was controlled to achieve 50 to 75 micro-strains, and this load was applied for 50 cycles.

The fingerprint dynamic modulus was then computed using the data of the last five cycles. The dynamic modulus ratio, the ratio of the fingerprint dynamic modulus to the dynamic modulus determined from the previous dynamic modulus test, was calculated. This value should be between 0.9 and 1.1 in an acceptable test.

For the cyclic fatigue test, a repeated pull-pull load was applied at a frequency of 10 Hz on the test specimen. A maximum displacement of the AMPT actuator was controlled, testing was conducted at three strain levels to yield a wide range of fatigue life (from 1,000 to 100,000). During this test, load cycles, applied loads, and sample deflections were recorded. Additionally, the software computed and recorded the tensile stress, tensile strain, phase angle and stiffness.

3.3 Summary

In this chapter, sixteen asphalt binders and the mixture design used in this study were described. In addition, the sample conditioning processes utilized, the binder and mix testing plans, and the testing methods used were also discussed. The results of the testing data analyses are presented in the following chapters.

CHAPTER 4 – BINDER TEST RESULTS AND ANALYSIS

To characterize the binder properties, modified LAS, DSR, BBR, and frequency sweep tests were conducted. The following index parameters computed based on these tests were employed to compare the binder properties: fatigue life, G*sin(δ), loss tangent, crossover frequency, rheological index, and Glover-Rowe value. These parameters will be used to develop the relationships between binder properties and mix fatigue performance in Chapter 7. Additionally, the binder characterization after two types of aging – 40-hr PAV aging on binders and 4 hr @ 135°C + 5 days @ 95°C aging on loose mixes – was compared to evaluate the effect of two aging methods on binder properties. In this section, no statistical analysis was conducted as all the binder testing results were single data.

4.1 LAS Binder Fatigue Property

In LAS testing, two types of tests are performed in succession: a frequency sweep which is designed to obtain information on the rheological properties and an amplitude sweep which is intended to measure the damage characteristics of the material. In the standard LAS test (AASHTO TP101), the loading in the amplitude sweep test is increased linearly from zero to 30% within 300s, and the strain-amplitude rate (CSR) is 30%/300 s, which equals 0.001 s^{-1}. Wang et al. (2015) developed a modified LAS test: in addition to the frequency sweep and standard amplitude sweep, additional two amplitude sweep tests with standard strain range of 30% were performed within

600s and 900s. In the modified LAS test, the failure point is defined as the peak in stored pseudostrain energy (PSE) (**Figure 35**).

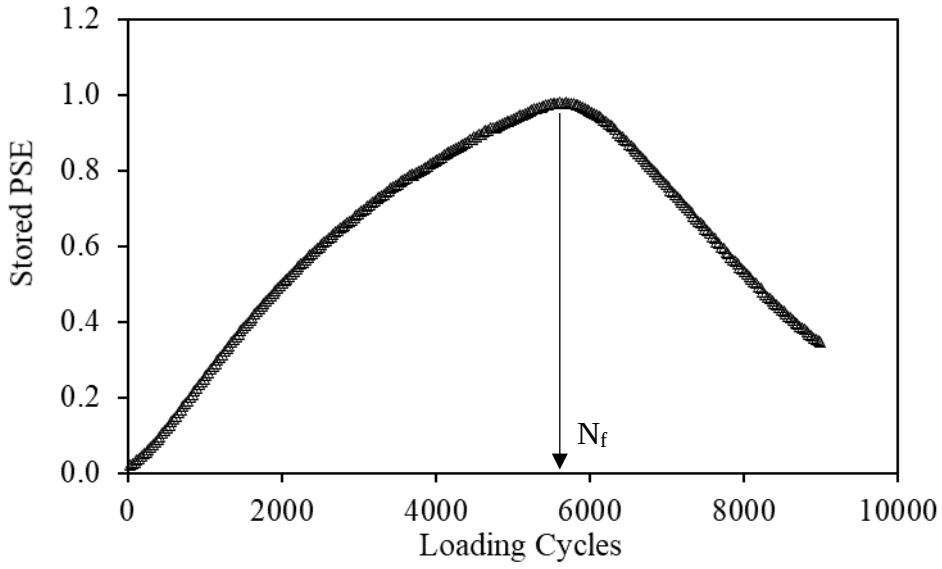

Figure 35. Example of Modified LAS Fatigue Failure Point

There are two important outputs for the modified LAS test: the pseudo stiffness (C) - damage parameter (S) curve (**Figure 36**), and the relationship between pseudostrain energy release rate (G^R) and cycles to failure (**Figure 37**). The C-S curve illustrates how fatigue damage evolves in the binder during the LAS test. The relationship between G^R and the fatigue life can be used to compare fatigue property between binders. For a given G^R, a higher fatigue life indicates a better fatigue cracking resistance. The relationship between G^R and cycles to failure is independent to loading modes and temperatures (Wang et al., 2015).

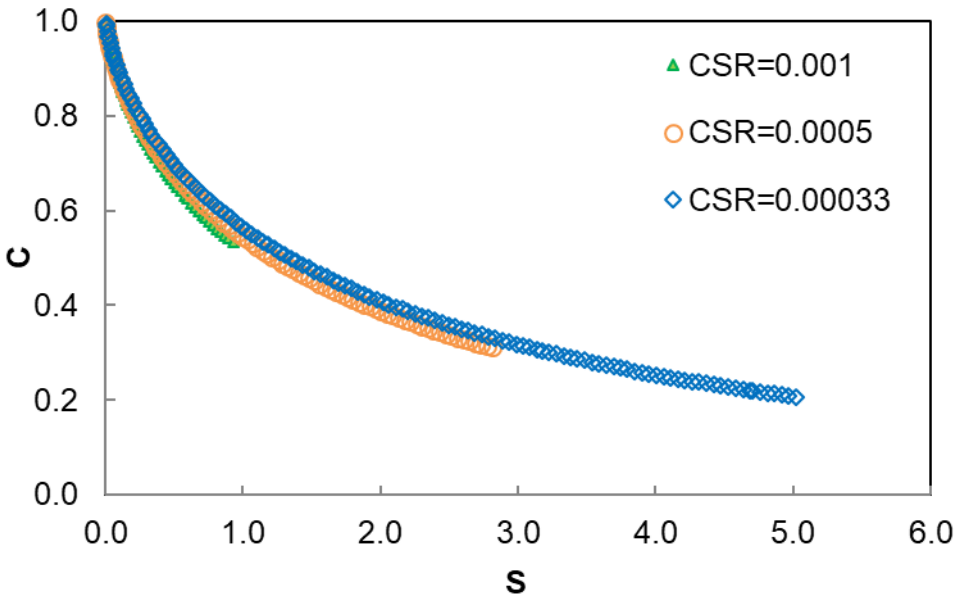

Figure 36. Example of C-S Curve in Modified LAS Fatigue Test

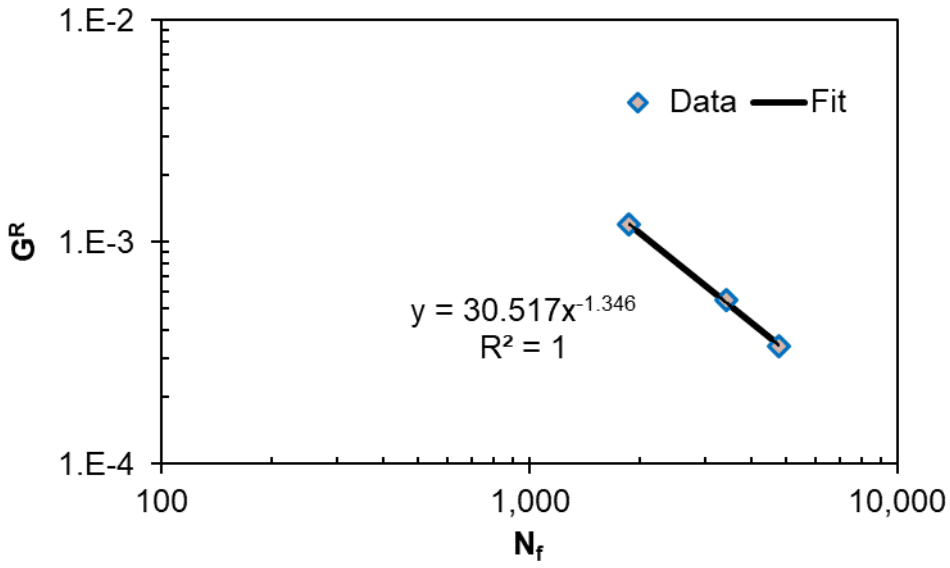

Figure 37. Example of G^R-N_f Curve in Modified LAS Fatigue Test

In this study, the modified LAS test was employed to analyze the binder fatigue property. LAS testing temperatures for all the binders are shown in **Table 10**. These testing temperatures were selected based on previous research (Soenen et al. 2004; Safaei and Hintz 2014). The outcome of

their research suggested that complex shear modulus (G*) in the LAS test should be within the range of 10–50 MPa to avoid a flow of binders and an adhesive failure between the DSR plates and asphalt specimen. **Figure 38** shows the G^R-N_f curves for all the binders used in the study. **Figure 39** and **Figure 40** show the cycles to failure at G^R = 0.0005 and 0.00001, respectively. Generally, the G^R-N_f curves of the polymer modified binders are above those of the non-polymer binders, indicating that the polymer modified binders could have a higher resistance to fatigue cracking than the non-polymer ones. Additionally, most of the G^R-N^f curves of the polymer modified binders are flatter than those of the non-polymer binders, indicating that the fatigue property of polymer modified binders could be less sensitive to the applied loading, compared to the non-polymer binders. Note that the LAS data for B6 will not be used to develop the relationship between binder properties and mix fatigue performance as the R^2 for its G^R-N^f curve was very low (0.26).

Table 10. Testing Temperatures in Modified LAS

Binder ID #	Testing Temperature, °C
B1	22
B2	22
B3	22
B4	15
B5	20
B6	11
B7	17
B8	23
B9	22
B10	22
B11	22
B12	27
B13	15
B14	20
B15	11
B16	23

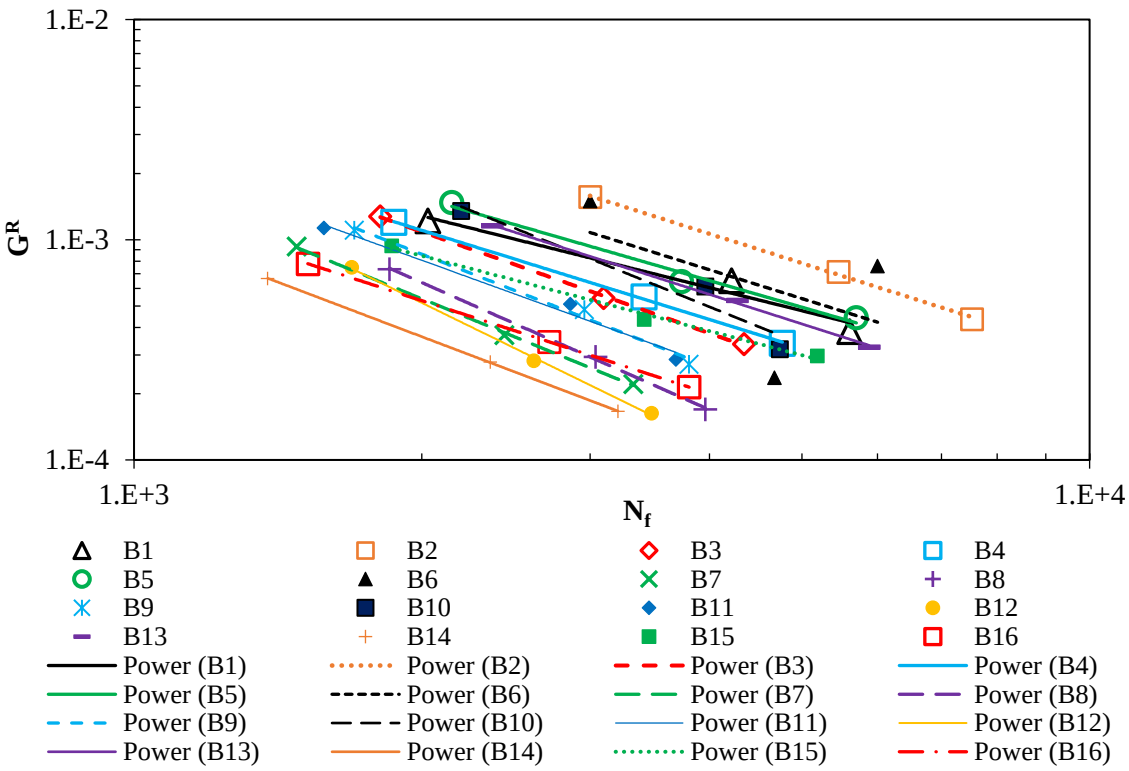

Figure 38. LAS Testing Results

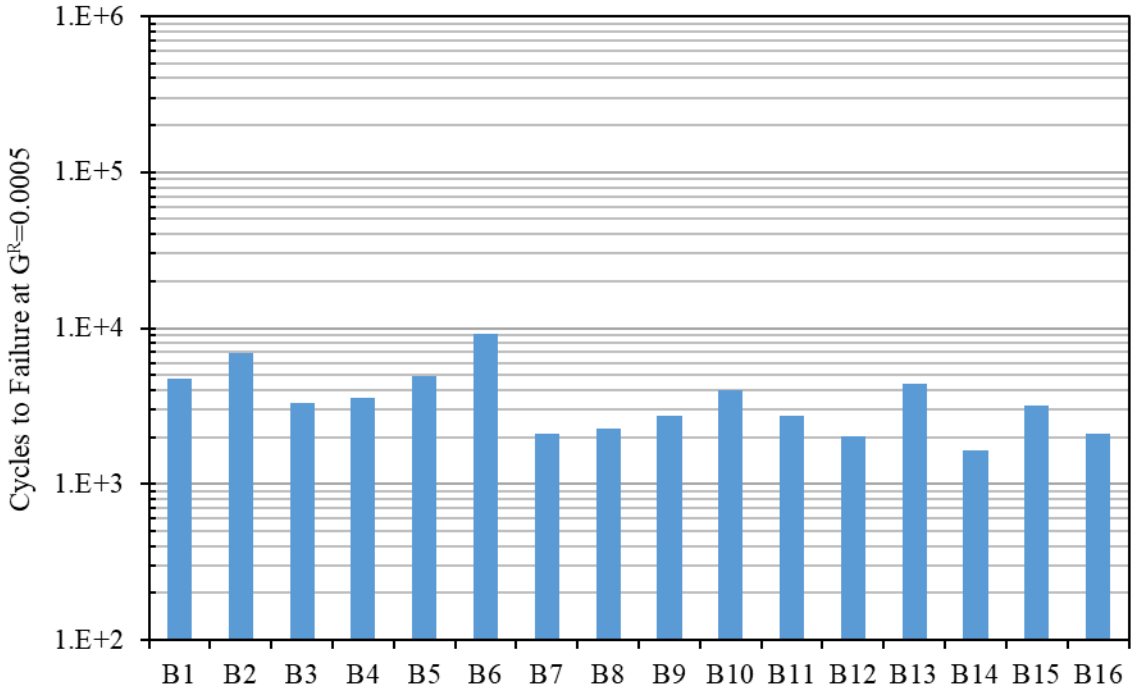

Figure 39. LAS N_f of Binders at $G^R = 5\times10^{-4}$

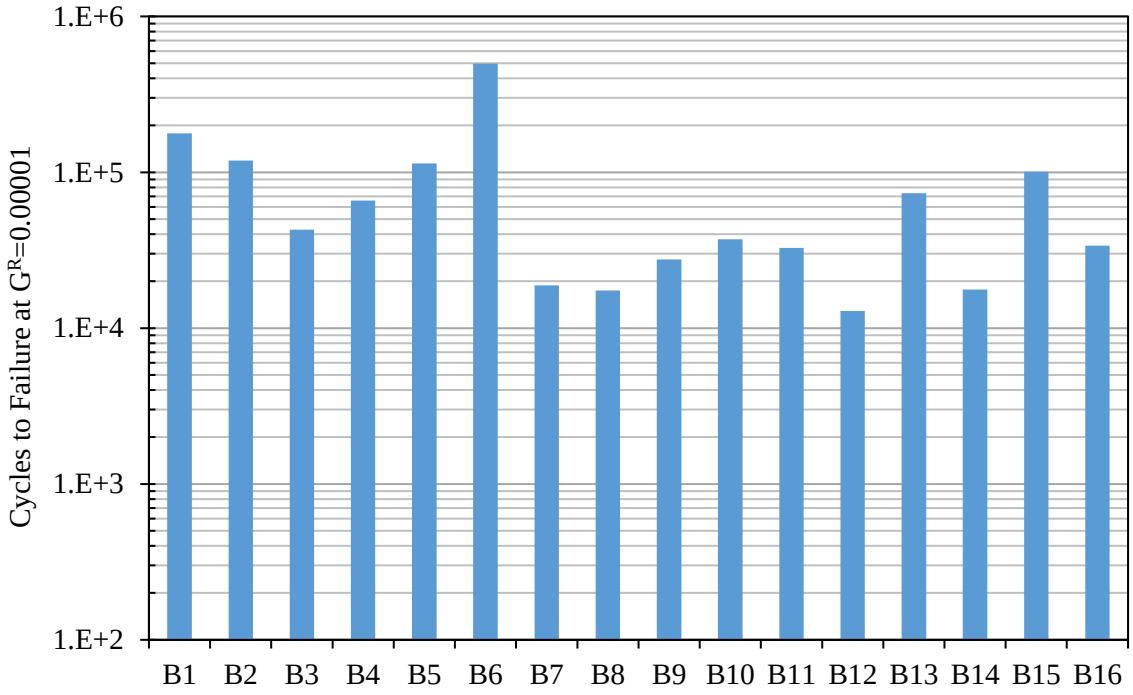

Figure 40. LAS N_f of Binders at $G^R = 10^{-5}$

4.2 Performance Grades

Nine binders (3, 4, 6, 7, 8, 11, 13, 15, and 16) were recovered from the corresponding bending beam specimens after the fatigue testing. DSR and BBR tests were conducted on the extracted binders to determine their PG according to AASHTO M320. Note no additional aging was performed on the extracted binders since they already had a long-term aging. **Table 11** shows the performance grades of the nine binders. The specific findings are summarized as follows:

1) For the high temperature grade, B6 and B11 had the continuous grades greater than 100°C, which is expected as B6 incorporates high polymer content and B11 is an oxidized binder. B7 and B15 could be the softest binders at a high pavement temperature since they showed the lowest grade of 76.8°C. The high temperature PG grades for the remaining binders

varies from 80.3° to 91.0°C. It is well known that a binder with a higher grade at high temperature could have a higher stiffness and better rutting resistance.

2) For the low temperature grade, B15 shows the lowest continuous grade, followed by B6 and B4 and B7; Binder 11 had the highest grade; other binders had similar continuous grade. It is expected that a binder with a lower PG grade could have a better resistance to thermal cracking. Moreover, it was also observed that all the low temperature grades from m value, except for B15, are lower than those from the creep stiffness, indicating that the low temperature PG grades are controlled by m values for these binders.

Table 11. Performance Grades of Recovered Binders

Binder ID	$T_{cont.}$, High	$T_{cont.}$, Low S	$T_{cont.}$, Low m	Cont. Grade
B3	97.6	-24.2	-19.0	97.6 - 19.0
B4	86.6	-30.5	-27.7	86.6 - 27.7
B6	114.9	-37.0	-28.7	114.9 - 28.7
B7	80.3	-28.1	-27.3	80.3 - 27.3
B8	91.0	-26.3	-17.6	91.0 - 17.6
B11	101.5	-27.0	-15.0	101.5 - 15.0
B13	85.8	-36.3	-20.3	85.8 - 20.3
B15	76.8	-34.6	-35.4	76.8 - 34.6
B16	97.7	-23.4	-17.2	97.7 - 17.2

4.3 Delta Tc Parameter

Table 12 shows ΔTc results for the extracted binders. Generally, seven out of the nine binders had the ΔTc values that were more negative than the cracking onset limit of -2.5°C, indicating that these binders could have an identifiable risk of cracking after a long-term aging; six out of the nine binders had the ΔTc values that were lower than the significant cracking limit of -5°C, suggesting that these six binders could have a risk of significant cracking after a long-term aging. B13 had the

lowest ΔTc of -16°C, followed by B11 with ΔTc of -11.9°C. This was expected as both binders generally exhibited poor cracking resistance in the field pavement. B6 with a high polymer content showed a lower ΔTc than the other three binders with normal polymer contents, which was unexpected as a higher polymer content is generally supposed to improve the cracking resistance.

Table 12. Delta Tc of Recovered Binders

Binder ID No.	$T_{cont.}$, Low S	$T_{cont.}$, Low m	Delta Tc, °C	Expected Cracking Susceptibility
B3	-24.2	-19.0	-5.2	Medium
B4	-30.5	-27.7	-2.9	Low
B6	-37.0	-28.7	-8.3	Medium
B7	-28.1	-27.3	-0.9	Low
B8	-26.3	-17.6	-8.6	Medium
B11	-27.0	-15.0	-11.9	High
B13	-36.3	-20.3	-16.0	High
B15	-34.6	-35.4	0.8	Low
B16	-23.4	-17.2	-6.2	Medium

4.4 Complex Modulus and Phase Angle

Asphalt binder is a viscoelastic material, and its mechanical performance is dependent on both temperature and loading time. In this study, complex modulus (G*) and phase angle (δ) were utilized to characterize the viscoelastic behavior of the binders. To investigate the viscoelastic properties of binders, sweeps of multiple frequencies (from 0.1 to 100 rad/sec.) were conducted on binders using the DSR tests at different temperatures: 10°, 22°, 34° and 46°C.

Figure 41 and **Figure 42** show the measured G* and δ values at reduced frequencies, respectively. It was observed that G* values of the modified binder along the frequency had a similar trend with those of the unmodified binder: increasing with the increase in frequency. However, the δ values

of the modified binder along the frequency showed a different trend compared to the unmodified binder: the phase angle of the modified binder exhibited a plateau at higher temperature (lower frequency), while the phase angle of the unmodified binder continuously increased with the increase in temperature. The plateau in the phase angle curve could be caused by the polymer network as the binder at higher temperatures becomes softer and allows polymer network to produce more impact on the binder viscosity compared to lower temperatures.

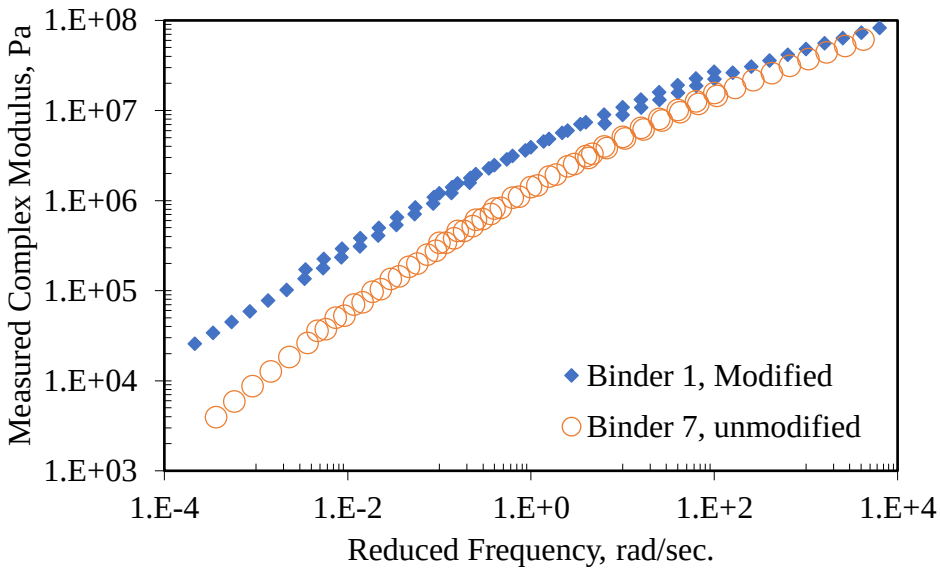

Figure 41. Typical Measured Complex Modulus

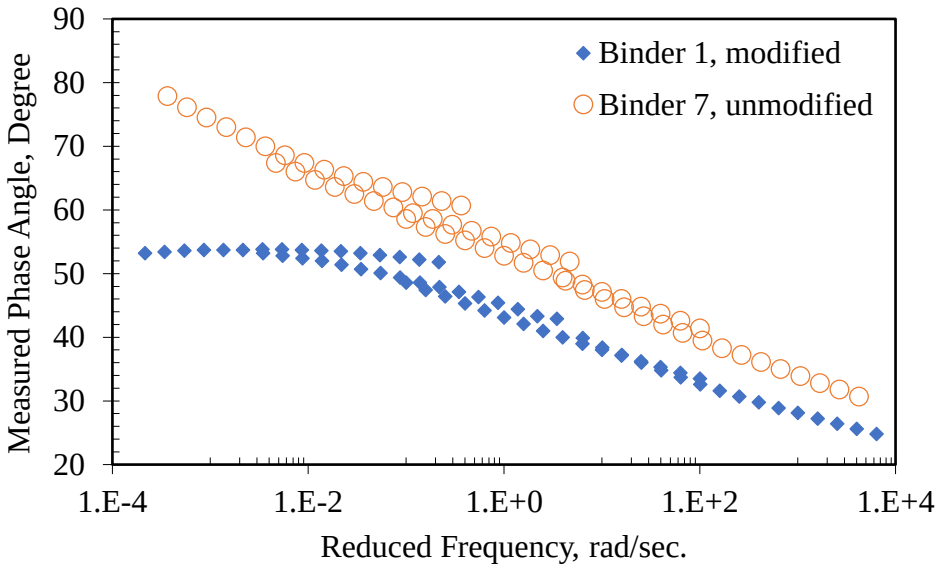

Figure 42. Typical Measured Phase Angles

In this study, the Christensen-Anderson (CA) model (**Equation 18**) was tried to predict the complex modulus and phase angle of the binders. In the CA model, a time-temperature shift factor (α_T) in the horizontal direction (**Equation 19**) was used. To investigate the prediction accuracy of the complex modulus and phase angle, the comparisons between the measured and predicted values for a modified binder (B15) and unmodified binder (B9) were conducted and shown in **Figure 43** and **Figure 44**. It was observed that the predicted and measured G* values were similar and the R^2 values for their correlations were higher than 0.99, while the predicted δ values of the modified binder did not fit the measured values, unlike the unmodified binder. Thus, the CA model was not suitable to conduct the phase angle prediction for polymer modified binders.

$$G^*(\omega) = Gg\left[1 + \left(\frac{\omega_0}{\omega}\right)^{(\log 2)/R}\right]^{-R/(\log 2)} \qquad (18)$$

Where,

G*(ω) = complex shear modulus at frequency (ω), in Pa,

Gg = glassy modulus, in Pa,

ω_o= cross over frequency, in rad/sec,

ω = frequency of interest, in rad/sec, and

R = rheological index.

$$\log \alpha_T = -C_1\left(\frac{T - T_d}{C_2 + |T - T_d|} - \frac{T_R - T_d}{C_2 + |T_R - T_d|}\right) \qquad (19)$$

Where,

α_T = time-temperature shift factor in horizontal direction,

C_1, C_2 = Kaelble fit parameters,

T = temperature, in °C

T_d = defining temperature, in °C and

T_R = reference temperature, in °C.

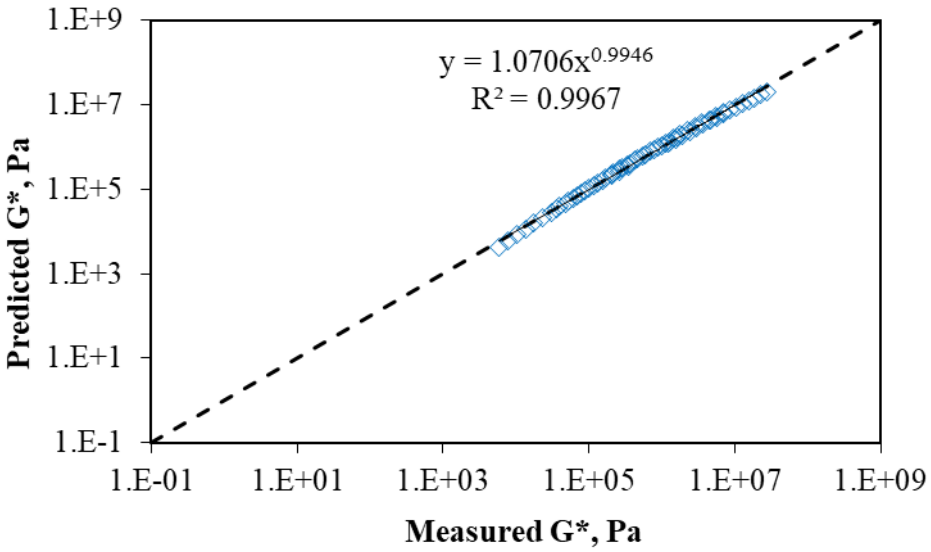

a) B15, Polymer Modified

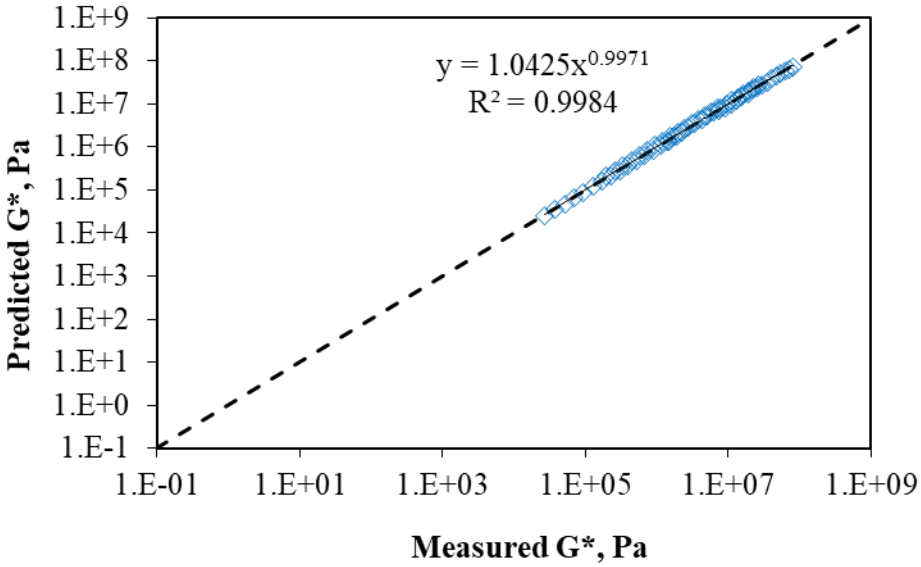

b) B9, Unmodified

Figure 43. Comparison of Predicted and Measured Complex Modulus of Binders

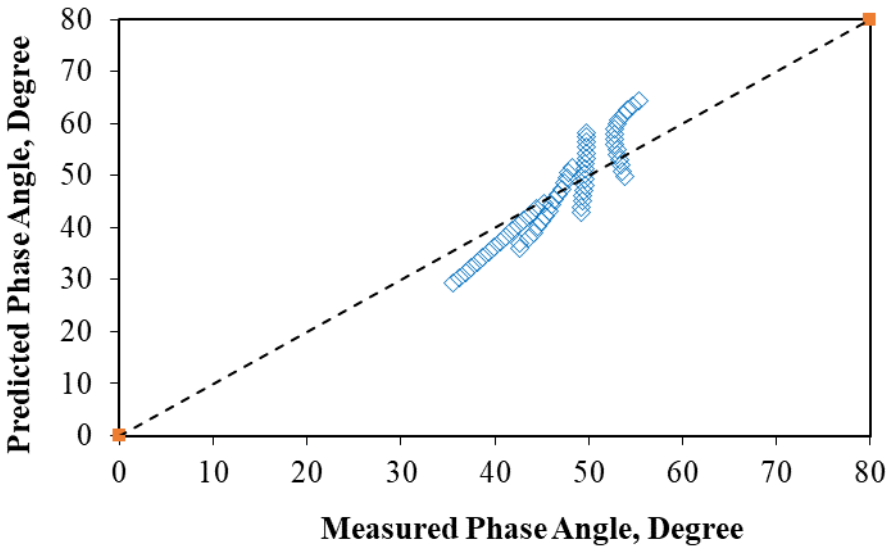

a) B15, Polymer Modified

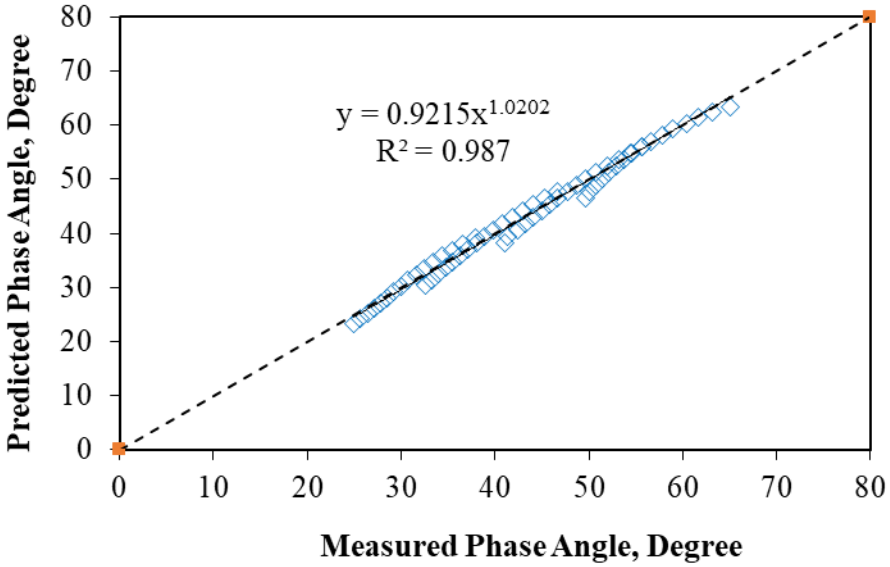

b) B9, Unmodified

Figure 44. Comparison of Predicted and Measured Phase Angle of Binders

Since the traditional CA model is unable to give an accurate prediction for phase angle of polymer modified binders, a modified CA model developed by Don Christensen was used in this study. The modified CA model comprises of a primary and secondary component. The primary

component represents the response of the bulk of the material (asphalt binder), while the secondary component represents the response of the polymer network. Two shift factor functions (horizontal shift and vertical shift factors) are used in the modified CA model to demonstrate the time-temperature superposition principle (TTSP) relationship of binders. The horizontal shift factor (α_T) is assumed to be the same for both components, while the vertical shift factor (b_T) varies for both. Mathematically, the modified CA can be expressed using **Equation 20**. **Figure 45** shows the predicted G* and δ for polymer modified binder 15 using the modified CA model. It was observed that the predicted G* and δ were close to the measured values. The good fits between the predicted and measured values were also found on other binders used in this study.

$$|G^*(\omega,T)| = \frac{1}{b_1(T_r)} CA_1(\omega_r,T_r) + \frac{1}{b_2(T_r)} CA_2(\omega_r,T_r) \qquad (20)$$

Where

CA_1 (ω_r, T_r) = the response of the primary component, as the model using the CA model at the reference temperature (Tr),

CA_2 (ω_r, T_r) = the response of the secondary component, as the model using the CA model at the reference temperature (Tr),

$b_{1(T)}$ = vertical shift factor for primary component

= $\frac{\rho_r T_r}{\rho T}$, T is temperature, Tr is reference temperature, ρ is density and ρ_r is density at reference temperature, and

$b_{2(T)}$ = vertical shift factor for secondary component

= k(T-Tr), and k is a coefficient typically have a value between 0.02 and 0.03.

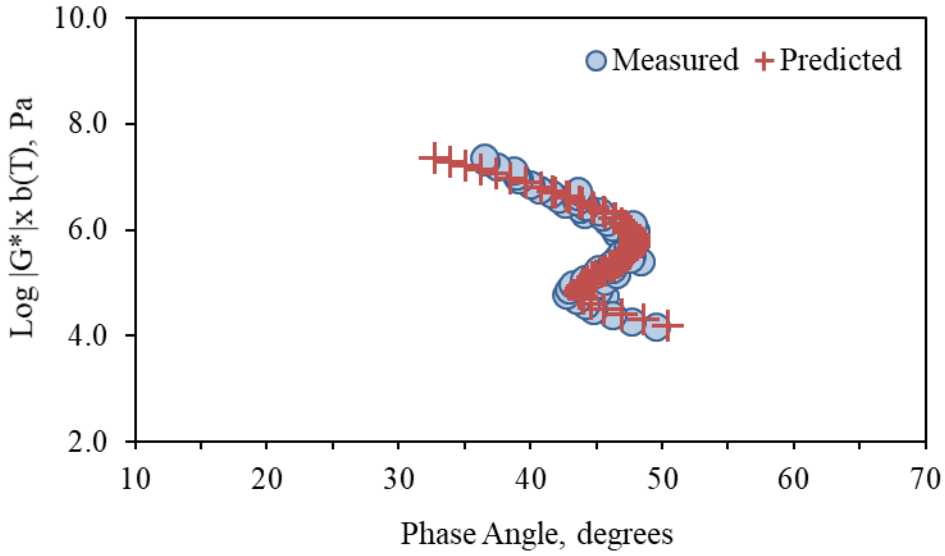

Figure 45. Measured and Predicted G* and δ for Binder 15

After validating the prediction accuracy of the modified CA model, it was used to produce the master curves of complex modulus and phase angle for each binder. **Figure 46** shows the master curves of complex modulus of 40 HR PAV-aged binders. B12 had the highest G* in the whole range of reduced frequency, followed by B10, B11 and B16. B15 showed lower G* values in most cases. **Figure 47** shows the master curves of phase angle of 40 HR PAV-aged binders. As shown in **Figure 47**, phase angles of modified binders showed similar trends along the reduced frequencies: at higher frequencies, phase angle increased with the decrease in frequency (the increase of temperature); at intermediate and lower frequencies (intermediate and higher temperatures), phase angles of modified binders exhibited plateaus and then slightly reduced with decreasing frequency; while phase angles of unmodified binders showed continuous increase with the decrease in frequency (the increase of temperature). This finding agrees with the previous study (Goodrich 1991; Airey et al., 2004). In addition, B12 showed the lowest phase angle at intermediate and high frequency, while Binder 15 showed the highest phase angle at intermediate

and high frequency. That was expected as B12 was the stiffest and most brittle, and B15 was the softest in most cases.

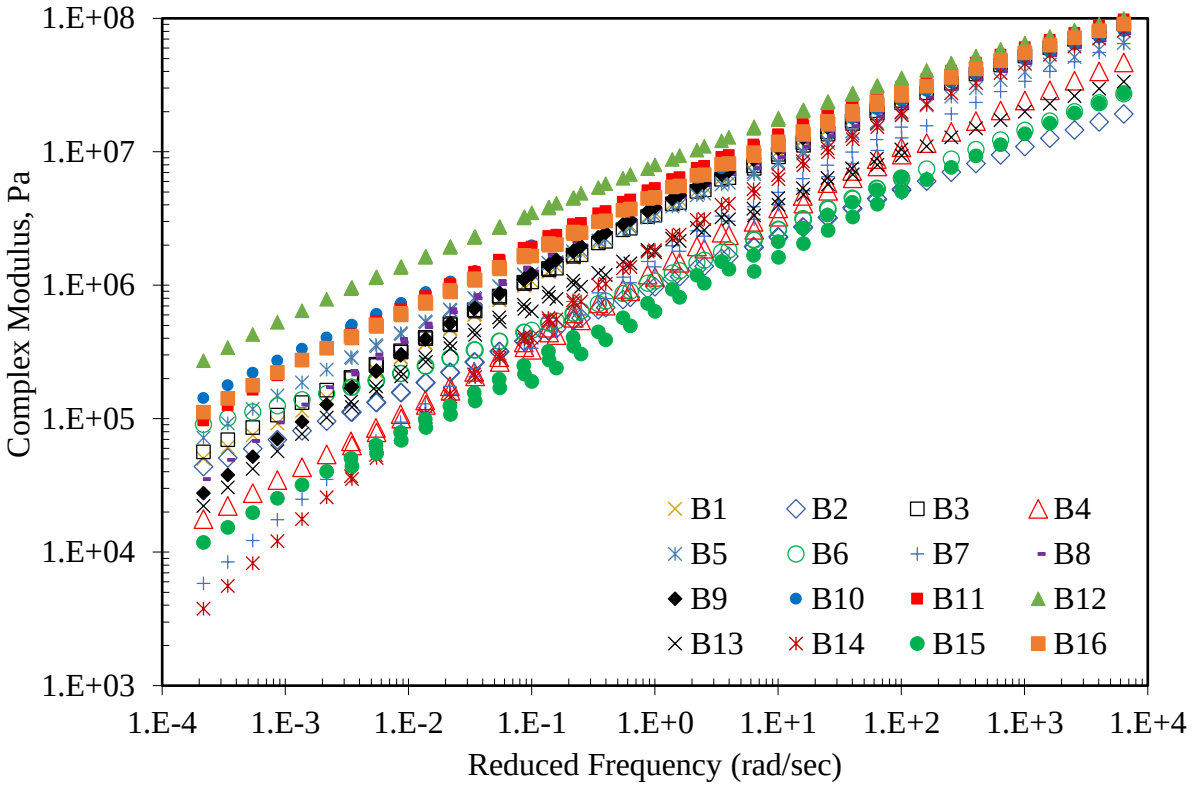

Figure 46. Master Curves of G* at 22 °C

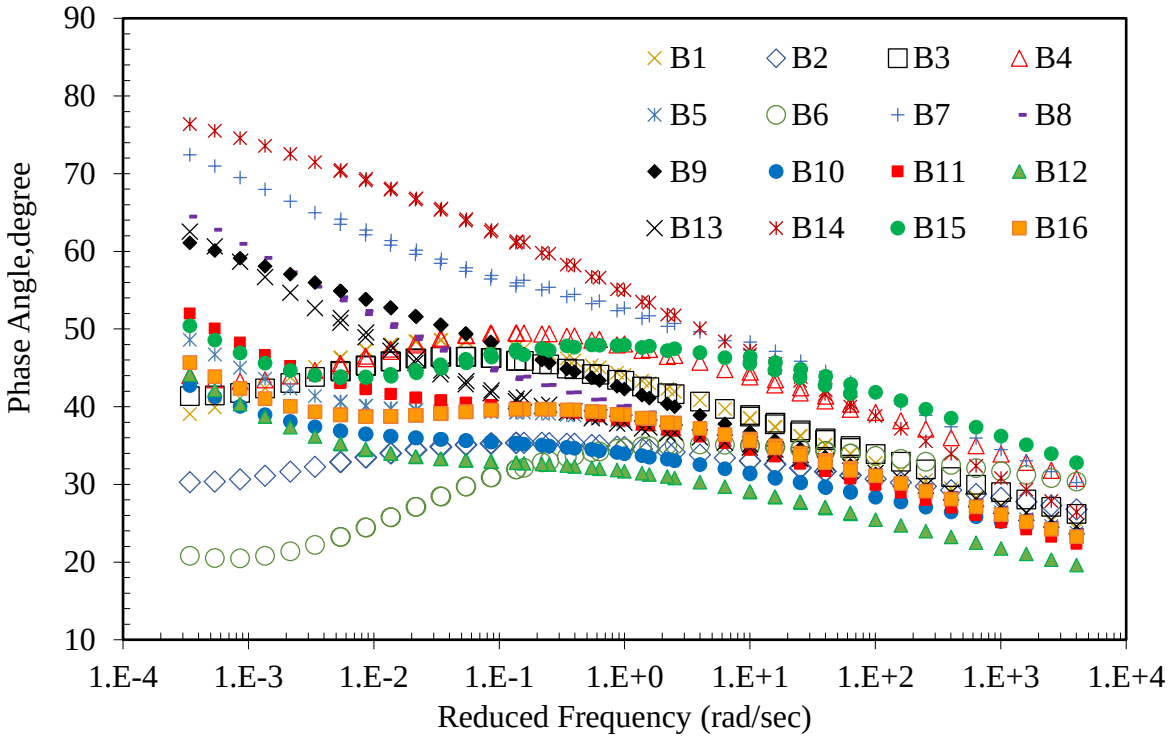

Figure 47. Master Curves of Phase Angle at 22 °C

4.5 Shear Loss Modulus

Shear Loss Modulus, G*sin(δ), represents the viscous component of G*. It is expected that a binder with a lower G*sin(δ) value could have a better resistance to fatigue cracking. To avoid premature fatigue cracks, the current SHRP specification sets a maximum limit of 5,000 kPa for G*sin(δ) at intermediate temperature. In this study, the intermediate continuous temperatures where G*sin(δ) =5000 kPa were measured on the extracted binders, as shown in **Table 13**. Based on the intermediate continuous temperatures, the expected cracking susceptibility is shown in **Table 13**. To investigate G*sin(δ) of all the binders, G*sin(δ) value for each binder was computed at 10° and 20°C and at 10 rad/sec using the frequency sweep testing results, as shown in **Figure 48**. As can be seen, polymer modified B1 and B3 showed the similar intermediate continuous temperatures and G*sin(δ) values with oxidized B11 and B12, indicating they might have similar fatigue

properties. This was unexpected as polymer modified binders generally have better fatigue property than oxidized binders.

Table 13. Intermediate Continuous Temperatures of Recovered Binders

Binder ID	Intermediate Continuous Temp., °C	Expected Cracking Susceptibility
B3	28.9	High
B4	21.4	Medium
B6	12.4	Low
B7	21.2	Medium
B8	21.6	Medium
B11	26.7	High
B13	16.3	Low
B15	12.2	Low
B16	28.9	High

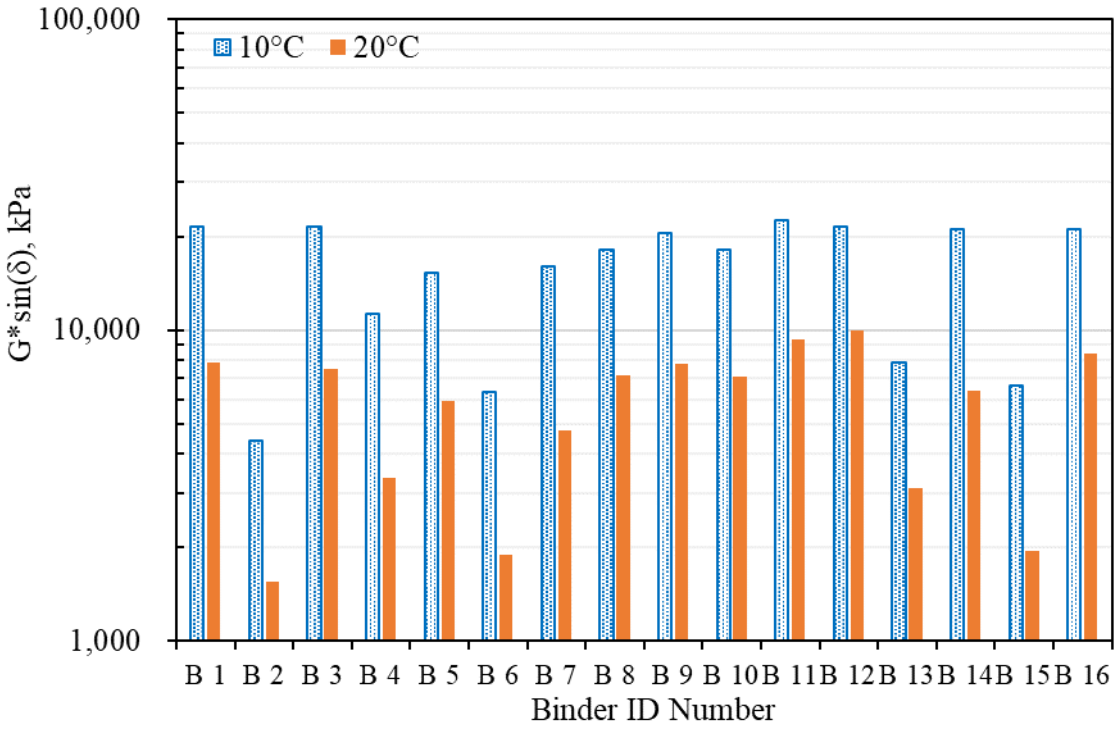

Figure 48. G*sin(δ) Values of 40-hr PAV-Aged Binders

4.6 Loss Tangent

In this study, loss tangent at 10°C and 10 rad/sec was computed using the master curves of 40-hr PAV-aged binders. **Figure 49** shows the loss tangent values of aged binders. A binder with a higher loss tangent is expected to have a better resistance to cracking. B12 exhibited the lowest loss tangent, suggesting that B12 may have the worst cracking resistance. That was expected as B12 was a brittle and oxidized binder. Straight B7 showed a higher loss tangent than most of polymer modified binders, which was unexpected as polymer modified binders generally have a higher fatigue behavior than straight binders.

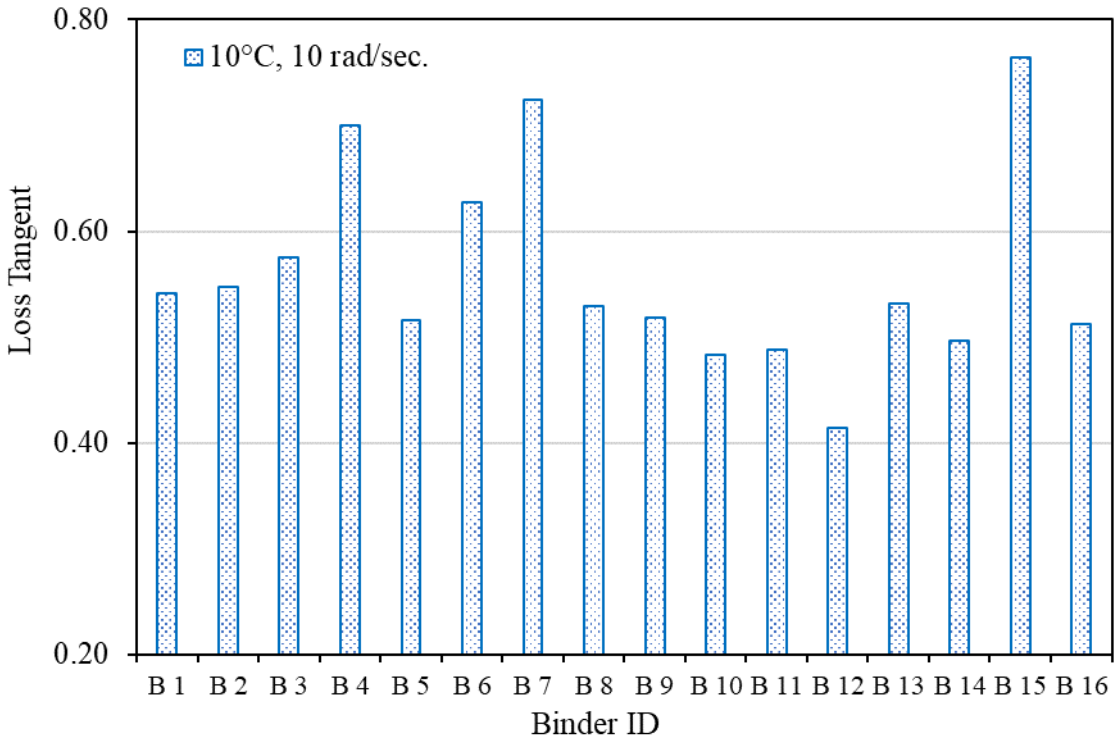

Figure 49. Loss Tangent of 40-hr PAV-Aged Binders

4.7 Crossover Frequency and Rheological Index

Generally, the combination of ωc and R is used to investigate the effect of aging on binder properties. As the asphalt binders age, ωc decreases and R increases, resulting in their position

shifting from the upper left to the lower right in the ωc-R plot. The binder at the lower right in the ωc-R plot is expected to have a lower cracking resistance compared to that at the upper left.

In this study, the combination of ω_c and R was employed to investigate its ability to distinguish the fatigue property of binders. **Figure 50** shows the ω_c versus R values for 16 binders. B2, B3 and B6 are at the lower right corner of the graph, indicating they could have worse cracking resistance than others even worse than the two oxidized binders. The unexpected results are likely due to the polymers in the binders which could result in a higher R and lower crossover frequency.

.

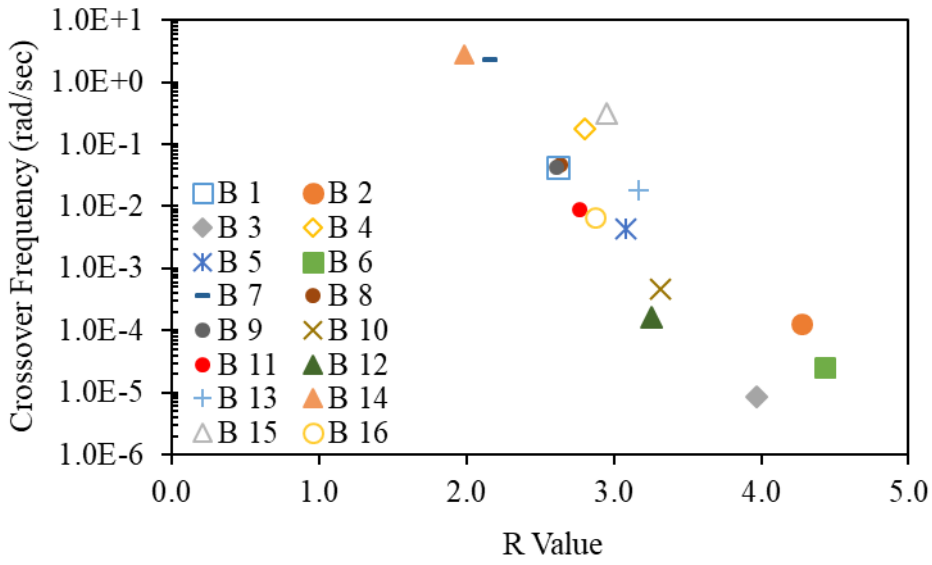

Figure 50. Crossover Frequency vs. R Value for All Binders

4.8 Glover-Rowe Parameter

In this study, the G-R parameter is used to investigate the fatigue property of binders. **Figure 51** and **Figure 52** show the black space and G-R values of 16 binders. Based on G-R values, most of the polymer modified binders had similar G-R values to straight B8 and B9 even lower G-R than straight B7, indicating that most of the polymer modified binders may have similar or lower cracking resistance compared to the straight binders, which was unexpected. Like ωc and R results, the unexpected results are likely because the polymers in the binders produced a higher stiffness and lower phase angle, resulting in a higher G-R value.

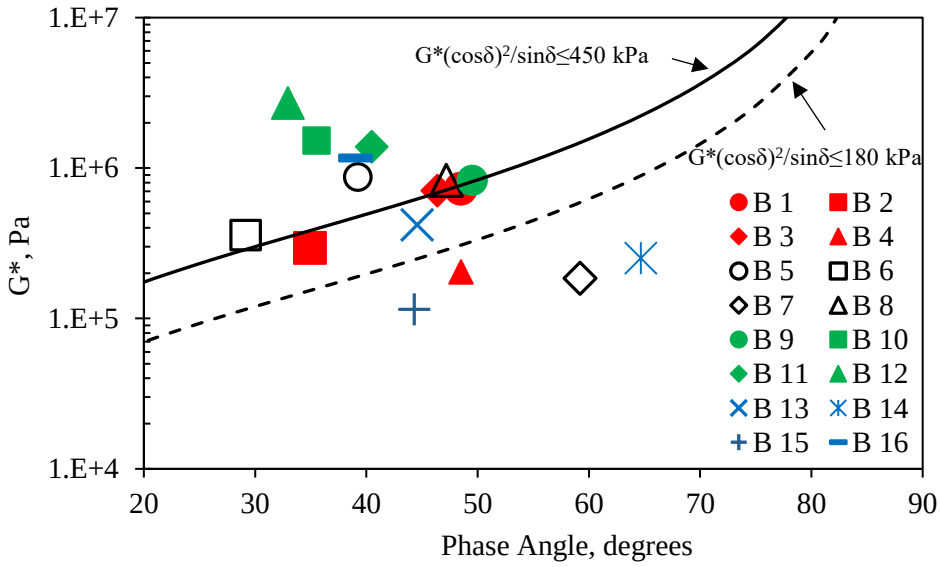

Figure 51. Black Space Plot for All Binders

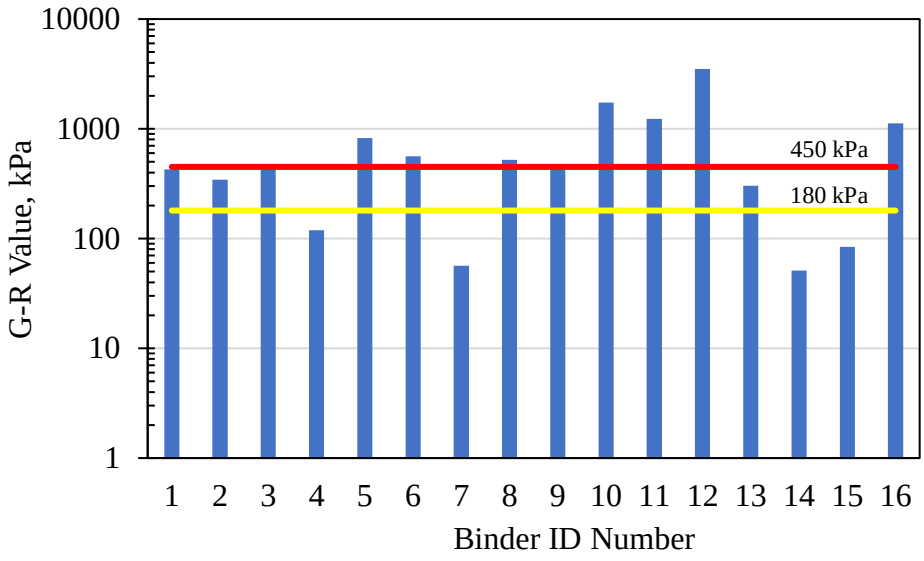

Figure 52. Glover-Rowe Values for All Binders

4.9 Comparison of Binder Aging and Loose Mix Aging

To compare the levels of binder aging after 40-hr PAV and 5-day loose mix aging at 95℃, DSR and frequency sweep tests were conducted on the binders. **Figure 53** shows the temperature grades for G*sin(δ) = 5,000 kPa. It was observed that all 40-hour PAV-aged binders exhibited a little bit lower temperature grades compared to the binders extracted from the long-term aged loose mixes, and the difference in binder temperature grades varied from 0.7 °C to 3.7 ℃.

In addition, G* and phase angle values from frequency sweep tests were compared between PAV-aged binders and mix-extracted binders, as shown in **Figures 53 to 62**. It was observed that that G* values and phase angles of all the PAV-aged binders, except for B6, B13, and B15, were similar to those of the corresponding mix-extracted binders at low and intermediate temperatures. The black space curves of PAV-aged binders with additives did not exhibited a good match with those of the corresponding mix-extracted binders at high temperatures. It is unknown what caused this difference for binders with additives at high temperatures.

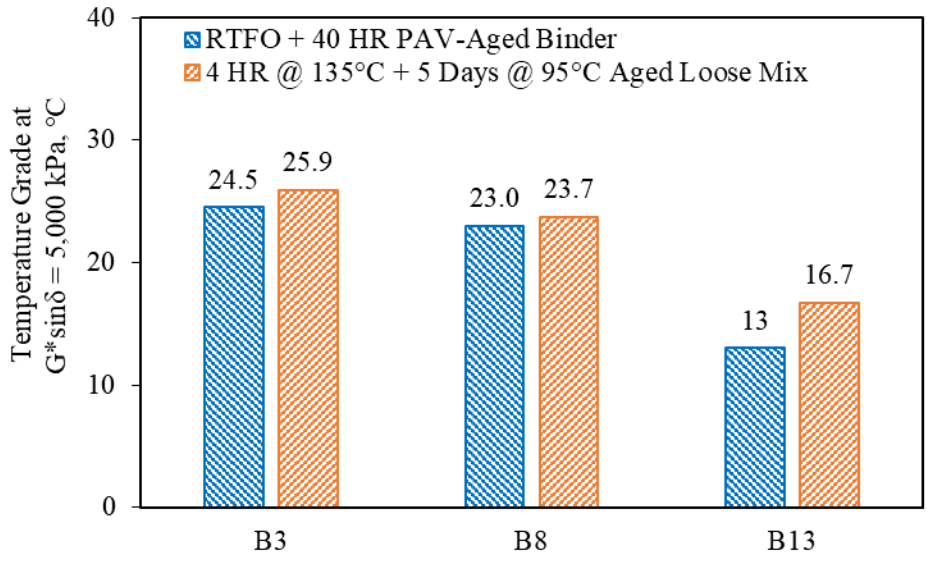

Figure 53. Intermediate Temperature Grades from DSR Tests

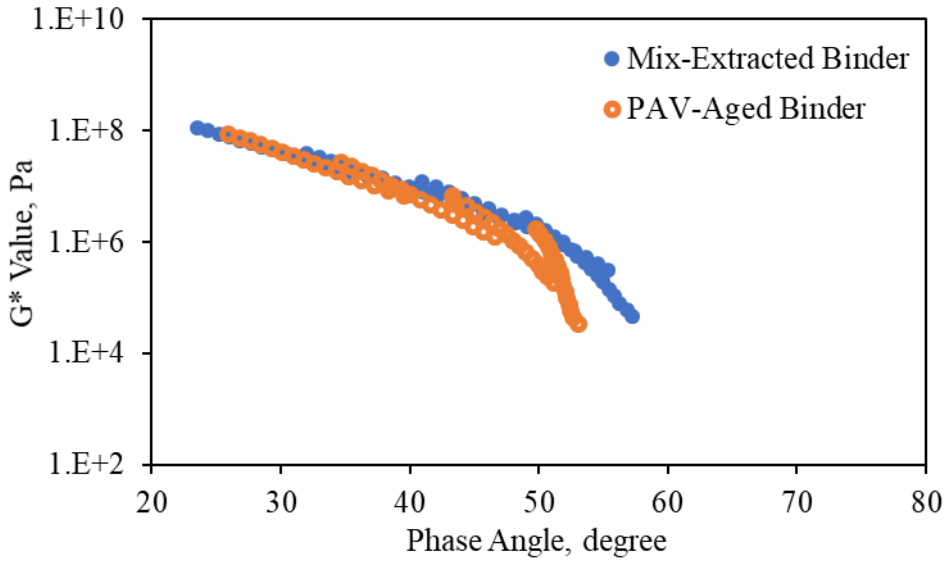

Figure 54. Black Space Diagram for Binder 3

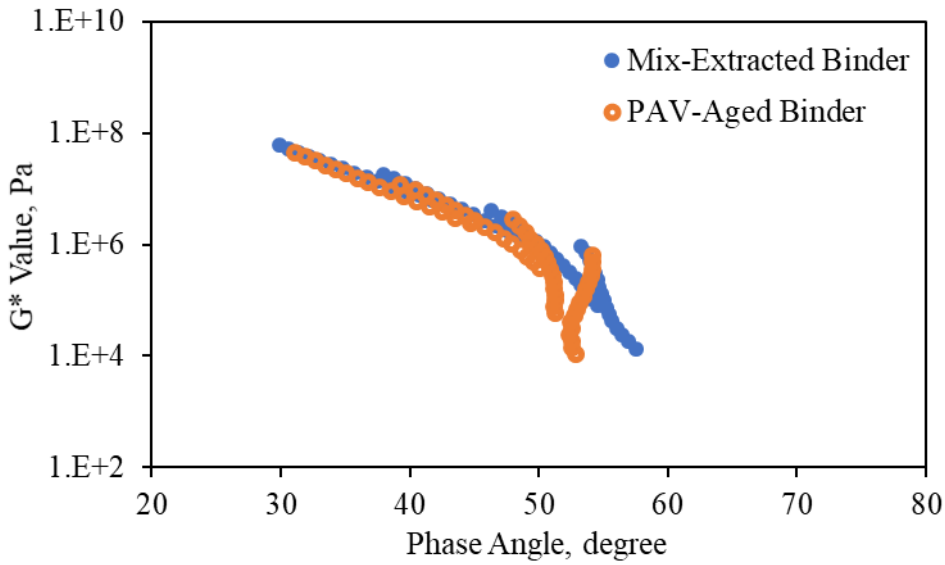

Figure 55. Black Space Diagram for Binder 4

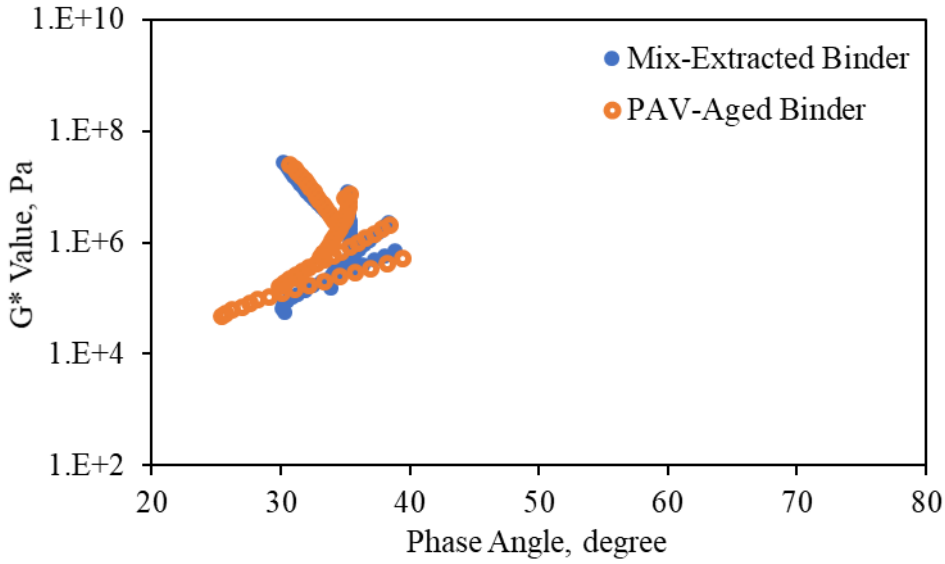

Figure 56. Black Space Diagram for Binder 6

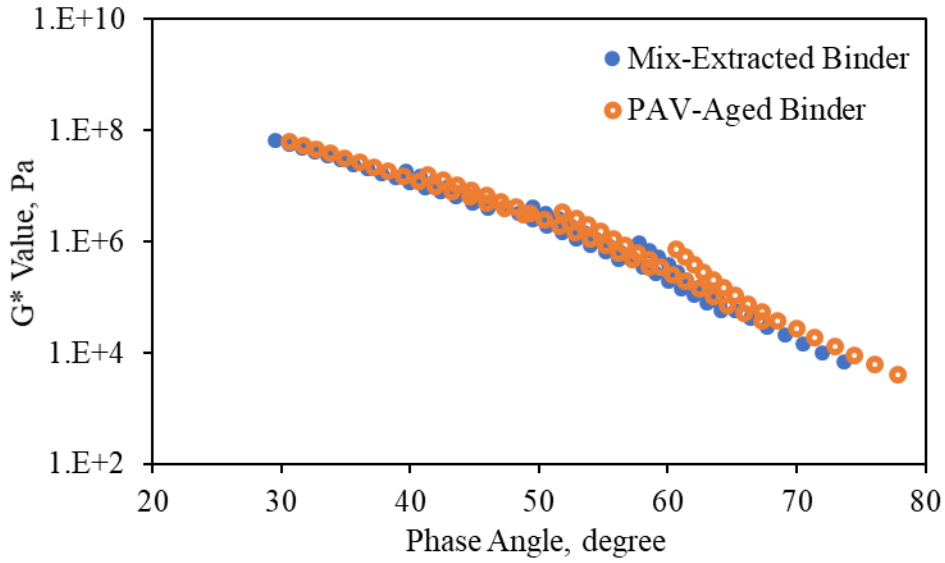

Figure 57. Black Space Diagram for Binder 7

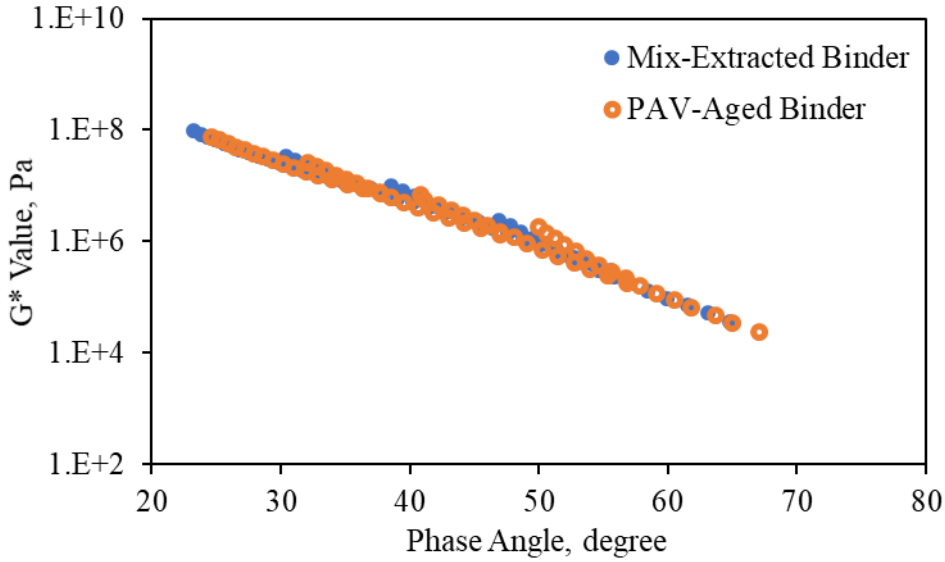

Figure 58. Black Space Diagram for Binder 8

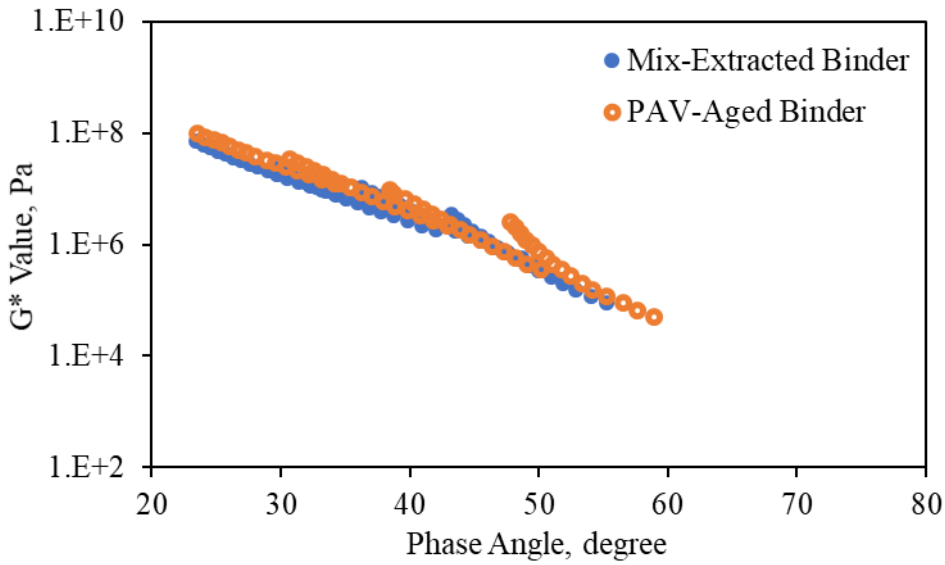

Figure 59. Black Space Diagram for Binder 11

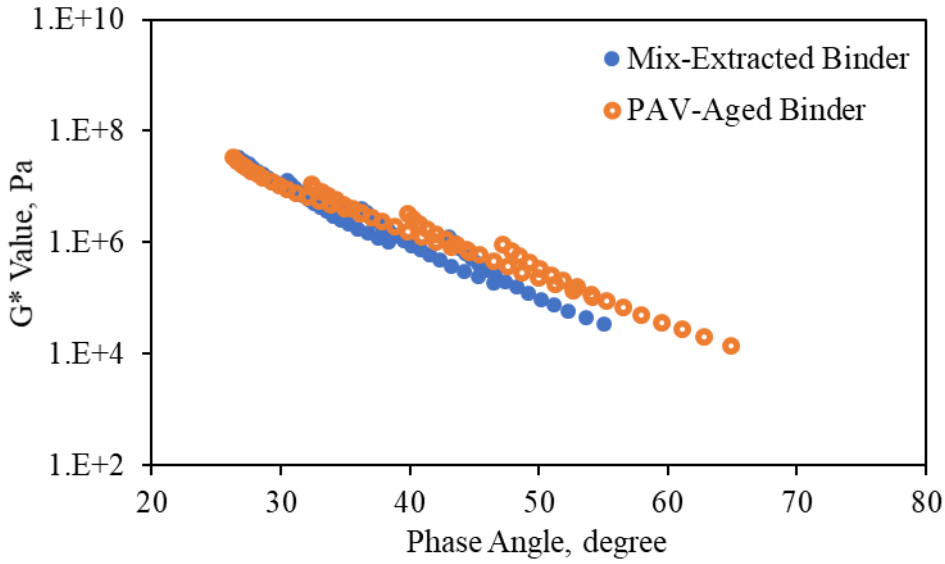

Figure 60. Black Space Diagram for Binder 13

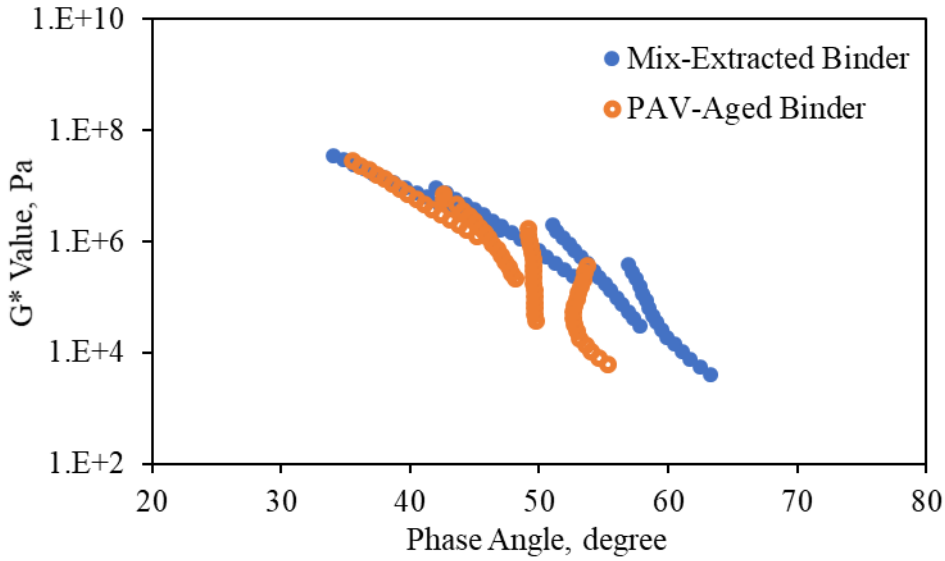

Figure 61. Black Space Diagram for Binder 15

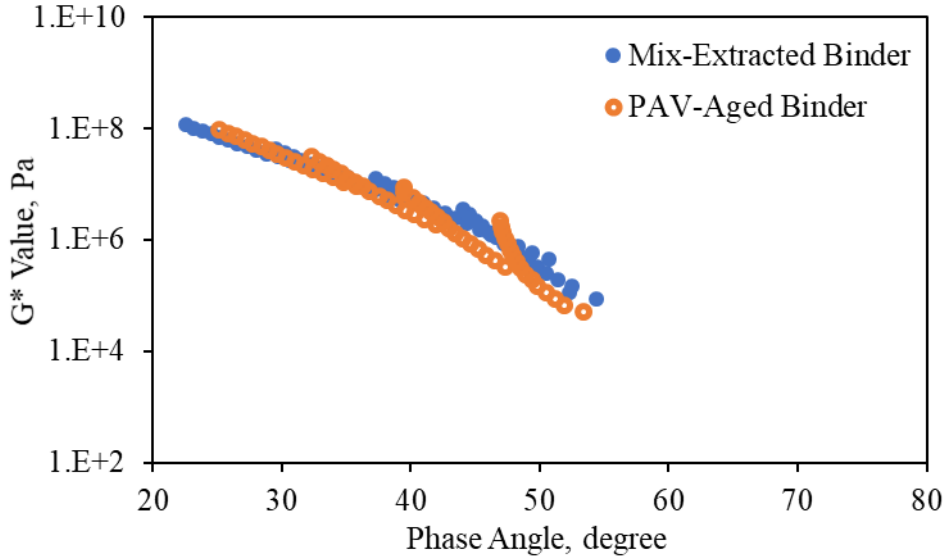

Figure 62. Black Space Diagram for Binder 16

4.10 Summary

In this chapter, the binder fatigue/fracture properties were investigated using linear amplitude sweep, dynamic shear rheometer, bending beam rheometer and frequency sweep tests. Based on

these tests, the following parameters were computed for developing the relationships between the binder properties and mix fatigue performance in Chapter 7: fatigue life, G*sin(δ), delta Tc, loss tangent, crossover frequency, rheological index, and Glover-Rowe value. In addition, a comparison between binder aging and mix aging was also discussed. The key findings based on the above analysis can be summarized as follows:

1) In terms of LAS fatigue life, the polymer modified binders could have a higher resistance to fatigue cracking than the non-polymer binders. This agrees with the previous research (Khattak and Baladi, 1998, 2001; Quintus et al., 2007; Willis et al., 2016).
2) The phase angles of the polymer modified binders showed a different trend along the reduced frequency compared to non-polymer binders: the modified binders generally exhibited a plateau in their phase angle master curves, while the non-polymer binders showed continuous increase in the phase angles with the decrease in frequency. This finding agrees with the previous study (Goodrich 1991; Airey et al., 2004).
3) The addition of polymers in the binders could make it difficult using the index parameters (e.g., crossover frequency, rheological index, and Glover-Rowe value) to compare the binder cracking properties. This is likely attributed to the following factors: the use of polymers increases the binder stiffness, decreases phase angle, and flattens the master curves, which is similar to the results caused by aging. However, aging generally reduces the fatigue resistance of binders, and polymers improve the fatigue properties of binders. In this case, the above parameters could produce an unexpected result.
4) At intermediate and low temperatures, all 40-hr PAV-aged binders exhibited similar G* values and phase angles with the corresponding binders extracted from the long-term aged loose mixes, except for B6, 13 and 15 on phase angles.

CHAPTER 5 – MIX TEST RESULTS AND ANALYSIS

To evaluate the effect of binders on the mix fatigue properties, the flexural fatigue, dynamic modulus and uniaxial fatigue tests were conducted on the mixes. Flexural fatigue tests were conducted on nine of sixteen mixes at two intermediate temperatures (10° and 20°C). Uniaxial fatigue tests were performed on all the sixteen mixes at two temperatures which depended on the binder PG grades. The traditional phenomenological approach and the dissipated energy approach were used to analyze the flexural fatigue data. The dissipated energy approach and the simplified viscoelastic continuum damage (S-VECD) approach was employed to investigate uniaxial fatigue.

5.1 Flexural Fatigue Results

5.1.1 Traditional Phenomenological Approach

The relationships between strain levels and fatigue lives are shown in **Figure 63** and **Figure 64**. Detailed flexural fatigue data are shown in **Appendix A**. The correlations between applied strain and fatigue life ($N_f = k_1(\frac{1}{\varepsilon_0})^{k_2}$) were developed by the regression analysis and coefficients are shown in **Table 14**. Based on **Figure 63** and **Figure 64**, the following observations are drawn:

1) In general, the fatigue life curves representing asphalt mixes with polymer modified binders were generally on the right side of the plot, suggesting better fatigue resistance than those with unmodified or oxidized binders, especially at 20°C. This agrees with the previous research (Khattak and Baladi, 1998, 2001; Quintus et al., 2007; Willis et al., 2016). The fatigue life curves at 10°C were closer together compared to those at 20°C,

indicating that the fatigue lives of these mixes became less different as the test temperature decreased.

2) Fatigue life for the mix containing B3 was higher than that for the mix with B16, although both binders had similar continuous grades (higher, intermediate and low temperature). The difference of fatigue life is likely due to polymer used in B3 while no polymer used in B16. Also, B11 had a lower intermediate continuous grade than B3, while the mix containing B11 showed significantly worse fatigue resistance than that with B3. This means that in some cases the intermediate grade could not distinguish the fatigue properties between straight binders and polymer modified binders.
3) At 10°C, the mixes with B4, B7 and B8 exhibited similar fatigue property. This pattern agrees with that in their intermediate continuous grades. At 20°C, however, the three mixes showed different fatigue properties. This indicates that the fatigue performance of these three binders had different sensitivity of temperature.
4) The regressions between applied strain and fatigue life in **Table 14** were used to examine the quality of the mixture data. The regression R^2 for the mix with B13 at 20°C and the mix with B16 at 10°C showed lower R^2 values than other mixes. Based on the distribution of the regressions' R^2 values, three standard deviations (SD) from the mean of R^2 distribution was 0.753, and the R^2 values of the two mixes above were higher than 0.753. Therefore, the R^2 values for these two mixes were within the normal distribution, indicating that the mixture data were acceptable.

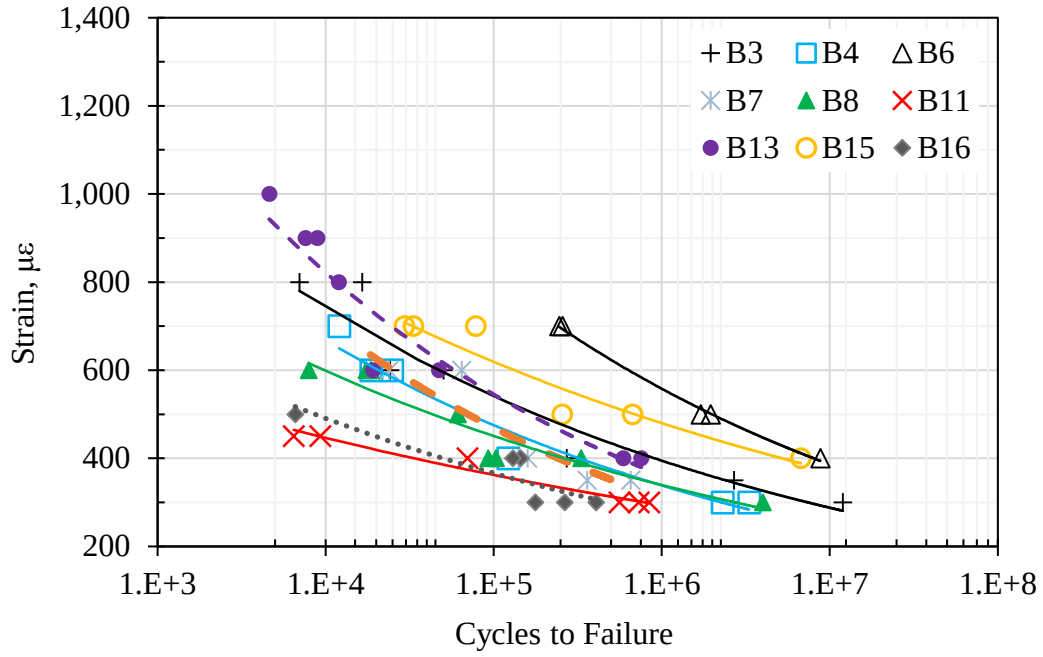

Figure 63. Cycles to Failure vs. Micro-strain at 10°C

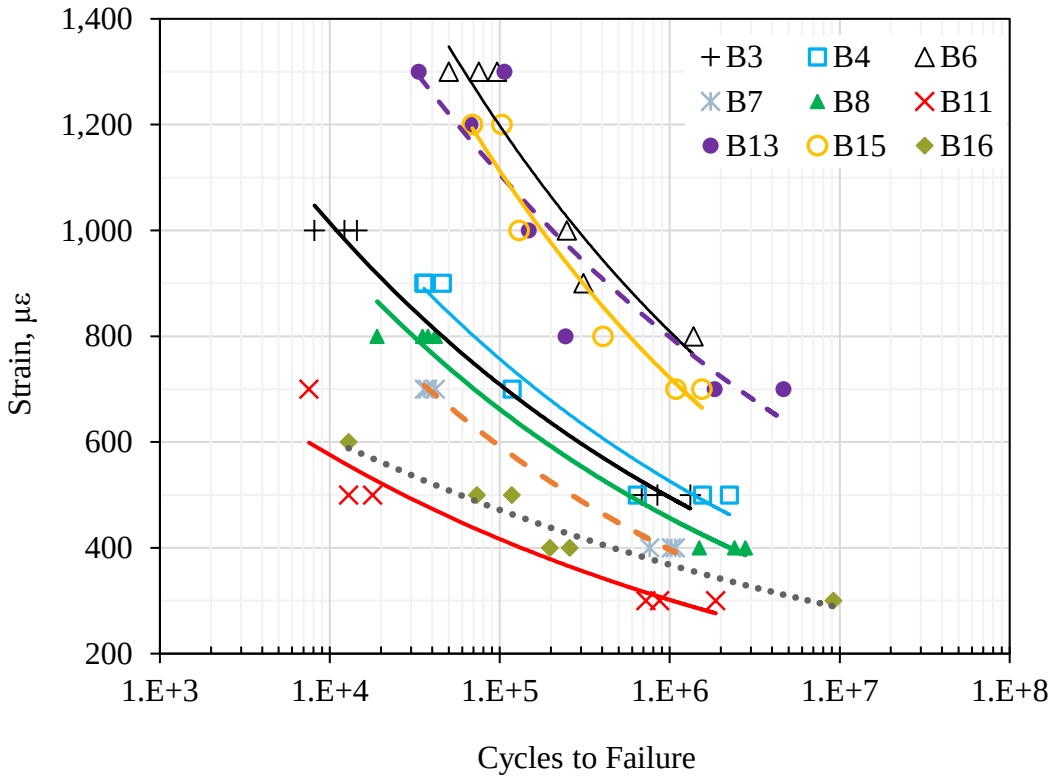

Figure 64. Cycles to Failure vs. Micro-strain at 20°C

Table 14. Regression Coefficients and R^2 for Strain-Fatigue Life Relationships

Mix ID		K_1	K_2	R^2
B3	20°C	$1.20*10^{23}$	6.342	0.986
	10°C	$4.25*10^{23}$	6.811	0.934
B4	20°C	$2.02*10^{22}$	6.006	0.949
	10°C	$2.38*10^{22}$	6.489	0.957
B6	20°C	$3.68*10^{21}$	5.374	0.995
	10°C	$1.33*10^{23}$	6.235	0.917
B7	20°C	$7.37*10^{20}$	5.723	0.917
	10°C	$1.69*10^{18}$	4.950	0.886
B8	20°C	$1.38*10^{22}$	6.074	0.928
	10°C	$2.23*10^{24}$	7.294	0.898
B11	20°C	$1.93*10^{22}$	6.597	0.926
	10°C	$1.99*10^{32}$	10.667	0.969
B13	20°C	$7.43*10^{22}$	5.848	0.828
	10°C	$2.69*10^{19}$	5.283	0.942
B15	20°C	$2.14*10^{20}$	5.024	0.945
	10°C	$2.11*10^{28}$	8.346	0.928
B16	20°C	$1.25*10^{28}$	8.630	0.931
	10°C	$1.63*10^{20}$	5.928	0.754

5.1.2 Dissipated Energy Approach

According to **Equations 8 to 10**, the relationship between cumulative dissipated energy to failure (W_N) and fatigue life (N_f) was developed for each mix, as shown in **Figure 65** and **Figure 66**. Regression coefficients of the W_N-N_f correlations ($W_N = A(N_f)^Z$) are presented in **Table 15**. Based on these transfer functions, the W_N required for a specific N_f was computed for each mix, as shown in **Figure 67** and **Figure 68**. For a given N_f, a higher W_N might mean a better resistance to fatigue cracking. Generally, the mixes with polymer modified binders showed higher W_N than those with non-polymer binders, regardless of 10° or 20°C. This indicates that polymer modified mixes could have better fatigue property than mixes with non-polymer binders. The similar trend was also found by other researchers (Khattak and Baladi, 1998, 2001; Quintus et al., 2007; Willis

et al., 2016). Note the W_N required for a specific N_f will be used for investigating the relationship between binder properties and mix fatigue performance in Chapter 7.

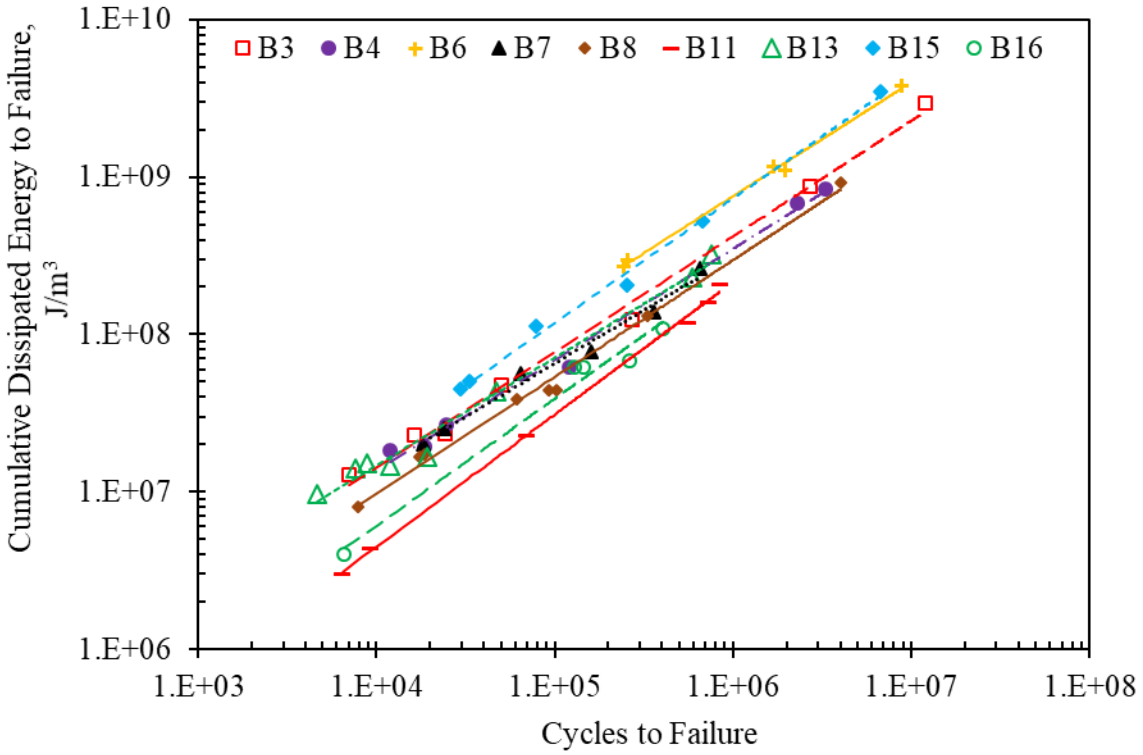

Figure 65. Cycles to Failure vs. Cumulative Dissipated Energy to Failure at 10°C

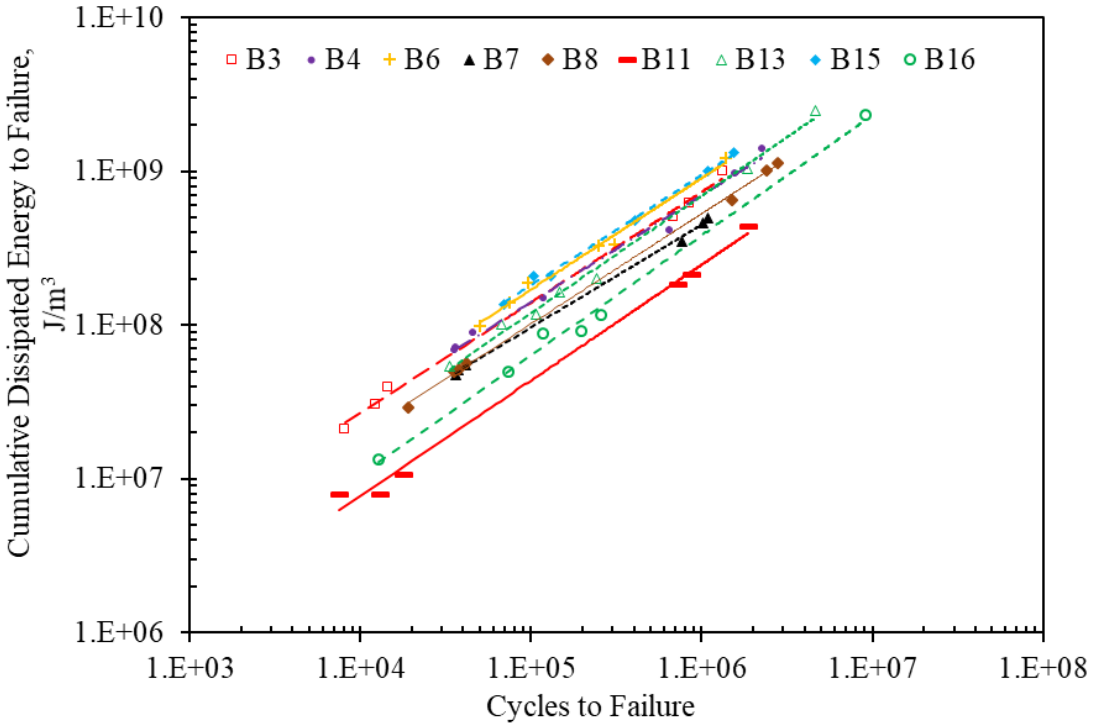

Figure 66. Cycles to Failure vs. Cumulative Dissipated Energy to Failure at 20°C

Table 15. Regression Coefficients and R^2 for Dissipated Energy Transfer Functions

Mix ID	Testing Temperature	A	Z	R^2
B3	20°C	17.372	0.710	0.996
	10°C	8.033	0.719	0.988
B4	20°C	15.757	0.708	0.992
	10°C	10.572	0.689	0.990
B6	20°C	40.445	0.630	0.958
	10°C	14.992	0.712	0.961
B7	20°C	14.270	0.683	0.999
	10°C	16.204	0.638	0.979
B8	20°C	13.654	0.698	0.999
	10°C	5.573	0.719	0.992
B11	20°C	2.911	0.758	0.992
	10°C	0.857	0.833	0.997
B13	20°C	5.649	0.777	0.985
	10°C	15.087	0.647	0.979
B15	20°C	37.883	0.653	0.985
	10°C	7.805	0.760	0.992
B16	20°C	3.118	0.783	0.992
	10°C	1.970	0.781	0.975

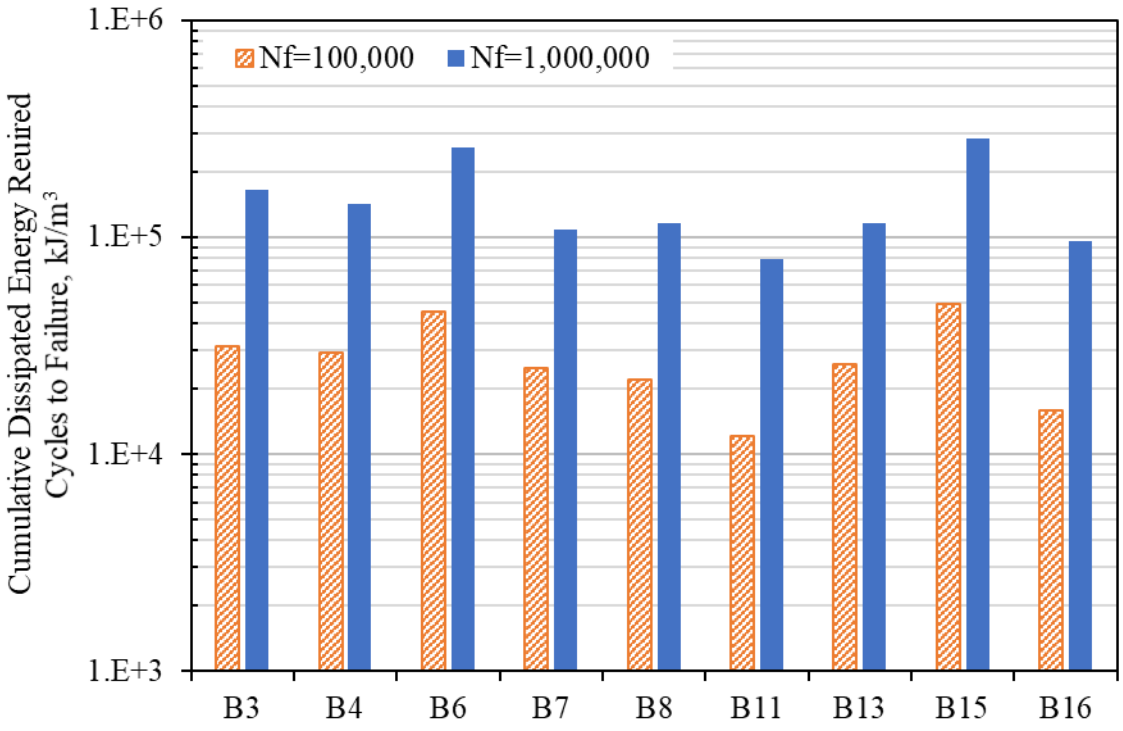

Figure 67. Cumulative Dissipated Energy Required for Specific N_f at 10°C

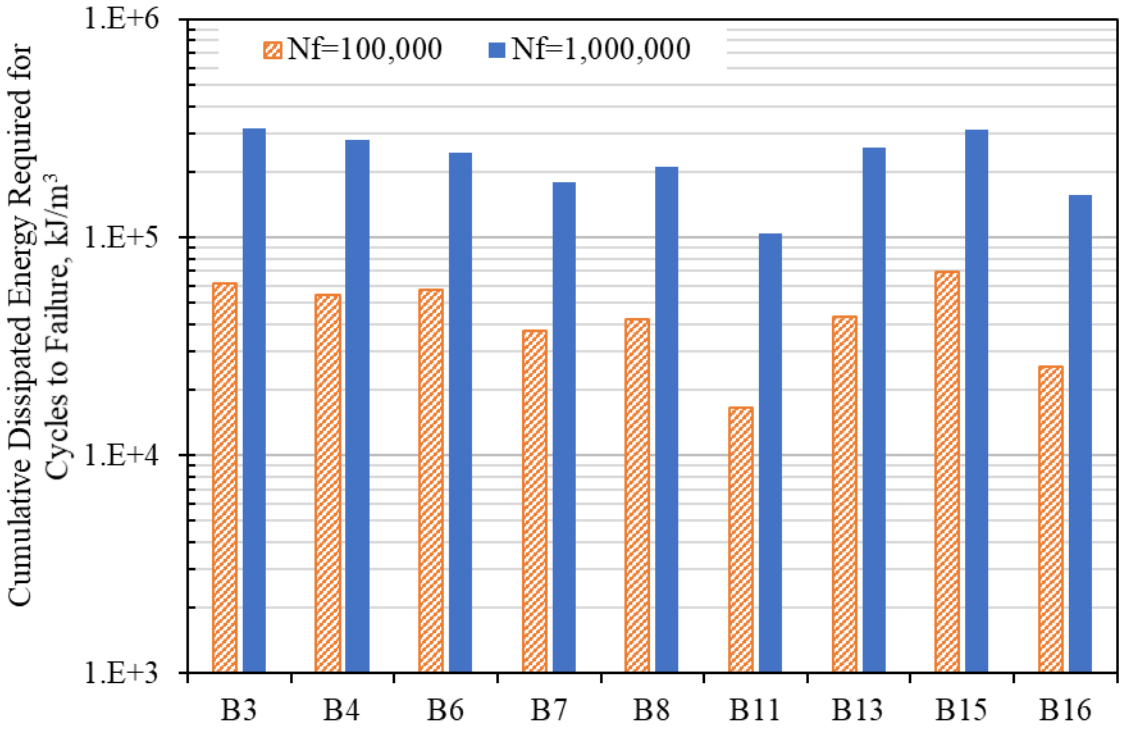

Figure 68. Cumulative Dissipated Energy Required for Specific N_f at 20°C

In the modified LAS and uniaxial fatigue tests, the pseudostrain energy release rate (G^R) is used to correlate to fatigue life. Similarly, a dissipated energy release rate (named as D^R) was used to develop a relationship with fatigue life in this study. D^R is defined as the rate of change of the averaged dissipated energy (per cycle) throughout the test, and it can be calculated by **Equation 21**. **Figure 69** and **Figure 70** show the D^R-N_f curves for mixes at 10° or 20°C, respectively. For a given D^R, a higher fatigue life indicates a better fatigue cracking resistance. The D^R-N_f relationships in **Figure 69** and **Figure 70** will be used to conduct a comparison between binder fatigue and mix fatigue performance in Chapter 7.

$$D^R = \frac{\int_0^{Nf} W_i}{N_f^2} = \left.\frac{W_N}{N_f}\right/_{N_f} \qquad (21)$$

Where,

W_i is the dissipated energy at cycle i,

W_N is the cumulative dissipated energy to failure, and

N_f is the number of cycles to failure.

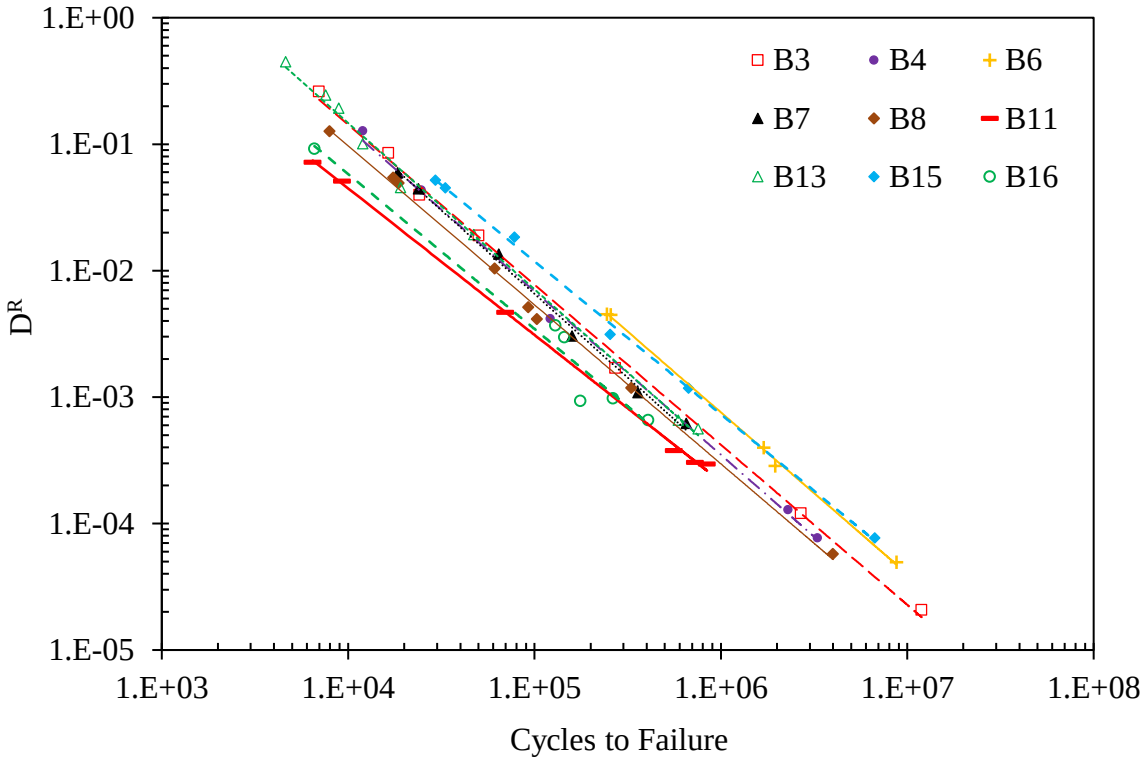

Figure 69. D^R-N_f Curves at 10°C

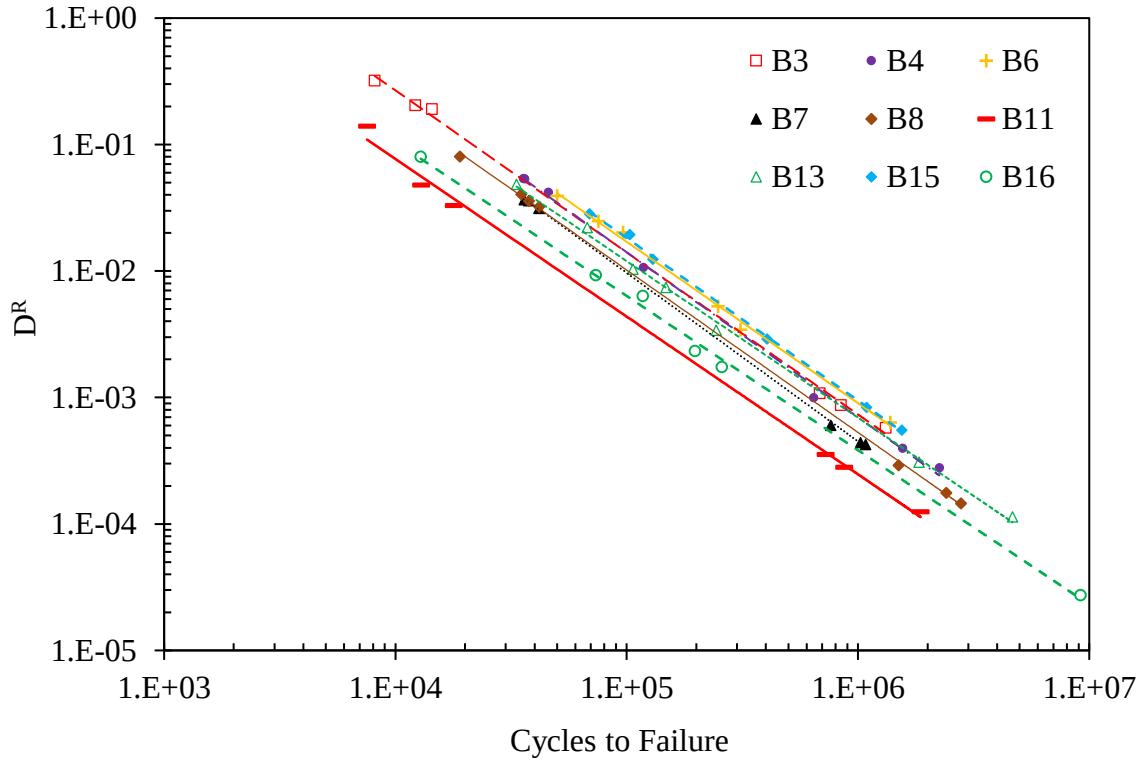

Figure 70. D^R-N_f Curves at 20°C

5.2 Uniaxial Fatigue Results

In this section, the data from the uniaxial fatigue tests were analyzed through two approaches: 1) the dissipated energy approach, and 2) the simplified viscoelastic continuum damage (S-VECD) approach. Detailed uniaxial fatigue test data are shown in **Appendix B**.

5.2.1 Dissipated Energy Approach

Like the flexural fatigue test, the dissipated energy approach was also employed to analyze the uniaxial fatigue data. However, the uniaxial tests were conducted at the temperatures: (high PG + low PG)/2 -3 and (high PG + low PG)/2 +3, and the test temperatures were varied for 16 mixes. Additionally, the temperature could have an impact on the W_N-N_f relationship. Therefore, it may not be reasonable to compare mix fatigue property directly using the W_N-N_f relationship from uniaxial fatigue tests. In this case, the fatigue lives of mixes at a specific temperature were calculated using the general transfer functions ($W_N = k_1(N_f)^{k_2}(\frac{1}{S_0})^{k_3}$). In the general transfer function, the flexural stiffness was introduced to account for the effect of temperature on fatigue property of the mixes. The general transfer function was generated for each mix using a solver function in Excel. Coefficients are summarized in **Table 16**. **Figure 71** compares the cumulative dissipated energy required for N_f =10,000. In general, the polymer modified mixes exhibited a higher dissipated energy required for N_f =10,000 compared to those with non-polymer binders, especially at 10°C, indicating polymer modified mixes could have better fatigue resistance than mixes with non-polymer binders. This is expected as polymers generally improve the fatigue properties of binders. Note the W_N required for N_f =10,000 will be used for investigating the relationship between binder properties and mix fatigue performance in Chapter 7.

Table 16. Coefficients for General Transfer Functions

Mix ID	k_1	k_2	k_3
B1	2.3E+04	0.733	0.120
B2	1.7E+04	0.665	0.000
B3	2.8E+04	0.595	0.000
B4	8.2E+07	0.799	1.176
B5	2.4E+07	0.843	1.102
B6	3.9E+04	0.733	0.242
B7	2.2E+07	0.723	0.922
B8	2.0E+09	0.868	1.616
B9	3.1E+07	0.885	1.191
B10	7.0E+04	0.810	0.395
B11	4.8E+08	0.741	1.392
B12	3.2E+04	0.727	0.312
B13	4.7E+14	0.826	3.036
B14	6.2E+07	0.750	1.106
B15	1.1E+10	0.704	1.625
B16	1.1E+07	0.734	0.895

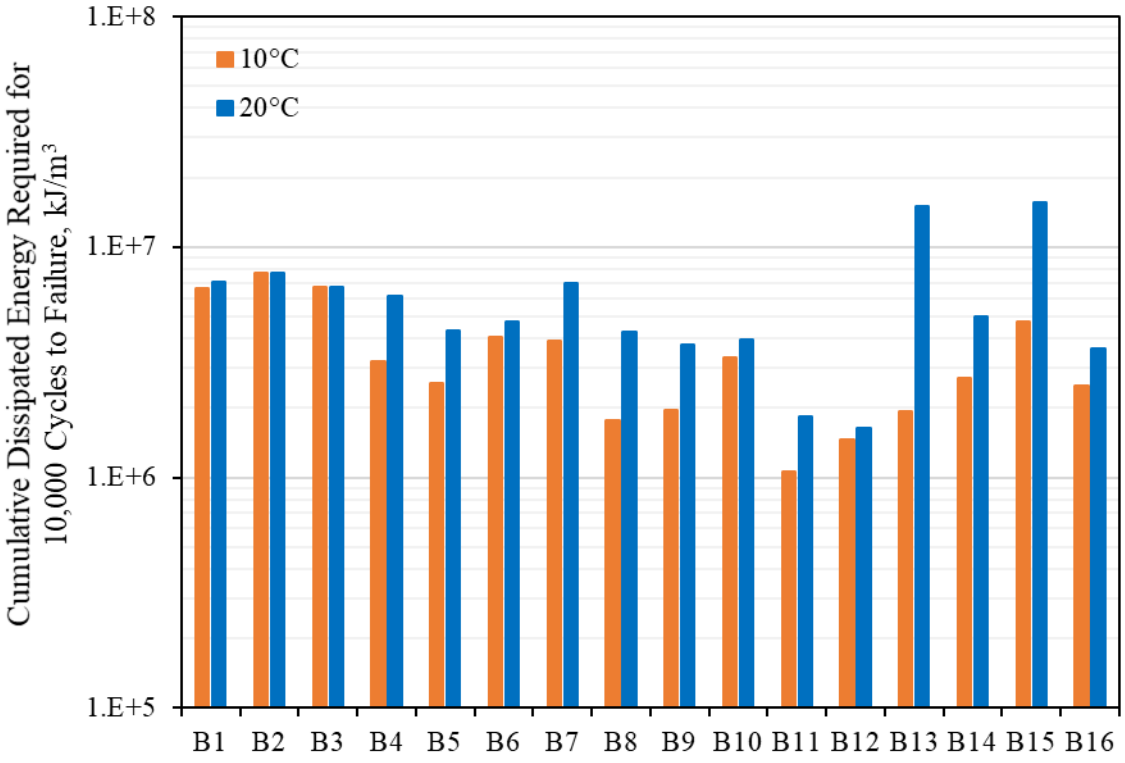

Figure 71. Cumulative Dissipated Energy Required for N_f =10,000

5.2.2 Simplified Viscoelastic Continuum Damage (S-VECD) Analysis

The S-VECD analysis of the uniaxial fatigue data was performed using the FlexMAT spreadsheet developed by the pavement research group at North Carolina State University. The S-VECD analysis included the following steps:

1. First, a storage modulus master curve was created based on the dynamic modulus test results by simultaneously optimizing sigmoidal model parameters and time-temperature shift factors. The master curve model was used to generate data that is used to determine the Prony series coefficients. The E(t) Prony series coefficients were used to determine α value which is a critical parameter for the damage calculation. Additionally, the dynamic modulus data were also used to determine the DMR value which is used for the calculation of pseudo secant modulus (C).
2. Uniaxial fatigue data were analyzed in two steps. The first part consisted of the data for the first half of the first loading path (from zero to first peak stress). The second part consisted of the rest of the data. For the first cycle of loading, full time history data was used to calculate the pseudo strain (ε^R) up until the peak tensile load. Then, pseudo stiffness (C) calculated based on the stress divided by the pseudo strain and DMR and damage parameter (S) was computed using DMR, pseudo stiffness and α value. For the rest of the loading history, pseudo stiffness and damage were computed using peak-to-peak stress and strain values in each cycle. Additionally, the fatigue life for the tested specimen was determined based on the peak in the phase angle data from the uniaxial fatigue test.
3. The C-S curve was developed for each specimen based on the calculated C and S values. The C-S curve could be fitted using a power law function (**Equation 22**). The C-S curve

is an important output of S-VECD analysis, which illustrates how fatigue damage evolves in the mix during the uniaxial fatigue test.

$$C = 1 - C_{11} S^{C_{12}} \qquad (22)$$

where

C = pseudo stiffness,

S = damage parameter, and

c_{11}, c_{12} = material constants.

4. Another important output of S-VECD analysis was G^R failure criterion. G^R is defined as the rate of change of the averaged released pseudo strain energy (per cycle) throughout the test. G^R could be calculated using **Equation 23**. The relationship between G^R and the fatigue life can be used to compare fatigue property between mixes. For a given G^R, a higher fatigue life indicates a better fatigue cracking resistance.

$$G^R = \frac{\int_0^{Nf} W_C^R}{N_f^2} \qquad (23)$$

Where, W_C^R is the released pseudo strain energy and N_f is the number of cycles to failure.

Figure 72 shows the correlations between G^R and N^f for all the mixtures. For a given G^R, a lower N_f value indicated quicker failure and poorer resistance to fatigue cracking. Previous research found that the number of cycles to failure at G^R = 100 correlated well with measured cracking in thick or thin pavements (Norouzi et al., 2016). **Figure 73** shows the cycles to failure at G^R=100 for all the mixes. Genarally, the mixes with the polymer modified binders had higher cycles to failure than those with the nonpolymer binders. The similar trend agrees with the previous study (Khattak and Baladi, 1998, 2001; Quintus et al., 2007; Willis et al., 2016). Specifically, B12

showed the worst fatigue property, followed by B11, B8 and B9, and B2 exhibited the best fatigue property, followed by B5 and B15.

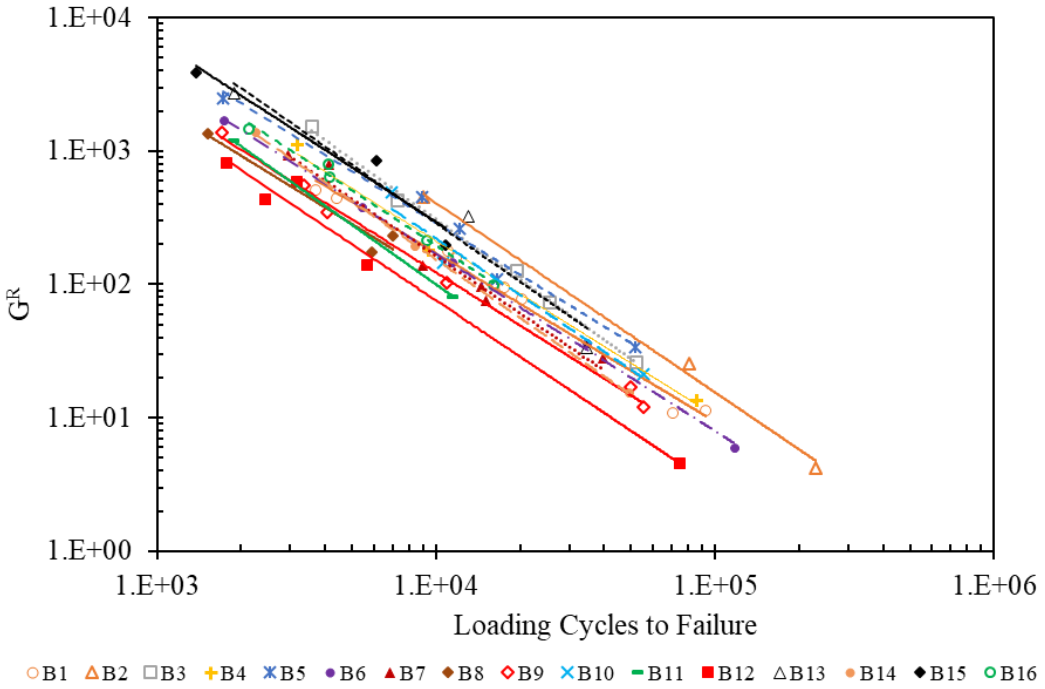

Figure 72. G^R Values vs. Cycles to Failure for 16 Mixes

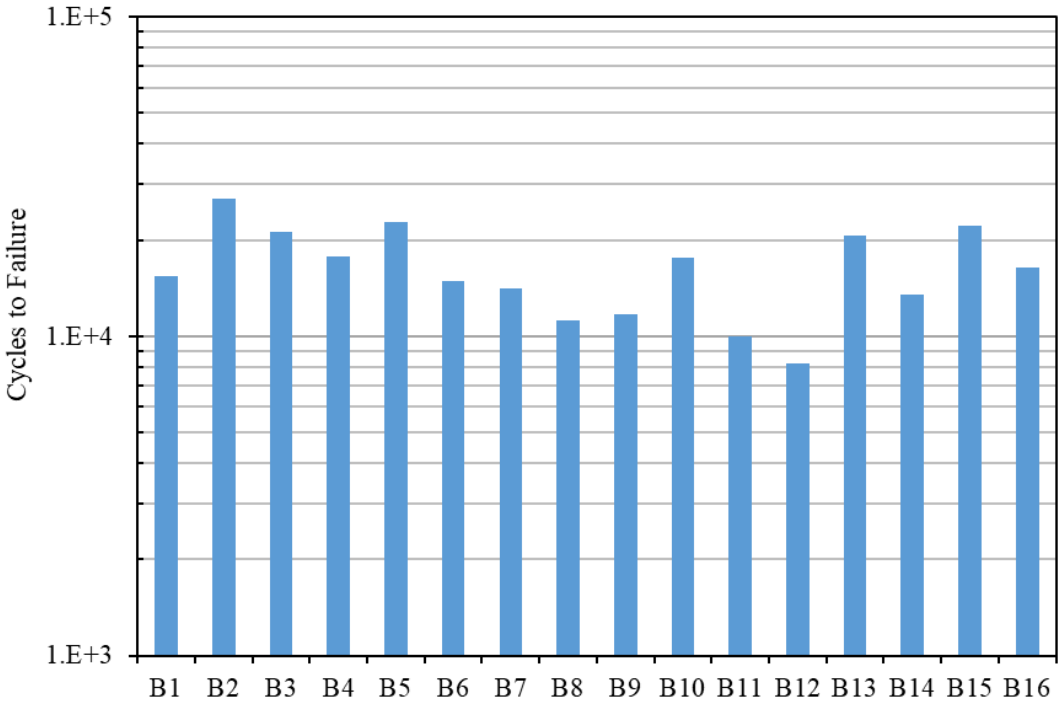

Figure 73. Loading Cycles to Failure at G^R = 100

5.3 Summary

In this chapter, the mix fatigue properties were investigated using the traditional phenomenological approach, the dissipated energy approach, and the S-VECD approach. Additionally, the temperature effect on mix fatigue property was discussed. Specific findings from these efforts include the following:

1) Flexural fatigue and uniaxial fatigue results indicate that the mixes containing the polymer modified binders generally exhibited a better fatigue property than the mixes with non-polymer binders, regardless of the results from the traditional phenomenological approach, or the dissipated energy approach, or the S-VECD approach. The finding is consistent with the previous study (Khattak and Baladi, 1998, 2001; Quintus et al., 2007; Willis et al.,

2016). This finding indicates that the use of polymer in asphalt pavement could improve the pavement durability.

2) The cumulative dissipated energy to failure showed a strong correlation with fatigue life, and its correlation is higher than the correlation between strain and fatigue life. The curves of cumulative dissipated energy - fatigue life at two temperatures almost overlapped or are parallel, which could improve the fatigue life prediction using these relationships.

CHAPTER 6 – EFFECT OF PAVEMENT STRUCTURE ON MIX FATIGUE PERFORMANCE

The fatigue performance of asphalt pavement is related not only to the fatigue property of asphalt mixtures but also to the pavement structure. To investigate the effect of pavement structure on mix fatigue performance, the mix fatigue performance was simulated in this chapter. Additionally, the simulation results will be used to correlate the binder fatigue/fracture properties in Chapter 7. A layered viscoelastic pavement analysis method was employed to simulate the pavement fatigue performance. More details about this approach are shown in the following sections.

6.1 Layered Viscoelastic Analysis Approach

The FlexPAVE program (formerly known as the layered viscoelastic pavement analysis for critical distresses (LVECD) program) was employed to simulate pavement fatigue performance. FlexPAVE was developed by the pavement research group at North Carolina State University. It applies three-dimensional (3-D) finite element analysis with moving loads to obtain the mechanical responses and uses the S-VECD model for the fatigue damage computations (Wang 2016, 2018). FlexPAVE program simulation includes the following primary processes (Norouzi 2015):

1) Calculate the pavement responses (stress and strain) of pavement structure through layered viscoelastic moving-load analysis. In this process, the pavement is simulated through a three-dimensional layered viscoelastic finite element with the moving load, and

the impact of loading frequency and temperature on asphalt material properties is considered.

2) Predict the damage evolution within the asphalt layer. In this step, the maximum tensile stress and strain, S-VECD model, and laboratory fatigue results are used to compute the pseudo stiffness, damage, and pseudo strain energy in each point in the finite element model of the asphalt layer.
3) Compute the damage factor and damage percentage. Based on the damage evolution with time in each point, the G^R value for each point at a given loading condition is calculated, and then the number of cycles to failure in each element is determined using the G^R versus N_f relationship from the laboratory uniaxial fatigue testing. After that, the damage factor is calculated as the ratio between the actual experienced numbers of loading cycles to the N_f value calculated. Finally, the damage percent of the pavement is calculated through **Equation 24**.

$$Percent\ Damage = \frac{\sum_{i=1}^{M}(damage\ factor)_i \times A_i}{\sum_{i=1}^{M} A_i} \quad (24)$$

Where,

i is the nodal point number for nodes which are located within the given reference cross-section,

M is the total number of nodal points located within the given reference cross-section in finite element mesh,

Ai is the area represented by nodal point i in the finite element mesh, and

$\sum A_i$ is the reference area.

6.2 Program Inputs

In this study, four pavement structures were employed to evaluate the fatigue performance of pavement. **Table 17** shows the structure information and layer material properties used in the study. The Enhanced Integrated Climate Model (EICM) database in FlexPAVE program was used for two locations: Orlando, FL and Minneapolis, MN. For each situation, 20-year design life was used.

Table 17. Structure and Material Inputs for FlexPAVE

Layer	Thickness, inch	Modulus, psi	Fatigue Parameter
AC	4, 6, 10, and 15	E*	S-VECD Results
Granular	10	30,000	--
Subgrade	∞	10,000	--

To simplify the traffic calculation in FlexPAVE simulation, a wheel load of 9,000 1b and dual tires with 110 psi tire pressure were used in the study. The default value of traffic design velocity of 60 miles/hour (27m/s) was selected. Equivalent single axle load (ESAL) on the asphalt pavement was calculated using the AASHTO empirical design equation (**Equation 25**). In the ESAL calculation, the functional class of the pavements was assumed as interstate roads and a design reliability of 95% was used for all pavement structures based on the recommended reliability values by AASHTO. The Z-statistic of -1.645 corresponding to the design reliability of 95% was calculated using Excel. A typical value of 0.45 was selected for S_0. A typical value of 4.2 for the initial serviceability and 2.5 for terminal serviceability were selected, respectively. Current daily traffic was back-calculated using the combination of **Equations 26 and 27**. A traffic growth rate of 4% was assumed in this study. **Table 18** presents the parameter values for W18 calculation. **Table 19** shows ESAL numbers and current daily traffic for four pavement structures.

$$\log(W_{18}) = Z_R S_0 + 9.36\log(SN_f + 1) - 0.20 + \frac{\log\left(\frac{\Delta PSI}{4.2 - 1.5}\right)}{0.4 + \left(\frac{1094}{(SN_f + 1)^{5.19}}\right)} + 2.32\log(M_r) - 8.07 \quad (25)$$

where,

W_{18} = the number of future ESALs,

Z_R = the Z-statistic corresponding to the design reliability,

S_0 = the standard deviation,

ΔPSI = the difference between the initial and terminal serviceabilities ($p_0 - p_t = 4.2 - 2.5$),

SN_f = the structural number, which is calculated by Equation 28, and

M_r = the modulus of subgrade reaction, in psi.

Table 18. Parameter Values for W_{18} Calculation

Design reliability, %	Z_R	S_0	ΔPSI	M_r	SN_f			
95	-1.645	0.49	1.7	10,000	3.58 for 4 in. AC	4.58 for 6 in. AC	6.58 for 10 in. AC	9.08 for 15 in. AC

$$Current\ Traffic = \frac{w_{18}}{Growth\ Factor\ \times 365} \quad (26)$$

$$Growth\ Factor = \frac{(1+g)^n - 1}{g} \quad (27)$$

$$SN_f = a_1 D_1 + a_2 m_2 D_2 \quad (28)$$

where,

a_1 = structure coefficient of AC layer, assumed as 0.5 for all mixes,

D_1 = thickness of AC layer,

a_2 = structure coefficient of granular base layer, computed using the following equation,

$$a_2=0.249\log(E_{base})-0.977$$

m_2 = drainage coefficient of granular base layer, assumed as 1.15, and

D_2 = thickness of granular base layer.

Table 19. ESAL Numbers and Current Daily Traffic

Pavement Structure	Total ESAL in Design Life of 20 years	Current Daily ESAL
4 in. AC	1.62E+06	149
6 in. AC	7.82E+06	720
10 in. AC	1.09E+08	10,052
15 in. AC	1.48E+09	136,141

6.3 Simulation Results

Figures 74 to 77 show the typical damage factor distribution for four asphalt pavement structures after 20-year traffic. For the thin pavement structures (4- and 6-inch AC), almost all the damage in the pavement was from the bottom-up cracking. For the 15-inch AC pavement, almost all the damage in the pavement was from the top-down cracking. For the 10-inch AC pavement, the damage in the pavement was from both types of cracking. The simulation results are reasonable as bottom-up cracking generally occurs in a thinner asphalt pavement and top-down cracking occurs in a thicker asphalt pavement.

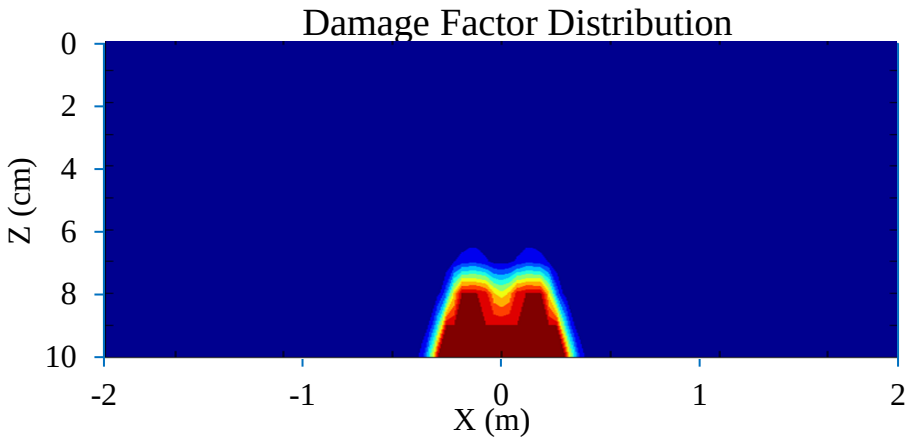

Figure 74. Typical Damage Factor Distribution for 4-inch AC Pavement

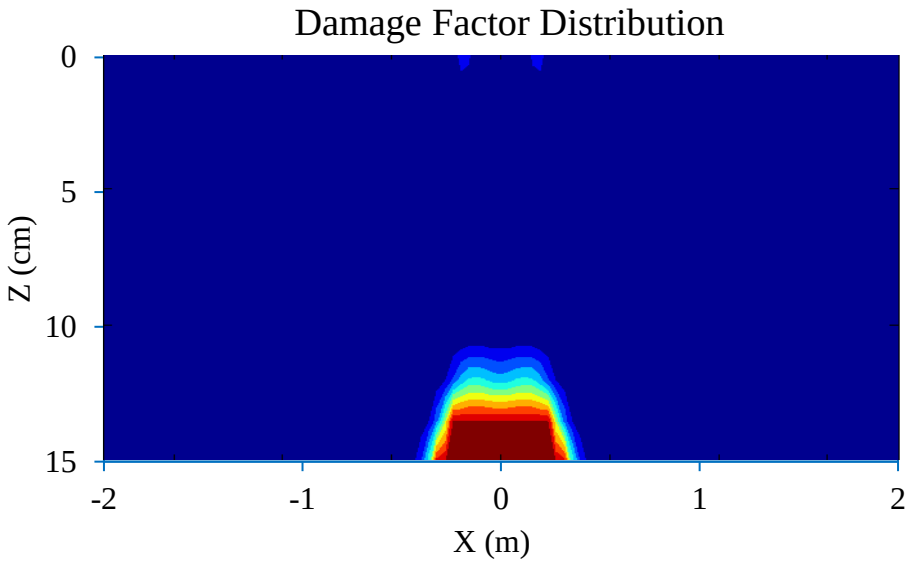

Figure 75. Typical Damage Factor Distribution for 6-inch AC Pavement

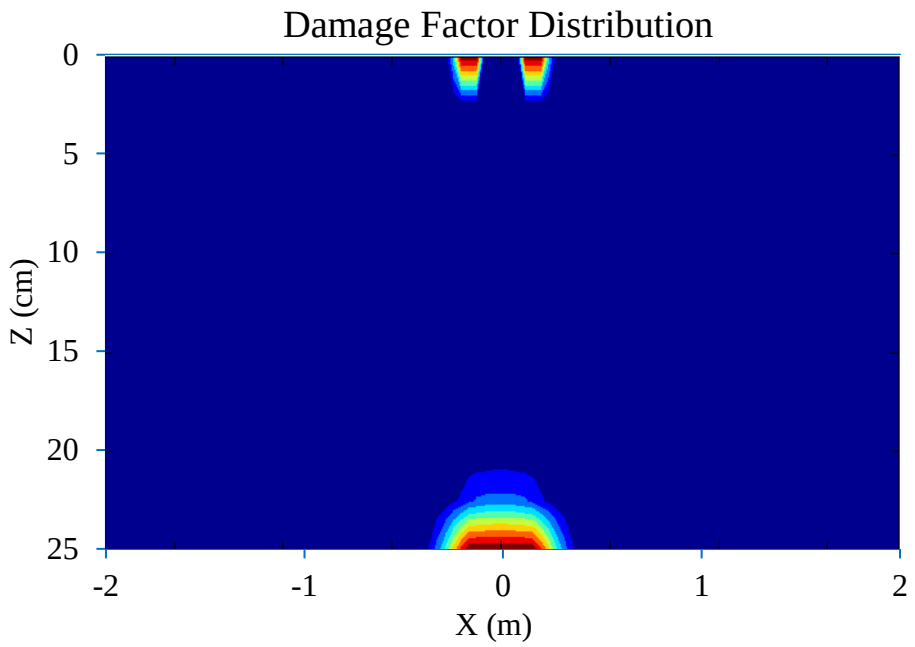

Figure 76. Typical Damage Factor Distribution for 10-inch AC Pavement

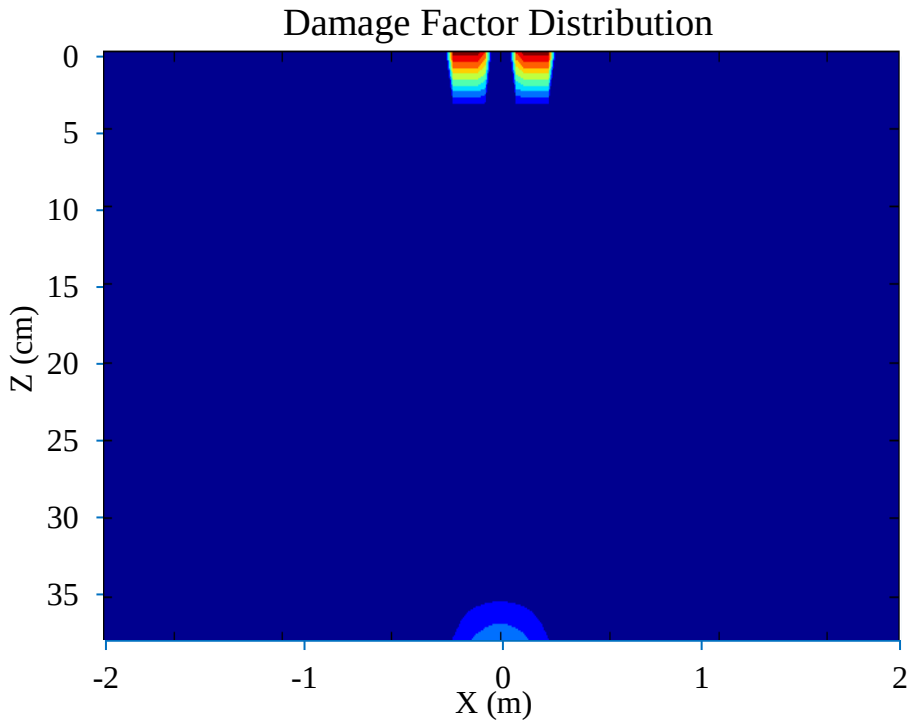

Figure 77. Typical Damage Factor Distribution for 15-inch AC Pavement

Figures 99 to 101 show the damage percent of asphalt pavements after 20-year traffic. Damage evolution with time for each pavement structure is shown in **Appendix C**. Generally, the pavement damage decreases with increasing AC thickness, and the pavements in FL showed more damage compared to those in MN. This is reasonable as a thicker AC layer reduces the stress and strain in the pavement structure, resulting in a lower damage in the pavement; the pavements in FL could have higher stress and strain under an applied loading compared to that in MN, leading to a higher damage in the pavement in FL.

For the thin pavement structures (4- and 6-inch AC), the ranking of the damage percent in the pavements was similar, regardless of AC thickness or location; the pavements with the polymer modified binders, except for that with B4, generally had lower damage percent than those with non-polymer binders. This is expected as the polymer modified binders generally had a better fatigue performance than non-polymer binders based on the previous study (Khattak and Baladi, 1998, 2001; Quintus et al., 2007; Willis et al., 2016).

For the thicker pavement structures (10- and 15-inch AC), the mix with B16 appeared the lowest damage percentage, followed by the mix with B5 and B11. It is unexpected that the mix with B11 had a lower damage percentage than most of the mixes as B11 is an oxidized binder. Moreover, the mixes containing the polymer modified B6 and B15 showed similar damage percentage to those with non-polymer B8 and Binder 13, while had a higher damage percentage than that with non-polymer B9. It is also unexpected since B6 and B15 had high polymer content. It is also unexpected as polymer modified binders generally had a better fatigue performance.

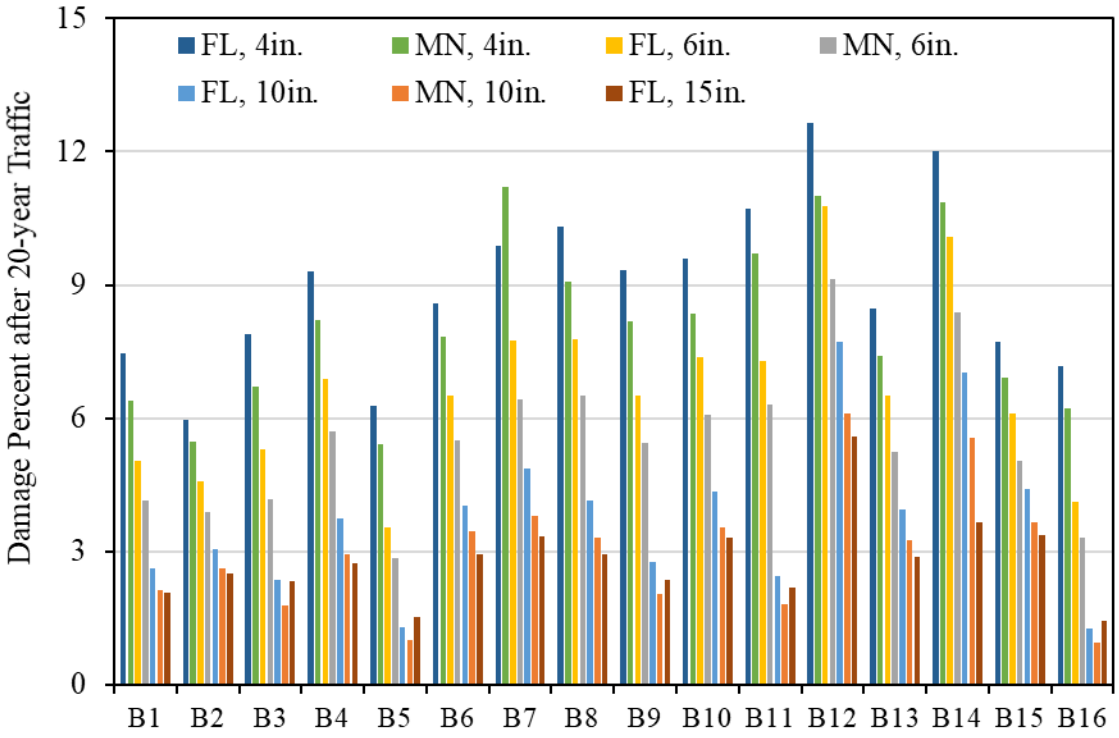

Figure 78. Damage Percent after 20-Year Traffic, All Pavement Structures

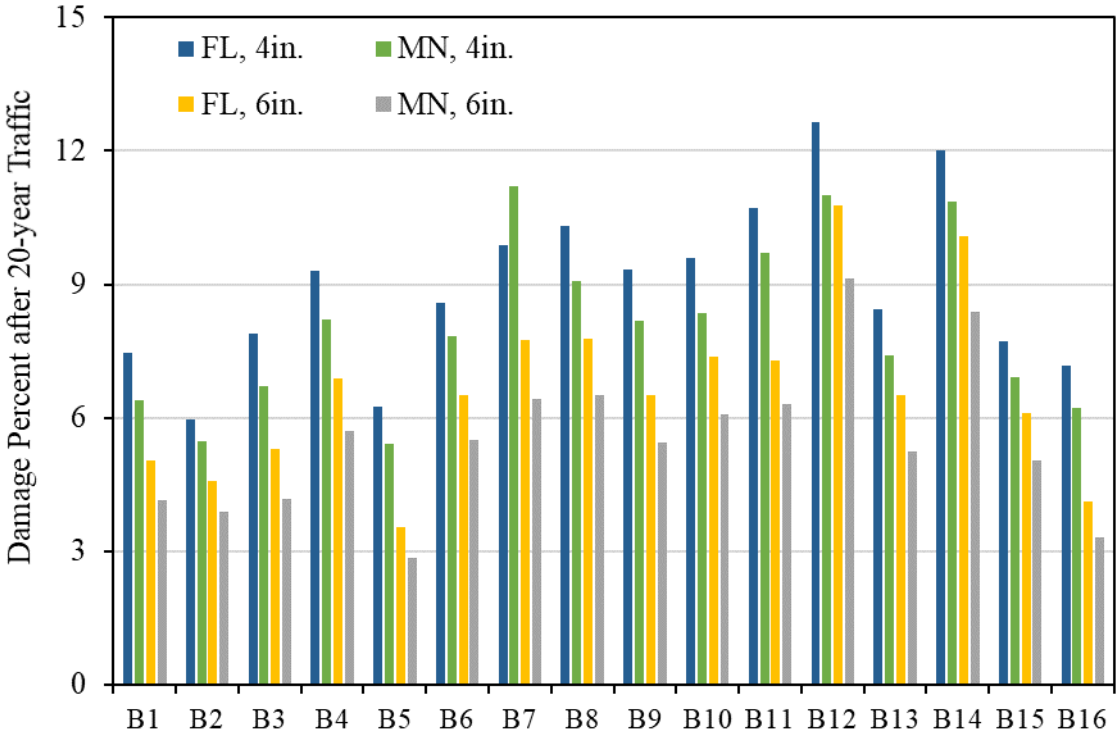

Figure 79. Damage Percent after 20-Year Traffic, 4- and 6-in. AC Pavements

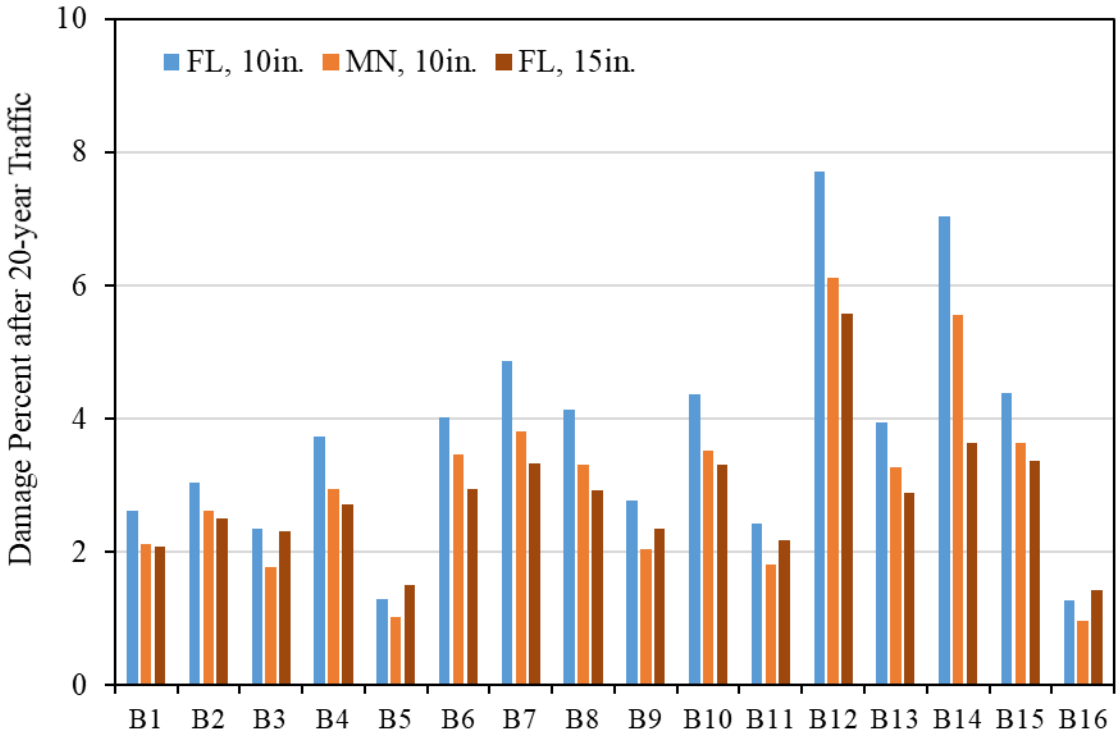

Figure 80. Damage Percent after 20-year Traffic, 10- and 15-in. AC Pavements

6.4 Summary

In this chapter, the structure effect on mix fatigue performance was investigated through the pavement performance simulation. The key findings can be offered based on the simulation results:

1) The mix with straight B12 always showed the worst fatigue performance, regardless of AC thickness or weather. This is expected since B12 is an oxidized binder. In most cases, the mixes with polymer modified B5 and B16 exhibited a better fatigue performance than other mixes.
2) For the 4- and 6-inch AC pavements, all the mixes with the polymer modified binders, except for B4 and B10, generally had a better fatigue performance than the mixes with the non-polymer binders. This is expected as the polymer modified binders generally had a better fatigue performance than non-polymer binders based on the previous study (Khattak and Baladi, 1998, 2001; Quintus et al., 2007; Willis et al., 2016).

3) For the 10- and 15-inch AC pavements, the mixes with the non-polymer binders (B9, B11, and B16) showed a lower damage percentage than most of the mixes with polymer modified binders. This is surprising as the mixes with polymer modified binders were expected to have a better fatigue performance than non-polymer binders.

CHAPTER 7– RELATIONSHIP BETWEEN ASPHALT BINDER AND MIX FATIGUE PROPERTY

In this chapter, the relationships between the binder and mix fatigue property were investigated. In the following sections, the comparison of LAS binder fatigue and mix fatigue results is first presented, followed by the correlations between binder properties and laboratory mix fatigue results. Finally, the relationships between binder properties and simulated pavement fatigue performance are discussed.

7.1 Relationship between Binder LAS Fatigue and Mix Fatigue

7.1.1 Comparison between LAS Results and Uniaxial Fatigue Results

Table 20 shows the comparison between binder LAS N_f and mix uniaxial N_f. **Figure 81** shows the examples of the relationships. It was observed that the correlations between binder LAS N_f and mix uniaxial N_f depended on the G^R values: binder LAS N_f showed slightly higher correlations with mix N_f at G^R=10, compared to mix N_f at G^R=100 and 200. R^2 values for the relationship between binder LAS N_f and mix N_f were higher than 0.50 in most cases. Note the LAS data for B6 was not used to develop the relationship between LAS N_f and mix N_f as the R^2 value (0.26) for its G^R-N_f curve was significantly lower than those for other binders (greater than 0.95).

Table 20. R^2 of Correlations between LAS Binder Fatigue and Mix Uniaxial Fatigue

	R^2		
	Mix N_f @ G^R=10	Mix N_f @ G^R=100	Mix N_f @ G^R=200
LAS N_f @ G^R =1*10^{-5}	0.52	0.36	0.31
LAS N_f @ G^R =1*10^{-4}	0.66	0.55	0.50
LAS N_f @ G^R =5*10^{-4}	0.61	0.58	0.56
LAS N_f @ G^R =7*10^{-4}	0.57	0.56	0.54

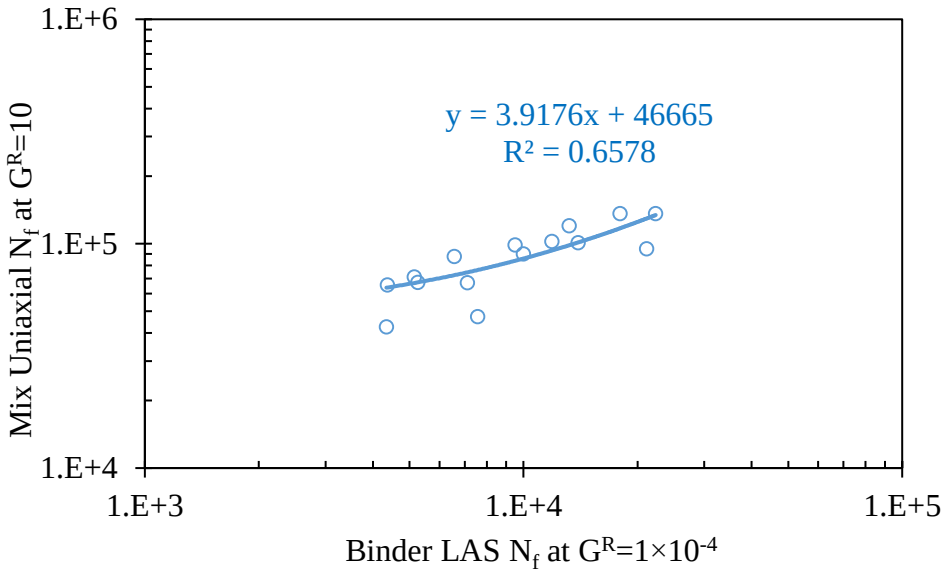

(a) Binder LAS N_f at $G^R=1\times10^{-4}$ and Mix Uniaxial N_f at $G^R=10$

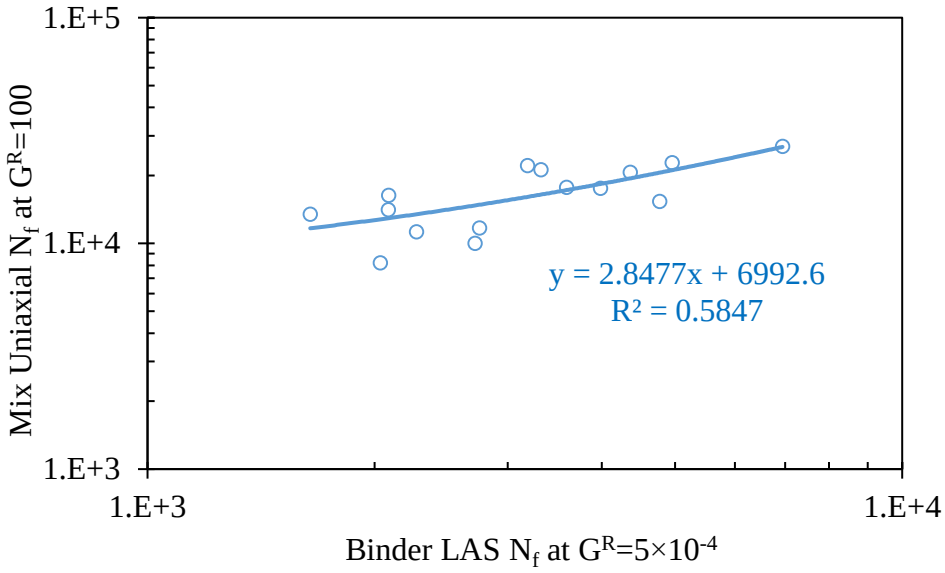

(b) Binder LAS N_f at $G^R=5\times10^{-4}$ and Mix Uniaxial N_f at $G^R=100$

Figure 81. Examples of Relationships between Binder LAS N_f and Mix Uniaxial N_f

7.1.2 Comparison between LAS Results and Flexural Fatigue Results

Table 21 shows the comparison between binder LAS fatigue and mix flexural fatigue. **Figure 82** and **Figure 83** show the examples of their relationships. R^2 values for the correlations between binder LAS N_f @ $G^R = 1*10^{-5}$ and mix flexural N_f varied from 0.59 to 0.77, which were higher than those for binder LAS N_f @ $G^R = 1*10^{-4}$ and $G^R = 5*10^{-4}$. Besides the LAS data for B6, the LAS data for B11 was not used in the correlation analysis as it was further away from other points and it was considered as an outlier.

Table 21. R^2 of Correlations between LAS Binder Fatigue and Mix Flexural Fatigue

	R^2					
	Mix N_f @ 10°C			Mix N_f @ 20°C		
	D^R=0.0001	D^R=0.001	D^R=0.01	D^R=0.0001	D^R=0.001	D^R=0.01
LAS N_f @ $G^R = 1*10^{-5}$	0.65	0.66	0.62	0.77	0.70	0.59
LAS N_f @ $G^R = 1*10^{-4}$	0.40	0.44	0.48	0.74	0.64	0.52
LAS N_f @ $G^R = 5*10^{-4}$	0.13	0.19	0.26	0.55	0.46	0.36

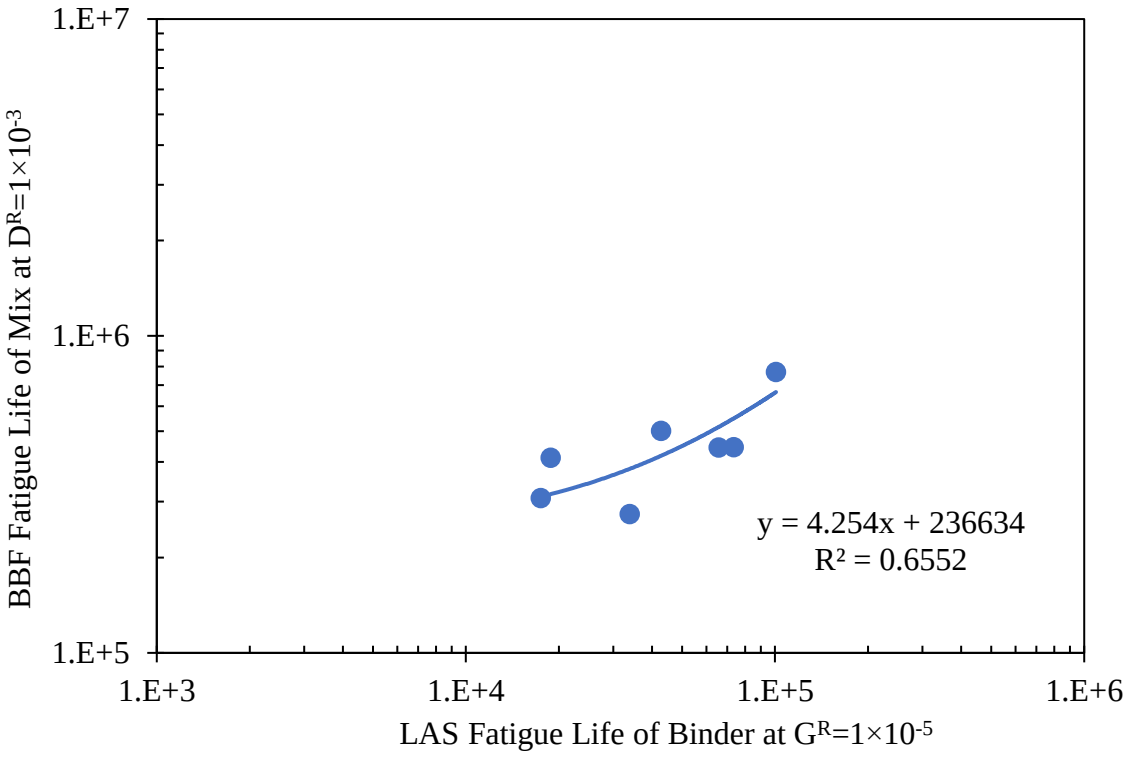

Figure 82. Example of Relationship between Binder LAS N_f vs. Mix Flexural N_f at 10°C

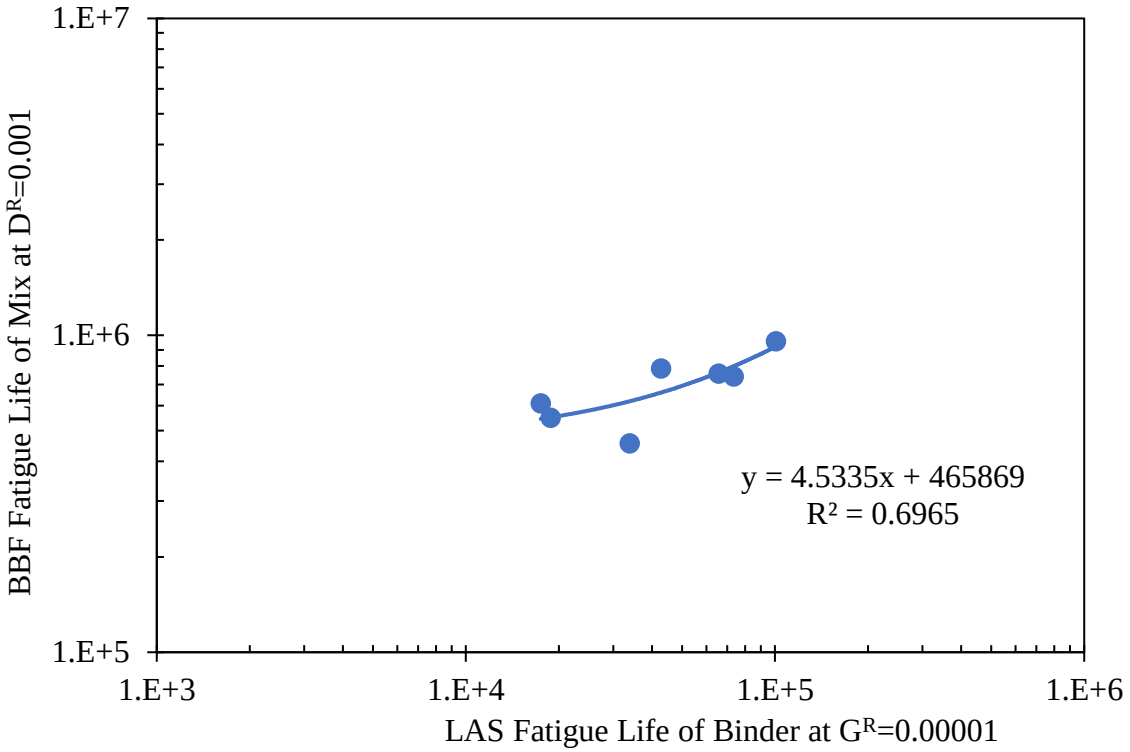

Figure 83. Example of Relationship between Binder LAS N_f vs. Mix Flexural N_f at 20°C

7.1.3 Comparison between Binder Fatigue and Mix Fatigue Using Change Rate of Dissipated Energy

In this section, the relationship between the change rate of dissipated energy and cycles to failure was used to investigate the connection between binder fatigue and mix fatigue. The change rate of dissipated energy (DE) at the plateau stage is computed using the slope of the linear part (the red lines in **Figures 84 to 86**) of the curve of dissipated energy in this study. In this study, the starting and ending points of the linear part were determined based on the turning points in the relationship between the slope of DE and loading cycles, as shown in **Figure 87**. The turning point selection could be a little subjective, which may affect the relationship between the change rate of dissipated energy and cycles to failure. However, this impact is not significant based on the previous study (Shen 2006).

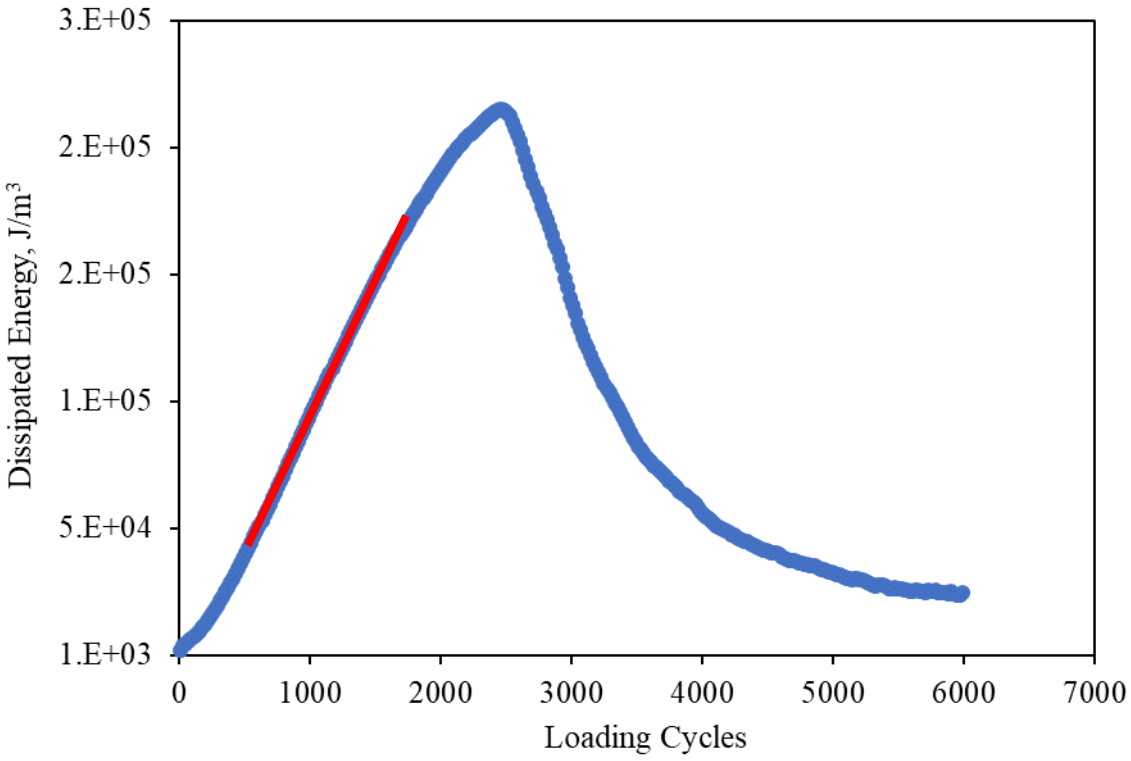

Figure 84. Change Rate of DE in LAS Fatigue Test: Slope of Red Line

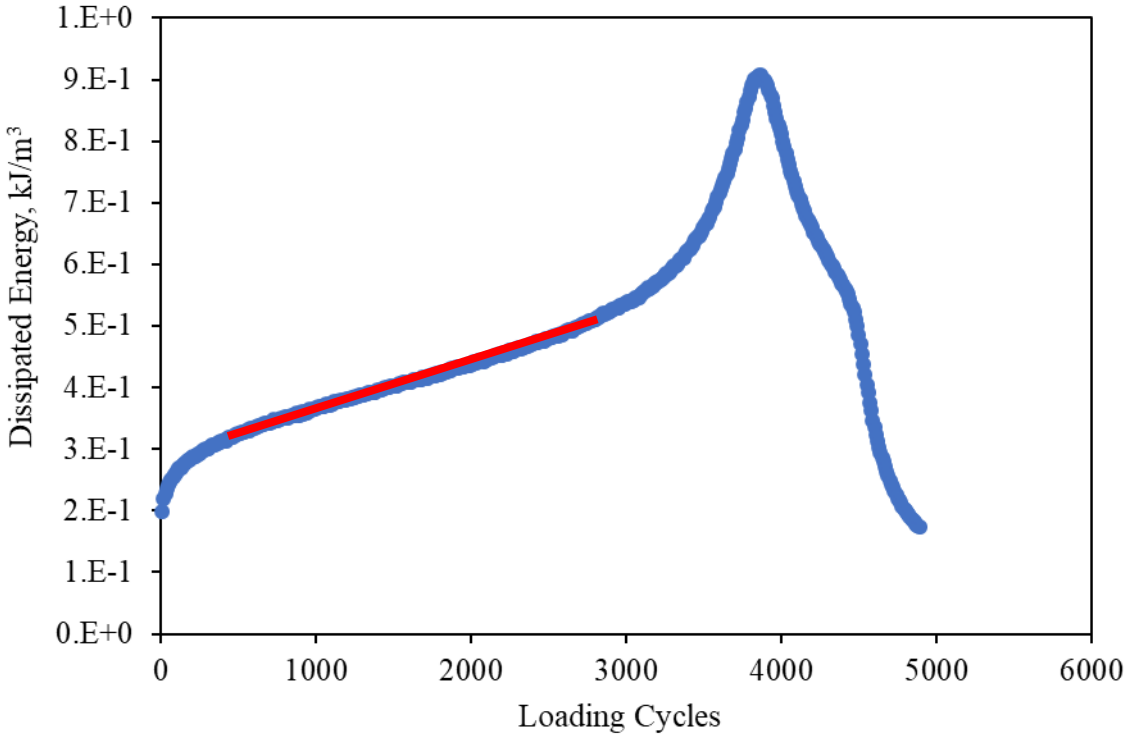

Figure 85. Change Rate of DE in Uniaxial Fatigue Test: Slope of Red Line

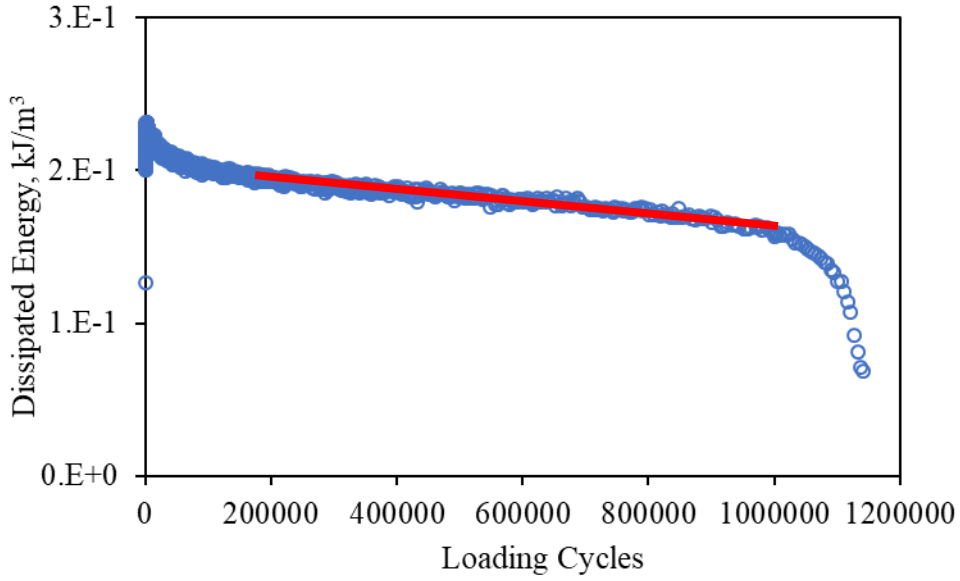

Figure 86. Change Rate of DE in Flexural Fatigue Test: Slope of Red Line

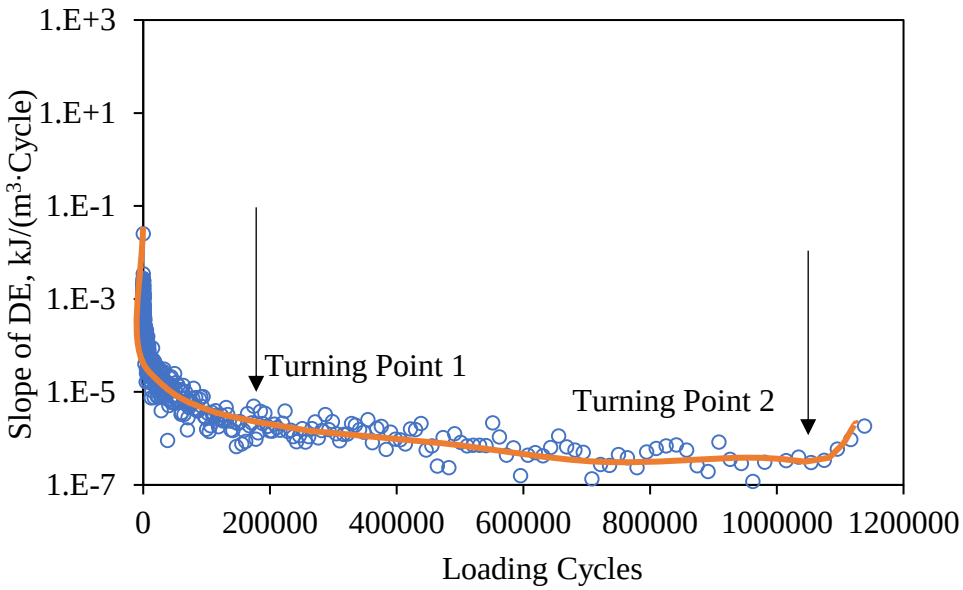

Figure 87. Typical Variation of Slope of DE in Flexural Fatigue Test

The cycles to failure and the change rate of dissipated energy for binders and mixes were plotted in the same graph (**Figure 88**). **Figure 88** had all the fatigue data of binders and mixes, including LAS, flexural fatigue and uniaxial fatigue at two temperatures. As can be seen, all the mix data points almost collapsed on the same line, regardless of the binder types, temperatures, or loading modes (flexural or uniaxial). Similarly, all the binder data collapsed on another line. This indicates that the relationship between the change rate of dissipated energy and cycles to failure was almost independent from loading modes, materials, and temperatures. This is in agreement with the previous findings (Shen et al., 2006).

In addition, the slope of the mix curve was similar to that of the binder curve, especially for non-polymer binders and mixes. This suggests that mix fatigue property could have a good relationship with binder fatigue property. For a given change rate of dissipated energy, the binders had higher fatigue life than the mixtures. This is likely attributed to the following factors: 1) the binder content

in binder sample is 100% and binder content in mix samples is 6.0% (6.42% for the mix with B10); 2) mix samples have some initial damage (e.g., cracking from compaction), while binder samples have no initial damage; and 3) aggregates and air voids in mixes block the connection of binder.

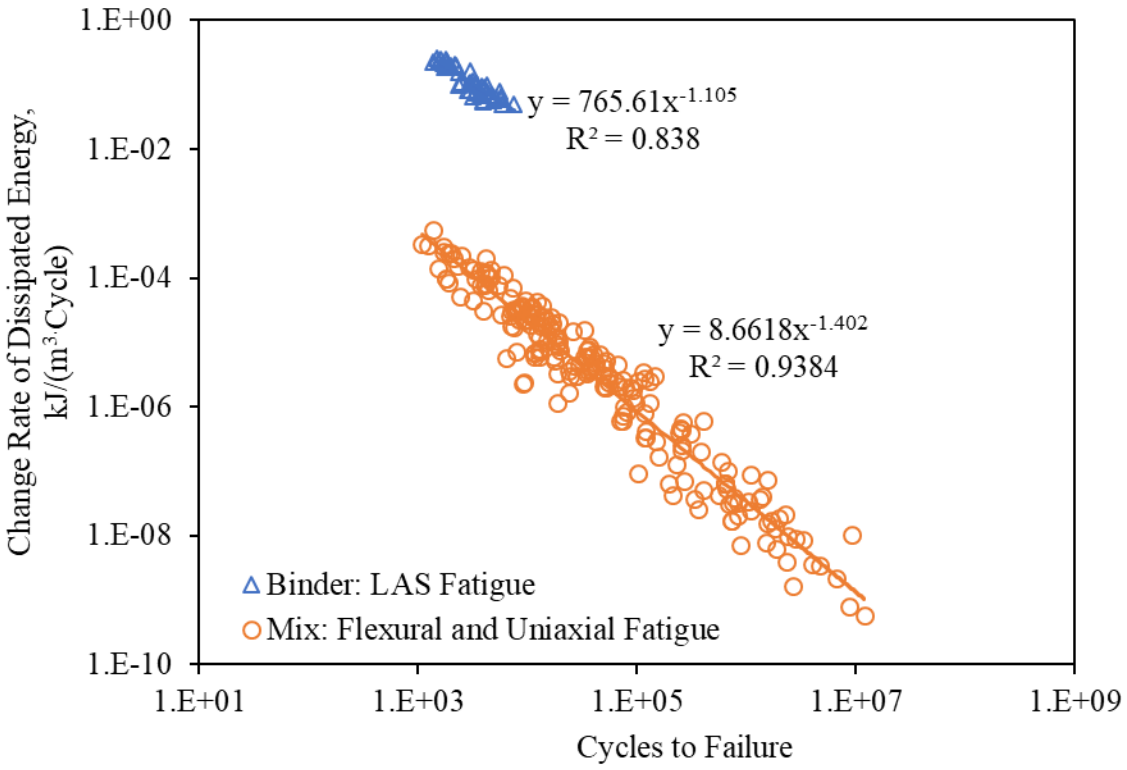

Figure 88. Cycles to Failure vs. Change Rate of DE for ALL Binders and Mixes

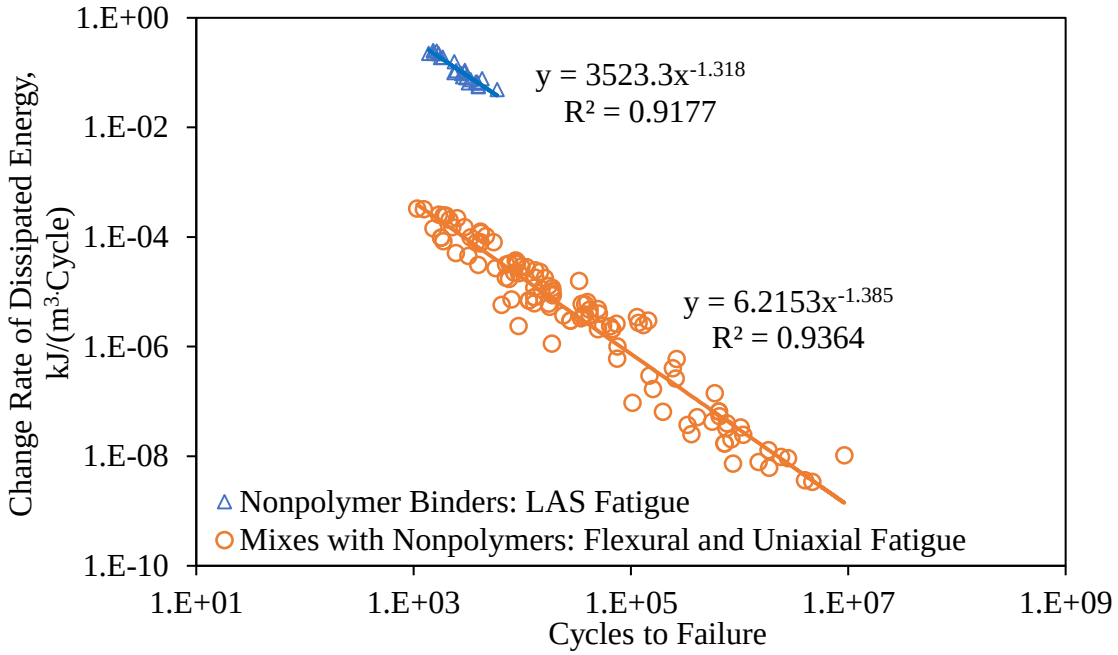

Figure 89. Cycles to Failure vs. Change Rate of DE for Non-Polymer Binders and Mixes

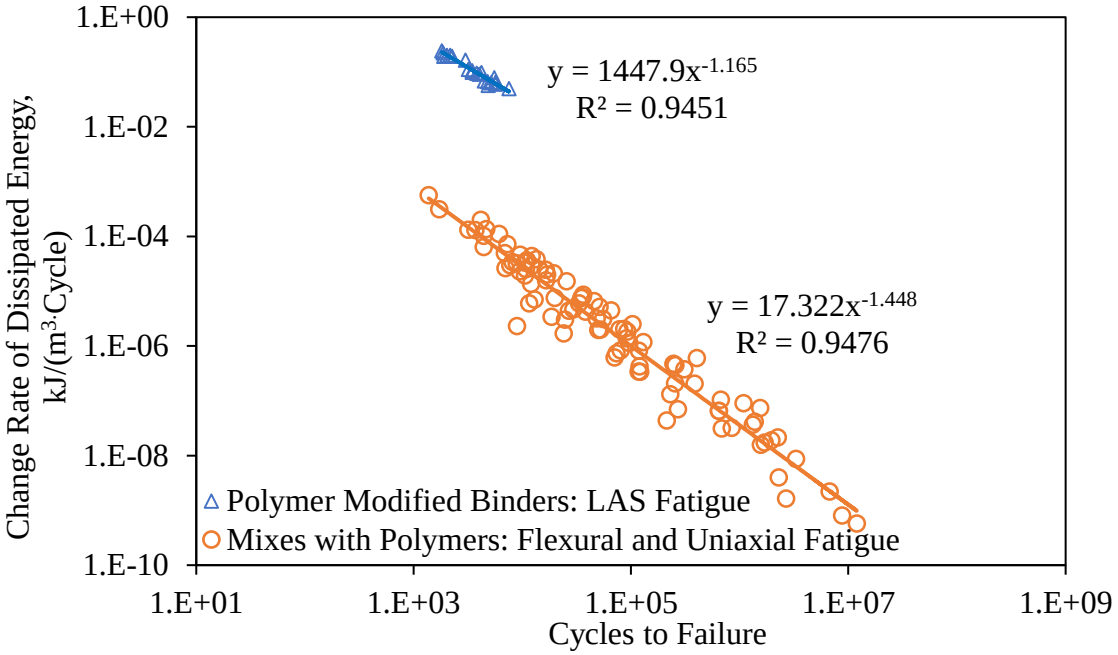

Figure 90. Cycles to Failure vs. Change Rate of DE for Polymer Modified Binders and Mixes

7.2 Relationship between Binder Properties and Laboratory Mix Fatigue Results

Tables 22 and 23 summarize the coefficients of determination (R^2) of the correlations between the binder properties and the mix fatigue results. **Figures 91 to 95** show the examples for the correlations. It may be noted in **Table 22** and that the correlation between binder Delta Tc and mix fatigue was made using the exponential functions, and other correlations were developed using the power law. Generally, G*sin (δ), loss tangent, Glover-Rowe parameter, and intermediate temperature grade showed weak correlations with the mix fatigue results. Crossover frequency and rheological index had no correlations with the mix fatigue results. The R^2 values for the correlations between the binder ΔTc values and the mix fatigue results varied from 0.4 to 0.76 when B6 and B13 were excluded, but no relationship appears when these two binders were included.

Table 22. R^2 of Correlations between Binder Properties and Mix Fatigue, 9 Binders

Binder Property		R^2 Value					
		Flexural Fatigue				Uniaxial Fatigue	
		N_f		CDE for N_f = 100,000		N_f @ G^R=100	CDE for N_f = 10,000 20°C
		10°C and 600 με	20°C and 600 με	10°C	20°C		
G*sin(δ)	10°C	0.34	0.34	0.11	0.32	0.04	0.20
	20°C	0.44	0.36	0.46	0.21	0.11	0.32
Loss Tangent	10°C	0.20	0.03	0.39	0.23	0.14	0.30
ωc	15°C	0	0	0	0	0	0
R	15°C	0.06	0.15	0.02	0.01	0.01	0.02
G-R	15°C	0.40	0.21	0.52	0.26	0.13	0.36
Inter. Temp.		0.56	0.40	0.59	0.33	0.10	0.35
ΔTc*		0.76 (0.07)	0.40 (0.02)	0.70 (0.20)	0.65 (0.19)	0.52 (0.06)	0.69 (0.01)

* First R^2 is for data without B6 and B13, and R^2 in brackets is for data with both binders.

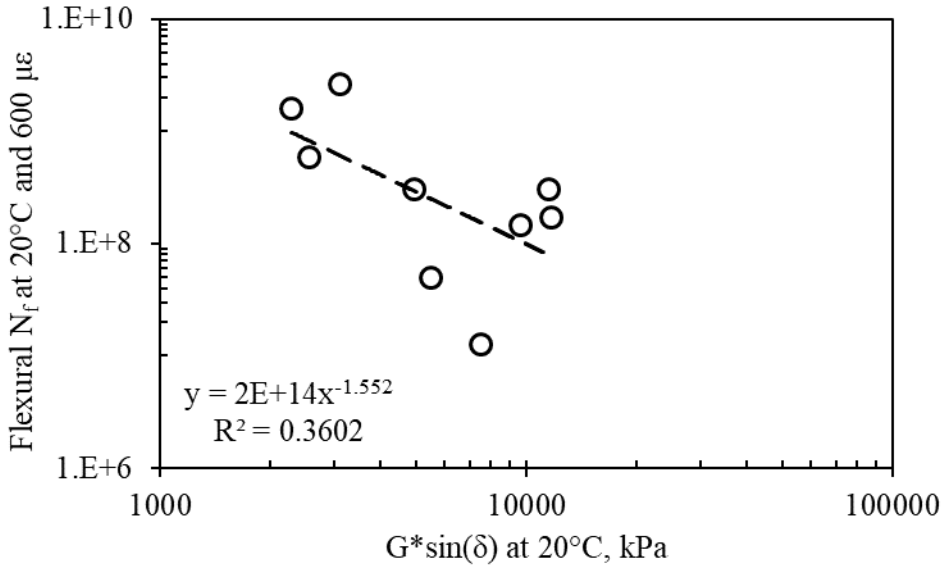

Figure 91. G*sin(δ) vs. Flexural Mix N_f

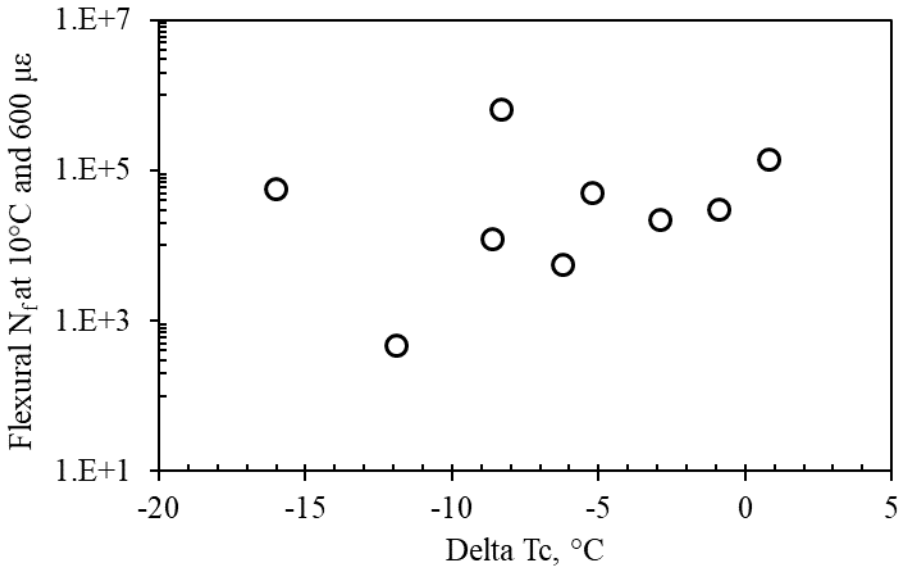

Figure 92. Delta Tc vs. Flexural Mix N_f at 10°C for All Data

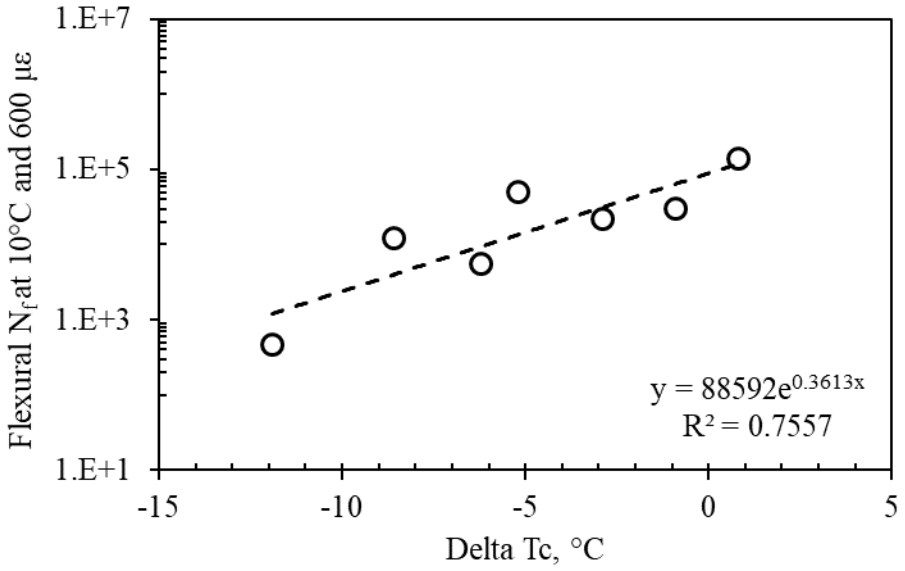

Figure 93. Delta Tc vs. BBF N_f at 10°C, without B6 and B13

Table 23. R^2 of Correlations between Binder Properties and Uniaxial Fatigue, 16 Binders

Binder Property		R^2 Value	
		N_f at G^R=100	CDE for N_f =10,000, 20°C
G*sin(δ)	10°C	0.37	0.37
	20°C	0.38	0.45
Loss Tangent	10°C	0.19	0.45
ωc	15°C	0.02	0.07
R	15°C	0.17	0.00
G-R	15°C	0.10	0.45

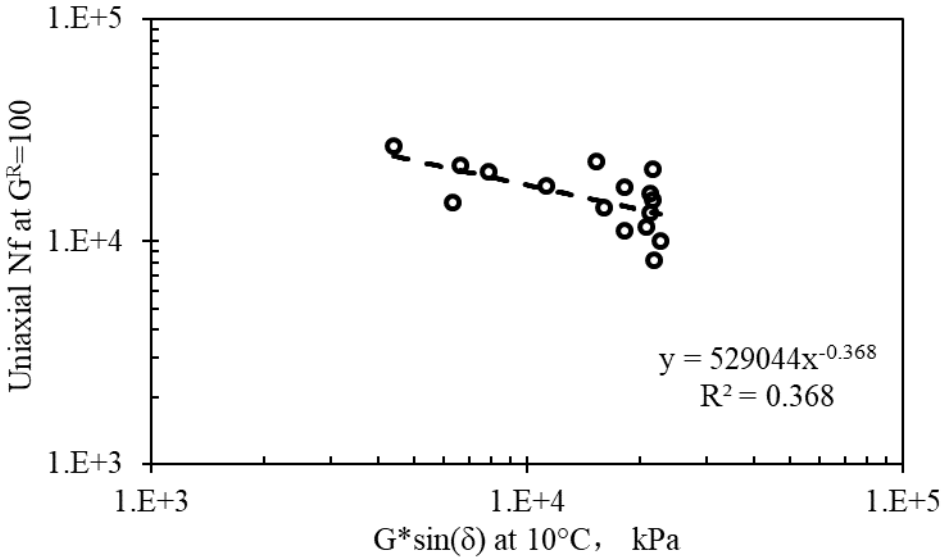

Figure 94. G*sin(δ) vs. Uniaxial Mix N_f

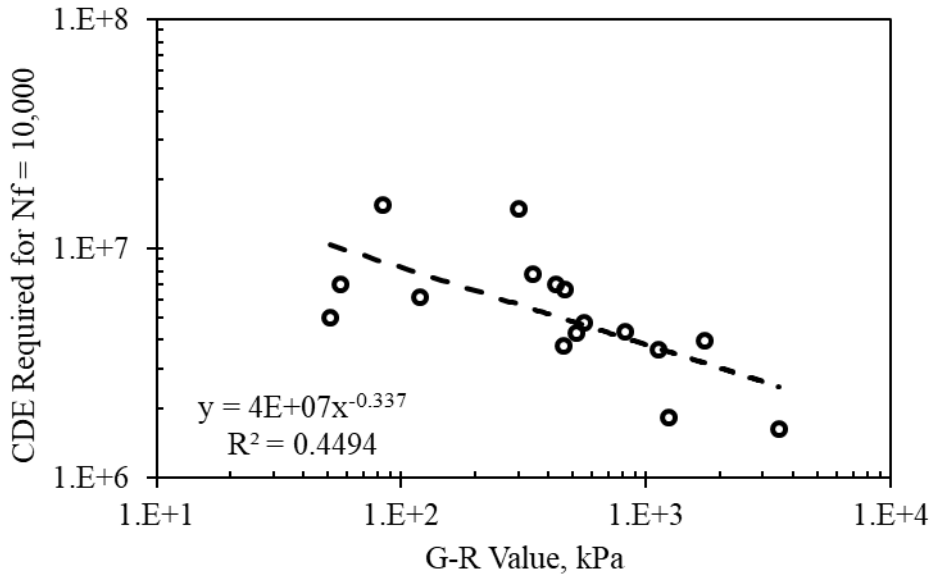

Figure 95. G-R Value vs. Cumulative Dissipated Energy for N_f =10,000 at 20°C

For the binders without additives (B7, B8, B9, B11 and B12), all the correlations between binder properties and uniaxial fatigue results are strong ($R^2 > 0.80$), as shown in **Table 24**. **Figures 117 to 119** show the examples for the correlations. This indicates that the use of polymers/additives in binders might affect the correlations between binder properties and mix fatigue performance. The similar trend was also found in the previous study (SHRP-A-404, 1994).

Table 24. R^2 of Correlations between Binder Properties and Uniaxial Fatigue Results, Binders without Polymers/Additives

Binder Property		N_f at G^R=100	CDE for N_f =10,000
G*sin(δ)	10°C	0.65	0.85
	20°C	0.86	0.91
Loss Tangent	10°C	0.92	0.83
ω_c	15°C	0.99	0.86
R	15°C	0.97	0.83
G-R	15°C	0.96	0.90

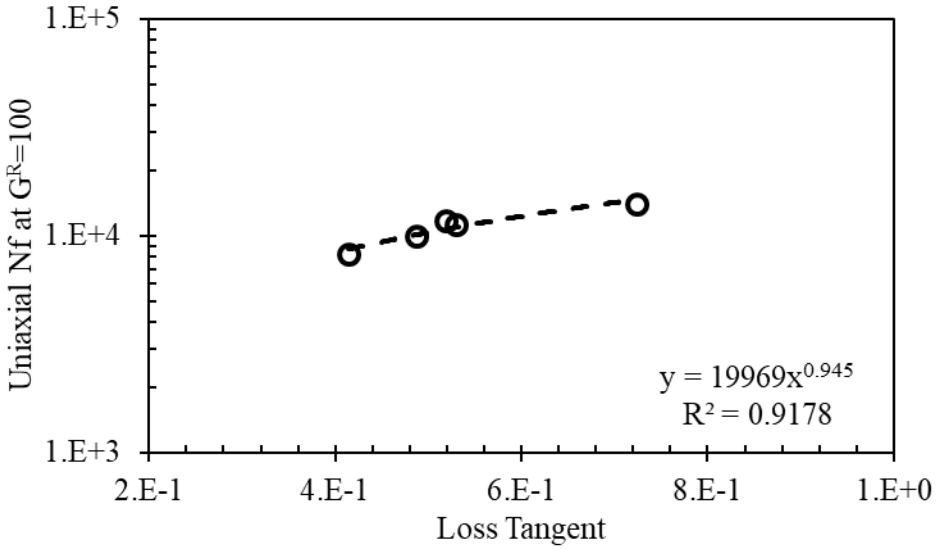

Figure 96. Loss Tangent vs. Uniaxial Mix N_f, Binders without Polymers/Additives

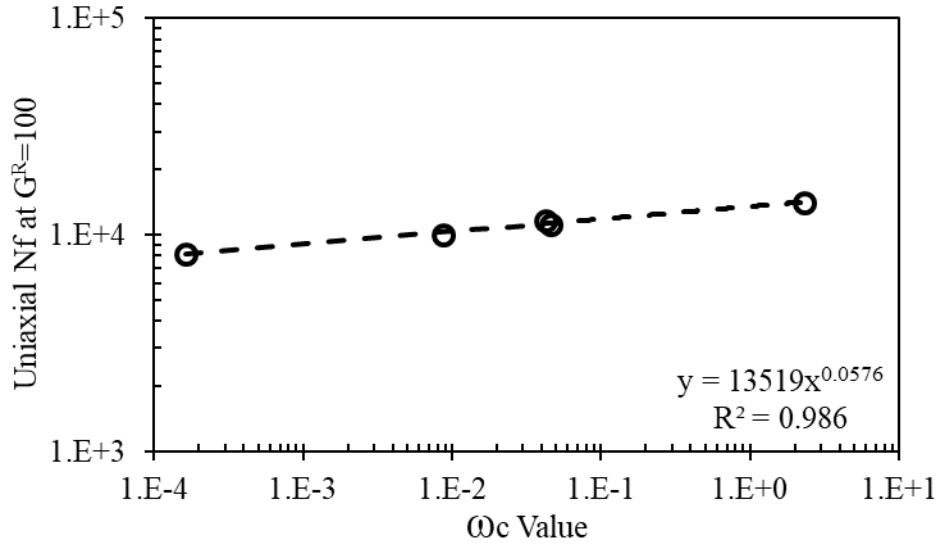

Figure 97. ω_c vs. Uniaxial Mix N_f, Binders without Polymers/Additives

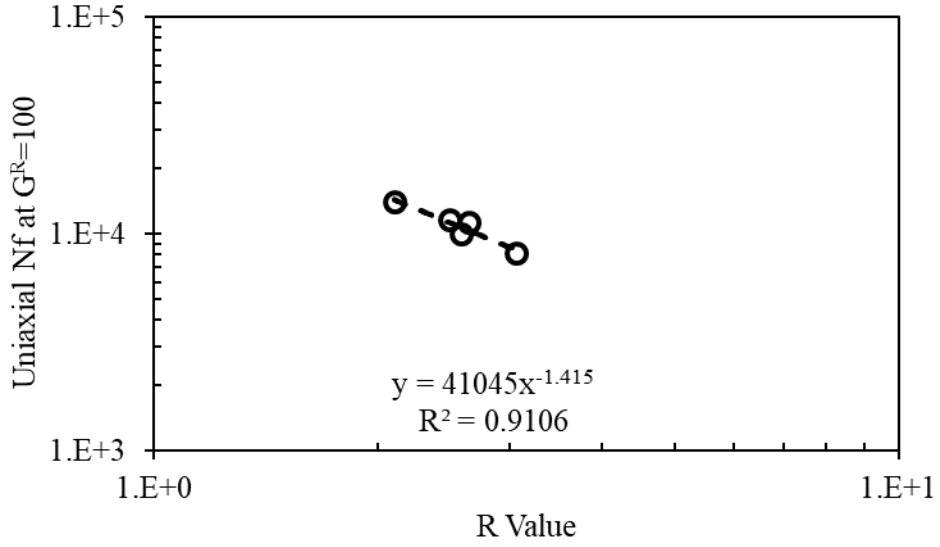

Figure 98. R vs. Uniaxial Mix N_f, Binders without Polymers/Additives

7.3 Relationship between Laboratory Fatigue and Simulated Pavement Fatigue Performance

The R^2 values for the correlations between the laboratory mix fatigue results and the simulated fatigue performance of 9.5-mm NMAS mixes are summarized in Error! Reference source not f

ound.**. Figures 99 to 101** show the examples for the correlations. In general, the correlations decreased with increasing thickness of the asphalt layer. For the 4-inch AC pavement, the laboratory mix fatigue results showed a good relationship with the simulated pavement damage in most cases. For the 6-inch AC pavement, the correlations reduced and most of R^2 values are lower than 0.5. When the AC thickness is equal or higher than 10 inches, R^2 values for the relationship between laboratory mix fatigue and simulated results were lower than 0.2 in most cases, indicating there may be no correlation between mix fatigue and simulated pavement performance. That could be attributed to the two factors: 1) the difference of the fatigue performance between the various mixes generally reduced with the decrease of applied strain; 2) the strain in the AC layer decreases with increasing thickness of the asphalt layer. Moreover, the S-VECD approach exhibited the highest correlation with the simulated damage, followed by the dissipated energy approach and the traditional strain-fatigue method. Note the mix with B16 had a worse flexural fatigue while it showed a great simulation performance, which made the B16 point further away from other points in **Figure 101**. The B16 point was considered as an outlier and was not used in the regression between flexural fatigue results and the simulated results.

Table 25. R^2 for Correlations between Laboratory Mix Fatigue and Simulated Damage

Parameter	Mix Number	Simulated Damage Percent (R^2)						
		4-in. AC, MN	4-in. AC, FL	6-in. AC, MN	6-in. AC, FL	10-in. AC, MN	10-in. AC, FL	15-in. AC, FL
Uniaxial N_f @ G^R=100	16	0.60	0.68	0.50	0.50	0.10	0.14	0.15
Uniaxial N_f @ G^R=100	9	0.61	0.85	0.67	0.59	0.02*	0.01*	0.07*
Flexural N_f @ G^R=0.001 and 10°C	8	0.37	0.70	0.31	0.34	0.18*	0.12*	0.24*
Flexural N_f @ G^R=0.001 and 20°C	8	0.61	0.74	0.40	0.39	0.19*	0.12*	0.22*
Flexural N_f @ 10°C and 600 με	8	0.28	0.57	0.22	0.21	0.33*	0.25*	0.36*
Flexural N_f @ 20°C and 600 με	8	0.53	0.56	0.29	0.26	0.18*	0.11*	0.15*

*The trend was reversed.

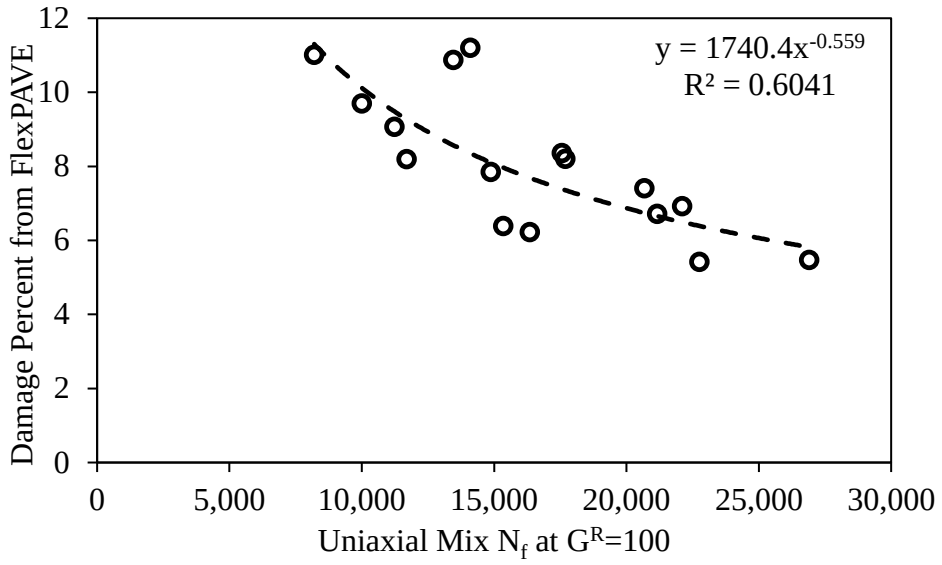

Figure 99. Mix Uniaxial N_f vs. Simulated Damage Percent, 4-in. AC, MN

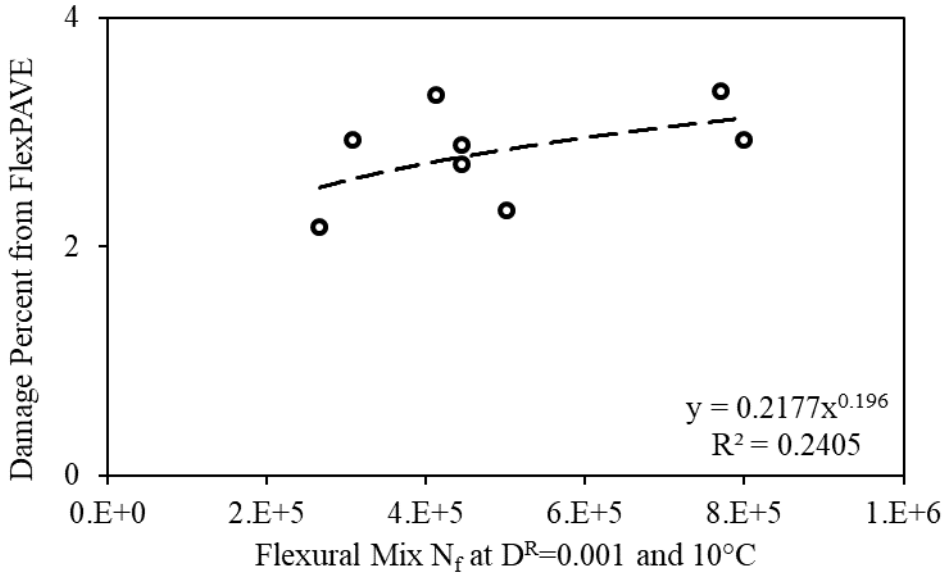

Figure 100. Flexural Mix N_f vs. Simulated Damage Percent, 15-in. AC, FL

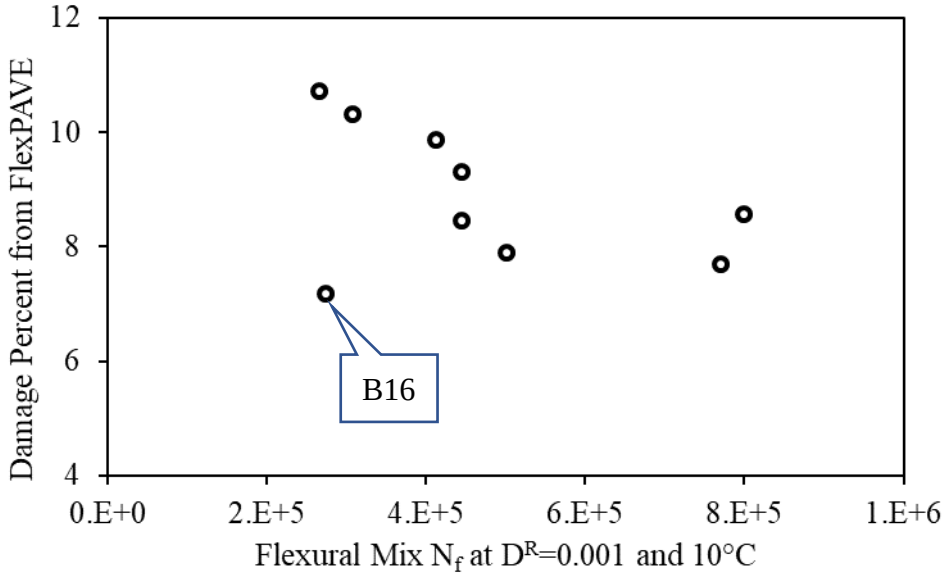

(a) With Binder 16

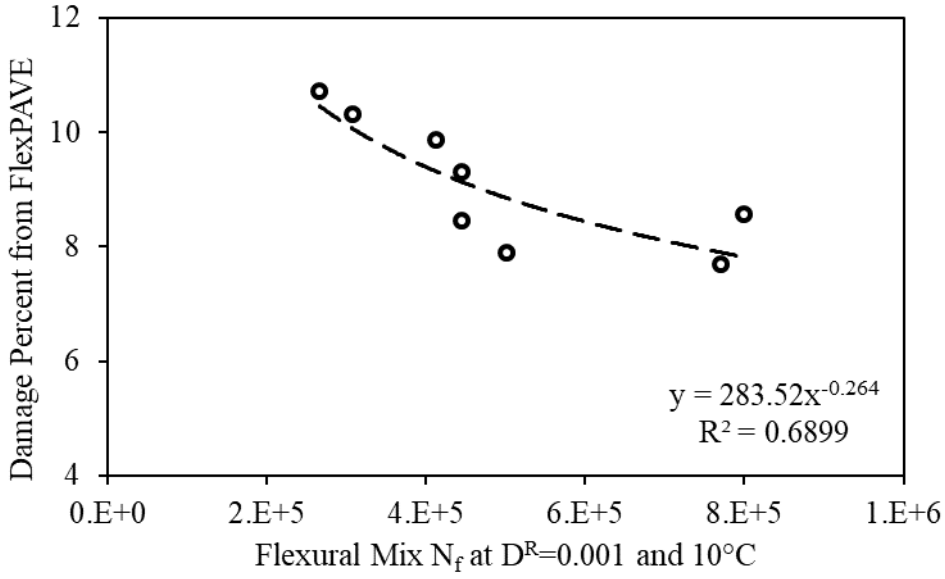

(b) Without Binder 16

Figure 101. Flexural Mix N_f vs. Simulated Damage Percent, 4-in. AC, FL

The ranking for the correlations between the binder properties and the simulated pavement damage is summarized in **Table 26**. It was observed that LAS binder fatigue life at G^R=0.00005 showed a much better correlation with the simulated pavement damage than others. Additionally, the correlations between LAS N_f and simulated damage reduced from good to poor level when the AC thickness increased from 4 inches to 15 inches. This trend agrees with that in the relationship between the mix fatigue and the simulated performance. **Figure 102** and **Figure 103** show the examples of correlations between LAS binder N_f and the simulated pavement damage for 4- and 15-in. AC pavements, respectively.

Table 26. Ranking for Correlations between Binder Properties and Simulated Damage

Simulated Damage Percent (R^2)						
4-in. AC, MN	4-in. AC, FL	6-in. AC, MN	6-in. AC, FL	10-in. AC, MN	10-in. AC, FL	15-in. AC, FL
LAS N_f (0.64)	LAS N_f (0.64)	LAS N_f (0.46)	LAS N_f (0.48)	LAS N_f (0.12)	LAS N_f (0.17)	LAS N_f (0.18)
G*sin(δ) (0.15)	G*sin(δ) (0.05)	G*sin(δ) (0.05)	G*sin(δ) (0.05)	G-R (0.09)	G-R (0.08)	G-R (0.02)

Note R^2 less than 0.2 means no relationship between binder properties and simulated damage.

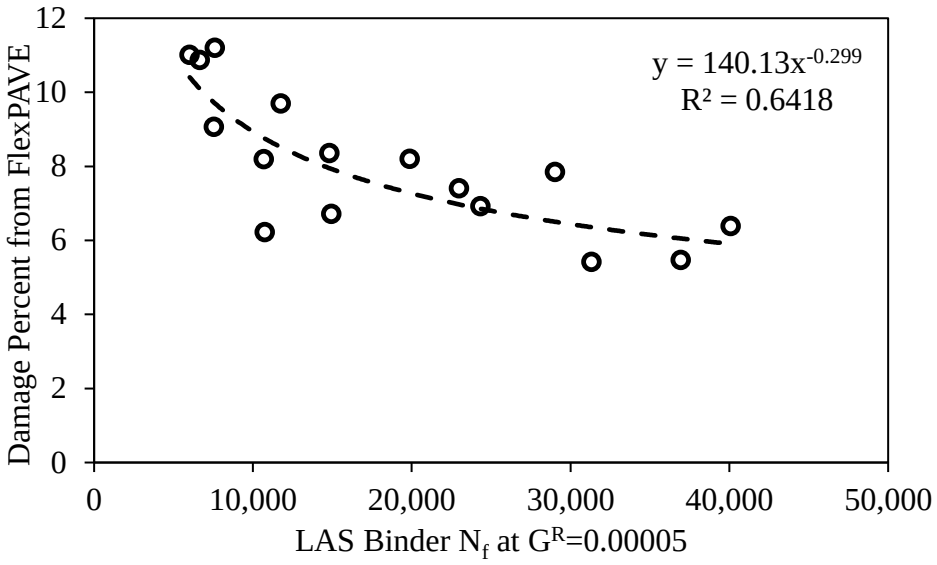

Figure 102. Binder LAS N_f vs. Simulated Damage Percent, 4-in. AC, MN

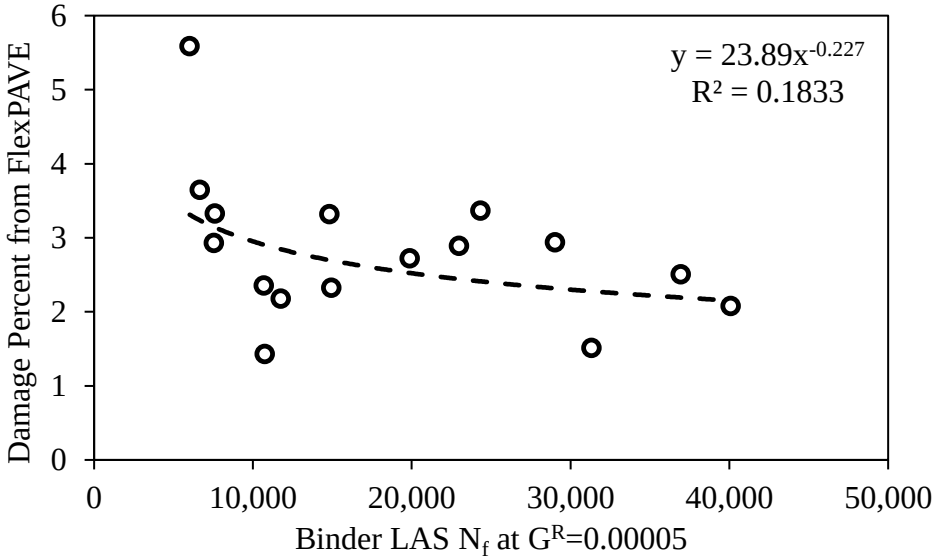

Figure 103. Binder LAS Nf vs. Simulated Damage Percent, 15-in. AC, FL

7.4 Summary

In this chapter, an effort was made to correlate the binder fatigue/fracture properties to the mix fatigue performance. The specific observations are as follows:

1) LAS binder N_f exhibited better correlations with laboratory/simulated mix fatigue performance compared to the other binder properties. This is likely attributed to the following factors: 1) LAS test involves the damage evolution in the binder under a repeated loading, which is similar to mix fatigue tests; 2) however, other binder properties (e.g., G*sin(δ), Delta Tc, loss tangent, crossover frequency, rheological index, and Glover-Rowe value) represent the rheological behavior of asphalt binders and do not involve the damage processes which happen in the asphalt mix under a repeated loading (e.g., crack initiation and propagation). Furthermore, the relationship between the change rate of dissipated energy and fatigue life indicated that the mix fatigue performance could have a good connection with LAS binder fatigue property, which agrees with the previous findings (Shen 2006). Therefore, the modified LAS test could be a promising test to evaluate the binder fatigue property.
2) Binder properties, including G*sin (δ), loss tangent, Glover-Rowe parameter, and intermediate temperature grade, showed weak correlations with the mix fatigue results. Crossover frequency and rheological index had no correlations with the mix fatigue results. The use of additives in binders could significantly affect the correlations between binder properties and laboratory mix fatigue performance. This trend was also found in the previous study (SHRP-A-404 1994).
3) Based on the simulated pavement damage results using FlexPAVE, the correlations between mix fatigue result and the simulated pavement damage decreased with increasing thickness of the asphalt layer. For the 4-inch AC pavement, the laboratory mix fatigue results showed a good relationship with the simulated pavement damage in most cases. However, no relationship was found when AC thickness is higher than 6 inches. This trend

was in agreement with the finding in the previous study (Stuart et al., 2001). That could be attributed to the two factors: 1) the difference of the fatigue performance between the various mixes generally reduced with the decrease of applied strain; 2) the strain in the AC layer decreases with increasing thickness of the asphalt layer.

CHAPTER 8 – FIELD VALIDATION USING 2009 GROUP EXPERIMENT SECTIONS

In this chapter, the relationship between the laboratory binder and mix properties and field pavement fatigue performance were investigated using 2009 group experimental sections on the NCAT pavement test track. Additionally, the simulated pavement fatigue performance of the test sections was also compared to the field performance. In the following sections, the information about 2009 group experimental sections is first presented, followed by the laboratory testing results and field performance of the test sections. After that, the relationships between the binder properties and pavement fatigue performance are discussed. Finally, the relationships between the simulated performance and field performance are investigated.

8.1 Test Sections Information

During the summer of 2009, five sections were built on the NCAT Test Track: S9, S10, S11, N10 and N11. All sections had an asphalt mix layer over an aggregate base built on a stiff subgrade layer. The asphalt mix layer consisted of three lifts (surface, intermediate, and base). **Table 27** summarizes the material properties and the production temperatures for asphalt mix layer. It was observed that the asphalt mixes in S9, S10 and S11 are virgin mixes without Reclaimed asphalt pavement (RAP), and the mixes in N10 and N11 include 50% RAP. Also, warm mix asphalt (WMA) technologies were used in S10, S11 and N11 and conventional hot mix asphalt (HMA) was used in S9 and N10. An unmodified PG 67-22 binder was used in all the base layer mixes.

Table 27. Asphalt Layer in Test Sections

Section ID	Description	Lift	NMAS (mm)	Virgin Binder	Asphalt Content, %	Production Temperature, °F
Control S9	HMA, without RAP	Surface	9.5	PG 76-22	6.1	335
		Intermediate	19.0		4.4	
		Base	19.0	PG 67-22	4.7	325
WMA S10	Foam-Based WMA, without RAP	Surface	9.5	PG 76-22	6.1	275
		Intermediate	19.0		4.7	
		Base	19.0	PG 67-22	4.7	
WMA S11	Additive-Based WMA, without RAP	Surface	9.5	PG 76-22	6.4	250
		Intermediate	19.0		4.6	
		Base	19.0	PG 67-22	5.0	
HMA-RAP N10	HMA, 50% RAP	Surface	9.5	PG 67-22	6.0	325
		Intermediate	19.0		4.4	
		Base	19.0		4.7	
WMA-RAP N11	Foam-Based WMA, 50% RAP	Surface	9.5	PG 67-22	6.1	275
		Intermediate	19.0		4.7	
		Base	19.0		4.6	

8.2 Material Properties of Test Sections

The fatigue property of the base layers (S9-3, S10-3, S11-3, N10-3 and N11-3) in five test sections was characterized through flexural and uniaxial fatigue tests. Flexural fatigue data were analyzed by the conventional strain-fatigue life relationship and the dissipated energy approach. Uniaxial fatigue data were investigated using the dissipated energy approach. **Figures 104 to 106** present the relationships between strain and cycles to failure, and cumulative dissipated energy and cycles to failure, respectively.

Based on the relationship between strain and fatigue life, three virgin mixes (S9-3, S10-3 and S11-3) had similar transfer functions. Compared to three virgin mixes, WMA mix with 50% RAP (N11-3) exhibited lower cycles to failure at high strain level (800 με), and higher cycles to failure at low strain level (200 με); HMA mix with 50% RAP (N10-3) showed lower cycles to failure at intermediate and high strain levels (400 and 800 με), and similar cycles to failure at low strain level (200 με). Additionally, transfer functions of both RAP mixes had steeper slopes than the three virgin mixes, indicating RAP mixes could have a greater sensitivity to strain levels. That was expected as the mixes with high RAP generally have a lower cracking resistance compared to the virgin mixes.

According to the relationship between the cumulative dissipated energy and cycles to failure from the flexural fatigue tests, all the mixes had similar transfer functions. Based on the relationship between the cumulative dissipated energy and cycles to failure from the uniaxial fatigue tests, WMA with 50% RAP (N11-3) could have slightly lower resistance to fatigue cracking than three virgin mixes. It is surprising that the transfer function of HMA with 50% RAP (N10-3) is further away from other four mixes. This is likely due to the testing variability or error as the strain data from one LVDT in this mix were observed to have a decrease or change little over loading cycles before failure point, while a normal strain on sample generally increases with increasing of loading before failure. In this case, the uniaxial fatigue data of HMA with 50% RAP (N10-3) was not used for the further analysis.

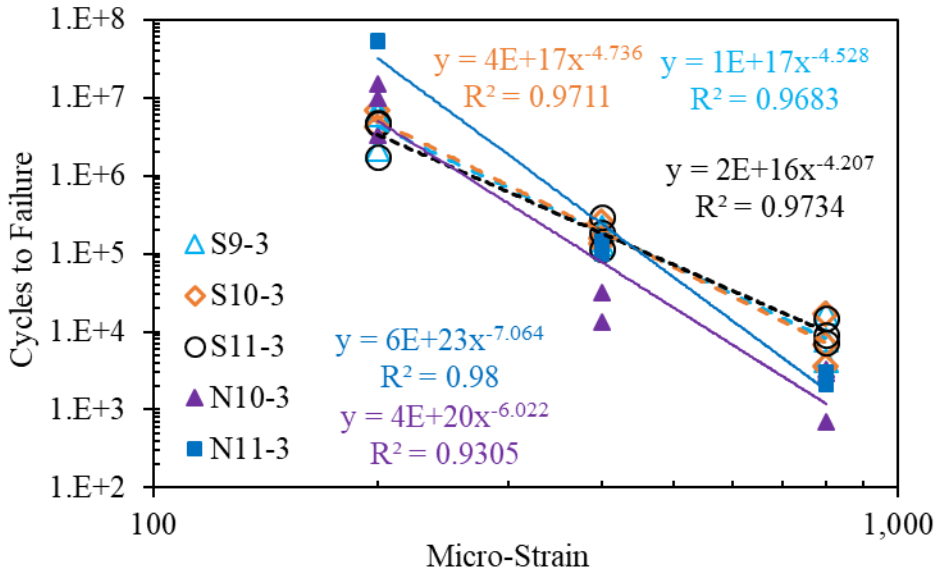

Figure 104. Strain vs. Cycles to Failure, Flexural Fatigue Test

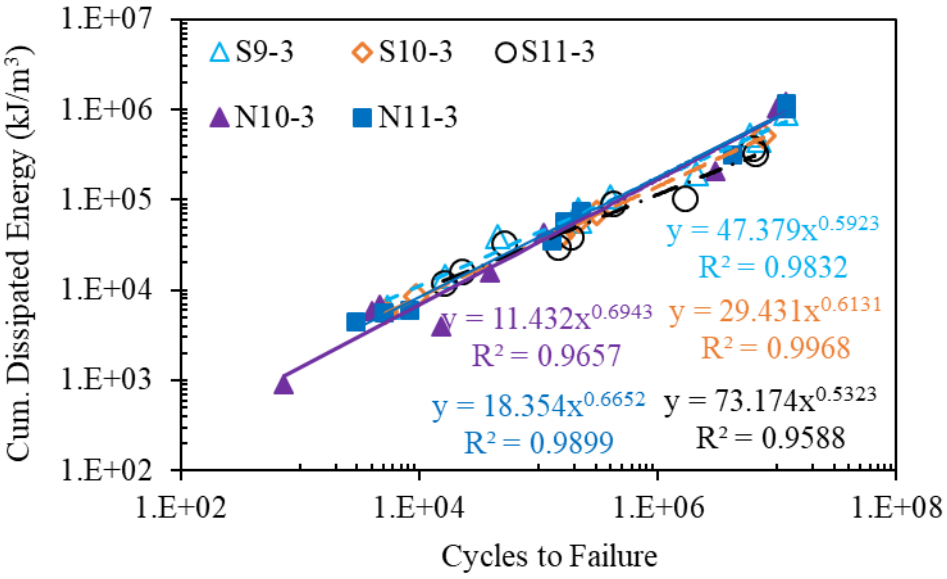

Figure 105. Cum. Dissipated Energy vs. Cycles to Failure, Flexural Fatigue Test

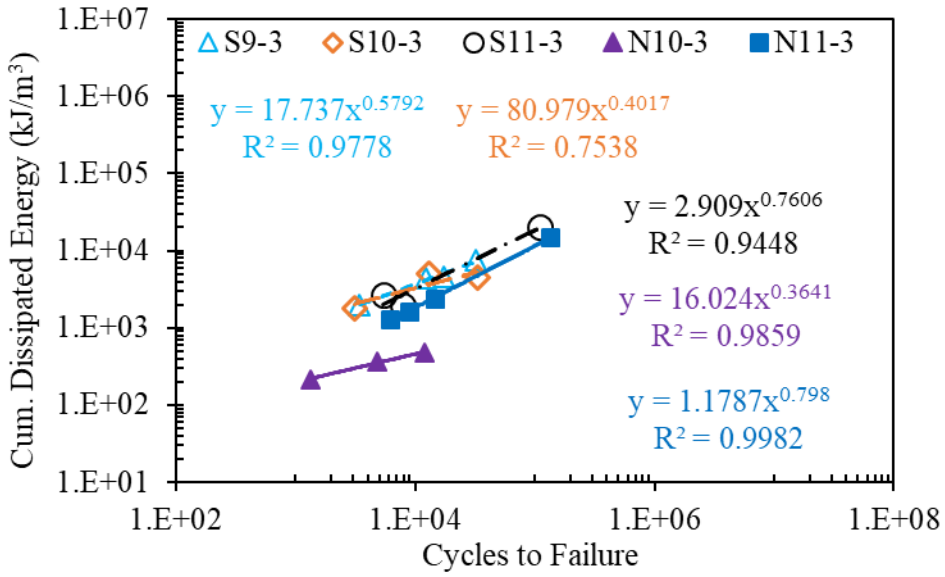

Figure 106. Cum. Dissipated Energy vs. Cycles to Failure, Uniaxial Fatigue Test

In addition, the binders extracted from the plant produced mixes were tested to investigate the fracture properties through DSR, BBR and frequency sweep tests. The fracture parameters calculated from the binder test results are summarized in **Table 28** and **Figures 107 to 110**.

Compared to three virgin mixes (S9-3, S10-3 and S11-3), two mixes with 50% RAP (N10-3 and N11-3) showed higher stiffness and lower phase angle, higher R values and lower crossover frequency, and more negative Delta Tc. This indicates that both 50% RAP mixes may have lower resistance to cracking than three virgin mixes (**Table 29**). That was expected as the mixes with high RAP are more brittle than virgin mixes.

In comparison with the HMA mixes, the corresponding WMA mixes exhibited slightly lower stiffness and higher phase angle, lower R values and higher crossover frequency, and less negative

Delta Tc. This means the lower production temperature in WMA could reduce the binder aging, resulting in a better cracking resistance, which was expected.

Table 28. Binder Properties for Base Layers

Binder Properties	S9-3, Virgin	S10-3, Virgin	S11-3, Virgin	N10-3, 50% RAP	N11-3, 50% RAP
	HMA	Foam WMA	Additive WMA	HMA	Foam WMA
G*sin(δ) at 15°C and 10 rad/sec., kPa	7,462	9,582	9,437	14,090	12,660
Loss Tangent at 10°C and 10 rad/sec.	0.54	0.58	0.84	1.95	2.15
R	2.3	2.2	2.1	2.8	2.7
ωc	1.932	2.655	4.702	0.008	0.023
G-R at 15° and 0.005 rad/sec., kPa	38	30	21	852	521
Intermediate Temperature Grade, °C	24.1	20.5	21.8	32.4	32.1
Delta Tc, °C	-3.6	-3.3	-2.1	-10.6	-10.2

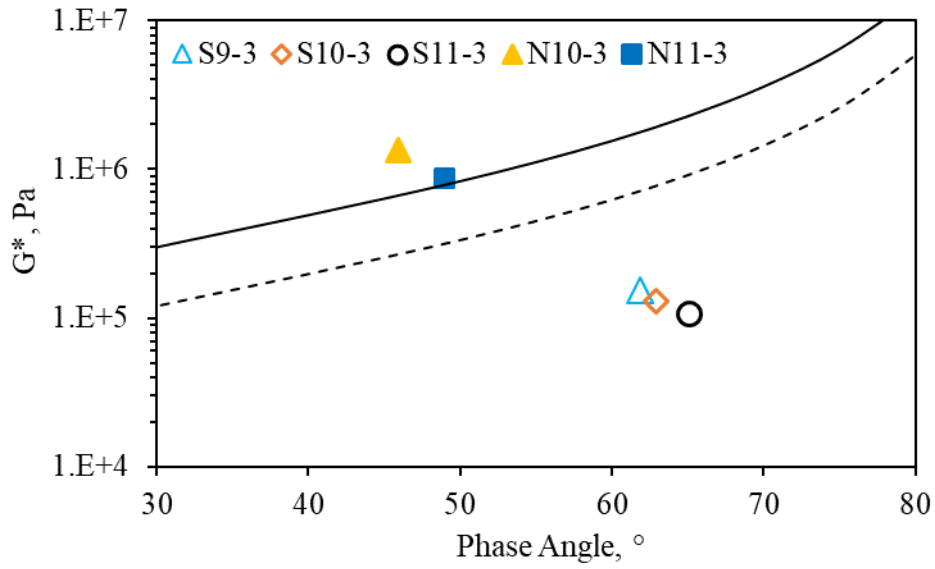

Figure 107. Black Space Plot for Mix-extracted Binders

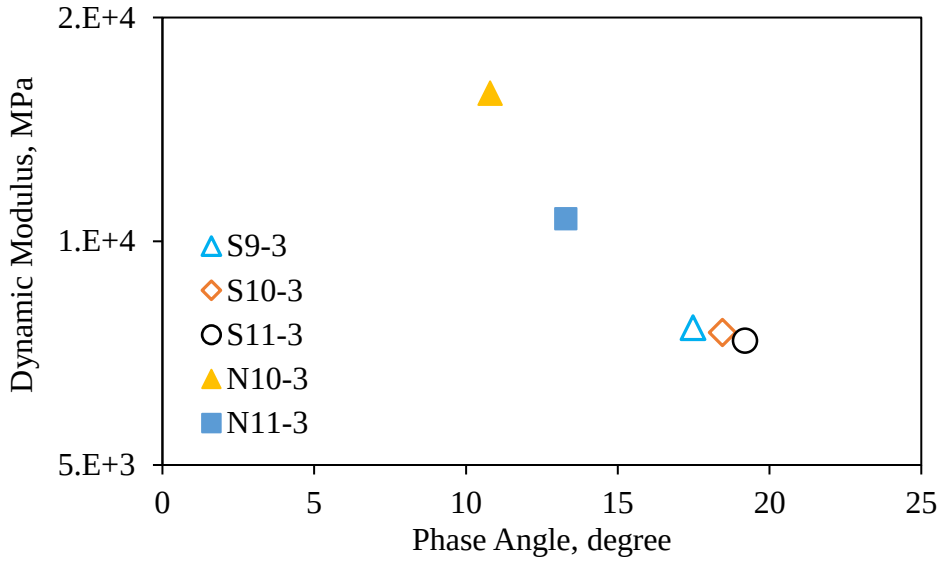

Figure 108. Black Space Plot for Mixes

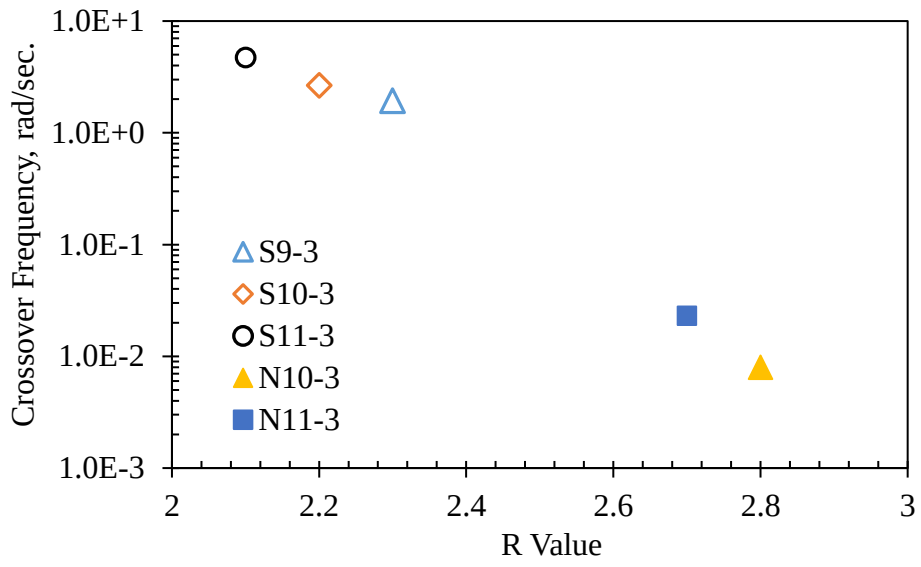

Figure 109. Crossover Frequency - R Value Space for Mix-extracted Binders

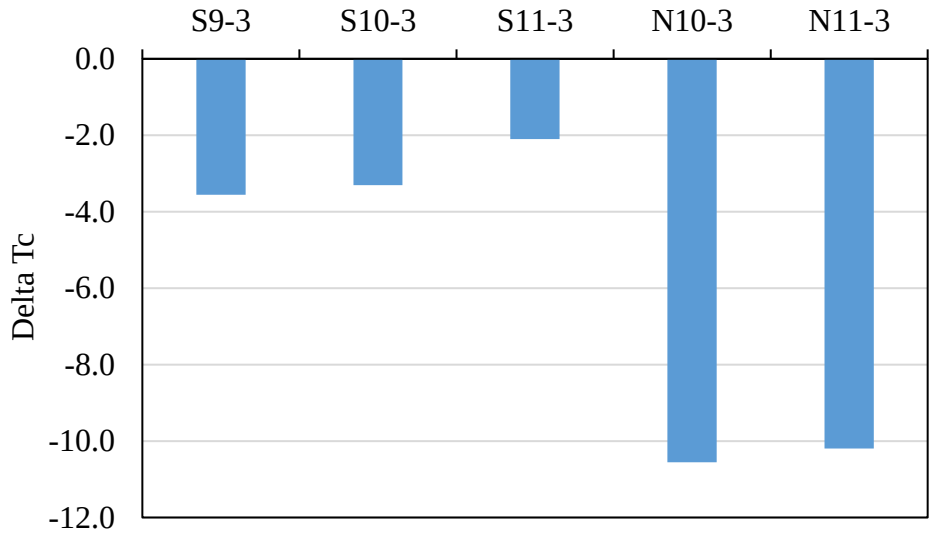

Figure 110. Delta Tc for Mix-Extracted Binders

Table 29. Expected Cracking Susceptibility Based on Binder Properties

Mix ID	Expected Cracking Susceptibility
S8-3	Low
S10-3	Low
S11-3	Low
N10-3	High
N11-3	High

8.3 Field Fatigue Performance of Test Sections

After the construction, five sections were opened to traffic. The fleet of triple-trailer trucks operated 16 hours per day, 5 days per week. During that time, routine weekly performance measurements were made, including rut depth, ride quality and visual inspection for cracking. Additionally, weekly strain and pressure measurements were made, and Falling Weight Deflectometer (FWD) tests were conducted three times per month. In this study, loading cycles, cracking and FWD data were used for the fatigue performance analysis.

Table 30 shows the field cracking performance at 17 million ESALs. It was observed that N10 HMA section with 50% RAP exhibited the least cracking, followed by N11 WMA section with 50% RAP, S9 control and S11 WMA. S10 WMA-foam section presented the most cracking. That is unexpected since the mixtures with high RAP could be more brittle and have lower cracking resistance. To determine the types of cracking (i.e., top-down, bottom-up), a series of cores were cut in each section in December 2013. It was found that longitudinal cracking extended only through the surface layer, while transverse cracks in the wheel-paths extended through the full depth of the asphalt pavement (Timm et al., 2016). Based on this observation, longitudinal cracks

were considered to be top-down and transverse cracks were considered to be bottom-up (Timm et al., 2016).

Table 30. Field Cracking at 17 million ESALs (Timm et al., 2016)

Section	Percentage of Wheelpaths		Percentage of Lane
	Longitudinal	Transverse and Area	
S9 Control	7	9	5
S10 WMA-foam	15	21	11
S11 WMA-additive	7	15	8
N10 RAP-HMA	0	1	0
N11 RAP-WMA	2	6	4

8.4 Relationship between Binder Properties and Mix Fatigue Performance

Table 31 shows the R^2 values for the correlations between the cracking parameters and laboratory and field mix fatigue performance. For laboratory mix fatigue life at the low strain level (200 με), the R^2 values varied from 0.59 to 0.76; at high strain level (800 με), R^2 values were higher than 0.80. All the trends at 800 με were expected, and the examples of the correlations are shown in **Figure 111** and **Figure 112**. However, all the trends at 200 με were reversed. This is because the ranking of mix BBF Nf at 200 με is different from those at 800 με. **Figure 113** and **Figure 114** indicate that the flexural fatigue life at 200 με increased with the increase of G*sin(δ) and the decrease of Delta Tc, which was unexpected as a binder with a low G*sin(δ) and high Delta Tc generally has a better cracking resistance.

For field pavement cracking, although the R^2 values of the relationships between the binder properties and transverse cracking area were high, varying from 0.54 to 0.87, all the trends were reversed and unexpected. An example for the unexpected trend is shown in **Figure 115**. Based on

the laboratory test results, it is expected that the mixes containing 50% RAP (N10-3 and N11-3) could have more cracking as they are susceptible to cracking. In contrast, N10 and N11 sections exhibited a better field fatigue performance at 17 million ESALs. That means that the laboratory binder and mix test results are not sufficient for characterizing the pavement fatigue performance. To investigate the in-situ fatigue performance, the pavement mechanistic analysis is needed.

Table 31. R^2 of Correlations between Binder Properties and Mix Fatigue Performance

Binder Properties	R^2 Values		
	Laboratory Mix N_f @ 200 με	Laboratory Mix N_f @ 800 με	Field Transvers Cracking
G*sin(δ) at 15°C and 10 rad/sec., kPa	0.65	0.80	0.60
Loss Tangent at 10°C and 10 rad/sec.	0.67	0.82	0.54
R	0.67	0.96	0.77
ωc	0.69	0.98	0.66
G-R at 15° and 0.005 rad/sec., kPa	0.70	0.99	0.87
Intermediate Temperature Grade, °C	0.59	0.88	0.73
Delta Tc, °C	0.76	0.99	0.69

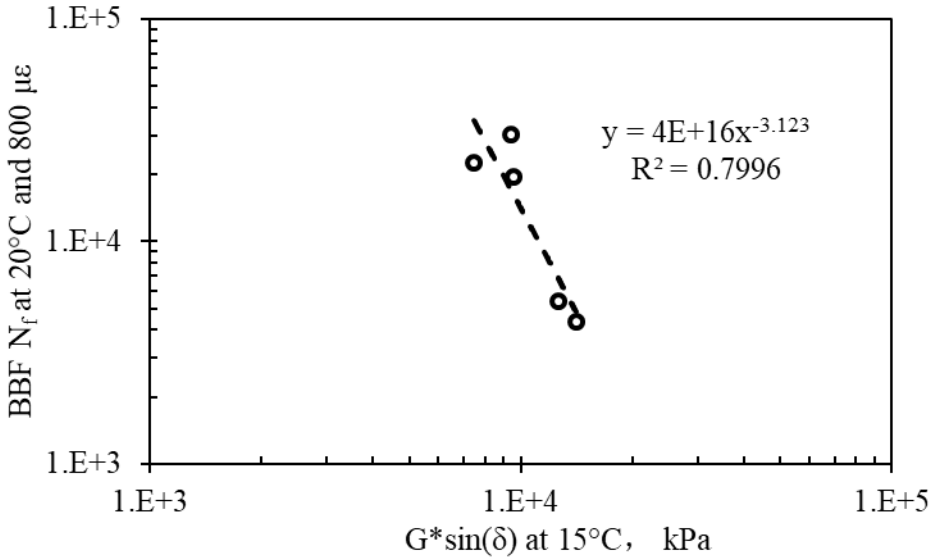

Figure 111. G*sin(δ) vs. Flexural N_f at 20°C and 800 με

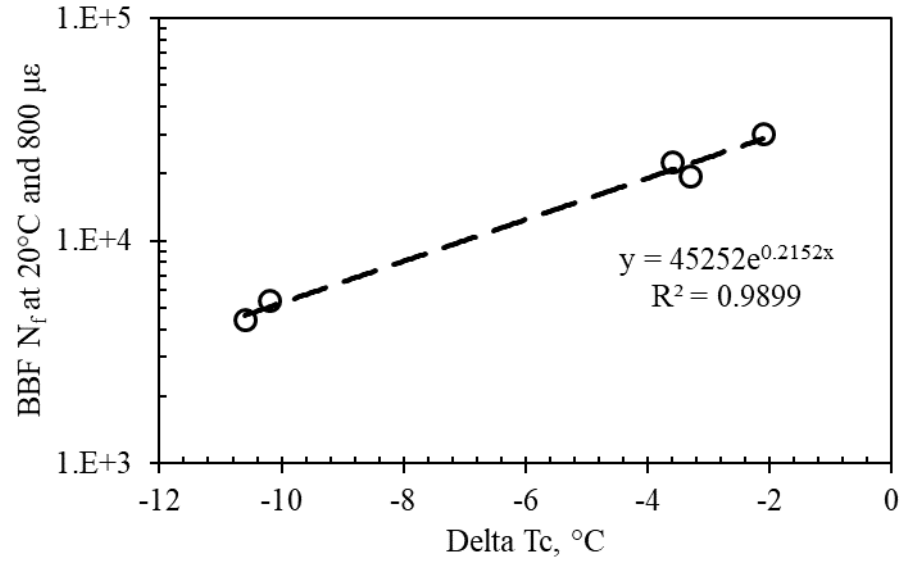

Figure 112. Delta Tc vs. Flexural N_f at 20°C and 800 με

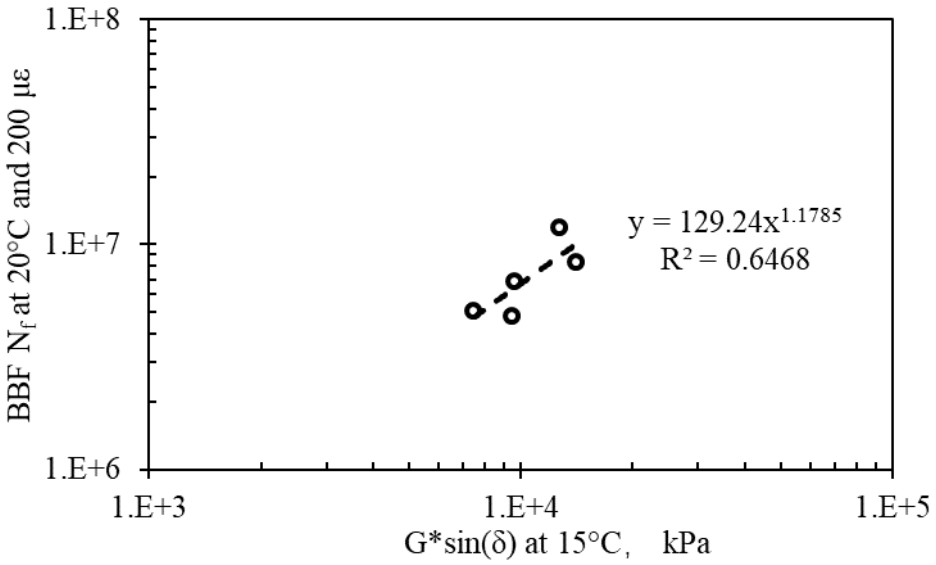

Figure 113. G*sin(δ) vs. Flexural N_f at 20°C and 200 με

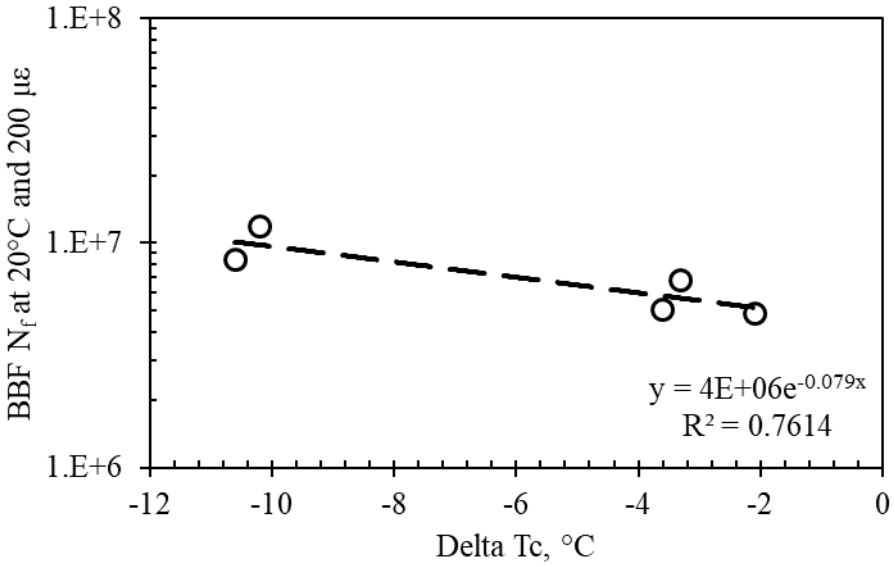

Figure 114. Delta Tc vs. Flexural N_f at 20°C and 200 με

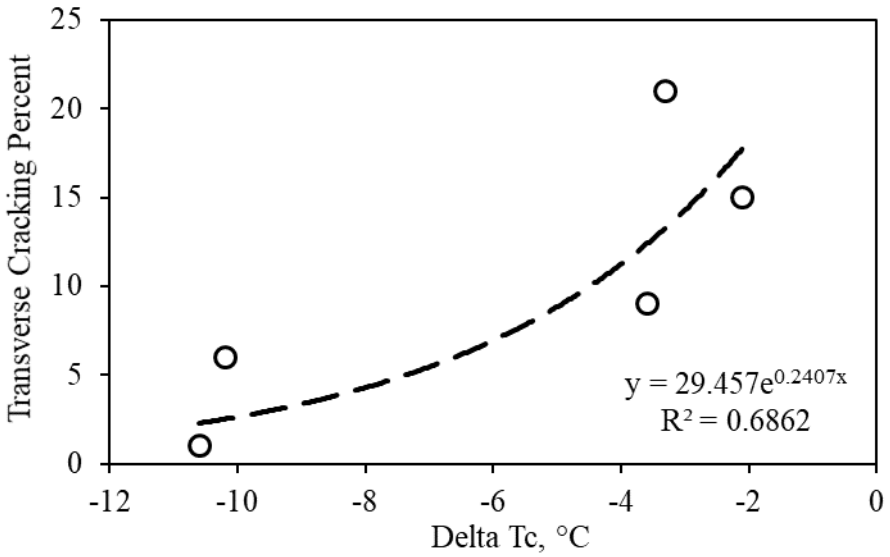

Figure 115. Delta Tc vs. Field Cracking

8.5 Pavement Fatigue Performance Simulation

Based on the above analysis, it is necessary to consider the effect of the pavement structure to evaluate the pavement fatigue performance. In this section, a simulation of the fatigue performance was conducted on five test sections using the combination of the mix fatigue functions and the layered elastic analysis. The Weslea program developed by Bjorn Birgisson, David Newcomb, and David Timm was employed to compute the maximum tensile stress and strain at the bottom of the asphalt layer. For Weslea inputs, the layer moduli at 20°C (68°F) were used and they were backcalculated from FWD deflection data using EVERCALC 5.0; the thickness of layer measured in the construction (as-built pavement thickness) was used; a single axle load of 21 kips with dual tires was employed. Additionally, the poison ratio for the asphalt layer, granular layer and subgrade materials are assumed as 0.35, 0.40 and 0.45, respectively.

The layer moduli at 20°C were computed based on the relationship between layer modulus and mid-depth temperature, which are shown in **Appendix E**. **Table 32** shows the moduli of three layers for each section at 20°C. It appears that subgrade modulus in all the sections is higher than that of granular layer. That is because the stiffer subgrade (native A-4 soil) was used in these sections. **Table 33** shows the as-built layer thicknesses for each section. The phase angles for the calculation of dissipated energy were computed based on the equation in **Figure 116**, which was developed based on the laboratory dynamic modulus results of 16 mixes used in this study.

Table 32. Backcalculated Moduli at 20°C

Section	Modulus, psi		
	AC Layer	Granular Layer	Subgrade
S9 Control	896,619	1,990	28,000
S10 WMA-foam	800,977	1,580	27,000
S11 WMA-additive	814,000	1,620	26,000
N10 RAP-HMA	1,061,620	2,180	46,200
N11 RAP-WMA	1,048,257	3,300	40,100

Table 33. As-built Pavement Thickness (Vargas and Timm 2012)

Section	AC Layer, inch	Granular Layer, inch
S9 Control	6.8	6.2
S10 WMA-foam	6.8	7.0
S11 WMA-additive	6.9	6.3
N10 RAP-HMA	7.5	3.4
N11 RAP-WMA	7.1	4.6

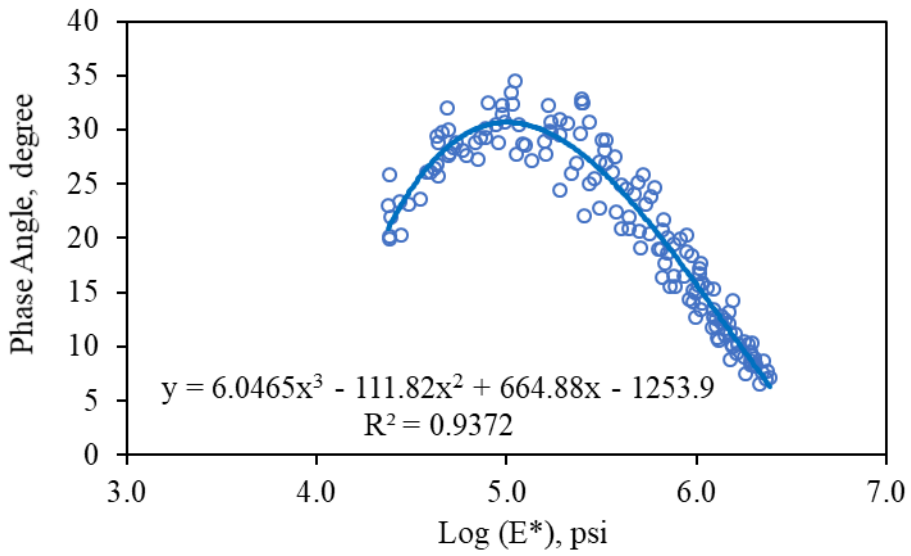

Figure 116. Phase Angle vs. Dynamic Modulus

After obtaining stress, strain and phase angle, the dissipated energy at the bottom of asphalt layer was calculated. **Figure 117** and **Figure 118** shows the calculated maximum tensile strain and dissipated energy at the bottom of the asphalt layer, respectively. It was observed that N10 and N11 sections had much lower tensile strain and dissipated energy compared to three virgin mix sections. This is attributed to the fact: AC and subgrade moduli in these two sections are higher than other sections. The computed dissipated energy was considered as a mean dissipated energy per cycle, and then fatigue life was computed using **Equation 29** which was transformed from the W_N-N_f relationship ($W_N = A(N_f)^Z$).

$$\frac{W_N}{N_f} = k_1(N_f)^{k_2-1} \qquad (29)$$

Where, $\frac{W_N}{N_f}$ is the mean dissipated energy per cycle.

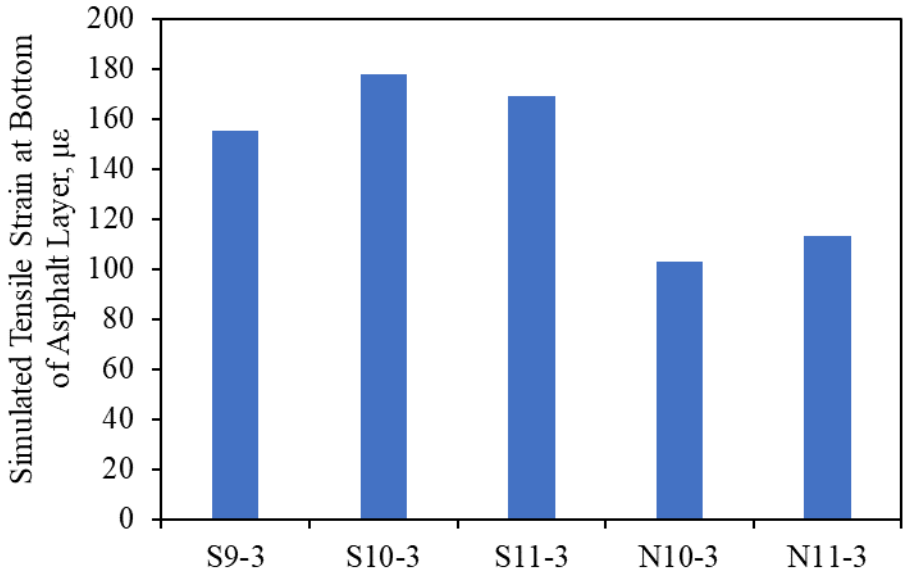

Figure 117. Calculated Tensile Strain at Bottom of Asphalt Layer at 20°C

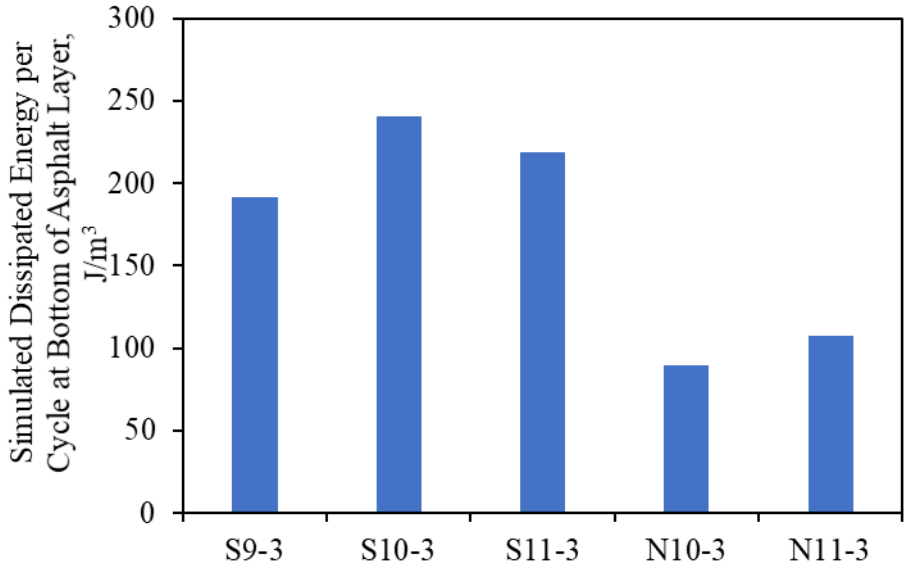

Figure 118. Calculated Dissipated Energy at Bottom of Asphalt Layer at 20°C

Fatigue life calculated by the W_N-N_f relationship is shown in **Figure 119** and **Figure 120**. For comparison purposes, fatigue life for each section was also calculated using the ε-N_f relationship, as shown in **Figure 121**. It appears two sections with 50% RAP base layer showed a higher simulated fatigue life than the three sections with the virgin mix base layer. For the sections with the virgin mix base layer, S9 section exhibited a slightly higher simulated fatigue life than other two sections. These trends in the simulated fatigue life are associated not only with material fatigue properties but with the pavement responses (stress and strain).

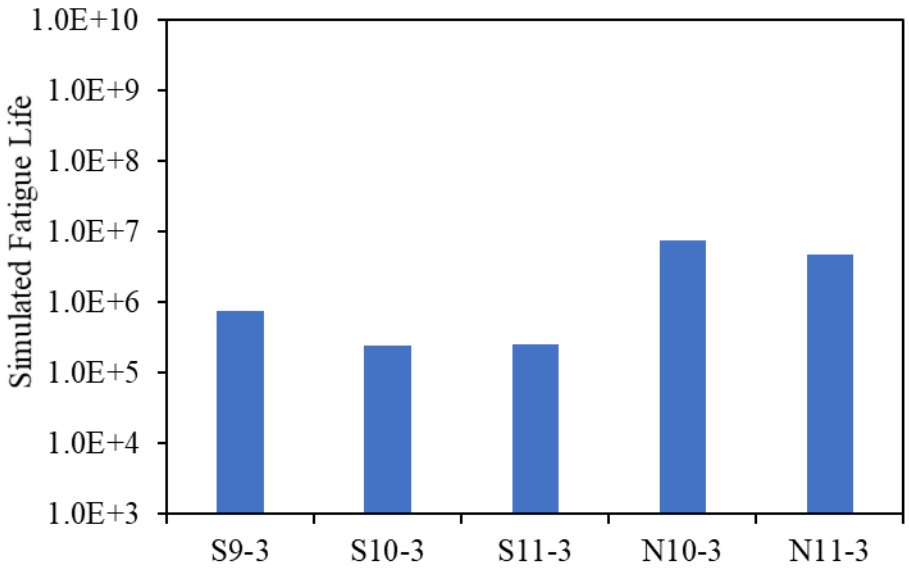

Figure 119. Simulated Fatigue Life Using W_N-N_f Relationship, Flexural Fatigue

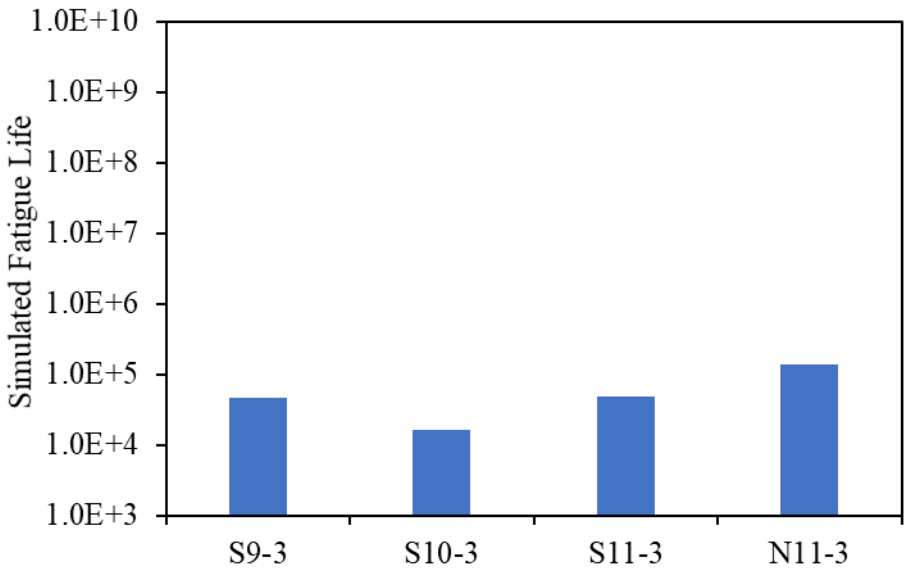

Figure 120. Simulated Fatigue Life Using W_N-N_f Relationship, Uniaxial Fatigue

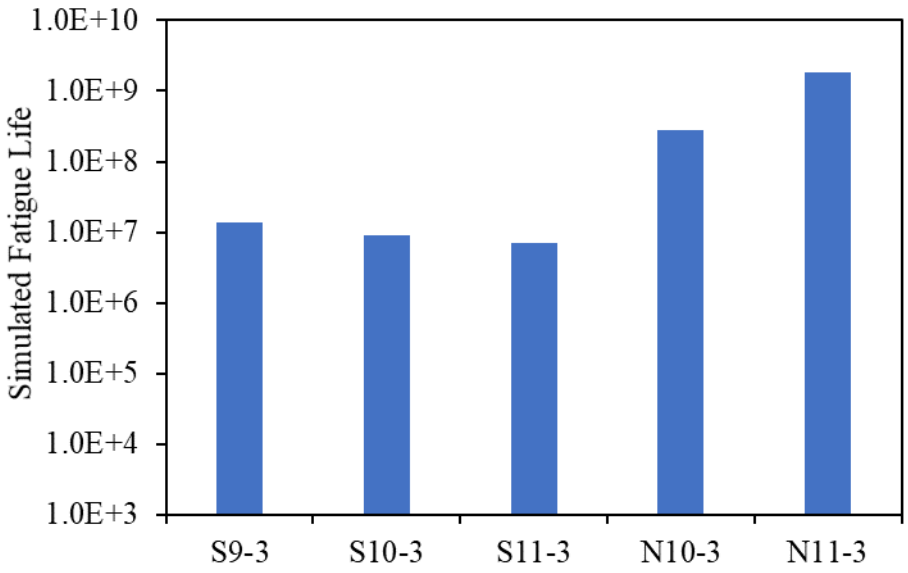

Figure 121. Simulated Fatigue Life Using ε-N_f Relationship, Flexural Fatigue

Figures 122 to 124 exhibit the relationships between the simulated fatigue life and the field transverse cracking. It was observed that the simulated fatigue life based on the DE-N_f relationship

had a strong correlation with the field cracking, regardless of flexural or uniaxial fatigue test. The simulated fatigue life based on the strain-fatigue life relationship had a fair correlation with field cracking, Thus, the relationship between the dissipated energy and fatigue life could be a better method to predict the pavement fatigue performance than the strain-fatigue life relationship.

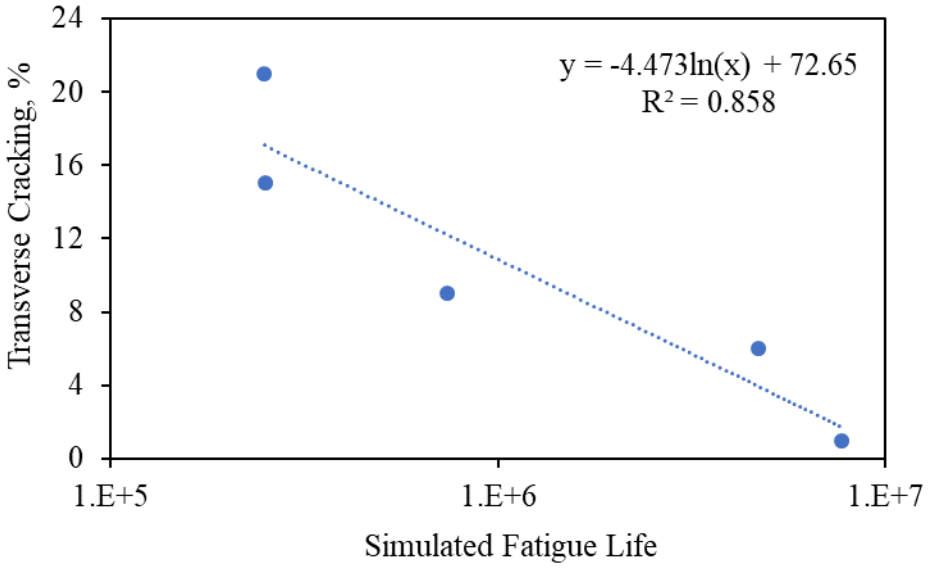

Figure 122. Field Cracking vs. Simulated Fatigue Life by W_N-Flexural N_f Relationship

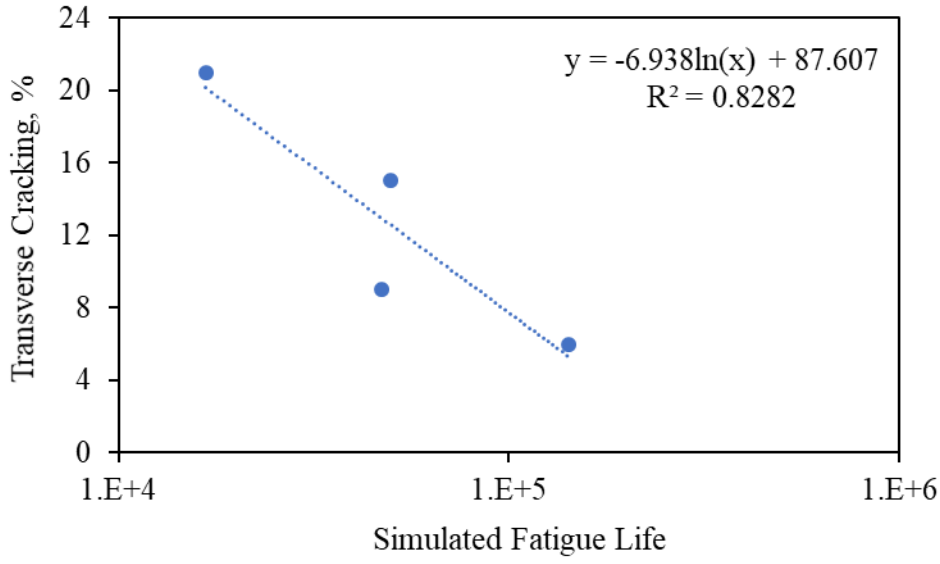

Figure 123. Field Cracking vs. Simulated Fatigue Life by W_N-Uniaxial N_f Relationship

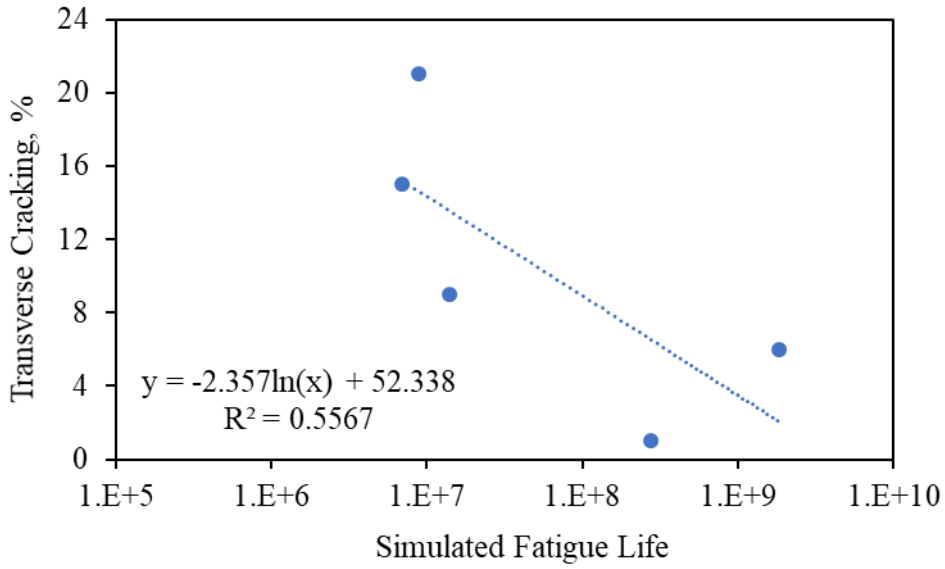

Figure 124. Field Cracking vs. Simulated Fatigue Life by ε-N_f Relationship

8.6 Summary

In this chapter, the relationship between the cracking parameters and the field pavement fatigue performance was investigated using 2009 Group Experiment sections. In addition, the fatigue performance of the test sections was simulated and then compared to the field performance. The following observations can be drawn based on the above analysis:

1) The ranking of five mixes based on binder properties and mix fatigue life from the laboratory tests did not agree with the ranking of the mixes based on the field cracking performance.
2) Based on the analysis of laboratory test results and field performance of the 2009 Group Experiment sections, it was found that laboratory binder properties and mix fatigue performance were important to determine the in-situ pavement fatigue performance.

However, they should be adjusted for the effect of pavement structure stiffness, which can be done through a mechanistic structural analysis.

3) Estimated fatigue life for five sections based on the W_N- N_f relationship exhibited a strong correlation (R^2>0.80) with field transverse cracking number. Compared to the strain-fatigue life relationship, the predicted pavement fatigue life by the W_N- N_f relationship exhibited a better correlation with the field fatigue performance.

CHAPTER 9 – CONCLUSIONS AND RECOMMENDATIONS

The objective of this study was to find another binder property and/or test method for evaluating asphalt binder fatigue property and to investigate the relationships between asphalt binder properties and mix fatigue performance. This study included 16 asphalt binders with common performance grades used in the United States. These binders were used to produce lab mixes for fatigue testing using a 9.5-mm nominal maximum aggregate size gradation with all virgin materials. Binder tests, including dynamic shear rheometer, bending beam rheometer, frequency sweep, and modified linear amplitude sweep, were conducted to determine binder fatigue life, loss modulus, loss tangent, crossover frequency, rheological index, and Glover-Rowe value. Dynamic modulus, uniaxial and flexural fatigue tests were conducted for the asphalt mixtures, and mixture fatigue performance was evaluated through the traditional phenomenological, dissipated energy, and simplified viscoelastic continuum damage methods. Correlations between binder and mix fatigue characteristics were investigated by the generalized linear model. Key findings and conclusions drawn from the results of this study are as follows:

1) Based on the binder and mixture fatigue test results, the polymer modified asphalt binders showed better resistance to fatigue cracking than the unmodified binders. This finding agreed with those from previous studies (Khattak and Baladi, 1998, 2001; Quintus et al., 2007; Willis et al., 2016).
2) The correlations between the binder G*sin (δ), loss tangent, crossover frequency, rheological index, and Glover-Rowe value and the mixture fatigue performance

characteristics were different for polymer modified and unmodified asphalt binders. This is likely attributed to the presence of polymers in the modified asphalt binders.

3) Compared to the other binder properties evaluated in this study, the modified LAS test results showed the best correlation with the laboratory/simulated mixture fatigue performance. This is likely due to the fact that the modified LAS test involves the damage evolution in the binder under repeated loading, which is similar to the process for testing the fatigue resistance of asphalt mixtures.
4) The correlations between mixture test results and the simulated pavement fatigue damage decreased with increasing thickness of the asphalt layer. The asphalt mixtures would last longer at lower tensile strain levels in the laboratory tests. However, the simulated pavement fatigue damage would not change significantly for thicker pavements with lower tensile strains at the bottom of the asphalt layer as the pavement fatigue damage changed from bottom-up to top-down fatigue cracking.
5) Based on the analysis of laboratory test results and field performance of the 2009 Group Experiment sections, it was found that laboratory binder properties and mix fatigue performance were important to determine the in-situ pavement fatigue performance. However, they should be adjusted for the effect of pavement structure stiffness, which can be done through a mechanistic structural analysis.

In this study, all the asphalt binders were PAV aged for 40 hours, and all the mixtures were long-term aged in the loose mix condition for 5 days at 95^{o}C. Other aging conditions should be further evaluated in the future. In addition, mixture testing was conducted for one design aggregate

gradation. Further mixture testing should be done for more aggregate types, sizes and gradations. Furthermore, more field test sections should be used to validate the correlations found in this study.

REFERENCES

Airey, G. D., Rahimzadeh, B., & Collop, A. C. (2004). Linear rheological behavior of bituminous paving materials. Journal of Materials in Civil Engineering, 16(3), 212-220.

Al-Qadi, I. L., Ozer, H., Lambros, J., El Khatib, A., Singhvi, P., Khan, T., ... & Doll, B. (2015). *Testing protocols to ensure performance of high asphalt binder replacement mixes using RAP and RAS*. Illinois Center for Transportation/Illinois Department of Transportation.

Al-Qadi, I. L., Wu, S., Lippert, D. L., Ozer, H., Barry, M. K., & Safi, F. R. (2017). Impact of high recycled mixed on HMA overlay crack development rate. Road Materials and Pavement Design, 18(sup4), 311-327.

Anderson, R. M., King, G. N., Hanson, D. I., & Blankenship, P. B. (2011). Evaluation of the relationship between asphalt binder properties and non-load related cracking. *Journal of the Association of Asphalt Paving Technologists*, 80.

Anderson, R. M. *Asphalt Mixture Characteristics Affecting Durability Cracking*. 2014. http://pavement.engineering.asu.edu/wordpress/wp-content/uploads/2014/12/15-AsphaltMixtureCharacteristicsAffectingDurabilityCracking-Anderson.pdf.

Bahia, H. U., Hanson, D. I., Zeng, M., Zhai, H., Khatri, M. A., & Anderson, R. M. (2001). *Characterization of modified asphalt binders in superpave mix design* (No. Project 9-10 FY'96).

Balbissi, A.H. (1983). *A comparative Analysis of the Fracture and Fatigue Properties of Asphalt Concrete and Sulphex*, Ph.D. Dissertation, Texas A&M University, College Station, TX.

Bennert, T., & Maher, A. (2008). Field and laboratory evaluation of a reflective crack interlayer in New Jersey. *Transportation Research Record: Journal of the Transportation Research Board*, (2084), 114-123.

Corrigan, M. (2016). REOB: ETG Status and Emerging Knowledge. https://engineering.purdue.edu/~ncaupg/Activities/2016/presentations/Corrigan_REOB_NCAUPG_Mar2016.pdf. (accessed July 1, 2018).

Daniel, J. S., & Kim, Y. R. (2001). Laboratory evaluation of fatigue damage and healing of asphalt mixtures. *Journal of Materials in Civil Engineering*, 13(6), 434-440.

Daniel, J. S., & Kim, Y. R. (2002). Development of a simplified fatigue test and analysis procedure using a viscoelastic, continuum damage model (with discussion). *Journal of the Association of Asphalt Paving Technologists*, 71.

Deacon, J. A., Harvey, J. T., Tayebali, A., & Monismith, C. L. (1997). Influence of binder loss modulus on the fatigue performance of asphalt concrete pavements. *Journal of the Association of Asphalt Paving Technologists*, 66, 633-668.

Elwardany, M. D., Yousefi Rad, F., Castorena, C., & Kim, Y. R. (2017). Evaluation of asphalt mixture laboratory long-term ageing methods for performance testing and prediction. *Road Materials and Pavement Design*, 18(sup1), 28-61.

Gibson, N., Qi, X., Shenoy, A., Al-Khateeb, G., Kutay, M. E., Andriescu, A., ... & Harman, T. (2012). *Performance testing for Superpave and structural validation* (No. FHWA-HRT-11--45).

Goodrich, J. L. (1991). Asphaltic binder rheology, asphalt concrete rheology and asphalt concrete mix properties (with discussion). *Journal of the Association of Asphalt Paving Technologists*, 60.

Hintz, C., Velasquez, R., Johnson, C., & Bahia, H. (2011). Modification and validation of linear amplitude sweep test for binder fatigue specification. *Transportation Research Record: Journal of the Transportation Research Board*, (2207), 99-106.

Khattak, M., & Baladi, G. (1998). Engineering properties of polymer-modified asphalt mixtures. *Transportation Research Record: Journal of the Transportation Research Board*, (1638), 12-22.

Khattak, M., & Baladi, G. (2001). Fatigue and permanent deformation models for polymer-modified asphalt mixtures. *Transportation Research Record: Journal of the Transportation Research Board*, (1767), 135-145.

Johnson, C. M., Bahia, H. U., & Wen, H. (2007, September). *Evaluation of strain-controlled asphalt binder fatigue testing in the dynamic shear rheometer*. In Proceedings of the 4th International SIIV Congress (pp. 1-11).

Little, D. N., Lytton, R. L., Williams, D., & Chen, C. W. (2001). *Microdamage healing in asphalt and asphalt concrete, Volume 1: microdamage and microdamage healing, project summary report* (No. FHWA-RD-98-141). Turner-Fairbank Highway Research Center.

Mannan, U. A., Islam, M. R., & Tarefder, R. A. (2015). Effects of recycled asphalt pavements on the fatigue life of asphalt under different strain levels and loading frequencies. *International Journal of Fatigue*, 78, 72-80.

Moore, N. (2016). *Evaluation of Laboratory Cracking Tests Related to Top-Down Cracking in Asphalt Pavements*. Master Thesis, Auburn University, Auburn, AL.

Kim, Y.R. (1988). *Evaluation of Healing and Constitutive modeling of Asphalt Concrete by Means of the Theory of Nonlinear Viscoelasticity and Damage Mechanics*, Ph.D Dissertation, Texas A&M University, College Station, Texas.

Kim, Y. R., Little, D. N., & Benson, F. C. (1990). Chemical and mechanical evaluation on healing mechanism of asphalt concrete (with discussion). *Journal of the Association of Asphalt Paving Technologists*, 59.

Roque, R., Birgisson, B., Drakos, C., & Dietrich, B. (2004). Development and field evaluation of energy-based criteria for top-down cracking performance of hot mix asphalt (with discussion). *Journal of the Association of Asphalt Paving Technologists*, 73.

Roque, R., Zou, J., Kim, Y. R., Baek, C., Thirunavukkarasu, S., Underwood, B.S. and Guddati, M. N. (2010). NCHRP Web-only document 162: *Top-Down Cracking of Hot-Mix Asphalt Layers: Models for Initiation and Propagation*.

Rowe, G. M. (1996). *Application of the Dissipated Energy Concept to Fatigue Cracking in Asphalt Pavements*. Ph.D. thesis, University of Nottingham.

Shen, S. (2006). *Dissipated Energy Concepts for HMA Performance: Fatigue and Healing*, Ph.D. Dissertation, University of Illinois at Urbana-Champaign, Urbana, Ill.

Shen, S., Airey, G. D., Carpenter, S. H., & Huang, H. (2006). A dissipated energy approach to fatigue evaluation. *Road materials and pavement design*, 7(1), 47-69.

Si, Z., Little, D. N., & Lytton, R. L. (2002). Characterization of microdamage and healing of asphalt concrete mixtures. *Journal of materials in civil engineering*, 14(6), 461-470.

Stuart, K.D., Mogawer, W.S., & Romero, P. (2001). *Validation of the Superpave Asphalt Binder Fatigue Cracking Parameter Using the FHWA's Accelerated Loading Facility* (No. FHWA-01-093).

Tayebali, A. A., Deacon, J. A., Coplantz, J. S., Harvey, J. T., & Monismith, C. L. (1994). *Fatigue Response of Asphalt-Aggregate Mixes: Part I Test Method Selection* (No. SHRP A-404).

Tayebali, A. A., Deacon, J. A., Coplantz, J. S., Finn, F. N., & Monismith, C. L. (1994). *Fatigue Response of Asphalt-Aggregate Mixes: Part II Extended Test Program* (No. SHRP A-404).

Timm, D. H., West, R. C., & Taylor, A. J. (2016). Performance and Fatigue Analysis of High Reclaimed Asphalt Pavement Content and Warm-Mix Asphalt Test Sections. *Transportation Research Record: Journal of the Transportation Research Board*, (2575), 196-205.

Tran, N., Turner, P., and Shambley, J. (2016). *Enhanced Compaction to Improve Durability and Extend Pavement Service Life: A Literature Review*. NCAT Report 16-02R.

Tsai, B. W., Monismith, C. L., Dunning, M., Gibson, N., D'Angelo, J., Leahy, R., ... & Jones, D. (2005). Influence of asphalt binder properties on the fatigue performance of asphalt concrete pavements. *Journal of the Association of Asphalt Paving Technologists*, 74, 733-789.

Underwood, B. S., Kim, Y. R., & Guddati, M. N. (2010). Improved calculation method of damage parameter in viscoelastic continuum damage model. *International Journal of Pavement Engineering*, 11(6), 459-476.

University of California, Berkeley, Asphalt Research Program, and Institute of Transportation Studies. (1994). *Fatigue Response of Asphalt-Aggregate Mixes, Report SHRP-404*, Washington, D.C.: National Research Council, Strategic Highway Research Program.

Vargas-Nordcbeck, A., & Timm, D. H. (2012). Rutting characterization of warm mix asphalt and high RAP mixtures. *Road Materials and Pavement Design*, 13(sup1), 1-20.

Velasquez, R., Tabatabaee, H., & Bahia, H. (2011). Low temperature cracking characterization of asphalt binders by means of the single-edge notch bending (SENB) test. *Journal of the Association of Asphalt Paving Technologists*, 80, 583.

Von Quintus, H., Mallela, J., & Buncher, M. (2007). Quantification of effect of polymer-modified asphalt on flexible pavement performance. *Transportation Research Record: Journal of the Transportation Research Board*, (2001), 141-154.

Vrtis, M. (2017). *Investigation of Deflection Basins to Identify Structural Distresses within Flexible Pavements*. Ph.D. Dissertation, Auburn University, Auburn, AL.

Willis, J. R., Timm, D. H., & Kluttz, R. (2016). Performance of a highly polymer-modified asphalt binder test section at the national center for asphalt technology pavement test track. *Transportation Research Record: Journal of the Transportation Research Board*, (2575), 1-9.

Xie, Z. Turner, P., Taylor, A., Tran, N., and McCurdy, A. (2018). Laboratory Evaluation of Performance Properties of Asphalt Binders and Mixes Containing a New Rejuvenator, *Journal of Association of Asphalt Paving Technologists*, 86, 2018, in process.

Yoo, P. J., & Al-Qadi, I. L. (2008). The truth and myth of fatigue cracking potential in hot-mix asphalt: Numerical analysis and validation. *Journal of Association of Asphalt Paving Technologists*, 77, 549.

Zhang, J., Sabouri, M., Guddati, M. N., & Kim, Y. R. (2013). Development of a failure criterion for asphalt mixtures under fatigue loading. *Road Materials and Pavement Design*, 14(sup2), 1-15.

Zhou, F., Hu, S., & Scullion, T. (2007). Development and verification of the overlay tester based fatigue cracking prediction approach (No. FHWA/TX-07/9-1502-01-8).

APPENDIX A. Flexural Fatigue Data

Table 34. Bending Beam Fatigue Test Data at 20°C

Binder ID	Air Voids (%)	Micro-strain	Initial Stiffness (MPa)	Fatigue Cycles	Coefficient of Variation, %
B3	6.3	1000	5,495	12,196	28
	6.0	1000	6,134	14,412	
	7.3	1000	5,232	8,128	
	6.3	500	6,439	844,630	35
	6.0	500	6,429	683,911	
	6.4	500	6,738	1,320,788	
B4	6.4	900	4,522	45,972	15
	6.8	900	4,575	35,789	
	6.3	900	4,620	36,307	
	5.4	700	4,928	118,394	
	6.2	500	4,535	1,562,248	54
	6.7	500	4,947	2,249,486	
	7.2	500	4,930	643,181	
B6	6.3	1300	2,103	96,605	31
	6.9	1300	2,118	50,118	
	7.0	1300	1,950	75,422	
	6.5	1000	2,152	248,313	
	6.9	900	1,990	310,217	
	7.4	800	2,199	1,379,060	
B7	7.7	700	4,801	35,995	8
	7.4	700	4,842	37,692	
	6.7	700	4,484	41,686	
	7.4	400	5,156	1,024,275	18
	7.5	400	5,135	761,494	
	7.7	400	5,151	1,079,775	
B8	8.3	800	4,279	41,807	37
	7.9	800	4,324	37,800	
	7.0	800	4,769	18,999	
	6.8	800	4,747	35,075	
	6.9	400	5,722	1,496,235	30
	7.2	400	5,204	2,791,472	
	6.5	400	5,408	2,405,747	
B11	7.6	700	5,734	7,542	
	6.9	500	6,791	12,919	23
	7.3	500	6,731	17,885	
	6.7	300	7,288	870,963	54

	7.1	300	6,864	1,865,663	
	6.8	300	7,935	724,435	
B13	6.8	1300	2,111	33,400	74
	7.9	1300	1,717	106,332	
	6.0	1200	2,216	67,413	
	6.4	1000	2,384	147,910	
	6.9	800	2,823	243,594	
	7.9	700	2,376	1,839,006	61
	7.0	700	2,552	4,663,908	
B15	6.7	1200	2,238	103,117	28
	7.5	1200	2,027	68,984	
	7.1	1000	2,200	129,817	
	6.1	800	2,800	404,265	
	6.1	700	2,636	1,547,331	25
	6.9	700	2,832	1,090,184	
B16	7.2	600	6876	12882	
	7.5	500	6712	73493	33
	6.6	500	8424	117489	
	6.7	400	6984	197242	19
	7.0	400	7535	258027	
	7.4	300	6595	9172759	

Table 35. Bending Beam Fatigue Test Data at 10°C

Binder ID	Air Voids (%)	Micro-strain	Initial Stiffness (MPa)	Fatigue Cycle	Coefficient of Variation, %
B3	7.6	800	8,747	16,453	57
	6.9	800	9,240	6,985	
	7.0	600	9,916	24,126	50
	6.8	600	9,786	50,118	
	5.8	400	9,767	271,227	
	7.1	350	10,137	2,686,375	
	7.8	300	9,574	11,953,635	
B4	7.2	700	8,045	12,022	
	6.4	600	7,804	18,620	20
	6.4	600	8,382	24,759	
	6.8	400	7,812	121,618	
	7.0	300	7,744	2,293,066	25
	6.3	300	8,332	3,301,794	
B6	6.9	700	4,960	38,128	68
	7.6	700	4,128	245,470	
	7.3	700	4,658	257,039	
	6.5	500	5,311	386,070	63
	7.3	500	4,212	1,957,341	
	6.8	500	5,132	1,703,138	
	6.6	400	5,482	8,785,166	
B7	7.6	600	8,163	18,460	71
	7.3	600	7,774	23,850	
	7.3	600	6,903	64,379	
	7.1	400	7,873	159,098	
	7.3	350	8,472	653,130	41
	7.3	350	8,377	358,921	
B8	6.7	600	8,933	18,674	40
	6.8	600	9,364	7,943	
	7.3	600	8,981	17,478	
	7.7	500	8,620	61,129	
	7.1	400	8,393	331,131	77
	7.7	400	9,087	103,117	
	7.3	400	9,505	92,789	
	7.0	300	9,375	4,000,214	
	7.7	500	8,620	61,129	

B11	6.6	450	9494	6456	25
	6.9	450	8904	9278	
	7.4	400	8945	69783	
	6.6	300	9386	560187	20
	7.1	300	11485	841395	
	6.5	300	10799	727221	
B13	7.7	1000	4,676	4,623	
	6.8	900	5,041	8,912	11
	6.7	900	4,933	7,585	
	7.2	800	4,563	11,988	
	6.5	600	5,774	47,315	60
	6.5	600	5,768	19,109	
	6.8	400	6,123	591,107	17
	6.8	400	6,321	755,672	
B15	6.0	700	6,434	78,072	58
	7.0	700	6,532	29,427	
	6.0	700	6,784	33,304	
	6.3	500	6,498	670,913	64
	6.9	500	6,304	255,074	
	6.2	400	6,583	6,715,577	
B16	7.0	500	9143	6594	
	7.0	400	10383	144543	8
	7.8	400	12329	129817	
	7.0	300	9225	176468	41
	6.9	300	10048	264038	
	7.4	300	10091	407380	

APPENDIX B. Uniaxial Fatigue Data

Table 36. Uniaxial Fatigue Test Data

Binder ID	Testing Temperature	Air Voids (%)	N_f	G^R
B1	30°C	6.5	9.3E+04	1.1E+01
		6.7	3.7E+03	5.1E+02
		7.2	1.1E+04	1.8E+02
		6.9	4.4E+03	4.4E+02
	36°C	6.6	1.8E+04	9.3E+01
		6.9	7.1E+04	1.1E+01
		7.1	2.0E+04	7.7E+01
		7.1	1.2E+04	1.6E+02
B2	21°C	6.5	2.3E+05	4.2E+00
		6.5	8.1E+04	2.5E+01
		6.5	9.0E+03	4.5E+02
	27°C	6.7	1.2E+05	5.2E+00
		7.6	2.1E+05	3.9E+00
		7.0	1.3E+04	1.5E+02
B3	15°C	6.7	5.2E+04	2.6E+01
		6.7	3.6E+03	1.5E+03
		6.7	3.7E+03	4.4E+02
	21°C	6.9	5.3E+04	1.1E+01
		6.6	2.6E+04	7.4E+01
		6.5	2.0E+04	1.3E+02
		6.8	7.3E+03	4.2E+02
	27°C	6.7	1.7E+04	7.8E+01
		6.6	4.2E+03	7.3E+02
B4	15°C	7.1	9.4E+03	1.8E+02
		7.3	3.2E+03	1.1E+03
		7.1	8.6E+04	1.4E+01
	21°C	7.3	9.6E+03	3.0E+02
		7.2	4.7E+03	1.1E+03
		7.1	1.1E+04	2.0E+02
B5	21°C	7.1	7.6E+03	1.6E+02
		7.3	5.2E+04	3.4E+01
		7.1	1.7E+03	2.5E+03
	27°C	7.3	1.7E+04	1.1E+02
		7.5	1.2E+04	2.6E+02
		7.3	8.9E+03	4.5E+02

B6	24°C	6.7	1.2E+05	5.9E+00
		6.5	3.5E+04	3.6E+01
		6.5	1.2E+04	1.4E+02
	30°C	6.9	5.5E+03	3.7E+02
		7.1	1.8E+03	1.7E+03
B7	12°C	6.5	4.1E+03	7.8E+02
		7.1	1.5E+04	7.6E+01
	18°C	6.9	8.9E+03	1.4E+02
		7.0	3.0E+03	9.2E+02
		6.8	4.0E+04	2.8E+01
		7.5	1.5E+04	9.6E+01
B8	12°C	6.5	2.8E+04	3.6E+01
		6.9	7.0E+03	2.3E+02
		6.8	1.5E+03	1.4E+03
		7.3	5.9E+03	1.8E+02
	18°C	6.5	2.0E+03	1.9E+03
		6.5	1.3E+04	1.4E+02
		6.5	5.1E+04	2.5E+01
	24°C	7.2	1.5E+04	1.4E+02
		7.1	3.9E+03	8.2E+02
		7.0	1.9E+03	1.8E+03
B9	19.5°C	7.4	1.7E+03	1.4E+03
		7.2	4.1E+03	3.5E+02
		6.9	5.5E+04	1.2E+01
	25.5°C	6.8	1.1E+04	1.0E+02
		7.2	3.4E+03	5.5E+02
		7.0	5.0E+04	1.7E+01
B10	24°C	6.7	6.9E+03	4.9E+02
		7.2	5.5E+04	2.1E+01
		7.3	1.1E+04	1.4E+02
	30°C	6.5	9.2E+04	1.5E+01
		7.4	2.0E+04	7.6E+01
		6.6	7.8E+03	2.5E+02
B11	21°C	7.5	1.2E+03	3.5E+03
		7.3	1.9E+03	1.2E+03
		7.7	1.2E+04	8.1E+01
	27°C	7.3	9.9E+03	3.3E+02
		7.6	1.1E+03	3.4E+03

		7.4	1.3E+04	7.6E+01
B12	27°C	7.2	3.2E+03	5.9E+02
		6.9	2.5E+03	4.3E+02
	33°C	7.2	1.8E+03	8.0E+02
		7.2	5.7E+03	1.4E+02
		7.1	7.5E+04	4.5E+00
B13	6°C	6.8	3.9E+04	2.4E+01
		7.1	2.3E+03	1.3E+03
		6.8	2.5E+03	1.1E+03
	12°C	7.0	3.5E+04	3.4E+01
		6.7	1.9E+03	2.7E+03
		6.8	1.3E+04	3.2E+02
	18°C	6.8	1.6E+04	7.9E+01
		6.8	8.7E+03	3.7E+02
		7.0	5.4E+03	9.8E+02
		7.1	1.8E+04	1.0E+02
B14	12°C	7.6	2.3E+03	1.4E+03
		7.4	8.4E+03	1.9E+02
		7.0	5.0E+04	1.5E+01
	18°C	7.2	3.8E+03	4.1E+02
		7.2	1.9E+04	5.1E+01
		7.3	2.5E+03	1.3E+03
B15	9°C	7.6	1.1E+04	2.0E+02
		7.2	4.4E+03	4.6E+02
		7.1	2.7E+04	2.4E+01
	15°C	6.8	1.4E+04	3.6E+02
		6.9	6.1E+03	8.5E+02
		7.1	1.4E+03	3.9E+03
B16	21°C	7.5	4.1E+03	8.0E+02
		7.4	9.3E+03	2.1E+02
	27°C	7.6	1.6E+04	9.8E+01
		7.3	4.2E+03	6.4E+02
		7.4	2.1E+03	1.5E+03

APPENDIX C. Damage Evolution in FlexPAVE Simulation

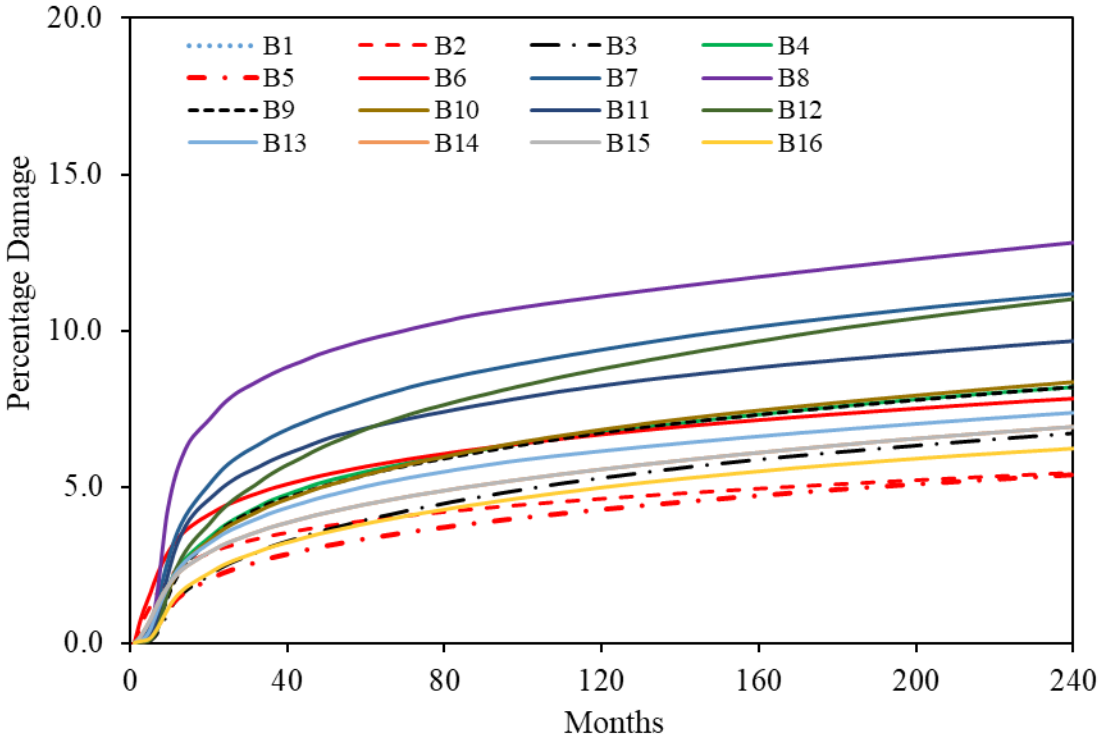

Figure 125. Damage Evolution for 4-inch Pavement in MN

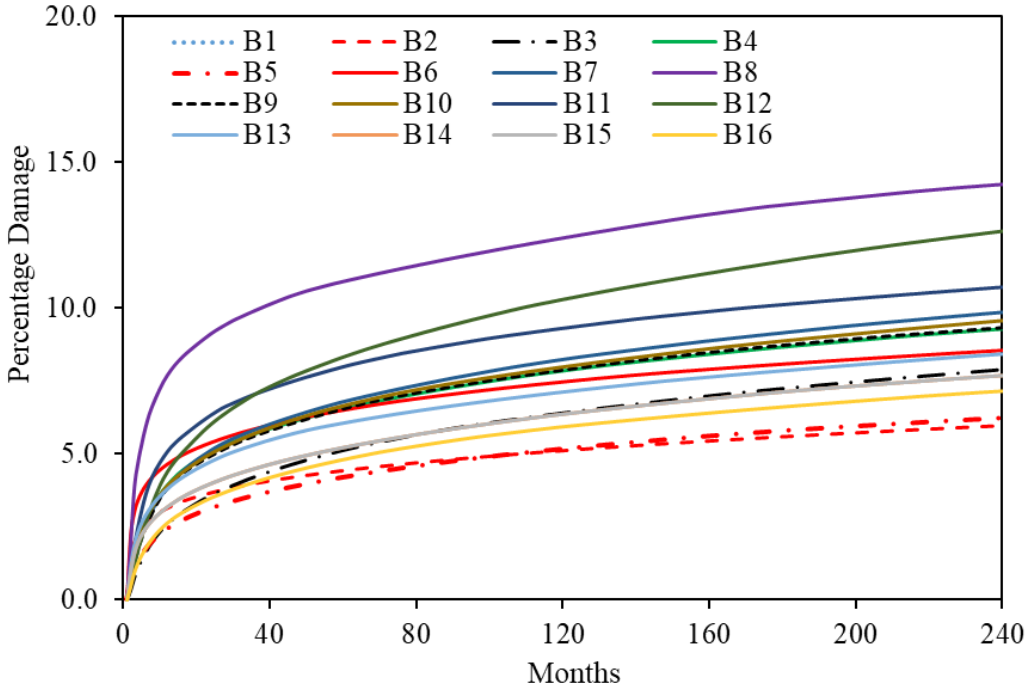

Figure 126. Damage Evolution for 4-inch Pavement in FL

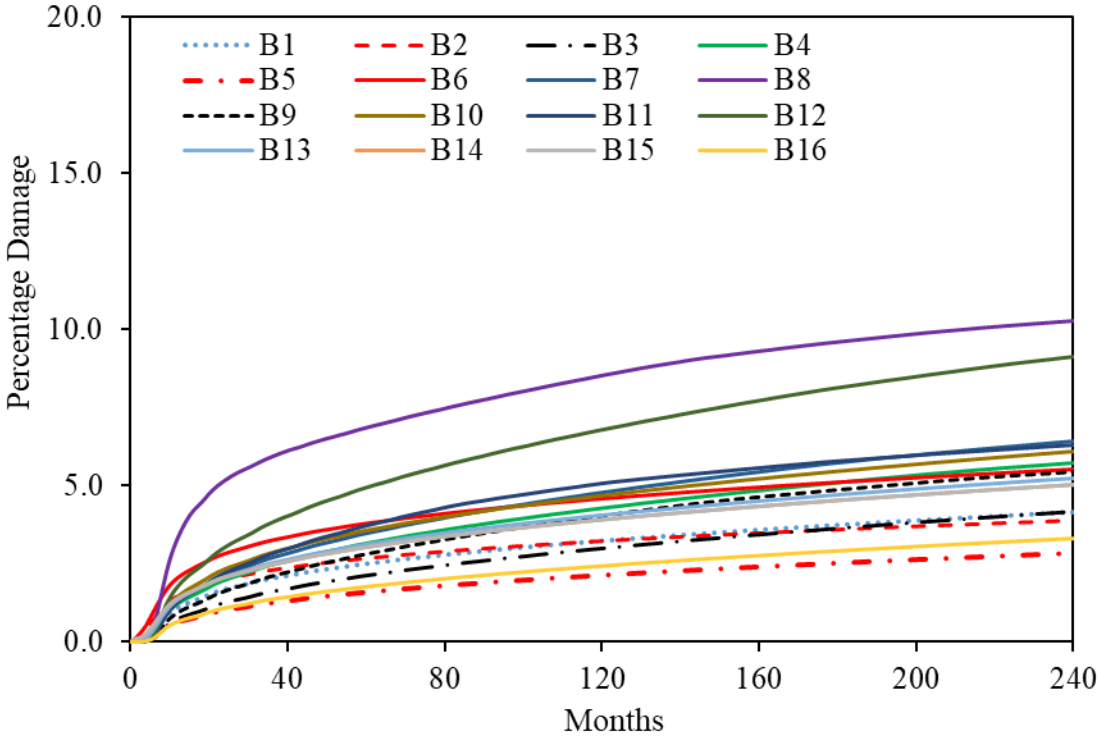

Figure 127. Damage Evolution for 6-inch Pavement in MN

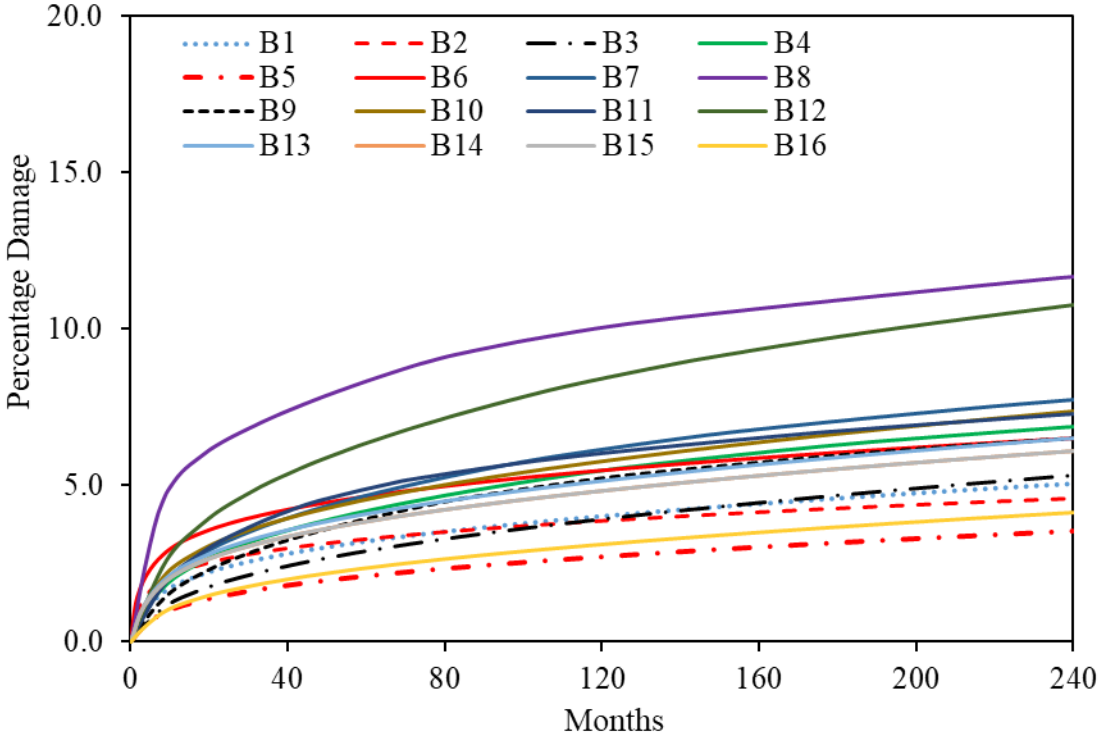

Figure 128. Damage Evolution for 6-inch Pavement in FL

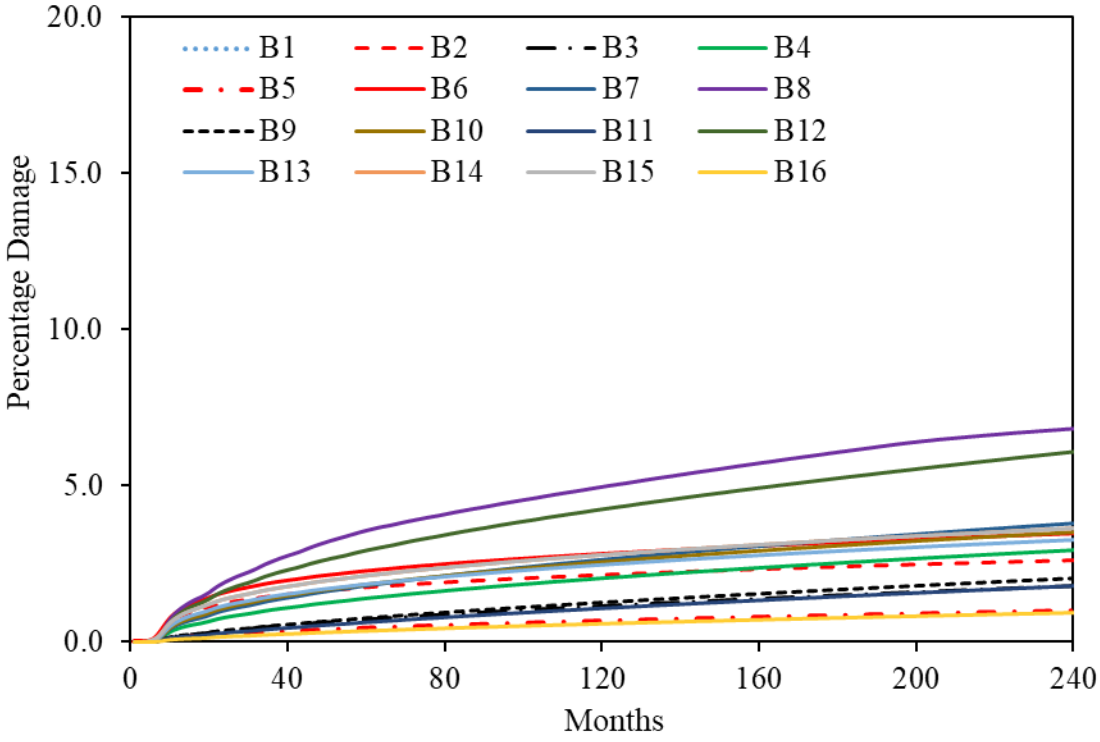

Figure 129. Damage Evolution for 10-inch Pavement in MN

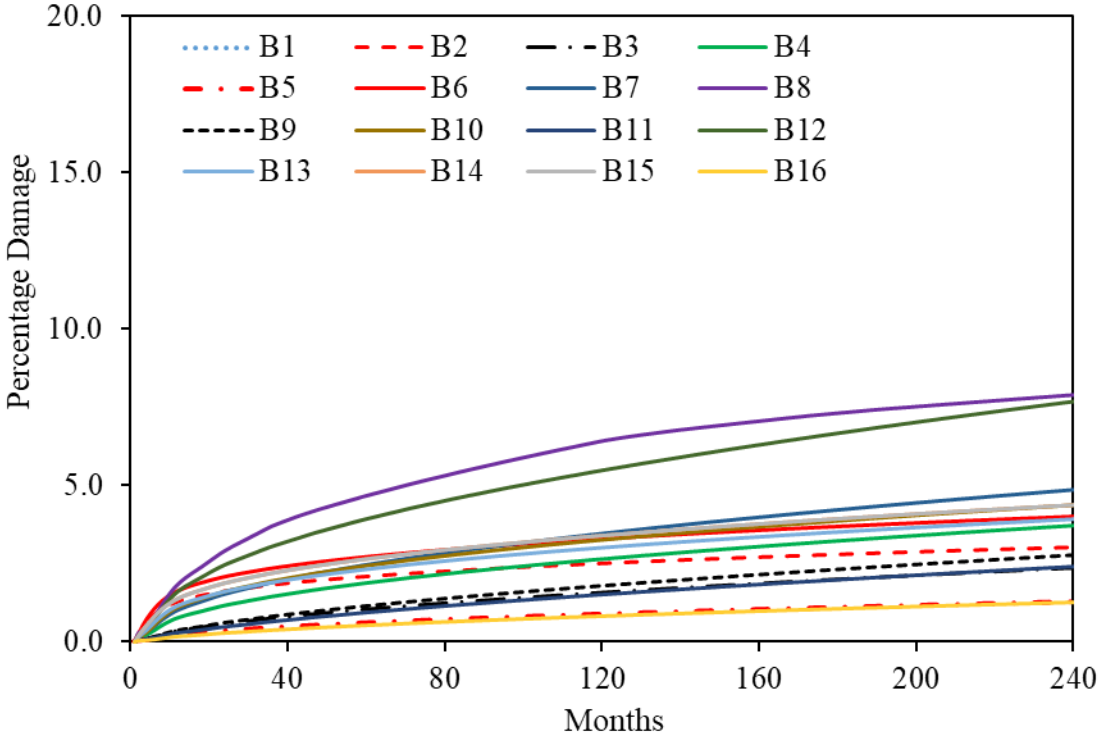

Figure 130. Damage Evolution for 10-inch Pavement in FL

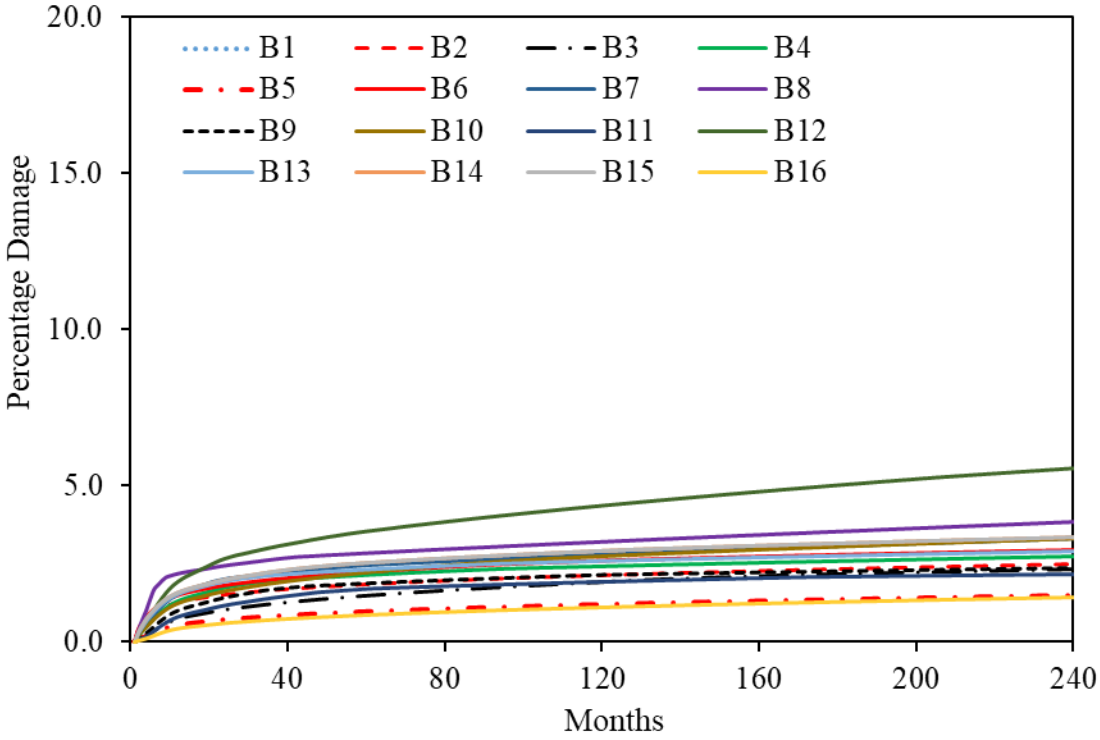

Figure 131. Damage Evolution for 15-inch Pavement in FL

APPENDIX D. Binder Property Parameters

Table 37. PAV-Aged Binder Property Parameters

Parameters		B1	B2	B3	B4	B5	B6	B7	B8	B9	B10	B11	B12	B13	B14	B15	B16
G*sin(δ)	10°C	21624	4403	21597	11275	15283	6307	15989	18207	20650	18161	22597	21655	7869	21233	6636	21180
	20°C	7871	1549	7517	3350	5943	1903	4743	7136	7807	7088	9309	10038	3111	6423	1952	8450
Loss Tangent	15°C	0.54	0.55	0.58	0.70	0.52	0.63	0.72	0.53	0.52	0.48	0.49	0.41	0.53	0.50	0.76	0.51
ωc		4.2E-02	1.3E-04	8.6E-06	1.8E-01	4.4E-03	2.6E-05	2.3E+00	4.6E-02	4.2E-02	4.7E-04	8.7E-03	1.6E-04	1.8E-02	2.7E+00	3.1E-01	6.6E-03
R		2.45	3.21	2.29	2.32	2.65	2.56	2.1	2.65	2.49	2.91	2.58	3.06	3.14	2.1	2.28	2.44
G-R	15°C	428	344	465	119	824	560	56	521	459	1731	1234	3511	302	51	84	1120

APPENDIX E. Backcalculated Modulus versus Mid-Depth Temperature

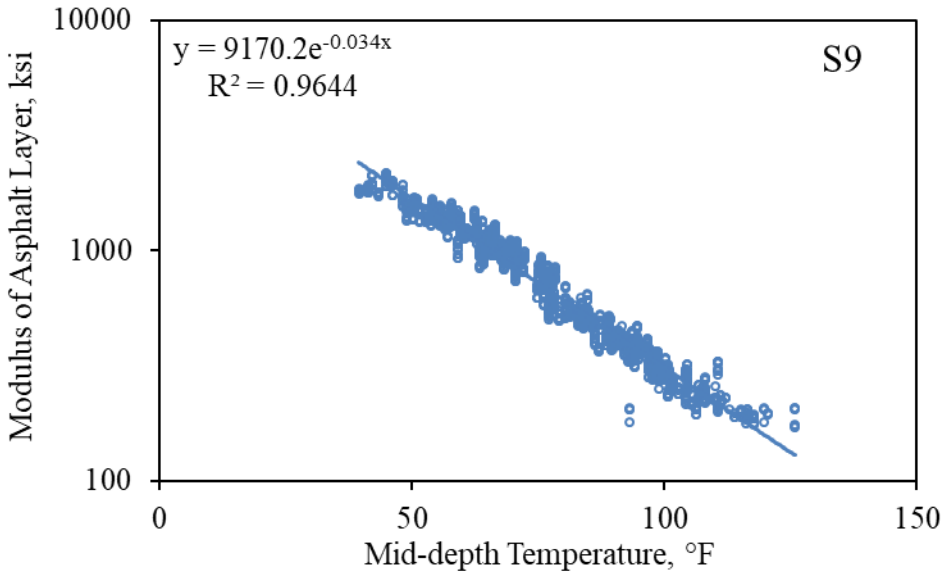

Figure 132. Backcalculated AC Modulus vs. Mid-depth Temperature, S9

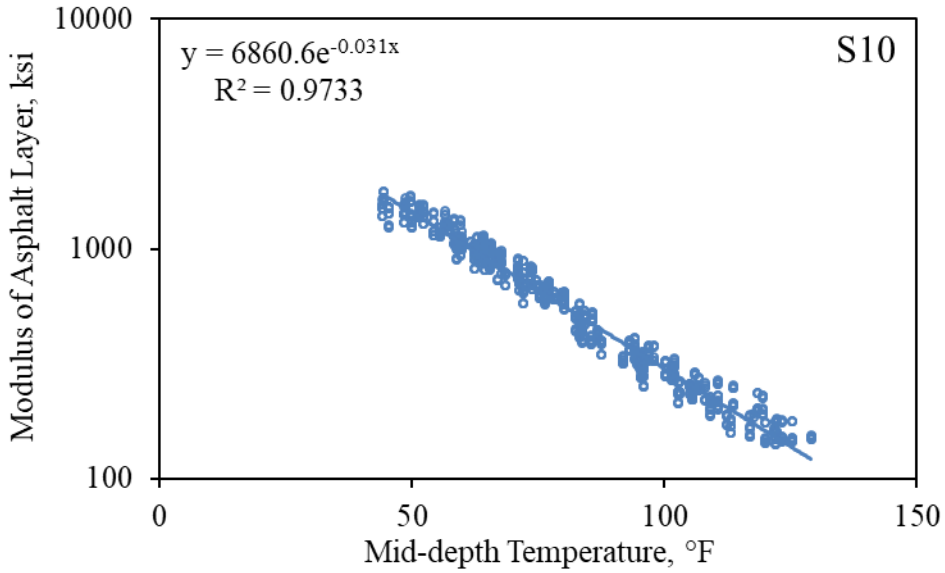

Figure 133. Backcalculated AC Modulus vs. Mid-depth Temperature, S10

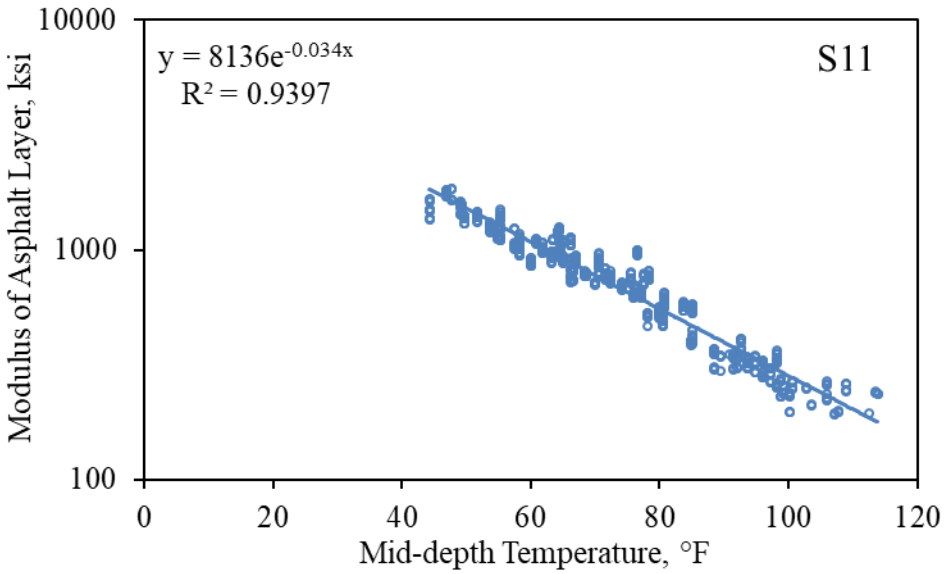

Figure 134. Backcalculated AC Modulus vs. Mid-depth Temperature, S11

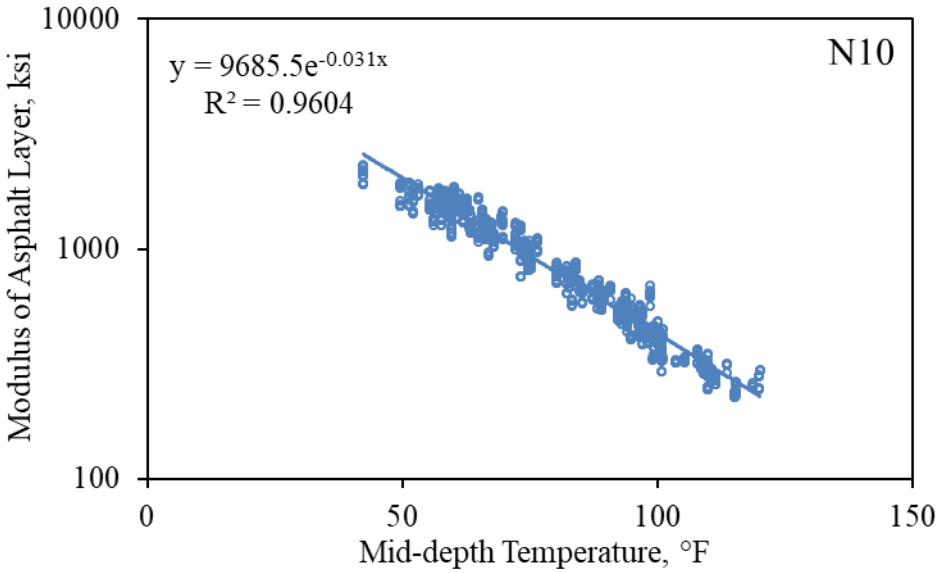

Figure 135. Backcalculated AC Modulus vs. Mid-depth Temperature, N10

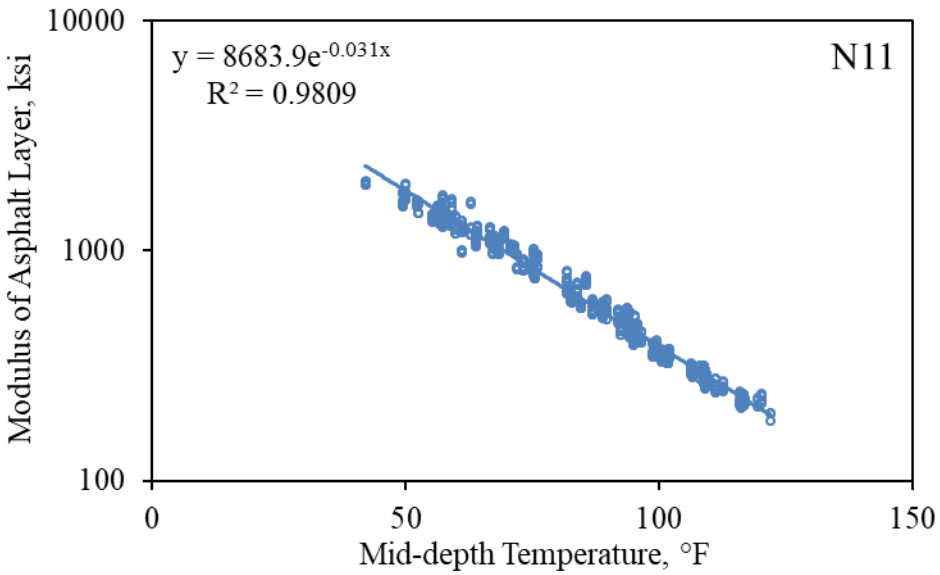

Figure 136. Backcalculated AC Modulus vs. Mid-depth Temperature, N11

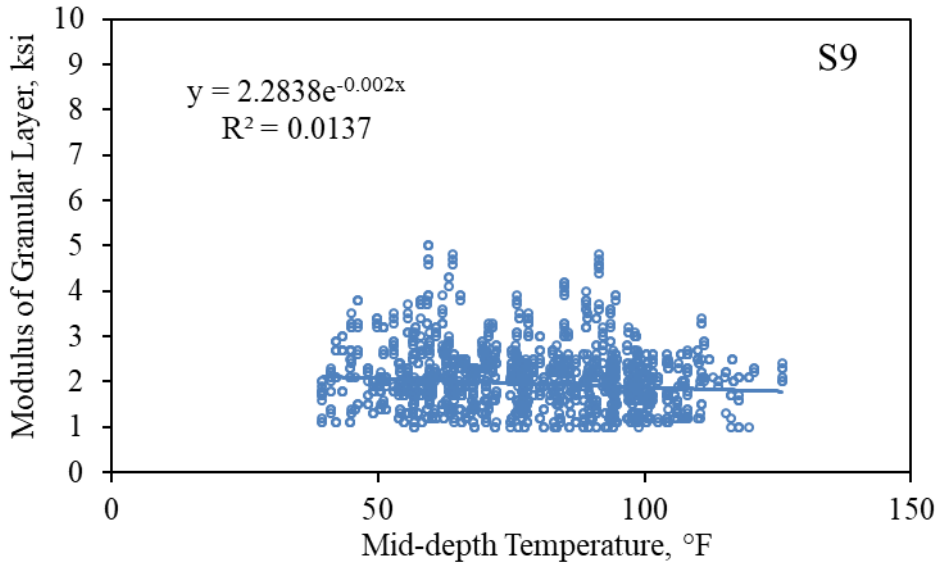

Figure 137. Backcalculated Modulus of Granular Layer vs. Mid-depth Temperature, S9

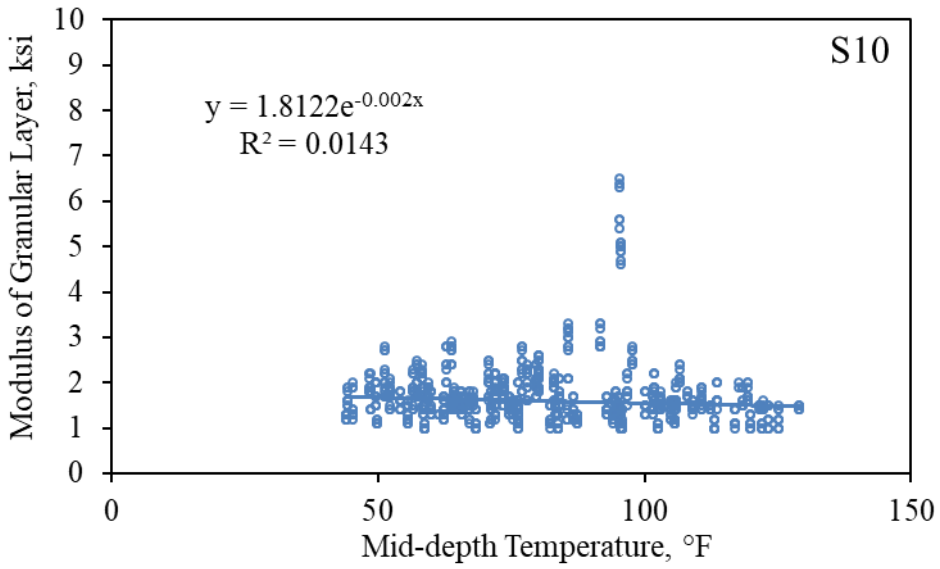

Figure 138. Backcalculated Modulus of Granular Layer vs. Mid-depth Temperature, S10

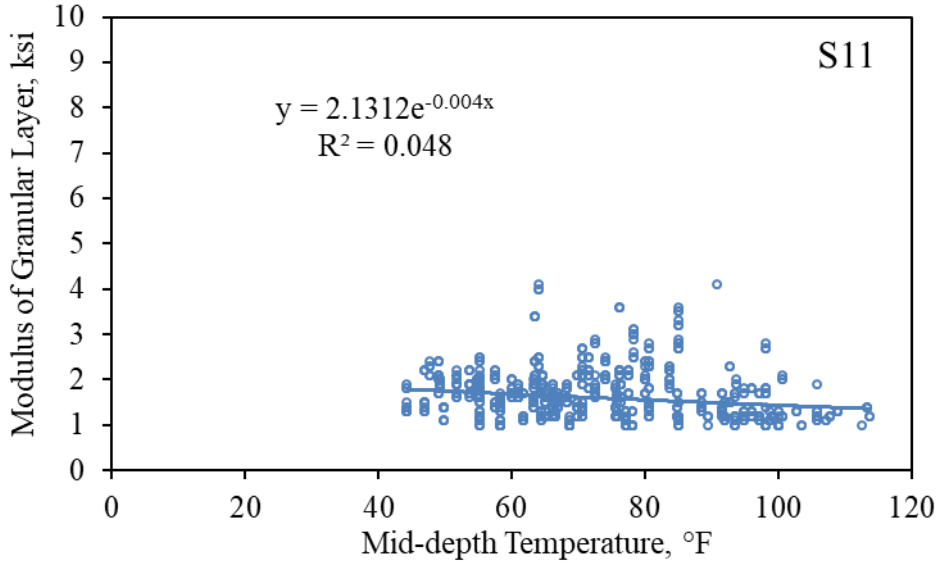

Figure 139. Backcalculated Modulus of Granular Layer vs. Mid-depth Temperature, S11

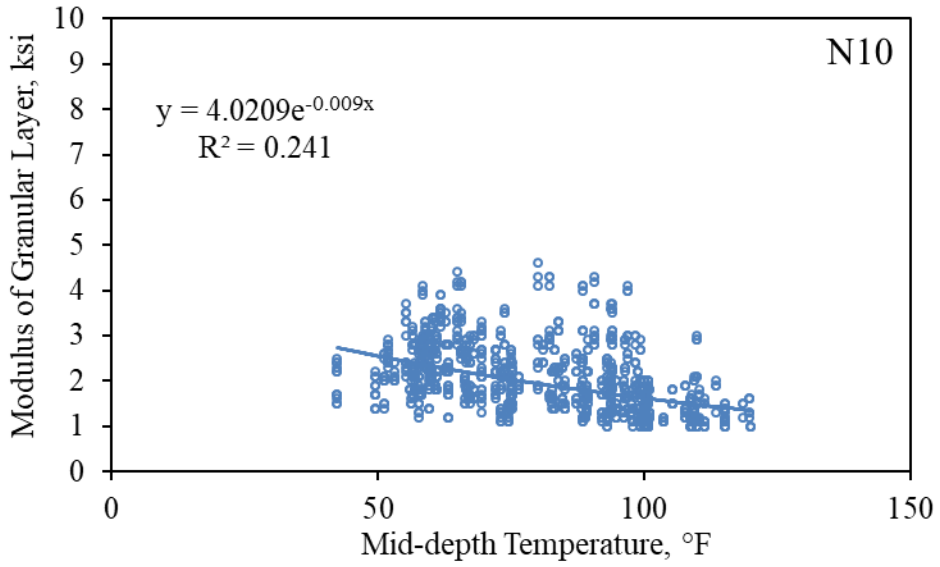

Figure 140. Backcalculated Modulus of Granular Layer vs. Mid-depth Temperature, N10

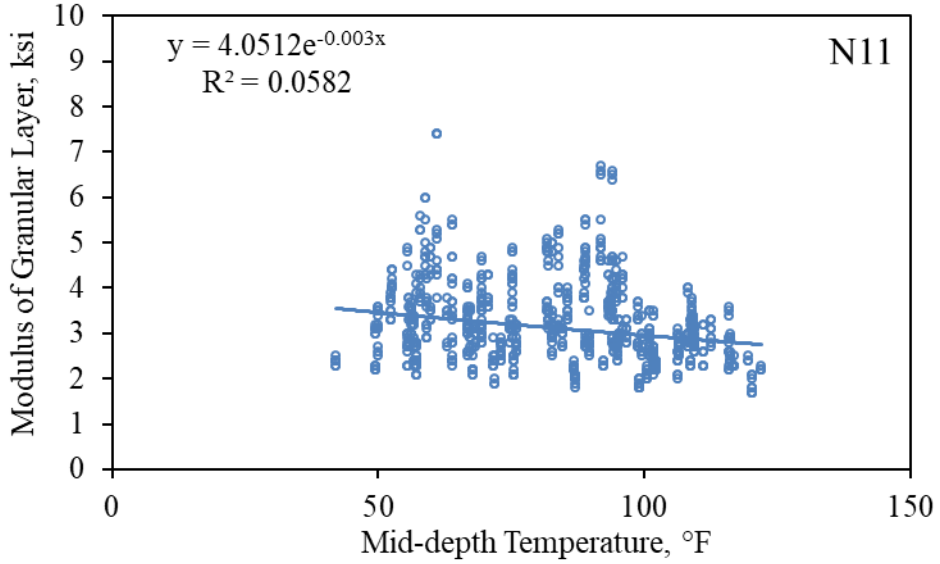

Figure 141. Backcalculated Modulus of Granular Layer vs. Mid-depth Temperature, N11

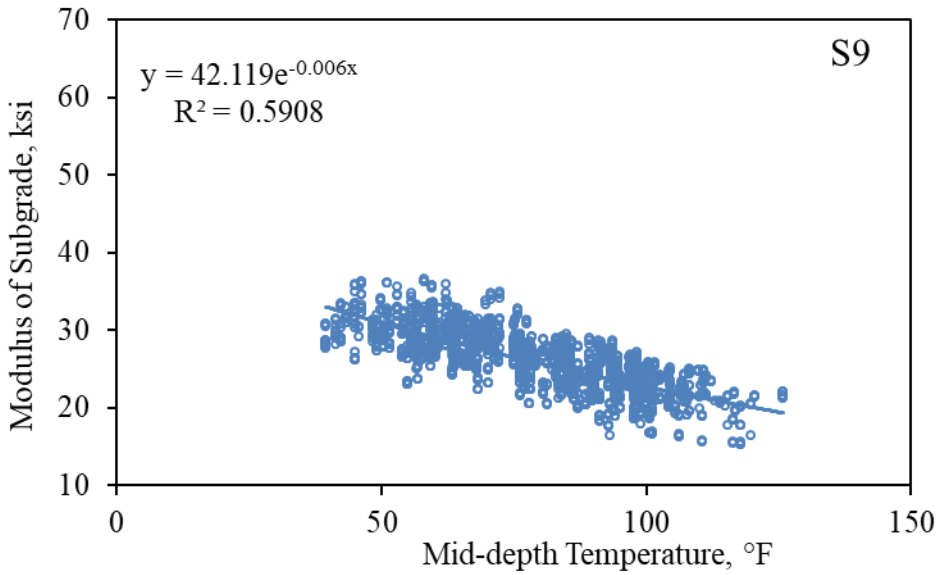

Figure 142. Backcalculated Modulus of Subgrade vs. Mid-depth Temperature, S9

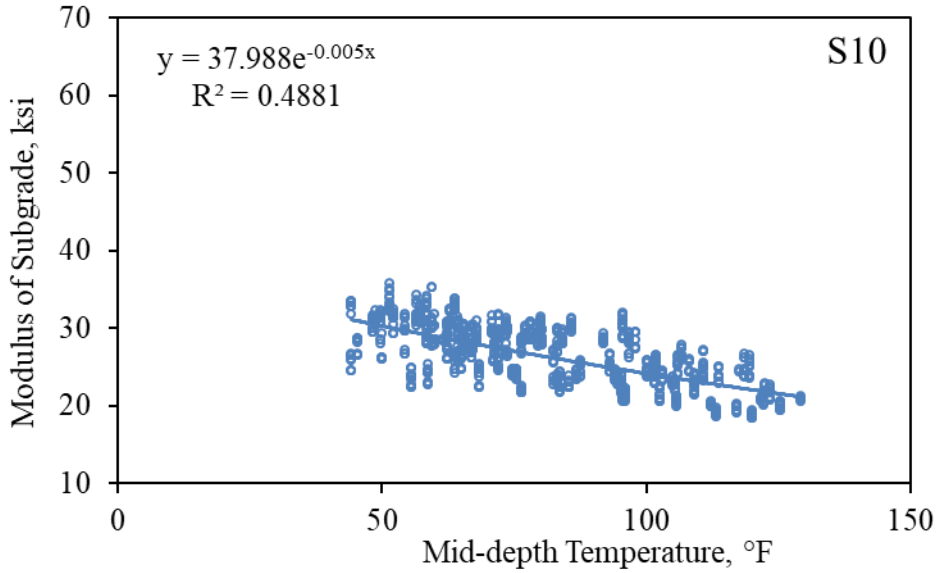

Figure 143. Backcalculated Modulus of Subgrade vs. Mid-depth Temperature, S10

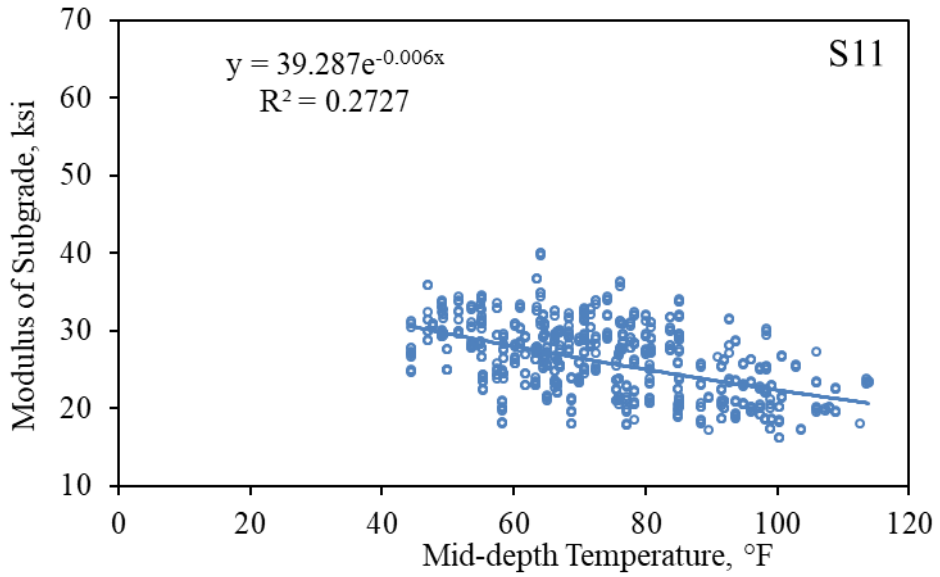

Figure 144. Backcalculated Modulus of Subgrade vs. Mid-depth Temperature, S11

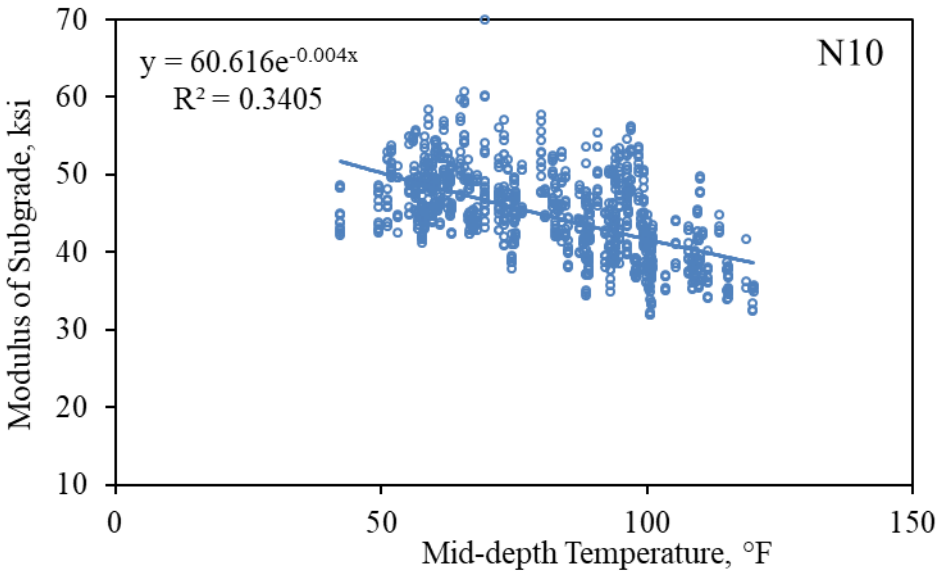

Figure 145. Backcalculated Modulus of Subgrade vs. Mid-depth Temperature, N10

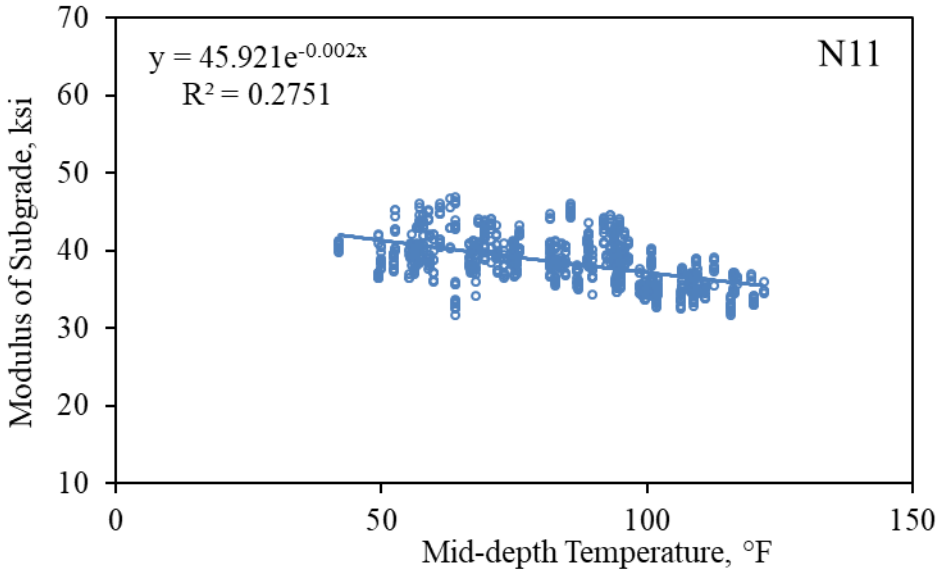

Figure 146. Backcalculated Modulus of Subgrade vs. Mid-depth Temperature, N11